Multiscale Modeling of T cells in *Mycobacterium tuberculosis* Infection

by

Louis R Joslyn

A dissertation submitted in partial fulfillment
of the requirements for the degree of
Doctor of Philosophy
(Bioinformatics)
in the University of Michigan
2021

Doctoral Committee:

Professor Denise E. Kirschner, Co-Chair
Professor Jennifer J. Linderman, Co-Chair
Assistant Professor Sriram Chandrasekaran
Associate Professor Marisa C. Eisenberg
Professor Kayvan Najarian

Louis R. Joslyn

louisjos@umich.edu

ORCID iD: 0000-0002-7260-6568

Acknowledgements

There are many individuals who supported me on this journey and contributed to my intellectual and personal development. First, I would like to thank my co-mentors, Dr. Denise Kirschner and Dr. Jennifer Linderman, for their exceptional mentorship. Denise and Jennifer are an excellent team, and I can think of no better duo for co-advisors. Denise's collaborative spirit, bold ideas, and never-say-no attitude will serve as continued inspiration throughout my career. Jennifer's professionalism, devotion to her students, and guidance through the many hurdles of academia exemplify what it means to be a research advisor. I will forever be thankful that I had the opportunity to be mentored by both Denise and Jennifer. Their energy and enthusiasm for science is contagious.

Thank you to the rest of my committee: Dr. Sriram Chandrasekaran, Dr. Marisa Eisenberg, and Dr. Kayvan Najarian, who have provided key insights, stimulating scientific conversation, and productive suggestions. Your positivity and support have been instrumental during every step of this dissertation. To Julia Eussen and the rest of the Bioinformatics staff, thank you for answering my many questions about the program, for planning departmental events, and providing general support for all the bioinformatics students.

Thank you to all members, past and present, of the Kirschner and Linderman Labs. Your scientific advice, company, support, and willingness to identify a "Friday-afternoon task" made this journey a fun one.

To my friends in Michigan and across the country, thank you for the genuinely great times. Life is easier as part of a community, and I count myself lucky to have such a fantastic community around me.

To my family, whose support provides the foundation for my growth. Mom, you are a constant source of strength, the epitome of hard work, and manage to do it all with a smile. Dad, you've shown me that finding your path sometimes involves identifying just the right key. You are the ultimate motivator. Nick, your technical abilities may only be matched by your ability to flat-out grind. You've inspired me countless times and I will forever cherish that we were able to be roommates during the past few years.

To Alex, words cannot express how much you mean to me. Thank you for your endless support, kindness, patience, and love. I look forward to our future and the next 'big adventures' that await.

Table of Contents

List of Tables

List of Figures

List of Appendices

Abstract

Tuberculosis (TB), caused by infection with *Mycobacterium tuberculosis* (Mtb), is one of the deadliest infectious diseases in the world and remains a significant global health burden. Central to the immune response against Mtb are T cells, a type of adaptive immune cell that can kill infected cells, secrete cytokines to activate other immune cells, and orchestrate the broader immune response. Over the past few decades, experimental studies have significantly furthered our understanding of T-cell biology and function during Mtb infection. However, these findings have yet to translate to a clinically effective TB vaccine. As a complementary approach to experimental studies, systems biology and computational modeling can provide context to T-cell function by describing T-cell interactions with other immune cells across multiple scales. In this thesis we utilize a systems biology approach to characterize T-cell behavior, function, and movement across multiple physiological and temporal scales during Mtb infection. In addition, we develop a whole-host model of the immune response to Mtb.

Following infection with Mtb, the immune response leads to the development of multiple lung granulomas – organized structures composed of immune cells that surround bacteria. Using a previously developed agent-based model of granuloma formation and function, we explore the role of T cells within the granuloma and predict that T-cell exhaustion, a type of T-cell dysfunction, is prevented from occurring by the physical structure of the granuloma. Next, we develop a novel whole lung model that tracks the formation of multiple granulomas. Using this model, we predict that a special type of T-cell, called a multi-functional CD8+ T cell, is key in preventing dissemination events - when bacteria escape one granuloma and seed the formation of a new one elsewhere in the lung. We also present a model of T-cell priming, proliferation, and differentiation within the lymph nodes and blood following TB vaccination and illustrate that non-human primates and humans respond similarly when receiving TB vaccination.

We mathematically link the whole lung model and lymph node and blood model to create a whole-host model of the immune response following Mtb infection. We show that this model can capture various aspects of human and non-human primate TB disease and predict that biomarkers in the blood may only faithfully represent events in the lung at early time points after infection. Using this model, we predict that resident memory T cells are important mediators of protection against reinfection with Mtb and additionally predict the lifespan of these crucial cells in humans. Finally, we develop a protocol for calibrating mathematical and computational models to experimental datasets.

Overall, this dissertation builds on our knowledge of the various roles T cells play in responding to Mtb infection, presents a set of computational models for evaluating the T-cell response to either infection or vaccination, and identifies mechanisms that control different outcomes across multiple scales following Mtb infection, reinfection, or vaccination.

1 Introduction

1.1 Motivation

Few diseases have been as continuing and ever-present in human history as tuberculosis (TB). Known under various names such as consumption, the robber of youth and the white plague, the symptomatic course of TB is referenced in the writings of Hippocrates (1), the Old Testament of the Bible (2) and ancient Chinese medical texts (3) dating back thousands of years. In just the past two centuries, TB has killed an estimated one billion people (4). *Mycobacterium tuberculosis* (Mtb), the causative agent of TB, is inhaled into the lungs and initiates the immune response. Unlike other infections, the immune response to Mtb is typically delayed due to the slow growth of the bacteria during early stages of infection (5–8). The immune response following infection leads to the development of multiple lung granulomas which serve to immunologically restrain and physically contain bacteria (9). Although antibiotic therapy can cure TB, lengthy drug treatment regimens lead to non-compliance, and multi-drug resistant cases of TB are rising worldwide. Additionally, there is currently no highly effective TB vaccine for adults. If future interventions are to be successful in eliminating TB, they require a better understanding of the mechanisms that drive a successful and protective immune response against Mtb.

T cells are key players in orchestrating an effective immune response against most pathogens. As part of the immune response during Mtb infection, T cells can kill infected cells, secrete cytokines that activate other immune cells, and generally have critical functions against Mtb (10–12). The adaptive immune response during Mtb infection is driven primarily by T cells and requires integration of events across multiple spatial and temporal scales.

While a licensed vaccine against TB, known as Bacille Calmette-Guérin (BCG), was developed approximately 100 years ago, its efficacy ranges from 0-80% in adults and it is most effective in preventing the childhood form of TB (13,14). Despite advancements within the past few

decades, promising new findings related to T-cell biology have not translated to a new clinically effective vaccine against Mtb (15). As a complementary approach to experimental studies, computational modeling can provide context to T-cell behavior in natural infection as well as vaccination scenarios by describing T-cell interactions with other immune cells and mapping T-cell behavior across multiple physiological scales.

Computational modeling can provide additional support for experimental inquiries and lead to quantitative predictions about the role of T cells in infection that can be used for clinical translation. In this thesis, I employ a systems biology approach using multiple modalities to study TB. I introduce several multi-scale mathematical and computational models that characterize T cell behavior, function, and movement during Mtb infection. Using these models, I show how T cell behaviors are affected at sites of infection, offer insight into critical T cell functions, and identify mechanisms that lead to protective immune responses during Mtb infection with implications for vaccine development.

1.2 The global impact of tuberculosis

Tuberculosis kills three people per minute worldwide and is one of the world's most common infectious diseases stretching back for millennia (16). In 2019, an estimated 10 million individuals contracted symptomatic TB disease and approximately 1.4 million people died worldwide (16). The World Health Organization estimates that approximately one-quarter of the world's population -1.8 billion people - are currently infected with Mtb (16).

Symptomatic TB, clinically described as active TB, is characterized by cough, fever, night sweats, weight loss and chest pains. Of the approximately 1.8 billion individuals infected worldwide, approximately 10% will develop symptomatic disease (16). Infected individuals that do not show symptomatic outward signs of disease may simply harbor the pathogen and are clinically characterized as latently infected (LTBI). As latent infection can persist for years, LTBI individuals represent a large reservoir of individuals that could potentially become active TB cases, if individuals become immuno-suppressed (e.g., co-infection with HIV, old age, or treated with immunosuppressive drug regimens) (17,18). While individuals are clinically defined

as latently or actively infected, it is now widely understood that infected individuals actually lie upon a spectrum of disease states that include latent and active disease (19,20).

1.3 Tuberculosis treatment and vaccines

The standard of care against TB requires an antibiotic regimen. The current World Health Organization recommended regimen treats active forms of TB using isoniazid, rifampin, ethambutol and pyrazinamide across 6 months of treatment (21). This unusually long and complicated regimen against bacterial infection reflects the difficulties of treatment against TB. Worldwide patient non-compliance, treatment withdrawal, and bacterial mutations are leading to emergent drug-resistant strains of bacteria (22). Thus, new drugs that can quickly ameliorate disease by targeting novel host or bacterial mechanisms are desperately needed to resolve the global TB epidemic.

A highly efficacious vaccine against TB would represent the ultimate weapon against TB. BCG, the world's most widely administered vaccine, is the only currently licensed vaccine against TB. BCG has been used as a live attenuated vaccine against TB since 1921 but only has acceptable efficacy against childhood forms of TB and variable efficacy in adults (13,14,23,24). Currently, there are 12 TB vaccines in various stages of clinical trials (15). These candidate vaccines employ diverse formulations that attempt to stimulate different aspects of the immune system. The candidates include attenuated versions of Mtb, mycobacterial whole-cell vaccines, viral-vector vaccines and subunit vaccines, with the later formulization utilized heavily in TB vaccine efforts of the past decade (25,26). In order to achieve the ambitious goals of the 'EndTB' strategy to eliminate TB by 2050 (27), the world requires a highly efficacious vaccine that outperforms BCG's current protective profile. To this date, that goal has not been met in clinical trials.

There are multiple theories as to why an efficacious vaccine against TB has been elusive (15,25,28–32). Global funding commitments are diminishing and fail to provide adequate resources for TB researchers worldwide (33,34). However, beyond resources and global focus, the most prominent reason for the lack of a highly efficacious TB vaccine is that little is known about the mechanisms of a truly protective immune response against Mtb. Risk factors, genetic defects, and deletion studies have identified mechanisms of a poor host immune response, but

questions still persist about what constitutes a protective immune response and why the majority of infections are latent (29,35). Further, the route of administration for a vaccine may impact its efficacy and altering the route of administration may provide maximal protection (36). If armed with a better understanding of the immune response to Mtb, we could develop effective vaccines against TB.

1.4 The immune response to Mtb and the formation of tuberculosis granulomas

Infection begins when a pathogen enters the body. In TB, pathogen encounter begins when an individual inhales Mtb that are expelled within aerosolized droplets from the cough or breath of a contagious individual (37). Upon landing within the lower respiratory tract of the lung environment, Mtb actuates the innate immune response and Mtb is phagocytized by alveolar macrophages (38). Intracellular Mtb are able to replicate within the environment of the macrophages and are able to avoid being killed during phago-lysosomal fusion (39,40). Eventually, Mtb initiate cellular lysis and burst from the infected macrophage (Figure 1), stimulating phagocytosis by nearby macrophages (41–43). These macrophages secrete molecules, i.e. cytokines and chemokines, to signal the recruitment of more monocytes from the blood, including neutrophils, macrophages and dendritic cells, to the site of infection.

Together, this recruitment forms the beginnings of a granuloma, the pathological hallmark of TB (44). The granuloma, a mass of immune cells that surround bacteria in a typically spherical structure, is an attempt by the immune system to isolate and eliminate bacteria and plays a central role in disease dynamics. Multiple granulomas form following infection as granuloma development can begin with as few as a single initial bacterium entering the pulmonary alveoli (45). Activated macrophages surround infected macrophages and extracellular bacteria at the center of the granuloma. Dendritic cells sample antigen from within the granuloma and migrate to the lung-draining lymph nodes (LN) to stimulate the adaptive immune system, i.e. the development of antigen specific lymphocytes (B- and T-cells). Upon priming, and differentiation, effector T cells generated within the LN enter the blood (Figure 1.1) and circulate throughout the body until they are recruited to the sites of infection by chemotactic signals. T cells recruited to the lung environment in response to an Mtb infection migrate to the site of the granuloma and form a lymphocytic cuff that constitutes the outer layer of the granuloma (Figure

1.1). T cells play crucial roles in antimicrobial processes through cytokine secretion, induction of macrophage activation and apoptosis, and cellular mediated killing (11,12,46–53). However, compared to other infectious diseases, T cells are slow to enter the granuloma environment and only arrive in large numbers approximately one month following infection (8). The slow arrival of this critical cell type mirrors the slow growth of Mtb at early stages of infection, which delays 'danger signals' necessary for a prompt T-cell response (7).

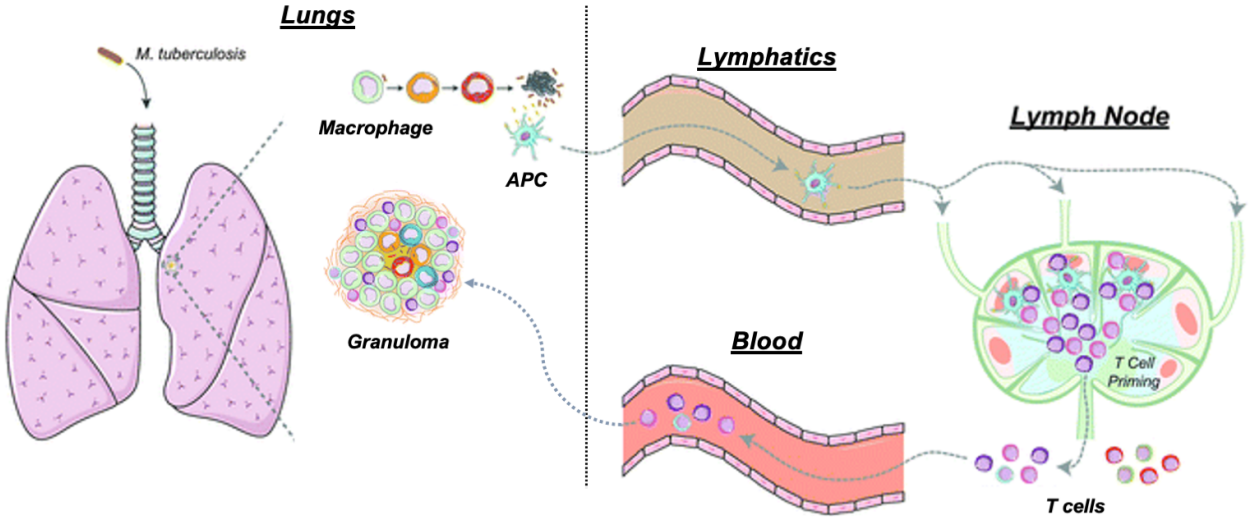

Figure 1.1 Overview of the immune response and granuloma formation during Mtb infection.
Mtb infection is a complex process that occurs across multiple time scales and organs. Following inhalation of the bacteria by the host, the innate immune response is activated. Mtb is phagocytized and replicates within macrophages, eventually bursting from within the macrophages to the local lung environment. More monocytes (precursors to macrophages) are recruited to sites of infection. Antigen presenting cells sample antigens within the infected tissues, traffic through the lymphatics system and enter a lung-draining lymph node wherein they prime a T-cell response. T cells migrate through blood and enter the lung environment approximately 1 month following inhalation of Mtb, initiating an adaptive immune response at the site of infection. Together, immune cells surround Mtb, completing the formation of the granuloma. Figure adapted from (54).

Across time, granulomas reflect an on-going battle between host and pathogen. From the perspective of the host, a successful granuloma employs a balanced immune response to contain the pathogen to a local environment within the lung and halts the spread of bacteria throughout the host (Figure 1.2). From the perspective of the pathogen, the bacteria are physically protected from the immune system by the structure of a granuloma, such that Mtb can persist in an unaffected manner for years. Importantly, this battleground between host and pathogen is highly dynamic across time (55). Should the host immune response be successful, granulomas will

sterilize the bacteria and eventually resolve. However, should the pathogen succeed, granulomas are unable to control bacterial growth, leading to bacterial escape and dissemination to other spots in lung, or even elsewhere in the body. Not much is known about the exact mechanisms of bacterial escape and dissemination across the lung (56). In Chapter 3, we develop a whole-lung model of Mtb infection to predict mechanisms of dissemination.

Multiple granulomas develop within a single host and intuition suggests that all granulomas must indirectly influence one another through recruitment and stimulation of the same host immune system. However, each granuloma takes a heterogeneous course of development over time (45), perhaps due to the structure of the local lung environment, granuloma location relative to blood vessels or airways, or heterogeneity of cell types present within the granuloma (57). Little is known about the factors that control differential outcomes in patients across the course of disease, but it is speculated that all the granulomas in a single host collectively shape the course of disease (20), perhaps through their shared interactions with the adaptive immune system. In Chapter 5, we develop a whole-host modeling framework and predict heterogeneous whole-host outcomes in TB are driven primarily by proliferation and differentiation of T cells within the lung-draining lymph nodes during early stages of infection.

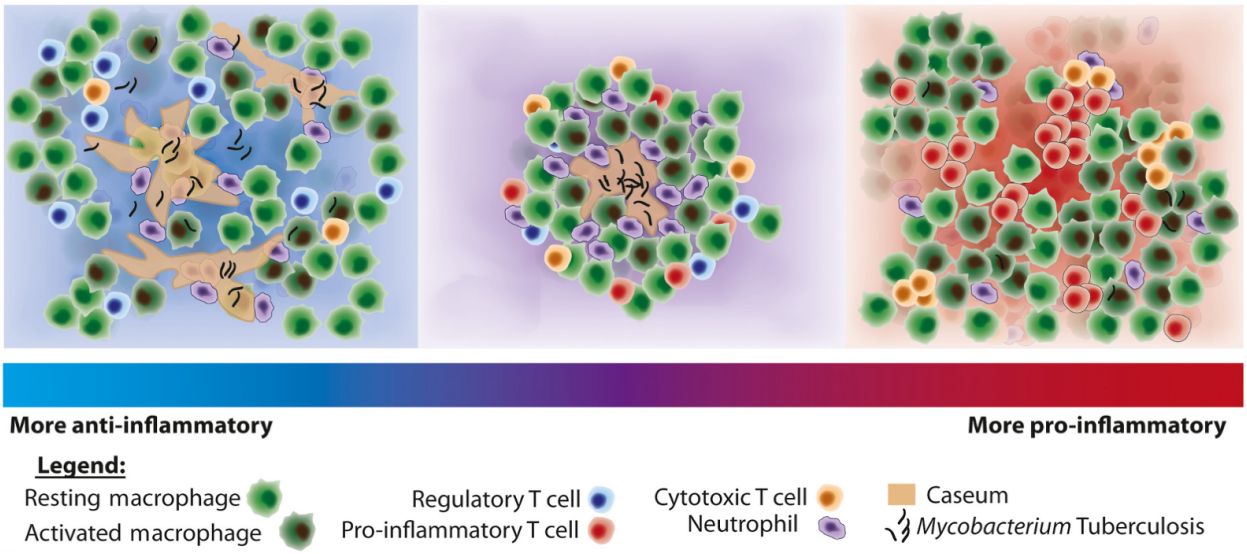

Figure 1.2 A dynamic, balanced immune response contains Mtb to the granuloma.
Conceptual images of granuloma formation across a spectrum of anti-inflammatory or pro-inflammatory responses. A balanced immune response contains Mtb and results in proper granuloma formation but may not always sterilize

bacteria. We list the main cellular mediators of pro- and anti-inflammatory responses. Note, T-cells play a role in both pro- and anti-inflammatory responses and contribute to cell death via cytotoxicity. Figure adapted from (55).

1.5 T cells and their role in the immune response to Mtb infection

1.5.1 Antigen specificity and naïve T cells

When an infecting pathogen evades or survives the innate immune response, it activates the adaptive immune response, a critical aspect of which is the T cell, a type of lymphocyte that expresses T cell antigen receptors (TCRs) on its surface. T cells are generated within a lymphoid organ called the thymus and undergo maturation and thymic education through positive and negative selection – a complex process through which cells are genetically selected to recognize specific molecular structures called antigen (58). Following maturation, naïve T cells circulate between blood and lymphoid organs in search of antigen for which they are 'specific' (i.e. they have been selected to recognize a specific foreign antigen through the maturation process). The frequency of cells that are specific to each antigen is very low, ranging as low as 1 per million cells or less due to the inherent diversity of TCRs (59). When these matches are found, naïve T cells undergo activation and differentiation.

T cells can only recognize an antigen presented within the proper context. That is, TCRs will only selectively bind to antigen that has been mounted and presented onto specialized molecules called major histocompatibility complexes (MHC). Together, the antigen and MHC complex displayed on the cell surface of an antigen presenting cell (APC) is called peptide-MHC. Endogenous antigens are presented through the MHC class I pathway of antigen presentation, which can be recognized by CD8+ T cells. In contrast, exogenous antigens, such as pathogenic proteins are loaded on MHC class II complexes and can be recognized by CD4+ T cells. Upon activation, CD4+ T cells provide helper functions by modulating and stimulating the functions of other immune cells, whereas CD8+ T cells directly kill infected host cells.

1.5.2 Priming, differentiation and effector expansion

T cell priming occurs when a naïve T cell encounters its specific antigen and binds with the APC for an extended period of time, typically within the lymph nodes. Priming acts to accumulate activation signals within a T cell prior to cellular proliferation and differentiation. Priming, proliferation and differentiation of T cells is central to the effector expansion phase necessary to

carry out an adaptive immune response. Simply put, effector expansion is an effort by the body to optimize the immune response by creating a large number of T cells that can all respond to the same antigen.

In addition to TCR and co-stimulatory signals (reviewed in (60)), cytokines play an important role in polarizing T cell proliferation and differentiation toward the generation of effector cells with a certain functional phenotype (61). For example, interleukin-12 (IL-12) production by APCs direct CD4+ precursors to differentiate to a Th1 cell type: a cell that typically produces large levels of interferon gamma (IFN-γ) (62). After differentiation and effector expansion, T cells exit the lymph nodes and travel through the blood stream for recruitment to the sites of infection.

During chronic antigen stimulation, a subpopulation of T cells will exhibit a type of dysfunction epitomized by the loss of functional and proliferative capabilities. This type of dysfunction is called T cell exhaustion and can be phenotypically characterized by a series of inhibitory receptors, the most studied of which include PD-1 CTLA-4 and LAG-3 (63,64). In cancer and chronic viral infections, this subpopulation has been fairly well-defined, and a blockade of these inhibitory receptors has even reversed exhaustion to rescue T cell functional capabilities (65,66). In TB, T-cell exhaustion is relatively understudied, and further research could provide important clues to infection dynamics within the granuloma. In Chapter 2, I investigate T-cell exhaustion using an *in silico* model of granuloma formation paired with experimental studies by collaborators. We show that granuloma structure actually prevents widespread T-cell exhaustion.

1.5.3 Memory T cells

In most infections, the vast majority of effector T cells generated during immune response die as an immune response wanes, and only a small fraction persists as long-lived memory cells. These cells, unified by their relatively long lifespans and ability to generate a quick response upon pathogen re-encounter, can be delineated into three major cell populations: effector memory T cells, central memory T cells and resident memory T cells. Each of these populations can be chiefly separated according to physiologic location: effector memory T cells recirculate between blood and tissue and lack lymph node homing receptors, whereas central memory T cells circulate between blood and lymph nodes but are not thought to migrate into tissue (67). Newly

identified resident memory T cells are a non-circulatory cell type that resides within the previously infected tissue. Effector memory T cells and resident memory T cells are thought to derive from effector cells and readily exert effector function to contain pathogen upon reinfection (68–71). Whereas resident memory T cell longevity is not yet known, effector memory T cell survival is not thought to be as durable as central memory T cells, whose continued maintenance can last through an entire lifetime in an antigen-independent manner (72).

1.5.4 T cells in TB

In the human immune response to Mtb infection, the adaptive immune response is primarily composed of CD4+ T cells that play critical roles and functions against Mtb. Unlike other infections, T cells are slow to enter the site of infection within the lungs and arrive in large numbers approximately one month after primary infection. In fact, this delayed onset of adaptive immunity is a prominent characteristic of TB immunology and pathology and is thought to originate due to the delayed migration of APCs to the lymph node (5). The reason for this delay is unclear but is thought to originate due to the slow growth of Mtb within the lungs, which delays 'danger signals' necessary from prompt immune response (7). Upon activation, effector expansion, and arrival into the lung environment, T cells surround the outer layers of the granuloma in a characteristic lymphocytic cuff spatial configuration.

1.5.5 CD4+ T cells

It is well established within TB literature that a CD4+ Th1 response is required for resistance against Mtb infection (73). In fact, the Tuberculin Skin Test (TST) - a popular TB test wherein tuberculin is injected intradermally - takes advantage of a CD4+ T cell driven delayed hypersensitivity reaction to identify individuals who are currently or have previously been infected with Mtb. In both mice and NHP experiments, animals with deficiencies in CD4+ T cells have increased susceptibility to Mtb (10,74). Further, humans with HIV infection have a depleted CD4+ T cell population and are at increased risk of developing active TB (75).

CD4+ T cells secrete cytokines that have critical functions against Mtb and assist in orchestrating the broader immune response to Mtb. IFN-γ is a cytokine secreted by CD4+ T cells that is a driving factor for the resistance against Mtb (10,76), as evidenced by the susceptibility of

individuals born with genetic mutations that affect IFN-γ production (77). While IFN-γ can be secreted by other cells, work in mice has shown that IFN-γ derived from CD4+ T cells is critical to control Mtb and IFN-γ from other cells is not sufficient for protection (78). Not all CD4+ T cells exhibit a single functionality or secrete only a single cytokine. Poly-functional CD4+ T cells are T cells that can produce multiple cytokines (79). Typically, these include IFN-γ, TNF-α, and IL-2, where TNF-α and IFN-γ can act synergistically to enhance the ability of macrophages to contain intracellular Mtb (80), and IL-2 induces proliferation and activation of other T cells. In addition to synergistic interactions with IFN-γ, TNF-α has known critical functions against Mtb from pharmacological blockade, knock-out and modeling studies (17,81,82). Despite these known functions against Mtb, the potential of polyfunctional CD4+ T cells as a correlate of protection is still uncertain. Contradictory evidence suggests that polyfunctional CD4+ T cells are associated with both resistance to Mtb and susceptibility to Mtb (reviewed in (79,83)). Therefore, much still remains unknown about the mechanisms CD4+ T cells employ in a protective response against Mtb.

1.5.6 CD8+ T cells

Known primarily for their capacity to kill infected cells via secretion of granzymes and perforin, CD8+ T cells can also secrete cytokines such as IFN-γ or TNF-α (84). Changes in CD8+ T cell function have been described during active TB (85). Compared to latently infected or healthy patients, active TB cases had circulating Mtb-specific CD8+ T cells that showed reduced cytotoxic activity (86). In another study of active TB disease, CD8+ T cells located within granulomas also showed impaired expression of granulysin and cytotoxic function, suggesting CD8+ T cell dysfunction may lead to more progressive forms of TB disease (87). Data from previous modeling efforts (50) and non-human primate studies (47) have shown support for the critical role of both cytokine production and cytotoxic CD8+ T cell functions against Mtb. Despite this emerging evidence, CD8+ T cells are understudied in TB relative to CD4+ T cell populations but offer an intriguing target for future therapies against Mtb.

1.6 Experimental Models in TB

The computational and mathematical models I develop in this dissertation are calibrated to multiple experimental datasets. In particular, various animal models have been helpful to understanding of TB pathology and immunology. Key species that have been used include mice,

zebrafish, rabbits, guinea pigs and non-human primates (88). Depending on the scientific question at-hand, these experimental models have varying utility. For example, mice may represent an animal more inclined toward progressive disease studies than rabbits, which are relatively resistant to infection as an experimental model and have traditionally been used in treatment evaluation studies (89).

1.6.1 Mice

Due to their short life cycle, cost-effectiveness, and the abundance of genetic resources, mice are perhaps the most used animal model in all of biomedical science. In TB research, mouse models remain the preferred animal model. However, despite a relatively similar immune response as humans, mice have a distinctly unique disease pathology, wherein inflammatory but non-necrotic granulomas form in the popular mouse models BALB/c and C57BL/6 (90). Additionally, the mouse model does not exhibit latent stages of infection, but rather exhibits a chronic state of elevated bacterial load that eventually progresses to bacteremia and morbidity. In contrast, the human bacterial burden is considerably reduced following the onset of adaptive immunity.

Recently, some techniques have enabled the mouse model of TB to better recapitulate aspects of latent infection. Notably, these include the 'Kramnick mouse model' (a mouse strain with a recessive allele, C3HeB/FeJ mice) and the ultra-low dose model of infection. The Kramnick model develops necrotic granulomas that are highly encapsulated, but disease is highly progressive, and the mice are considered to have a 'super-susceptibility to tuberculosis' (91). The ultra-low dose model inoculates C57BL/6 (B6) mice with a 1-3 bacterium of Mtb (H37Rv) strains and shows promise in recapitulating necrotic, well-formed granulomas that exhibit heterogeneity in overall bacterial burdens and disease outcomes (92). However, this model has yet to be adopted by the wider TB research community.

1.6.2 Non-human primates

Non-human primates (NHP) were first used in the mid 20th century to study antituberculosis drugs (93) and have re-emerged as the animal model that most faithfully represents the spectrum of TB outcomes. Depending on experimental design and species, NHPs can exhibit active, latent and reactivation TB. Cynomolgus macaques can develop either latent or active TB, whereas rhesus macaques are relatively more susceptible to Mtb (94). All NHPs are outbred, and typically

infected with a low-dose of Mtb. NHP studies have used PET-CT imaging to monitor disease progression or treatment efficacy across time (94). Further, NHPs are able to capture a heterogeneous array of granuloma outcomes and bacterial burdens within a single monkey (94–97). There are, however, significant disadvantages to the NHP model. In addition to animal rights concerns, animals require BSL-3 facilities, require significant financial resources and reagents are not as readily available as other animal models.

1.7 Computational models of TB

1.7.1 Multiscale Modeling

Reductionist approaches in science, used to dissect biological systems into parts and identify the role of each part in isolation, have proven to be very powerful in understanding the fundamental principles of each part. However, within the human body, biological processes require the simultaneous action of systems of molecules and processes, take place across multiple spatial and temporal scales, and require interactions between scales in order to yield the phenomena that is empirically evident. In particular, the immune response during Mtb infection requires the integration of multiple events across cellular, tissue, and multi-organ scales, across time scales ranging from seconds to years. Systems biology and multi-scale modeling are approaches that offer a way to embrace this complexity and connect these multiple phenomena into a framework that can be used to better understand the role the adaptive immune system during granuloma formation, development and maintenance as well as the broader role for the adaptive immune system in host-level TB outcomes. Formally, multiscale modeling is a mathematical or computational model that accounts for more than one level within the spatial or temporal domains (98). Modeling approaches complement experimental studies, as predictions and observations from one modality can be tested or validated in the other.

1.7.2 Ordinary differential equations and agent-based models capture immune response within the lung

Ordinary differential equation (ODE) models and agent-based models (ABMs) are two types of models that can be employed within a multi-scale modeling framework. ODE models are a type of continuous mathematical model that has been formulated to capture the average behaviors of species (or populations) over time. In particular, within TB, ODEs were used as the first

modeling platform to capture overall lung dynamics following infection (99,100). Additionally, these models have been used to describe macrophage presentation of bacteria (101), and explain the impact of macrophage polarization on granuloma outcome (102).

Unlike ordinary differential equation modeling, agent-based modeling (ABM) (also known as individual-based modeling) is a stochastic, discrete modeling framework that tracks the interactions of agents (discrete entities) across spatial and temporal scales. Each agent behaves according to a set of rules and interactions on a predefined environment. Importantly, within ABMs, heterogeneity arises naturally as ABMs are able to generate a complex, systems emergent behavior from a set of rule-based descriptions. ABMs were used as the first spatial modeling framework of granuloma formation, in a framework that tracked multiple immune cell and bacterial interactions across time, where the emergent behavior of the model was granuloma formation (103). This ABM framework, called *GranSim*, became explicitly multi-scale with the introduction of receptor-ligand dynamics, described by a system of ODEs, and molecular diffusion (represented as partial differential equations) (82,104). Predictions using one modeling technique can be further validated within another model system. For example, the role of TNF and drug binding kinetics during TB reactivation was a prediction that was validated both in an ODE model (81) and an ABM platform (105). ABM and ODE model formulations within TB are extensively covered in a review of all TB models (106).

1.7.3 Models of T-cell responses within the lung-draining lymph node

Historically, ODEs represent the preferred model of choice when tracking T cell dynamics. For example, ODEs have been used to predict T cell turnover and *in vivo* death rates (107), predict T cell homeostasis and thymic flux kinetics (108), and describe T cell dynamics in response to infection (109). Additionally, ODE models have been used extensively to investigate within-host dynamics of T cells during HIV infection ((110,111), reviewed in (112)). Finally, ODEs have the resolution necessary to explain contradicting hypothesis in T cell literature, as shown by the use of CD8+ T cell differentiation models (113).

There have been several efforts to model the initiation of adaptive immunity within a lung draining lymph node. For example, Marino et al. developed a mathematical model of T cell priming in lymph nodes and eventual migration to the lungs to display that inoculation dose does

not influence priming of T cell responses in mice lymph nodes (114). Additionally, Gong et al. utilized a 3D ABM and ODEs to model T cell generation within the lymph node and lymph node output (68,115). In particular, ODE models of T cell activation and differentiation have proven especially useful as a sub-compartment within a hybrid multi-scale model, as they provide a coarse-grained approximation of the events that yield an adaptive immune response (116–119). As such, they offer potential utility within a larger, whole-host model of Mtb infection.

1.7.4 Whole host modeling efforts

As Mtb infection is a process that involves more than just a single granuloma and a lymph node several efforts have been made to scale in-host modeling frameworks to a whole host. First among these efforts are two compartment models that link the lymph node and lung. Several two-compartment models have captured cellular activation and priming within the lymph node as well as cellular movement between lung and lymph nodes (114,120–122). Additionally, several models have linked individual granulomas to lung-draining lymph nodes (102,116). On the whole, these studies have found that mechanisms leading to the generation of greater CD4+ T-cell priming and activation may be key to sterilizing bacteria within an established or developing granuloma.

Other efforts have included three-compartment models that capture the physiological granuloma, lymph nodes and blood compartments across time. These modeling frameworks predicted potential biomarkers for infection outcomes (118) and improved representation of dendritic cell trafficking into the lymph node (123). In contrast, others have used a bubble modeling framework to track the development of multiple granulomas within a single lung across time, although this framework did not specifically model events at the granuloma scale (124,125). The natural next step is to integrate blood and lymph node models, together with a whole-lung modeling framework in order to develop a modeling framework that can be used to study adaptive immune responses to Mtb, identify mechanisms related to whole-host outcomes, and, in the future, test various therapeutic interventions on a virtual patient. In Chapter 5, I present a whole-host modeling framework.

1.8 Calibrating and evaluating computational models

1.8.1 Calibrating complex models

Prior to making useful predictions about relationships and mechanisms between various biological agents, a model must be able to replicate experimental outcomes and recapitulate the known temporal dynamics of the represented biological system. Formally, the process of model calibration is the altering of model inputs (initial conditions and/or parameters) until model outcomes satisfy one or more criteria. These criteria are typically experimental data that model outcomes should match across time.

There is a large literature that covers calibration of mathematical models. As reviewed in Read et al., popular approaches can leverage the power of optimization schemes to minimize the difference between experimental data and model outcomes (126). However, not all models can or should be minimized to a single metric for each outcome. Bayesian calibration approaches represent a suite of techniques that have been used to successfully identify regions of parameter space wherein the distribution of model outcomes matches the distribution of experimental outcomes (127–129). However, if the distribution of experimental outcomes cannot be sufficiently derived from the experimental data, or a modeler requires a continuous parameter space for their calibrated model, Bayesian calibration techniques might not be the best approach. As such, there is an opportunity for new calibration protocols that can improve upon previous Bayesian calibration efforts should a modeler find themselves with such constraints. In Chapter 6, I develop a new calibration protocol that utilizes parameter density estimate to calibrate complex biological models.

1.8.2 Evaluating models with uncertainty and sensitivity analysis

Modeling of complex biological systems often incorporates large numbers of interactions between model components across time. Uncertainty and sensitivity analysis approaches provide interpretability for these models by relating variability in model outputs and model inputs to identify the key drivers of a system outputs. Formally, uncertainty analysis measures variability in model output generated by variability in model input, whereas sensitivity analysis assesses how different model inputs can be apportioned to variations in model outputs (106,130).

As complex biological system models are too large for analytical evaluation of local parameter sensitivity, global sensitivity analysis tools are the best approach. In particular, partial rank

correlation coefficients (PRCC) is a global method that can be used to detect non-linear monotonic relationships between lists of parameter combinations and subsequent simulation outcomes. Typically, this process begins with a Latin Hypercube Sampling (LHS) to sample the parameter space and generate the lists of parameter combinations (130). Although, other efficient sampling schemes, such as Sobol Sequences (131), can be utilized to sample parameter space.

In TB modeling, these approaches can not only help establish relationships between model outcomes and parameters, but provide a guide for parameter estimation, identify critical mechanisms within the system as a whole, and help with model tuneability (117). Sampling and sensitivity analysis techniques are used throughout this dissertation to compare computational model outcomes to experimental datasets and perform analysis of the computational models.

1.9 Dissertation Summary

In this thesis, I employ a multi-scale modeling approach to understand the mechanistic role of T cells during the immune response to Mtb infection (Figure 3). In particular, I first perform a study where I investigate the spatial dynamics of T cells in TB granulomas and predict that the granuloma structure itself may prevent a form of T-cell dysregulation called T-cell exhaustion. In Chapter 3, I present a whole lung model and characterize the role that T cells play in preventing spread of bacteria throughout the lung. In Chapter 4, I utilize a lymph node and blood model that tracks the T-cell response to Mtb antigens and show similarities between the NHP and human response to a TB vaccine. In Chapter 5, I utilize the two modeling frameworks presented in Chapters 3 and 4 to develop a whole-host modeling framework and identify mechanisms that lead to controlled or uncontrolled disease. I further utilize the whole-modeling framework to identify T cells as main mediators of protection against reinfection with Mtb. Finally, in Chapter 7, I present a method for calibrating complex, multi-scale modeling frameworks. Throughout this thesis, I characterize T cell responses across and within various organs and at the site of infection. This dissertation highlights the important, and often protective roles, of T cells in driving the heterogeneity of TB disease and infection outcomes across cellular, tissue, and whole-host scales (Figure 1.3). Finally, this dissertation presents a whole-modeling framework of Mtb infection that has future implications for evaluating therapeutics against TB.

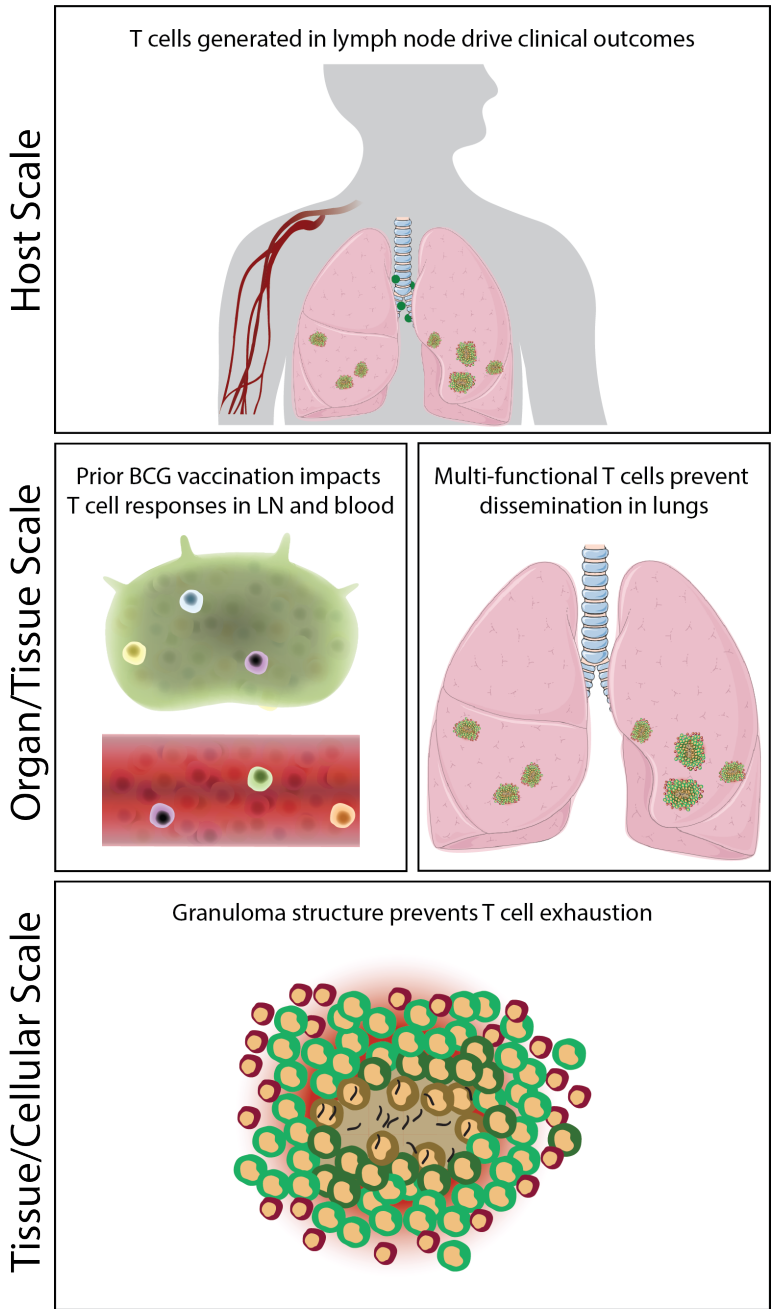

Figure 1.3 Multiscale modeling of T-cell response during Mtb infection.
Throughout this dissertation, we employ computational modeling techniques to track spatiotemporal interactions across multiple scales occurring between T-cells, other immune cells, and bacteria during Mtb infection and vaccination scenarios. Beginning at the cellular and tissue scale, we use an ABM model called GranSim to show that the granuloma structure prevents T-cell exhaustion. We then develop and present a multiple-granuloma model of infection within the lungs and predict multi-functional T cells present dissemination of bacteria. Additionally, we show that prior BCG vaccination can impact the T-cell response to vaccines currently in the clinical trial pipeline. Finally, we present a whole-host modeling framework of Mtb infection and predict T cells as drivers of heterogenous clinical outcomes in TB as well as cellular mediators of protection against reinfection. Lung image adapted from Medical Servier Art.

1.10 References

1. Maczel M, Dutour O. The bioarchaeology of tuberculosis: a global view on a reemerging disease. C.A. Roberts & J.E. Buikstra. University Press of Florida, Gainesville, 2003. 344 pp. ISBN 0-8130-2643-1. International Journal of Osteoarchaeology [Internet]. 2005;15(5):385–6. Available from: https://onlinelibrary.wiley.com/doi/abs/10.1002/oa.741
2. Daniel VS, Daniel TM. Old Testament Biblical References to Tuberculosis. Clinical Infectious Diseases [Internet]. 1999 Dec 1;29(6):1557–8. Available from: https://doi.org/10.1086/313562
3. Brothwell D, Sandison AT. Diseases in antiquity. A survey of the diseases, injuries and surgery of early populations. Diseases in antiquity A survey of the diseases, injuries and surgery of early populations. 1967;
4. Fauci AS. Addressing the Tuberculosis Epidemic: 21st Century Research for an Ancient Disease. JAMA [Internet]. 2018 Oct 2;320(13):1315–6. Available from: https://doi.org/10.1001/jama.2018.12852
5. Ernst JD. The immunological life cycle of tuberculosis. Nature Reviews Immunology [Internet]. 2012;12(8):581–91. Available from: https://doi.org/10.1038/nri3259
6. Wolf AJ, Desvignes L, Linas B, Banaiee N, Tamura T, Takatsu K, et al. Initiation of the adaptive immune response to *Mycobacterium tuberculosis* depends on antigen production in the local lymph node, not the lungs. The Journal of experimental medicine [Internet]. 2007/12/24. 2008 Jan 21;205(1):105–15. Available from: https://pubmed.ncbi.nlm.nih.gov/18158321
7. Matzinger P. The evolution of the danger theory. Interview by Lauren Constable, Commissioning Editor. Expert review of clinical immunology [Internet]. 2012 May;8(4):311–7. Available from: https://pubmed.ncbi.nlm.nih.gov/22607177
8. Urdahl KB, Shafiani S, Ernst JD. Initiation and regulation of T-cell responses in tuberculosis. Mucosal Immunology [Internet]. 2011;4(3):288–93. Available from: https://doi.org/10.1038/mi.2011.10
9. Ehlers S, Schaible U. The Granuloma in Tuberculosis: Dynamics of a Host–Pathogen Collusion. Frontiers in Immunology [Internet]. 2013;3:411. Available from: https://www.frontiersin.org/article/10.3389/fimmu.2012.00411
10. Diedrich CR, Mattila JT, Klein E, Janssen C, Phuah J, Sturgeon TJ, et al. Reactivation of latent tuberculosis in cynomolgus macaques infected with SIV is associated with early peripheral T cell depletion and not virus load. PLoS ONE. 2010;5(3).
11. Yao S, Huang D, Chen CY, Halliday L, Wang RC, Chen ZW. CD4 + T Cells Contain Early Extrapulmonary Tuberculosis (TB) Dissemination and Rapid TB Progression and Sustain Multieffector Functions of CD8 + T and CD3 − Lymphocytes: Mechanisms of CD4 + T Cell Immunity . The Journal of Immunology. 2014;192(5):2120–32.
12. Sakai S, Mayer-Barber KD, Barber DL. Defining features of protective CD4 T cell responses to *Mycobacterium tuberculosis*. Vol. 29, Current Opinion in Immunology. 2014. p. 137–42.
13. Sterne JAC, Rodrigues LC, Guedes IN. Does the efficacy of BCG decline with time since vaccination? International Journal of Tuberculosis and Lung Disease. 1998;2(3):200–7.
14. Pitt JM, Blankley S, McShane H, O'Garra A. Vaccination against tuberculosis: How can we better BCG? Microbial Pathogenesis [Internet]. 2013;58:2–16. Available from: https://www.sciencedirect.com/science/article/pii/S0882401012002070
15. Andersen P, Scriba TJ. Moving tuberculosis vaccines from theory to practice. Nature Reviews Immunology. 2019.

16. WHO. WHO Global Tuberculosis Report 2019. World Health Organization Press. 2019.
17. Harris J, Keane J. How tumour necrosis factor blockers interfere with tuberculosis immunity. Clinical & Experimental Immunology [Internet]. 2010 Jul 1;161(1):1–9. Available from: https://doi.org/10.1111/j.1365-2249.2010.04146.x
18. Keane J, Bresnihan B. Tuberculosis reactivation during immunosuppressive therapy in rheumatic diseases: diagnostic and therapeutic strategies. Current Opinion in Rheumatology [Internet]. 2008;20(4). Available from: https://journals.lww.com/co-rheumatology/Fulltext/2008/07000/Tuberculosis_reactivation_during_immunosuppressive.13.aspx
19. Lin PL, Flynn JL. The End of the Binary Era: Revisiting the Spectrum of Tuberculosis. The Journal of Immunology. 2018;201(9):2541–8.
20. Barry CE, Boshoff HI, Dartois V, Dick T, Ehrt S, Flynn JA, et al. The spectrum of latent tuberculosis: Rethinking the biology and intervention strategies. Vol. 7, Nature Reviews Microbiology. 2009. p. 845–55.
21. Nahid P, Dorman SE, Alipanah N, Barry PM, Brozek JL, Cattamanchi A, et al. Executive Summary: Official American Thoracic Society/Centers for Disease Control and Prevention/Infectious Diseases Society of America Clinical Practice Guidelines: Treatment of Drug-Susceptible Tuberculosis. Clinical Infectious Diseases [Internet]. 2016 Oct 1;63(7):853–67. Available from: https://doi.org/10.1093/cid/ciw566
22. Palomino JC, Martin A. Drug Resistance Mechanisms in *Mycobacterium tuberculosis*. Antibiotics (Basel, Switzerland) [Internet]. 2014 Jul 2;3(3):317–40. Available from: https://pubmed.ncbi.nlm.nih.gov/27025748
23. Trunz BB, Fine PEM, Dye C. Effect of BCG vaccination on childhood tuberculous meningitis and miliary tuberculosis worldwide: a meta-analysis and assessment of cost-effectiveness. The Lancet. 2006;367(9517):1173–80.
24. Fine PEM. Variation in protection by BCG: implications of and for heterologous immunity. The Lancet. 1995;346(8986):1339–45.
25. Ahsan MJ. Recent advances in the development of vaccines for tuberculosis. Therapeutic Advances in Vaccines [Internet]. 2015;3(3):66–75. Available from: http://journals.sagepub.com/doi/10.1177/2051013615593891
26. Hatherill M, White RG, Hawn TR. Clinical Development of New TB Vaccines: Recent Advances and Next Steps. Frontiers in Microbiology [Internet]. 2020;10:3154. Available from: https://www.frontiersin.org/article/10.3389/fmicb.2019.03154
27. Uplekar M, Weil D, Lonnroth K, Jaramillo E, Lienhardt C, Dias HM, et al. WHO's new end TB strategy. Vol. 385, The Lancet. 2015. p. 1799–801.
28. Davenne T, McShane H. Why don't we have an effective tuberculosis vaccine yet? Expert review of vaccines [Internet]. 2016/05/03. 2016 Aug;15(8):1009–13. Available from: https://pubmed.ncbi.nlm.nih.gov/27010255
29. Nagelkerke NJD, de Vlas SJ, Mahendradhata Y, Ottenhoff THM, Borgdorff M. The search for a tuberculosis vaccine: An elusive quest? Tuberculosis [Internet]. 2006;86(1):41–6. Available from: https://www.sciencedirect.com/science/article/pii/S1472979205000491
30. Ginsberg AM, Ruhwald M, Mearns H, McShane H. TB vaccines in clinical development. Tuberculosis. 2016;99:S16–20.
31. Andersen P, Doherty TM. Opinion: The success and failure of BCG — implications for a novel tuberculosis vaccine. Nature Reviews Microbiology [Internet]. 2005;3(8):656–62. Available from: http://www.nature.com/doifinder/10.1038/nrmicro1211

32. Bhatt K, Verma S, Ellner JJ, Salgame P. Quest for Correlates of Protection against Tuberculosis. Vol. 22, Clinical and Vaccine Immunology. 2015. p. 258–66.
33. Frick M. Funding for tuberculosis research—an urgent crisis of political will, human rights, and global solidarity. International Journal of Infectious Diseases [Internet]. 2017;56:21–4. Available from: https://www.sciencedirect.com/science/article/pii/S1201971216316307
34. Pai M. Covidization of research: what are the risks? Nature Medicine [Internet]. 2020;26(8):1159. Available from: https://doi.org/10.1038/s41591-020-1015-0
35. Tufariello JM, Chan J, Flynn JL. Latent tuberculosis: mechanisms of host and bacillus that contribute to persistent infection. The Lancet Infectious Diseases [Internet]. 2003;3(9):578–90. Available from: https://www.sciencedirect.com/science/article/pii/S1473309903007412
36. Darrah PA, Zeppa JJ, Maiello P, Hackney JA, Wadsworth MH, Hughes TK, et al. Prevention of tuberculosis in macaques after intravenous BCG immunization. Nature. 2020;577(7788):95–102.
37. Williams CM, Abdulwhhab M, Birring SS, de Kock E, Garton NJ, Townsend E, et al. Exhaled *Mycobacterium tuberculosis* output and detection of subclinical disease by face-mask sampling: prospective observational studies. The Lancet Infectious Diseases. 2020;20(5):607–17.
38. Corleis B, Dorhoi A. Early dynamics of innate immunity during pulmonary tuberculosis. Immunology Letters [Internet]. 2020;221:56–60. Available from: https://www.sciencedirect.com/science/article/pii/S0165247819305723
39. Gideon HP, Flynn JL. Latent tuberculosis: What the host "sees"? Immunologic Research. 2011;50(2–3):202–12.
40. Flynn JL, Chan J. Immunology of Tuberculosis. Annual Review of Immunology [Internet]. 2001 Apr 1;19(1):93–129. Available from: https://doi.org/10.1146/annurev.immunol.19.1.93
41. Lin PL, Pawar S, Myers A, Pegu A, Fuhrman C, Reinhart TA, et al. Early events in *Mycobacterium tuberculosis* infection in cynomolgus macaques. Infection and Immunity. 2006;
42. Cadena AM, Flynn JL, Fortune SM. The importance of first impressions: Early events in *Mycobacterium tuberculosis* infection influence outcome. Vol. 7, mBio. 2016.
43. Flynn J, Chan J, Lin PL. Macrophages and control of granulomatous inflammation in tuberculosis. Mucosal Immunology. 2011;
44. O'Garra A, Redford PS, McNab FW, Bloom CI, Wilkinson RJ, Berry MPR. The Immune Response in Tuberculosis. Annual Review of Immunology [Internet]. 2013 Mar 21;31(1):475–527. Available from: https://doi.org/10.1146/annurev-immunol-032712-095939
45. Lin PL, Ford CB, Coleman MT, Myers AJ, Gawande R, Ioerger T, et al. Sterilization of granulomas is common in active and latent tuberculosis despite within-host variability in bacterial killing. Nature Medicine. 2014;20(1):75–9.
46. Serbina N v, Lazarevic V, Flynn JL. CD4(+) T cells are required for the development of cytotoxic CD8(+) T cells during *Mycobacterium tuberculosis* infection [Internet]. Vol. 167, J Immunol. 2001. p. 6991-7000. Available from: http://www.ncbi.nlm.nih.gov/cgi-bin/Entrez/referer?http://www.jimmunol.org/cgi/content/abstract/167/12/6991
47. Lin PL, Flynn JL. CD8 T cells and *Mycobacterium tuberculosis* infection. Seminars in Immunopathology [Internet]. 2015;37(3):239–49. Available from: http://link.springer.com/10.1007/s00281-015-0490-8
48. Stenger S, Hanson DA, Teitelbaum R, Dewan P, Niazi KR, Froelich CJ, et al. An antimicrobial activity of cytolytic T cells mediated by granulysin. Science [Internet]. 1998;282(5386):121–5. Available from:

http://www.ncbi.nlm.nih.gov/pubmed/9756476%5Cnhttp://www.sciencemag.org/cgi/doi/10.1126/science.282.5386.121
49. Boom WH, Canaday DH, Fulton SA, Gehring AJ, Rojas RE, Torres M. Human immunity to M. tuberculosis: T cell subsets and antigen processing. In: Tuberculosis. 2003. p. 98–106.
50. Sud D, Bigbee C, Flynn JL, Kirschner DE. Contribution of CD8+ T Cells to Control of *Mycobacterium tuberculosis* Infection. The Journal of Immunology. 2014;176(7):4296–314.
51. Prezzemolo T, Guggino G, La Manna MP, Di Liberto D Di, Dieli F, Caccamo N. Functional signatures of human CD4 and CD8 T cell responses to *Mycobacterium tuberculosis*. Vol. 5, Frontiers in Immunology. 2014.
52. Chen CY, Huang D, Wang RC, Shen L, Zeng G, Yao S, et al. A critical role for CD8 T cells in a nonhuman primate model of tuberculosis. PLoS Pathogens. 2009;5(4).
53. Gallegos AM, Pamer EG, Glickman MS. Delayed protection by ESAT-6-specific effector CD4+ T cells after airborne M. tuberculosis infection. Journal of Experimental Medicine. 2008;205(10):2359–68.
54. Linderman JJ, Cilfone NA, Pienaar E, Gong C, Kirschner DE. A multi-scale approach to designing therapeutics for tuberculosis. Integrative Biology (United Kingdom) [Internet]. 2015;7(5):591–609. Available from: http://xlink.rsc.org/?DOI=C4IB00295D
55. Cicchese JM, Evans S, Hult C, Joslyn LR, Wessler T, Millar JA, et al. Dynamic balance of pro- and anti-inflammatory signals controls disease and limits pathology. Immunological Reviews. 2018;285(1):147–67.
56. Martin CJ, Cadena AM, Leung VW, Lin PL, Maiello P, Hicks N, et al. Digitally Barcoding *Mycobacterium tuberculosis* Reveals *In vivo* Infection Dynamics in the Macaque Model of Tuberculosis . mBio. 2017;8(3).
57. Cadena AM, Fortune SM, Flynn JL. Heterogeneity in tuberculosis. Nature Reviews Immunology. 2017;17(11):691–702.
58. Klein L, Kyewski B, Allen PM, Hogquist KA. Positive and negative selection of the T cell repertoire: what thymocytes see (and don't see). Nature Reviews Immunology [Internet]. 2014;14(6):377–91. Available from: https://doi.org/10.1038/nri3667
59. Jenkins MK, Moon JJ. The role of naive T cell precursor frequency and recruitment in dictating immune response magnitude. The Journal of Immunology. 2012;188(9):4135–40.
60. Magee CN, Boenisch O, Najafian N. The role of costimulatory molecules in directing the functional differentiation of alloreactive T helper cells. American journal of transplantation : official journal of the American Society of Transplantation and the American Society of Transplant Surgeons [Internet]. 2012/07/03. 2012 Oct;12(10):2588–600. Available from: https://pubmed.ncbi.nlm.nih.gov/22759274
61. Martinez-Sanchez ME, Huerta L, Alvarez-Buylla ER, Villarreal Luján C. Role of Cytokine Combinations on CD4+ T Cell Differentiation, Partial Polarization, and Plasticity: Continuous Network Modeling Approach. Frontiers in Physiology [Internet]. 2018;9:877. Available from: https://www.frontiersin.org/article/10.3389/fphys.2018.00877
62. Mikhalkevich N, Becknell B, Caligiuri MA, Bates MD, Harvey R, Zheng W. Responsiveness of naive CD4 T cells to polarizing cytokine determines the ratio of Th1 and Th2 cell differentiation. The Journal of Immunology. 2006;176(3):1553–60.
63. Jiang Y, Li Y, Zhu B. T-cell exhaustion in the tumor microenvironment. Vol. 6, Cell Death and Disease. 2015.

64. Wherry EJ. T cell exhaustion. Nature Immunology [Internet]. 2011;12(6):492–9. Available from: https://doi.org/10.1038/ni.2035
65. Pardoll DM. The blockade of immune checkpoints in cancer immunotherapy. Nature reviews Cancer [Internet]. 2012 Mar 22;12(4):252–64. Available from: https://pubmed.ncbi.nlm.nih.gov/22437870
66. Velu V, Titanji K, Zhu B, Husain S, Pladevega A, Lai L, et al. Enhancing SIV-specific immunity *in vivo* by PD-1 blockade. Nature [Internet]. 2008/12/10. 2009 Mar 12;458(7235):206–10. Available from: https://pubmed.ncbi.nlm.nih.gov/19078956
67. Willinger T, Freeman T, Hasegawa H, McMichael AJ, Callan MFC. Molecular Signatures Distinguish Human Central Memory from Effector Memory CD8 T Cell Subsets. The Journal of Immunology [Internet]. 2005 Nov 1;175(9):5895. Available from: http://www.jimmunol.org/content/175/9/5895.abstract
68. Gong C, Linderman JJ, Kirschner D. Harnessing the heterogeneity of T cell differentiation fate to fine-tune generation of effector and memory T cells. Frontiers in Immunology. 2014;5(FEB).
69. Roberts AD, Ely KH, Woodland DL. Differential contributions of central and effector memory T cells to recall responses. Journal of Experimental Medicine. 2005;202(1):123–33.
70. Youngblood B, Hale JS, Kissick HT, Ahn E, Xu X, Wieland A, et al. Effector CD8 T cells dedifferentiate into long-lived memory cells. Nature. 2017;552(7685):404–9.
71. Harrington LE, Janowski KM, Oliver JR, Zajac AJ, Weaver CT. Memory CD4 T cells emerge from effector T-cell progenitors. Nature [Internet]. 2008 Mar 5;452(7185):356–60. Available from: http://dx.doi.org/10.1038/nature06672
72. Leignadier J, Hardy M-P, Cloutier M, Rooney J, Labrecque N. Memory T-lymphocyte survival does not require T-cell receptor expression. Proceedings of the National Academy of Sciences [Internet]. 2008 Dec 23;105(51):20440. Available from: http://www.pnas.org/content/105/51/20440.abstract
73. Sakai S, Mayer-Barber KD, Barber DL. Defining features of protective CD4 T cell responses to *Mycobacterium tuberculosis*. Current opinion in immunology [Internet]. 2014 Aug;29:137–42. Available from: https://pubmed.ncbi.nlm.nih.gov/25000593
74. Leveton C, Barnass S, Champion B, Lucas S, de Souza B, Nicol M, et al. T-cell-mediated protection of mice against virulent *Mycobacterium tuberculosis*. Infection and immunity [Internet]. 1989 Feb;57(2):390–5. Available from: https://pubmed.ncbi.nlm.nih.gov/2492259
75. Corbett EL, Watt CJ, Walker N, Maher D, Williams BG, Raviglione MC, et al. The growing burden of tuberculosis: global trends and interactions with the HIV epidemic. Archives of internal medicine. 2003;163(9):1009–21.
76. Flynn JL, Chan J, Triebold KJ, Dalton DK, Stewart TA, Bloom BR. An essential role for interferon gamma in resistance to *Mycobacterium tuberculosis* infection. Journal of Experimental Medicine [Internet]. 1993 Dec 1;178(6):2249–54. Available from: https://doi.org/10.1084/jem.178.6.2249
77. Filipe-Santos O, Bustamante J, Chapgier A, Vogt G, de Beaucoudrey L, Feinberg J, et al. Inborn errors of IL-12/23- and IFN-γ-mediated immunity: molecular, cellular, and clinical features. Seminars in Immunology [Internet]. 2006;18(6):347–61. Available from: https://www.sciencedirect.com/science/article/pii/S1044532306001047
78. Green AM, Difazio R, Flynn JL. IFN-γ from CD4 T cells is essential for host survival and enhances CD8 T cell function during *Mycobacterium tuberculosis* infection. Journal of

immunology (Baltimore, Md : 1950) [Internet]. 2012/12/10. 2013 Jan 1;190(1):270–7. Available from: https://pubmed.ncbi.nlm.nih.gov/23233724
79. Lewinsohn DA, Lewinsohn DM, Scriba TJ. Polyfunctional CD4+ T Cells As Targets for Tuberculosis Vaccination. Frontiers in Immunology [Internet]. 2017;8:1262. Available from: https://www.frontiersin.org/article/10.3389/fimmu.2017.01262
80. Chan J, Xing Y, Magliozzo RS, Bloom BR. Killing of virulent *Mycobacterium tuberculosis* by reactive nitrogen intermediates produced by activated murine macrophages. Journal of Experimental Medicine [Internet]. 1992 Apr 1;175(4):1111–22. Available from: https://doi.org/10.1084/jem.175.4.1111
81. Marino S, Sud D, Plessner H, Lin PL, Chan J, Flynn JL, et al. Differences in reactivation of tuberculosis induced from anti-TNF treatments are based on bioavailability in granulomatous tissue. PLoS computational biology [Internet]. 2007/08/22. 2007 Oct;3(10):1909–24. Available from: https://pubmed.ncbi.nlm.nih.gov/17953477
82. Fallahi-Sichani M, El-Kebir M, Marino S, Kirschner DE, Linderman JJ. Multiscale Computational Modeling Reveals a Critical Role for TNF- Receptor 1 Dynamics in Tuberculosis Granuloma Formation. The Journal of Immunology [Internet]. 2011;186(6):3472–83. Available from: http://www.pubmedcentral.nih.gov/articlerender.fcgi?artid=3127549&tool=pmcentrez&rendertype=abstract
83. Caccamo N, Dieli F. Are polyfunctional cells protective in M. tuberculosis infection. Understanding Tuberculosis—Analyzing the Origin of *Mycobacterium tuberculosis* Pathogenicity. 2012;10:35245.
84. Rozot V, Vigano S, Mazza-Stalder J, Idrizi E, Day CL, Perreau M, et al. *Mycobacterium tuberculosis*-specific CD8+ T cells are functionally and phenotypically different between latent infection and active disease. European Journal of Immunology [Internet]. 2013 Jun 1;43(6):1568–77. Available from: https://doi.org/10.1002/eji.201243262
85. Axelsson-Robertson R, Loxton AG, Walzl G, Ehlers MM, Kock MM, Zumla A, et al. A broad profile of co-dominant epitopes shapes the peripheral *Mycobacterium tuberculosis* specific CD8+ T-cell immune response in South African patients with active tuberculosis. PloS one. 2013;8(3):e58309.
86. Smith SM, Klein MR, Malin AS, Sillah J, Huygen K, Andersen P, et al. Human CD8⁺ T Cells Specific for*Mycobacterium tuberculosis* Secreted Antigens in Tuberculosis Patients and Healthy BCG-Vaccinated Controls in The Gambia. Infection and Immunity [Internet]. 2000 Dec 1;68(12):7144. Available from: http://iai.asm.org/content/68/12/7144.abstract
87. Andersson J, Samarina A, Fink J, Rahman S, Grundström S. Impaired Expression of Perforin and Granulysin in CD8⁺ T Cells at the Site of Infection in Human Chronic Pulmonary Tuberculosis. Infection and Immunity [Internet]. 2007 Nov 1;75(11):5210. Available from: http://iai.asm.org/content/75/11/5210.abstract
88. Singh AK, Gupta UD. Animal models of tuberculosis: Lesson learnt. The Indian journal of medical research [Internet]. 2018 May;147(5):456–63. Available from: https://pubmed.ncbi.nlm.nih.gov/30082569
89. Dorman SE, Hatem CL, Tyagi S, Aird K, Lopez-Molina J, Pitt MLM, et al. Susceptibility to tuberculosis: clues from studies with inbred and outbred New Zealand White rabbits. Infection and immunity [Internet]. 2004 Mar;72(3):1700–5. Available from: https://pubmed.ncbi.nlm.nih.gov/14977978

90. Hoff DR, Ryan GJ, Driver ER, Ssemakulu CC, de Groote MA, Basaraba RJ, et al. Location of intra-and extracellular M. tuberculosis populations in lungs of mice and guinea pigs during disease progression and after drug treatment. PloS one. 2011;6(3):e17550.
91. Driver ER, Ryan GJ, Hoff DR, Irwin SM, Basaraba RJ, Kramnik I, et al. Evaluation of a Mouse Model of Necrotic Granuloma Formation Using C3HeB/FeJ Mice for Testing of Drugs against *Mycobacterium tuberculosis* Antimicrobial Agents and Chemotherapy [Internet]. 2012 Jun 1;56(6):3181. Available from: http://aac.asm.org/content/56/6/3181.abstract
92. Plumlee CR, Duffy FJ, Gern BH, Delahaye JL, Cohen SB, Stoltzfus CR, et al. Ultra-low Dose Aerosol Infection of Mice with *Mycobacterium tuberculosis* More Closely Models Human Tuberculosis. Cell Host & Microbe [Internet]. 2021;29(1):68-82.e5. Available from: https://www.sciencedirect.com/science/article/pii/S1931312820305618
93. Schmidt LH. STUDIES ON THE ANTITUBERCULOUS ACTIVITY OF ETHAMBUTOL IN MONKEYS*. Annals of the New York Academy of Sciences [Internet]. 1966 Apr 1;135(2):747–58. Available from: https://doi.org/10.1111/j.1749-6632.1966.tb45520.x
94. Scanga CA, Flynn JL. Modeling tuberculosis in nonhuman primates. Cold Spring Harbor Perspectives in Medicine. 2014;4(12).
95. Kaushal D, Mehra S, Didier PJ, Lackner AA. The non-human primate model of tuberculosis. Vol. 41, Journal of Medical Primatology. 2012. p. 191–201.
96. Flynn JL, Tsenova L, Izzo A, Kaplan G. Experimental Animal Models of Tuberculosis. In: Handbook of Tuberculosis. 2017. p. 389–426.
97. Flynn JL, Gideon HP, Mattila JT, Lin P ling. Immunology studies in non-human primate models of tuberculosis. Immunological Reviews. 2015;264(1):60–73.
98. Walpole J, Papin JA, Peirce SM. Multiscale Computational Models of Complex Biological Systems. Annual Review of Biomedical Engineering [Internet]. 2013 Jul 11;15(1):137–54. Available from: https://doi.org/10.1146/annurev-bioeng-071811-150104
99. Wigginton JE, Kirschner D. A Model to Predict Cell-Mediated Immune Regulatory Mechanisms During Human Infection with *Mycobacterium tuberculosis*. The Journal of Immunology. 2001;166(3):1951–67.
100. Antia R, Koella JC, Perrot V. Models of the within-host dynamics of persistent mycobacterial infections. Proceedings of the Royal Society of London Series B: Biological Sciences [Internet]. 1996 Mar 22;263(1368):257–63. Available from: https://doi.org/10.1098/rspb.1996.0040
101. Chang ST, Linderman JJ, Kirschner DE. Multiple mechanisms allow *Mycobacterium tuberculosis* to continuously inhibit MHC class II-mediated antigen presentation by macrophages. Proceedings of the National Academy of Sciences of the United States of America [Internet]. 2005 Mar 22;102(12):4530. Available from: http://www.pnas.org/content/102/12/4530.abstract
102. Marino S, Myers A, Flynn JL, Kirschner DE. TNF and IL-10 are major factors in modulation of the phagocytic cell environment in lung and lymph node in tuberculosis: A next-generation two-compartmental model. Journal of Theoretical Biology. 2010;265(4):586–98.
103. Segovia-Juarez JL, Ganguli S, Kirschner D. Identifying control mechanisms of granuloma formation during M. tuberculosis infection using an agent-based model. Journal of Theoretical Biology. 2004;231(3):357–76.

104. Cilfone NA, Perry CR, Kirschner DE, Linderman JJ. Multi-Scale Modeling Predicts a Balance of Tumor Necrosis Factor-α and Interleukin-10 Controls the Granuloma Environment during *Mycobacterium tuberculosis* Infection. PLoS ONE. 2013;8(7).
105. Fallahi-Sichani M, Kirschner DE, Linderman JJ. NF-??B signaling dynamics play a key role in infection control in tuberculosis. Frontiers in Physiology. 2012;3 JUN.
106. Kirschner D, Pienaar E, Marino S, Linderman JJ. A review of computational and mathematical modeling contributions to our understanding of *Mycobacterium tuberculosis* within-host infection and treatment. Current Opinion in Systems Biology [Internet]. 2017;3:170–85. Available from: http://linkinghub.elsevier.com/retrieve/pii/S2452310016300117
107. de Boer RJ, Perelson AS. Quantifying T lymphocyte turnover. Journal of Theoretical Biology [Internet]. 2013;327:45–87. Available from: https://www.sciencedirect.com/science/article/pii/S0022519313000076
108. Thomas-Vaslin V, Altes HK, de Boer RJ, Klatzmann D. Comprehensive Assessment and Mathematical Modeling of T Cell Population Dynamics and Homeostasis. The Journal of Immunology [Internet]. 2008 Feb 15;180(4):2240. Available from: http://www.jimmunol.org/content/180/4/2240.abstract
109. Morel PA, Faeder JR, Hawse WF, Miskov-Zivanov N. Modeling the T cell immune response: a fascinating challenge. Journal of pharmacokinetics and pharmacodynamics [Internet]. 2014/08/26. 2014 Oct;41(5):401–13. Available from: https://pubmed.ncbi.nlm.nih.gov/25155903
110. Kirschner DE, Webb GF, Cloyd M. Model of HIV-1 disease progression based on virus-induced lymph node homing and homing-induced apoptosis of CD4+ lymphocytes. 2000;
111. Bajaria SH, Webb G, Cloyd M, Kirschner D. Dynamics of Naive and Memory CD4+ T Lymphocytes in HIV-1 Disease Progression. JAIDS Journal of Acquired Immune Deficiency Syndromes [Internet]. 2002;30(1). Available from: https://journals.lww.com/jaids/Fulltext/2002/05010/Dynamics_of_Naive_and_Memory_CD4__T_Lymphocytes_in.6.aspx
112. Perelson AS, Ribeiro RM. Modeling the within-host dynamics of HIV infection. BMC biology [Internet]. 2013 Sep 3;11:96. Available from: https://pubmed.ncbi.nlm.nih.gov/24020860
113. Antia R, Ganusov V v., Ahmed R. The role of models in understanding CD8+ T-cell memory. Nature Reviews Immunology [Internet]. 2005;5(2):101–11. Available from: http://www.nature.com/doifinder/10.1038/nri1550
114. Myers AJ, Marino S, Kirschner DE, Flynn JL. Inoculation Dose of *Mycobacterium tuberculosis* Does Not Influence Priming of T Cell Responses in Lymph Nodes. The Journal of Immunology [Internet]. 2013 May 1;190(9):4707. Available from: http://www.jimmunol.org/content/190/9/4707.abstract
115. Gong C, Mattila JT, Miller M, Flynn JL, Linderman JJ, Kirschner D. Predicting lymph node output efficiency using systems biology. Journal of Theoretical Biology [Internet]. 2013;335:169–84. Available from: https://www.sciencedirect.com/science/article/pii/S0022519313002889
116. Marino S, El-Kebir M, Kirschner D. A hybrid multi-compartment model of granuloma formation and T cell priming in Tuberculosis. Journal of Theoretical Biology [Internet]. 2011;280(1):50–62. Available from: https://www.sciencedirect.com/science/article/pii/S0022519311001688

117. Kirschner DE, Hunt CA, Marino S, Fallahi-Sichani M, Linderman JJ. Tuneable resolution as a systems biology approach for multi-scale, multi-compartment computational models. Vol. 6, Wiley Interdisciplinary Reviews: Systems Biology and Medicine. 2014. p. 225–45.
118. Marino S, Gideon HP, Gong C, Mankad S, McCrone JT, Lin PL, et al. Computational and Empirical Studies Predict *Mycobacterium tuberculosis*-Specific T Cells as a Biomarker for Infection Outcome. PLoS Computational Biology. 2016;12(4).
119. Marino S, Kirschner D. A Multi-Compartment Hybrid Computational Model Predicts Key Roles for Dendritic Cells in Tuberculosis Infection. Computation [Internet]. 2016;4(4):39. Available from: http://www.mdpi.com/2079-3197/4/4/39
120. Marino S, Kirschner DE. The human immune response to *Mycobacterium tuberculosis* in lung and lymph node. Journal of Theoretical Biology [Internet]. 2004;227(4):463–86. Available from: https://www.sciencedirect.com/science/article/pii/S0022519303004429
121. Marino S, Pawar S, Fuller CL, Reinhart TA, Flynn JL, Kirschner DE. Dendritic Cell Trafficking and Antigen Presentation in the Human Immune Response to *Mycobacterium tuberculosis* . The Journal of Immunology. 2004;173(1):494–506.
122. MAGOMBEDZE G, GARIRA W, MWENJE E. THE ROLE OF DENDRITIC CELLS AND OTHER IMMUNE MECHANISMS DURING HUMAN INFECTION WITH *MYCOBACTERIUM TUBERCULOSIS*. International Journal of Biomathematics [Internet]. 2009 Mar 1;02(01):69–105. Available from: https://doi.org/10.1142/S1793524509000534
123. Marino S, Kirschner D. A Multi-Compartment Hybrid Computational Model Predicts Key Roles for Dendritic Cells in Tuberculosis Infection. Computation [Internet]. 2016;4(4):39. Available from: http://www.mdpi.com/2079-3197/4/4/39
124. Prats C, Vilaplana C, Valls J, Marzo E, Cardona PJ, López D. Local inflammation, dissemination and coalescence of lesions are key for the progression toward active tuberculosis: The bubble model. Frontiers in Microbiology. 2016;7(FEB).
125. Català M, Bechini J, Tenesa M, Pérez R, Moya M, Vilaplana C, et al. Modelling the dynamics of tuberculosis lesions in a virtual lung: Role of the bronchial tree in endogenous reinfection. PLoS Computational Biology. 2020;16(5).
126. Read MN, Alden K, Timmis J, Andrews PS. Strategies for calibrating models of biology. Briefings in Bioinformatics. 2018;
127. Menzies NA, Soeteman DI, Pandya A, Kim JJ. Bayesian Methods for Calibrating Health Policy Models: A Tutorial. PharmacoEconomics. 2017;35(6):613–24.
128. Rutter CM, Miglioretti DL, Savarino JE. Bayesian calibration of microsimulation models. Journal of the American Statistical Association. 2009;104(488):1338–50.
129. Jackson CH, Jit M, Sharples LD, de Angelis D. Calibration of complex models through bayesian evidence synthesis: A demonstration and tutorial. Medical Decision Making. 2015;35(2):148–61.
130. Marino S, Hogue IB, Ray CJ, Kirschner DE. A methodology for performing global uncertainty and sensitivity analysis in systems biology. Vol. 254, Journal of Theoretical Biology. 2008. p. 178–96.
131. Levitan YuL, Markovich NI, Rozin SG, Sobol IM. On quasirandom sequences for numerical computations. USSR Computational Mathematics and Mathematical Physics [Internet]. 1988;28(3):88–92. Available from: https://www.sciencedirect.com/science/article/pii/0041555388901814

2 Investigating T-cell Exhaustion within Tuberculosis Granulomas

This chapter is part of a published work:

Wong, EA*, Joslyn, LR*, Grant NL, Klein E, Lin PL, Kirschner DE, Flynn JL. "Low Levels of T cell Exhaustion in Tuberculosis Lung Granulomas". Infection and Immunity Aug 2018, 86 (9) e00426-18; DOI: 10.1128/IAI.00426-18.

2.1 Introduction

Tuberculosis (TB), caused by inhalation of the bacterium *Mycobacterium tuberculosis* (Mtb), continues to be a major global health problem. The World Health Organization estimates that more than 10 million people became ill with TB in 2016 alone, and 1.7 million deaths were caused by TB (1). TB is a chronic pulmonary disease. Consequently, the hallmarks of pulmonary *Mycobacterium tuberculosis* infection are granulomas that reside within the lungs. These organized structures are composed of host immune cells whose purpose is to contain or clear infection, creating a complex hub of immune and bacterial cell activity, as well as limiting pathology in the lungs. Due to substantial heterogeneity of granulomas, even within the same host, these structures can contain and kill Mtb but also can be a niche for bacterial survival, replication, and persistence (2). The host immune cells and Mtb bacilli and antigens interact within the granulomas for the entire course of infection, which, during clinically latent TB, can last the lifetime of the host (3). Macrophages are the primary host cell for infection, while CD4+ T cells have been shown to be critical for granuloma formation and maintenance through cytokine secretion and activation of other immune cells, including macrophages (4,5). Yet, given cellular activity and potential for frequent interactions between host immune cells and Mtb infected cells, it has been observed that a surprisingly low quantity of cytokine producing T cells (<10% of granuloma T cells) in non-human primate (NHP) granulomas (6). While various mechanisms could be limiting T cell function, one potential explanation for the low T cell responses within granulomas is T-cell exhaustion occurring due to chronic antigen stimulation from Mtb-infected cells.

In chronic viral infections and cancer, a subpopulation of T cells has been demonstrated to lose both functionality and proliferation capabilities over time in response to persistent antigen stimulation (7–12). This subpopulation of T cells enters an "exhausted" state, characterized by low cytokine production, low proliferation, and expression of a series of inhibitory receptors. The most well-studied of these receptors include PD-1, CTLA-4, and LAG-3, which interact with a range of ligands to activate negative regulatory pathways (13,14). While these inhibitory receptors may balance an overly activated immune response that could lead to disease pathology, the receptors can also prevent an effective immune response from clearing infections and tumor cells. In cancer and some infectious diseases, blockade of these inhibitory receptors reverses exhaustion and rescues T cell functions (15–20).

Since Mtb causes a chronic bacterial infection confined to a structured environment, it seems obvious that T cell exhaustion would occur within the critical site of granulomas. Not surprisingly, the contribution of T cell exhaustion to TB has been the subject of several studies. Patients with active TB were shown to have significantly higher PD-1 expression on their peripheral blood mononuclear cells (PBMC) compared to healthy controls, and blockade of inhibitory receptors in vitro enhanced T cell function (21–23). Additionally, increased antigen load was associated with decreased T cell responses in patients with high Mtb loads compared to patients with latent Mtb infections (24). Rhesus macaques with active or reactivated TB expressed more LAG-3 on their CD3+ T cells in their lung tissue compared to clinically latent animals (25). PD-1 expression significantly correlated with CTLA-4 expression on CD4+ T cells from tissues of Mtb-infected rhesus macaques (26). Mtb infections in mice increased the expression of PD-1 and LAG-3 as the infection progressed, and this was associated with increased T cell impairment (27). However, murine studies also suggested that presence of these inhibitory receptors may be beneficial for overall TB disease pathology and bacterial control, and are necessary to maintain antigen-specific effector T cells during Mtb infections (28,29), with detrimental outcomes when mice lacking PD-1 were infected with Mtb (30–32). While these studies examined T cell exhaustion in the periphery (patient studies) or in the whole lung (animal models), the frequency and role of exhausted T cells in individual granulomas is still unstudied and could provide important clues to overall infection dynamics as granulomas are the sites of infection in pulmonary TB.

We hypothesized T cell exhaustion could be contributing to the observed low frequencies of T cells producing cytokines in TB granulomas. We used a NHP model of TB that recapitulates human granuloma structure and disease to assess the extent of exhausted T cells and their function in lung granulomas. Very little evidence of T-cell exhaustion was found across NHP granulomas. Further, T-cell exhaustion in granulomas did not correlate with bacterial burden across granuloma samples.

While the *in vivo* data based on inhibitory receptors did not demonstrate large levels of T-cell exhaustion, the relationship between inhibitory markers and functional exhaustion is not abundantly clear. Recent studies have shown that inhibitory receptors can act as activation markers and that T cells can simultaneously express both inhibitory and activation markers (15,33–36). Therefore, it becomes difficult to distinguish T cell exhaustion using inhibitory receptors alone. To further explore the phenomenon of T cell exhaustion we utilized our existing computational model, *GranSim* (37–42). Within this chapter, we simulated a wide range of granuloma outcomes and incorporated varying levels of exhausted T cell phenotypes to ascertain the effects of T cell exhaustion on granuloma outcomes. Finally, we evaluated T cell dynamics across infection space and time in order to develop a hypothesis to explain the low levels of exhaustion observed in the NHP lung granulomas.

2.2 Methods

2.2.1 Animals, necropsy procedures, bacterial burden and staining for cell receptors

All animal care, necropsy procedures, and experimental protocols and procedures are fully described in the published version of this chapter (43). Briefly, NHP granuloma samples were assessed from 11 cynomolgus macaques. 34 lung granulomas were collected upon necropsy and 8 lung samples of complex TB disease (clusters, consolidations or TB pneumonia). Granuloma cells were stained for surface markers, inhibitory receptors and cytokines as part of prep for flow cytometry analysis. Granuloma bacterial burden was determined by plating granuloma homogenate and enumerating colony-forming units of Mtb. Immunofluorescence procedures are also described in the published version of this chapter.

2.2.2 Computational modeling with *GranSim*

All simulations utilize a 2D hybrid, agent-based model (ABM) called *GranSim* that captures environmental, cellular, and bacterial dynamics across molecular, cellular, and tissue scale events. As an established model, *GranSim* has been calibrated extensively to data from a non-human primate model of TB (37–41). At the molecular scale, *GranSim* incorporates cytokine and chemokine diffusion, secretion and degradation (44). *GranSim* also tracks individual immune cells on a 2D simulation grid of micro-compartments, including four macrophage states (resting, activated, infected, and chronically infected) and T-cell types (cytotoxic, IFN-γ producing, and regulatory). Granuloma formation at the tissue level is an emergent behavior of *GranSim*. See http://malthus.micro.med.umich.edu/*GranSim* for full model details and an executable file. The following methods provide detail on added mechanisms to *GranSim* so that we can use *GranSim* as a tool to study exhaustion in granulomas.

2.2.3 Model definitions, assumptions, and justifications

A great advantage of our *in silico* representation is that we can track cellular movement, behavior, and interaction across time. In *GranSim*, we define an interaction between a T cell and macrophage by the occurrence of a macrophage entering the double Moore neighborhood of a T cell (45–47) (i.e. Moore neighborhood is defined as all micro-compartments on the grid immediately adjacent to the one the cell is in; double Moore includes the next outer ring of micro-compartments). In particular, as we evaluate the possibility of T-cell exhaustion influencing the pathology of granuloma formation, we become solely interested in Exposure Events (EE), defined as the interactions between a T cell and an antigen "exposed" macrophage. In previous model versions, we defined an exposed macrophage according to three criteria: 1) If the cell contained any intracellular Mtb, 2) If, within the single Moore neighborhood of the macrophage, there exists any live or dead extracellular Mtb, and 3) If, within the single Moore neighborhood of the macrophage, there is another macrophage that was determined to be exposed during a previous timestep. Additionally, once a macrophage becomes exposed, it remains exposed for the entirety of its lifespan (41).

As noted in the introduction, chronic antigenic stimulation is sufficient to develop exhaustion within a T-cell population. Based on current literature, we model antigenic

stimulation via EE (48,49). We use EE as a standard of stimulation across a T-cell's lifetime to evaluate various analytical measures about T-cell exhaustion, including: individual T-cell exposure to antigens, average EE across T-cell populations, and determination of whether only a few T cells out of the entire population accrue the majority burden of EE.

Finally, we created a new parameter within *GranSim* to introduce an exhausted T-cell phenotype (this parameter was aptly named 'ExhaustionThreshold'). If the EE of an IFN-γ producing T cell or a cytotoxic T cell exceeds this preset threshold, then a T cell is marked as 'exhausted'. Once labeled, it loses all effector function, but continues to move around the grid until it dies from its natural lifespan (we do not assume there is an enhanced death rate for exhausted cells). Because we explore the possible role of exhaustion within granuloma formation, we crafted this parameter to represent the worst-case scenario: if a T cell exceeds the threshold, it immediately ceases effector function rather than for example, exhibiting a progressive loss of function. Other formulations are possible, but we have considered this case as an upper bound for quantifying exhaustion levels (yielding the worst-case scenario).

2.2.4 Computational platform and post-run analysis

GranSim is constructed through use of the C++ programming language, Boost libraries (distributed under the Boost Software License – www.boost.org), and the Qt framework for visualization (distributed under GPL – www.qt.digia.com). The ABM is cross-platform (Macintosh, Windows, Unix) and runs with or without visualization software. *GranSim* model simulations were performed locally and also on the XSEDE's OSG Condor pool resources. We relied on uncertainty analysis (UA) techniques to explore model parameter space. In particular, we used Latin Hypercube Sampling (LHS, reviewed in (50)) for UA. The LHS algorithm is a stratified Monte Carlo sampling method without replacement and was used to generate 1,500 unique parameter sets, which were simulated in replication 3 times (a total of 4,500 *in silico* simulations) for 200 days. When we matched our simulations to NHP granulomas, often the size of the high and median bacterial burden samples necessitated the use of a 200 by 200 micro-compartment simulation space, whereas the simulation space for sterile samples could be performed within 100 by 100 micro-compartments.

Analysis of statistical data derived on EE from simulations was performed using smoothScatter, ggplot2 and base packages in R and MATLAB. Additional analysis was conducted on more general data concerning granuloma-scale infection outcomes, granuloma formation, and concentration values of various effector molecules and CFU within the simulations.

2.2.5 Model calibration and defining exhaustion

Once the model was updated, we re-calibrated *GranSim* with respect to i) CFU totals, ii) CD3 totals, and iii) time based on 45 separate NHP granuloma sample data. Table A.1 shows the parameter ranges we used to generate an *in silico* bio-repository of 4,500 granulomas. Figure 1 outlines a portion of the comprehensive analysis we performed to compare T-cell exhaustion *in silico* versus the data derived on T-cell exhaustion *in vivo*.

Since the exact roles of individual inhibitory receptors as markers in the progression of T-cell exhaustion is unclear (35), we assume that a T cell is only truly exhausted if it co-expresses any two or more inhibitory receptors. Thus, when we compared T-cell exhaustion levels and markers *in vivo* against T-cell exhaustion *in silico*, the *in vivo* percentage of T-cells that are "exhausted" are actually the percent of T-cells that expressed 2 or more inhibitory receptors.

Out of the 4,500 granulomas in our *in silico* bio-repository, we matched simulations to samples according to our criteria, as shown in Table 2.1 of Figure 1. As an example, if we examine NHP Sample 13516_RLL 17_20, we were able to select 5 unique simulations that matched CFU and CD3 values across various simulation time points. For each of the 5 simulations, across every time point that matched the NHP sample's CFU and CD3+ T cell levels, we found the average percent of exhausted T cells (Table 2.2). For example, the first replication of simulation no. 33 matched CFU and CD3 counts across 5 different time points over the 200-day simulation. We averaged the exhausted T cells across each of the 5 days and found that the mean percentage of exhausted T cells when this simulation matched our criteria was 0.0%, with a standard deviation of ~1.5%.

Finally, we aggregated the data to provide a sense of overall model fit for each of the 45 NHP samples. Table 2.3 displays the median value across all the mean percentages of exhausted T cells for each sample's matching simulations. Thus, for Sample 13516_RLL 17_20, the

median percent of exhaustion across all the samples that matched was 0.0%. Flow cytometry data shows that this sample had 0.66% of T cells that displayed 2 or more inhibitory markers.

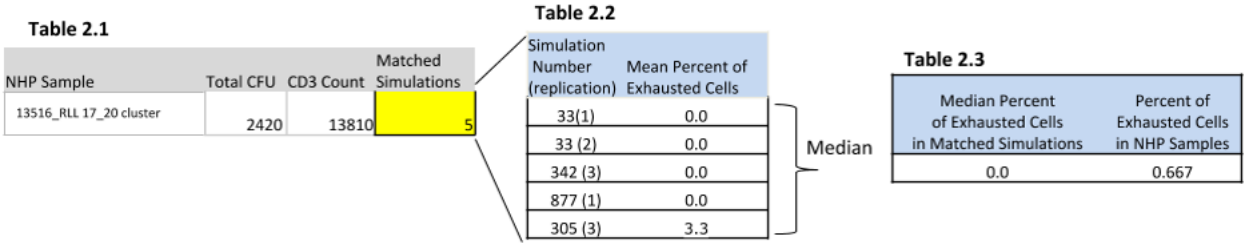

Figure 2.1 Example analysis of in silico versus in vivo T-cell exhaustion data.
Table 2.3 displays the direct comparison between exhaustion in our matching simulations and the level of observed exhaustion in NHP samples. Tables 2.1 and 2.2 explain our method of matching and aggregating data. Table 2.1 displays 1 of the 44 granuloma NHP samples that we used for calibration. The right-most column shows the number of simulations that matched to the NHP sample CFU values and CD3 Count. Each simulation could match the criteria across several time points. Table 2.2 shows each of the 5 simulations that calibrated to NHP sample 13516_RLL 17_20 cluster and the average percentage of exhausted T cells across the simulation timepoints that matched NHP sample criteria. Finally, we aggregated the data to display an overall sense of model fit by selecting the "median of the means" for each matching simulation. Thus, for NHP sample 13516_RLL 17_20 cluster, the median percent of exhaustion across all samples that matched was 0.0%. Flow cytometry data shows that this sample had 0.66% of T cells that showed two or more exhaustion markers.

2.2.6 Exposure event (EE) threshold selection

Initially, we created a biorepository of 4500 granulomas using the LHS technique. Within this biorepository, the EE threshold for T cell exhaustion ranged from 200 to 10000. We calculated the upper bound of 10000 interactions of the EE threshold as a T cell that has every location in a T cell double Moore Neighborhood occupied by an exposed macrophage throughout the entirety of its life (average of 3 days in our simulation), will accrue 10500 interactions. We selected 200 interactions as the lower level of EE because a T cell with 200 interactions has encountered exposed macrophages less than 2% of the time it has been alive – certainly, a sufficient EE threshold for a phenotype that is caused by chronic stimulation.

Figure 2.3 and Figure 2.4 were produced from a second biorepository of 4500 granulomas. This biorepository was created with the exact same parameter ranges as in Table A.1, but the EE threshold was set to 5236, the median of all simulations that matched the macaque granulomas. A threshold of 5236 EE seems reasonable, as 4320 interactions equals 1 interaction per minute through the average lifespan of a T cell.

2.3 Results

2.3.1 *GranSim* simulations match *in vivo* granuloma cell counts, bacterial burden and exhaustion levels

Full experimental data on T-cell exhaustion within NHP granulomas can be viewed in the published version of this chapter. Briefly, the *in vivo* data do not support widespread T cell exhaustion within TB granulomas. Furthermore, the *in vivo* data could not answer the following questions about T cell exhaustion: 1) What are the temporal dynamics of exhaustion in the granuloma? 2) Within the granuloma, are there areas where a T cell has greater likelihood of becoming exhausted? 3) Can we generally explain the presence of only low quantities of exhausted T cells? These questions require a technique that addresses both the spatial and temporal dynamics that are intrinsic to development of a T cell exhaustion phenotype. To further explore the relationship between T cell exhaustion and granuloma function, we turned to our existing computational model, *GranSim* (37–41). We simulated a wide range of granuloma outcomes, creating a library of granulomas using a Latin Hypercube Sampling algorithm (50). We also incorporated varying levels of exhausted T cell phenotypes to ascertain the effects of T cell exhaustion on granuloma outcomes. Finally, we evaluated T cell dynamics across infection time and space in order to develop a hypothesis to explain the low levels of exhaustion observed in the NHP studies herein.

After creating an *in silico* biorepository of 4,500 granulomas (see Methods), we found that every macaque granuloma sample has at least one corresponding simulation match. We selected three individual granuloma simulations that best matched bacterial burden and CD3+ T cell counts of the three NHP granuloma samples 2016_LLL GR B, 9515_RLL GR 20, 4017_LLL TB pneumonia to investigate the potential roles of exhaustion in granulomas. These were chosen to represent a spectrum of granuloma outcomes: sterile, median bacterial load, and high bacterial load samples, respectively. We directly compared these three NHP samples and their corresponding simulations from *GranSim* (Figure 2.2). The leftmost column represents a sample that was sterile at the time of necropsy (112 days post-infection with 0 CFU), the middle column shows a sample with median bacterial burden during the time of necropsy (84 days post-infection with 600 CFU), and the far-right column displays a high burden sample (70 days post-infection, with 138000 CFU). The first row displays the H&E of sections, while the second row

displays the PD-1 and CD3 expression in the matched granulomas. The third row displays an *in silico* snapshot taken at day 100 for each corresponding granuloma simulation (near time of necropsy of the NHPs). The fourth row represents a prediction: each figure is an *in silico* snapshot of the granuloma simulation at day 200. These comparisons support that the simulated granulomas both temporally and spatially capture the characteristics of the macaque granulomas.

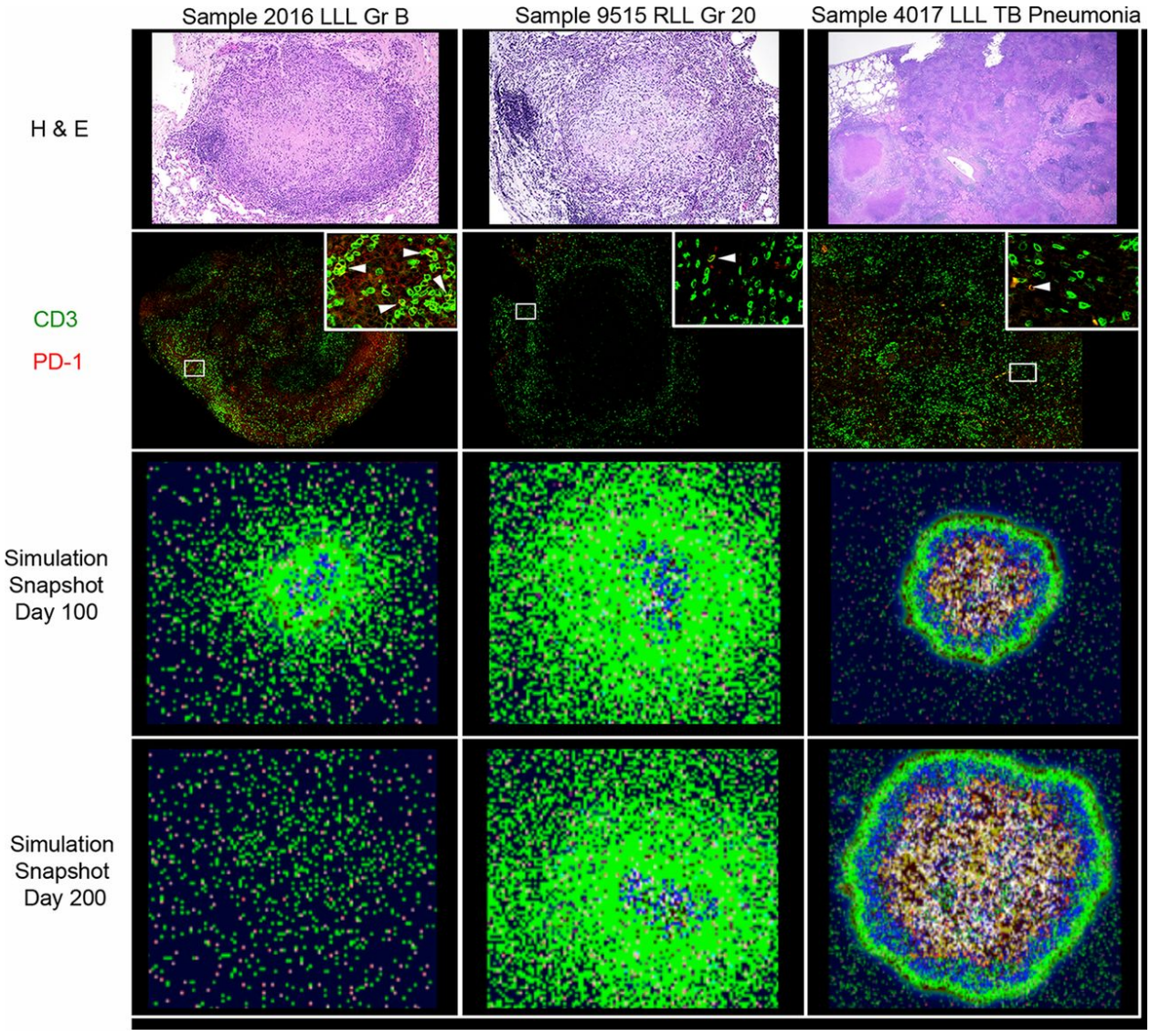

Figure 2.2 Comparison of macaque and simulated granulomas with varying levels of bacterial burden.

Row 1: H&E sections from granulomas excised from NHPs. Row 2: IHC staining showing spatial organization of PD-1 and CD3 expressing cells in lung granulomas excised from NHPs, green = CD3, red = PD1. Inset is a magnification of the region of interest (indicated by white box), where arrowheads indicate PD-1+CD3+ cells. Row 3: Simulated granuloma snapshots at day 100 (near the corresponding time of necropsy). Row 4: A snapshot prediction of the granuloma outcome if each simulation is continued until day 200. In both Rows 3 and 4, green - resting macrophages, blue - activated macrophages, orange - infected macrophages, red - chronically infected

macrophages, brown - extracellular bacteria, pink - gamma-producing T cells, purple - cytotoxic T cells, aqua - regulatory T cells, and white crosshatched – caseated.

2.3.2 Temporal and spatial analysis of *in silico* exhaustion

Under the assumption that T cell exhaustion occurs upon repeated exposure to antigen, we defined an Exposure Event (EE) as the interaction between a T cell and an antigen exposed macrophage in the granuloma. The range of EE across the 2945 simulations that matched the 44 macaque granuloma samples was 205 to 9199, with a median of 5236. Therefore, a threshold of 5236 EE was set as a conservative estimate of our exhaustion threshold, as 5000 interactions across the average life of a T cell (~ 3 days) equates to approximately 1 APC-T cell interaction per minute. We assume this number of interactions constitutes a reasonable threshold for T-cell exhaustion, a phenotype that only develops following chronic interactions between APC and T cells. We created a new biorepository of 4500 granulomas, using this EE threshold for exhaustion. Using the same three granulomas as in Figure 2.2, we performed a spatial and temporal analysis (out to 200 days) to investigate the location of exhausted T cells within granulomas (Figure 2.3). Row 1 displays the spatial location and magnitude of EE throughout the sterile (Figure 2.3A), median CFU (Figure 2.3B), and TB pneumonia (Figure 2.3C) simulations, where dark blue represents high density EE areas and white represents areas within the simulation that lack EE. Row 2 reveals the spatial location of T cells as they exceed the EE threshold and become labeled with an exhaustion phenotype. Each simulation (sterile – Figure 2.3D, median CFU – Figure 2.3E, TB pneumonia – Figure 2.3F) has its own scale ranging from white to dark blue, thus comparison from one EE map to another simulation's EE map should not be performed. Row 3 (Figure 2.3G, H, I) displays a plot of the level of overall exhaustion, across time, as a cumulative percentage of all T cells that were activated in the granuloma simulation. As these simulations show, many granulomas show little cumulative exhaustion throughout the simulation. Note the spatial location of exhaustion is similar for each type of granuloma; T cells only become exhausted when they enter the center of the granuloma and can accrue sufficient EE. Furthermore the cumulative exhaustion plots reveal that, across time, exhaustion accumulates faster in early time points (between days 25 and 50) than later time points (between days 100 and 200). However, as the granuloma matures and organizes, T cell exposure events decline, and the rate of exhaustion lowers or stabilizes.

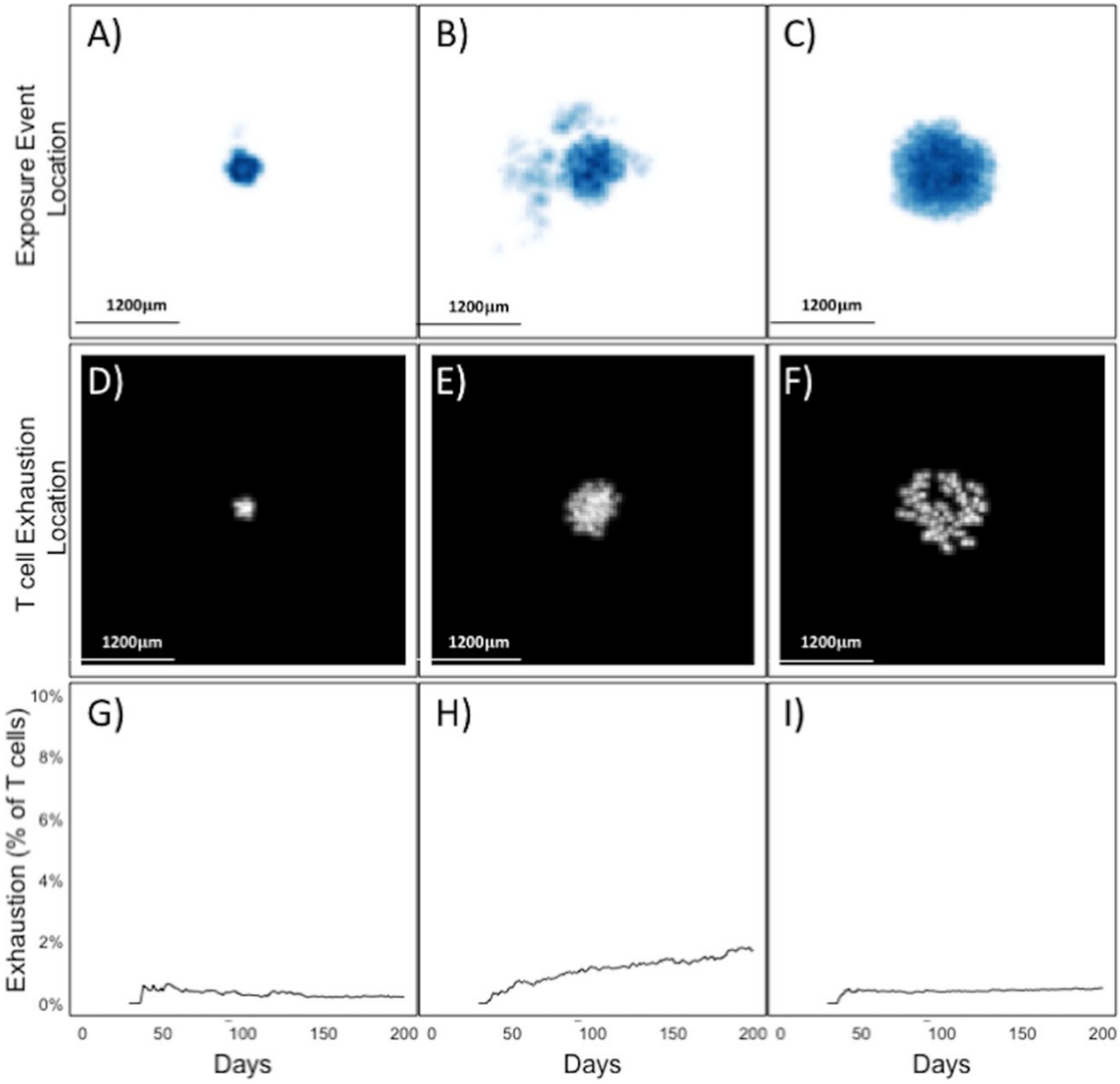

Figure 2.3 T-cell location within granulomas prevents T-cell exhaustion by reducing exposure events.

Row 1 (A,B,C): Cloud Maps showing the location of every EE in sterile, medium CFU, and TB pneumonia simulations. Dark blue represents areas of high numbers of EE and white represents a lack of EE. Row 2 (D, E, F): Heatmap location where T-cells (cytotoxic or IFN-γ producers) became exhausted. White represents the location of T cell at time of exhaustion. Row 3 (G, H, I): Time series graphs that display cumulative levels of exhaustion (as a percentage of total cytotoxic and IFN-γ producers) within corresponding simulations to Rows 1 and 2.

Based on the location of exhausted T cells in the simulations, it appears that cells are more likely to become exhausted as they penetrate deeper into the granuloma. As previously shown, Mtb bacilli are primarily located in the inner core of macrophages and within the necrotic center (52). As the structure becomes more organized, fewer T cells appear in this region. Thus, *GranSim* predicts that identifying large quantities of a T-cell exhaustion phenotype is unlikely after granuloma formation.

Using our biorepository of nearly 3000 simulated granulomas that matched to all 45 NHP granulomas, we compared observed levels of exhaustion (NHP granulomas) versus those obtained from simulations (Figure 2.4A). Note that we did not calibrate to the exhaustion levels found in NHP data, but instead calibrated the model to the NHP CFU and CD3+ T cell counts, and then compared exhaustion levels within these simulations to those obtained from NHP studies. The average difference between pairs in these two populations was not significant. That is, overall, our model was able to recapitulate the observed levels of exhaustion.

2.3.3 Extreme levels of *in silico* exhaustion drive unrealistic granuloma outcomes

Computational modeling allows us to artificially inflate the levels of T cell exhaustion in granulomas, to test the impact of widespread T-cell exhaustion on granuloma outcome. We selected the median bacterial burden simulation (Panel B from Figure 2.3) and re-simulated that same granuloma under hypothetical condition of decreasing EE threshold. We reasoned that a lower EE threshold would result in a larger number of T cells becoming exhausted, and a decreased ability of the granuloma to contain bacterial growth. We observe that inflated levels of exhaustion in the simulation lead to unfeasible granuloma outcomes, particularly in those granulomas whose EE threshold was less than 200 (Figure 2.4B). The previous simulation with an EE threshold of 5236 has a bacterial burden of about 288 CFU by day 200 (Figure 2.4C) and the simulation with an EE of 1 has 115,192,400 CFU (Figure 2.4D). To our knowledge and in our experience with macaque granulomas (51), these bacterial burdens are biologically unreasonable and can only be attained computationally when exhaustion levels are extremely high, well beyond the NHP findings. We conclude that T-cell exhaustion alone cannot explain the low-frequency of Mtb-responsive T cells in the granuloma, as the vast majority of T cells do not encounter stimulation by antigen sufficiently frequently to become exhausted.

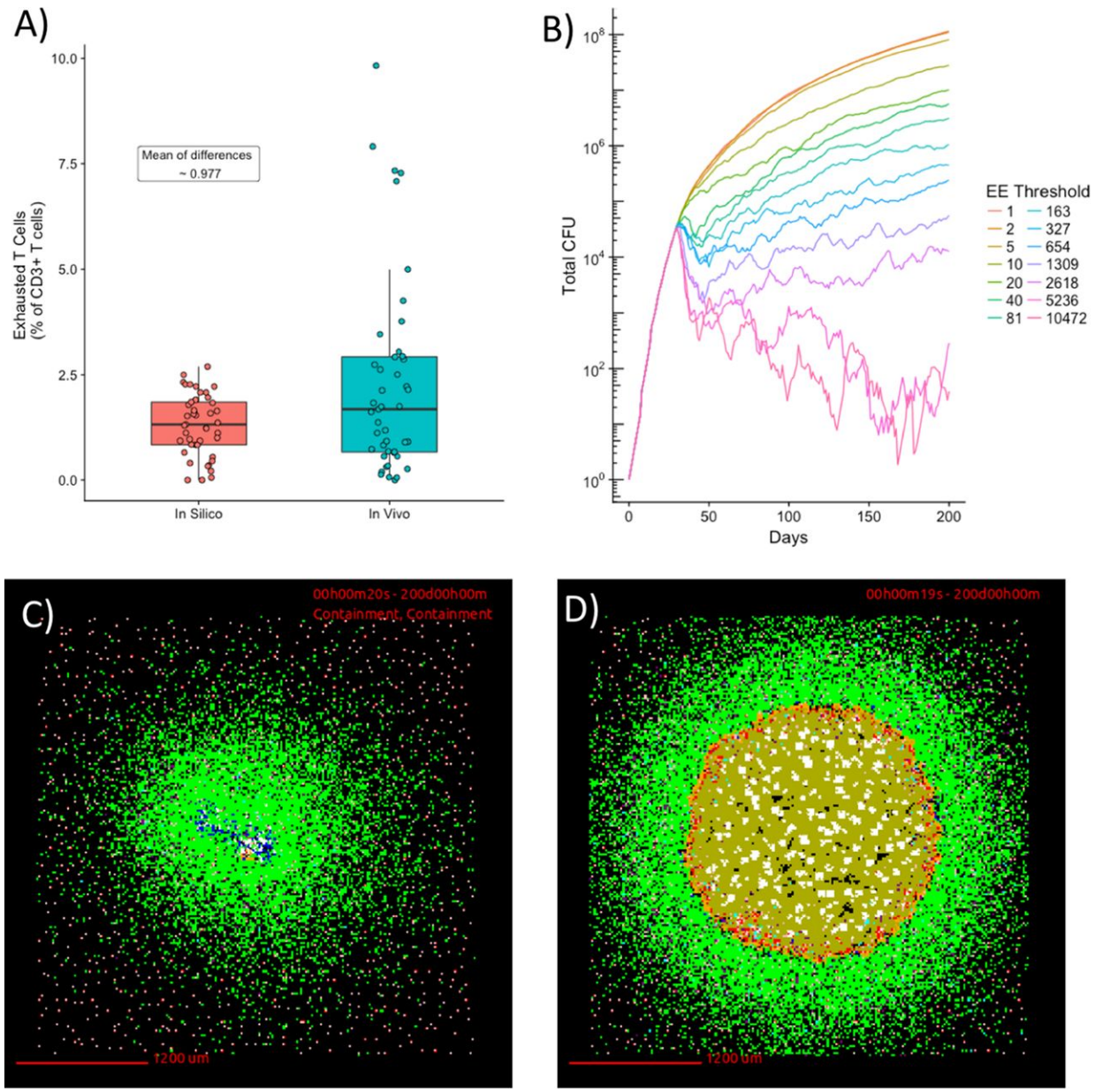

Figure 2.4 Artificially increasing T-cell exhaustion levels result in bacterial burdens that are not observed experimentally.

(A) A box and whisker plot demonstrating the distribution of exhaustion levels from NHP studies versus those obtained via simulation in the 45 macaque granulomas (blue) and the simulations that matched (red). (B) Graph of CFU vs time at varying EE thresholds. (C) Snapshot of granuloma with an EE threshold of 5236 taken at day 200. This granuloma represents a biologically feasible outcome and had a bacterial burden of 288 CFU. (D) Snapshot of granuloma with an EE threshold of 1 taken at day 200. This granuloma had a bacterial burden of 115192400 CFU.

2.4 Discussion

The presence and effect of T cell exhaustion has been studied in many chronic diseases. The chronic nature of Mtb infection and continued presence of bacterial antigens in granulomas

seemed to be an obvious scenario for development of exhausted T cells, which could explain the inability of some granulomas to completely eliminate bacteria. However, in NHP models of TB, both rhesus and cynomolgus macaques, we detect only limited apparent exhaustion of T cells within granulomas, based on the expression of inhibitory receptors.

To further investigate the lack of apparent exhaustion in granulomas, we turned to our computational, agent-based model of granuloma formation and function, *GranSim*. We demonstrated that *GranSim* can match macaque granuloma CFU and T cell counts datasets, and then explored the extent of exhaustion in the simulated granulomas. Like the NHP *in vivo* data, we found low levels of exhausted T cells within *in silico* granulomas. *GranSim* revealed that T cells could not readily penetrate into the macrophage or caseous layers of the granulomas, where most bacilli exist. Thus, the organized structure of the granuloma precludes widespread T cell exhaustion, in that macrophages and Mtb bacilli tend to be in the center of the granuloma, while T cells are concentrated in the lymphocyte cuff on the periphery of the granuloma. In fact, in cases of less organized pathology (TB pneumonia), we observed experimentally and computationally, somewhat higher levels of exhaustion, although still relatively low. Finally, we used our computational model to artificially inflate the level of T cell exhaustion in granulomas (by decreasing the threshold of T cell-APC interactions) and found that this would lead to exceptionally high bacterial burdens in granulomas. Such high bacterial burdens in individual granulomas are rarely seen in macaque models, even including those with substantial amounts of disease. Thus, we conclude that limited T cell exhaustion in granulomas is due to the relative infrequency of T cells contacting Mtb infected macrophages (or APCs carrying Mtb antigens), which is a key feature of the organized structure of granulomas.

Altogether, *in silico* data coupled with *in vivo* data support that the lack of T cell exhaustion in a chronic disease like TB is likely a result of the unique characteristic of the disease – containment of the Mtb bacilli within a well-structured granuloma. While the close proximity of bacterial antigens to the host immune cells seemed to be an obvious environment for T cell exhaustion, the structure and spatial arrangement of the immune cells in the granuloma may be responsible for the low levels of T cell exhaustion. T cells infiltrate the granulomas early in infection, but during chronic infection (>3 months), the vast majority of T cells are on the outer periphery of

the granuloma, away from bacteria and exposed macrophages in the center of the granuloma, thus preventing Mtb-T cell interactions, as also previously suggested by Kauffman et al. (25). Together, these data support and extend the notion that a balance of cytokine responses and T cell functionality are necessary for control of Mtb within granulomas, and that due to the spatial organization of the granuloma, T-cell exhaustion is likely not a major contributor to this balance at the local granuloma level.

2.5 References

1. WHO. WHO Global tuberculosis report 2016 [Internet]. World Health Organization Press. 2016. Available from: http://www.who.int/tb/publications/global_report/en/
2. Ehlers S, Schaible U. The Granuloma in Tuberculosis: Dynamics of a Host–Pathogen Collusion. Frontiers in Immunology [Internet]. 2013;3:411. Available from: https://www.frontiersin.org/article/10.3389/fimmu.2012.00411
3. Lin PL, Flynn JL. Understanding Latent Tuberculosis: A Moving Target. The Journal of Immunology. 2010;185(1):15–22.
4. Flynn JL, Chan J, Lin PL. Macrophages and control of granulomatous inflammation in tuberculosis. Mucosal immunology [Internet]. 2011/03/23. 2011 May;4(3):271–8. Available from: https://pubmed.ncbi.nlm.nih.gov/21430653
5. Russell DG. Who puts the tubercle in tuberculosis? Nature Reviews Microbiology. 2007;5(1):39–47.
6. Gideon HP, Phuah JY, Myers AJ, Bryson BD, Rodgers MA, Coleman MT, et al. Variability in Tuberculosis Granuloma T Cell Responses Exists, but a Balance of Pro- and Anti-inflammatory Cytokines Is Associated with Sterilization. PLoS Pathogens. 2015;11(1):1–28.
7. Zajac AJ, Blattman JN, Murali-Krishna K, Sourdive DJD, Suresh M, Altman JD, et al. Viral immune evasion due to persistence of activated T cells without effector function. The Journal of experimental medicine. 1998;188(12):2205–13.
8. Jiang Y, Li Y, Zhu B. T-cell exhaustion in the tumor microenvironment. Cell death & disease. 2015;6(6):e1792–e1792.
9. Boni C, Fisicaro P, Valdatta C, Amadei B, di Vincenzo P, Giuberti T, et al. Characterization of hepatitis B virus (HBV)-specific T-cell dysfunction in chronic HBV infection. Journal of virology. 2007;81(8):4215–25.
10. Urbani S, Amadei B, Tola D, Massari M, Schivazappa S, Missale G, et al. PD-1 expression in acute hepatitis C virus (HCV) infection is associated with HCV-specific CD8 exhaustion. Journal of virology. 2006;80(22):11398–403.
11. D'Souza M, Fontenot AP, Mack DG, Lozupone C, Dillon S, Meditz A, et al. Programmed death 1 expression on HIV-specific CD4+ T cells is driven by viral replication and associated with T cell dysfunction. The Journal of Immunology. 2007;179(3):1979–87.
12. Day CL, Kaufmann DE, Kiepiela P, Brown JA, Moodley ES, Reddy S, et al. PD-1 expression on HIV-specific T cells is associated with T-cell exhaustion and disease progression. Nature. 2006;443(7109):350–4.
13. Wherry EJ. T cell exhaustion. Nature Immunology [Internet]. 2011;12(6):492–9. Available from: https://doi.org/10.1038/ni.2035
14. Buggert M, Frederiksen J, Lund O, Betts MR, Biague A, Nielsen M, et al. CD4+ T cells with an activated and exhausted phenotype distinguish immunodeficiency during aviremic HIV-2 infection. AIDS (London, England). 2016;30(16):2415.
15. Pardoll DM. The blockade of immune checkpoints in cancer immunotherapy. Nature Reviews Cancer. 2012;12(4):252–64.
16. Ngiow SF, von Scheidt B, Akiba H, Yagita H, Teng MWL, Smyth MJ. Anti-TIM3 antibody promotes T cell IFN-γ–mediated antitumor immunity and suppresses established tumors. Cancer research. 2011;71(10):3540–51.
17. Velu V, Titanji K, Zhu B, Husain S, Pladevega A, Lai L, et al. Enhancing SIV-specific immunity *in vivo* by PD-1 blockade. Nature. 2009;458(7235):206–10.

18. Barber DL, Wherry EJ, Masopust D, Zhu B, Allison JP, Sharpe AH, et al. Restoring function in exhausted CD8 T cells during chronic viral infection. Nature. 2006;439(7077):682–7.
19. Trautmann L, Janbazian L, Chomont N, Said EA, Gimmig S, Bessette B, et al. Upregulation of PD-1 expression on HIV-specific CD8+ T cells leads to reversible immune dysfunction. Nature medicine. 2006;12(10):1198–202.
20. Singh A, Mohan A, Dey AB, Mitra DK. Inhibiting PD-1 pathway rescues M. tuberculosis specific IFN-γ producing T cells from apoptosis among pulmonary tuberculosis patients. J Infect Dis. 2013;208:603–15.
21. Shen L, Gao Y, Liu Y, Zhang B, Liu Q, Wu J, et al. PD-1/PD-L pathway inhibits M. tb-specific CD4+ T-cell functions and phagocytosis of macrophages in active tuberculosis. Scientific reports. 2016;6(1):1–9.
22. Jurado JO, Alvarez IB, Pasquinelli V, Martínez GJ, Quiroga MF, Abbate E, et al. Programmed death (PD)-1: PD-ligand 1/PD-ligand 2 pathway inhibits T cell effector functions during human tuberculosis. The Journal of Immunology. 2008;181(1):116–25.
23. Day CL, Abrahams DA, Lerumo L, van Rensburg EJ, Stone L, O'rie T, et al. Functional capacity of *Mycobacterium tuberculosis*-specific T cell responses in humans is associated with mycobacterial load. The Journal of Immunology. 2011;187(5):2222–32.
24. Phillips BL, Mehra S, Ahsan MH, Selman M, Khader SA, Kaushal D. LAG3 expression in active *Mycobacterium tuberculosis* infections. The American journal of pathology. 2015;185(3):820–33.
25. Kauffman KD, Sallin MA, Sakai S, Kamenyeva O, Kabat J, Weiner D, et al. Defective positioning in granulomas but not lung-homing limits CD4 T-cell interactions with *Mycobacterium tuberculosis*-infected macrophages in rhesus macaques. Mucosal immunology. 2018;11(2):462–73.
26. Jayaraman P, Jacques MK, Zhu C, Steblenko KM, Stowell BL, Madi A, et al. TIM3 mediates T cell exhaustion during *Mycobacterium tuberculosis* infection. PLoS pathogens. 2016;12(3):e1005490.
27. Reiley WW, Shafiani S, Wittmer ST, Moon JJ, Jenkins MK, Urdahl KB, et al. Distinct functions of antigen-specific CD4 T cells during murine *Mycobacterium tuberculosis* infection. Proceedings of the National Academy of Sciences. 2010;107(45):19408–13.
28. Sakai S, Kauffman KD, Sallin MA, Sharpe AH, Young HA, Ganusov V v, et al. CD4 T cell-derived IFN-γ plays a minimal role in control of pulmonary *Mycobacterium tuberculosis* infection and must be actively repressed by PD-1 to prevent lethal disease. PLoS pathogens. 2016;12(5):e1005667.
29. Barber DL, Mayer-Barber KD, Feng CG, Sharpe AH, Sher A. CD4 T cells promote rather than control tuberculosis in the absence of PD-1–mediated inhibition. The Journal of Immunology. 2011;186(3):1598–607.
30. Lázár-Molnár E, Chen B, Sweeney KA, Wang EJ, Liu W, Lin J, et al. Programmed death-1 (PD-1)–deficient mice are extraordinarily sensitive to tuberculosis. Proceedings of the National Academy of Sciences. 2010;107(30):13402–7.
31. Tousif S, Singh Y, Prasad DVR, Sharma P, van Kaer L, Das G. T cells from Programmed Death-1 deficient mice respond poorly to *Mycobacterium tuberculosis* infection. PloS one. 2011;6(5):e19864.
32. Larbi A, Fulop T. From "truly naïve" to "exhausted senescent" T cells: when markers predict functionality. Cytometry Part A. 2014;85(1):25–35.

33. Flynn JL, Klein E. Pulmonary tuberculosis in monkeys. A color atlas of comparative pathology of pulmonary tuberculosis. 2010;83–105.
34. Hokey DA, Johnson FB, Smith J, Weber JL, Yan J, Hirao L, et al. Activation drives PD-1 expression during vaccine-specific proliferation and following lentiviral infection in macaques. European journal of immunology. 2008;38(5):1435–45.
35. Hong JJ, Amancha PK, Rogers K, Ansari AA, Villinger F. Re-evaluation of PD-1 expression by T cells as a marker for immune exhaustion during SIV infection. PloS one. 2013;8(3):e60186.
36. Yi JS, Cox MA, Zajac AJ. T-cell exhaustion: characteristics, causes and conversion. Immunology. 2010;129(4):474–81.
37. Warsinske HC, Pienaar E, Linderman JJ, Mattila JT, Kirschner DE. Deletion of TGF-β1 increases bacterial clearance by cytotoxic t cells in a tuberculosis granuloma model. Frontiers in immunology. 2017;8:1843.
38. Pienaar E, Cilfone NA, Lin PL, Dartois V, Mattila JT, Butler JR, et al. A computational tool integrating host immunity with antibiotic dynamics to study tuberculosis treatment. Journal of theoretical biology. 2015;367:166–79.
39. Ray JCJ, Flynn JL, Kirschner DE. Synergy between individual TNF-dependent functions determines granuloma performance for controlling *Mycobacterium tuberculosis* infection. The Journal of Immunology. 2009;182(6):3706–17.
40. Cilfone NA, Perry CR, Kirschner DE, Linderman JJ. Multi-Scale Modeling Predicts a Balance of Tumor Necrosis Factor-α and Interleukin-10 Controls the Granuloma Environment during *Mycobacterium tuberculosis* Infection. PLoS ONE. 2013;8(7).
41. Cilfone NA, Ford CB, Marino S, Mattila JT, Gideon HP, Flynn JL, et al. Computational Modeling Predicts IL-10 Control of Lesion Sterilization by Balancing Early Host Immunity–Mediated Antimicrobial Responses with Caseation during *Mycobacterium tuberculosis* Infection . The Journal of Immunology. 2015;194(2):664–77.
42. Fallahi-Sichani M, El-Kebir M, Marino S, Kirschner DE, Linderman JJ. Multiscale Computational Modeling Reveals a Critical Role for TNF- Receptor 1 Dynamics in Tuberculosis Granuloma Formation. The Journal of Immunology [Internet]. 2011;186(6):3472–83. Available from: http://www.pubmedcentral.nih.gov/articlerender.fcgi?artid=3127549&tool=pmcentrez&rendertype=abstract
43. Wong EA, Joslyn L, Grant NL, Klein E, Lin PL, Kirschner DE, et al. Low Levels of T Cell Exhaustion in Tuberculous Lung Granulomas. Infection and Immunity. 2018;86(9).
44. Cilfone NA, Kirschner DE, Linderman JJ. Strategies for Efficient Numerical Implementation of Hybrid Multi-scale Agent-Based Models to Describe Biological Systems. Vol. 8, Cellular and Molecular Bioengineering. 2015. p. 119–36.
45. Utzschneider DT, Alfei F, Roelli P, Barras D, Chennupati V, Darbre S, et al. High antigen levels induce an exhausted phenotype in a chronic infection without impairing T cell expansion and survival. Journal of Experimental Medicine. 2016;213(9):1819–34.
46. Castellino F, Huang AY, Altan-Bonnet G, Stoll S, Scheinecker C, Germain RN. Chemokines enhance immunity by guiding naive CD8+ T cells to sites of CD4+ T cell–dendritic cell interaction. Nature. 2006;440(7086):890–5.
47. Riggs T, Walts A, Perry N, Bickle L, Lynch JN, Myers A, et al. A comparison of random vs. chemotaxis-driven contacts of T cells with dendritic cells during repertoire scanning. Journal of theoretical biology. 2008;250(4):732–51.

48. Bucks CM, Norton JA, Boesteanu AC, Mueller YM, Katsikis PD. Chronic antigen stimulation alone is sufficient to drive CD8+ T cell exhaustion. The Journal of Immunology. 2009;182(11):6697–708.
49. Zuniga EI, Harker JA. T-cell exhaustion due to persistent antigen: Quantity not quality? European journal of immunology. 2012;42(9):2285–9.
50. Marino S, Hogue IB, Ray CJ, Kirschner DE. A methodology for performing global uncertainty and sensitivity analysis in systems biology. Vol. 254, Journal of Theoretical Biology. 2008. p. 178–96.
51. Maiello P, DiFazio RM, Cadena AM, Rodgers MA, Lin PL, Scanga CA, et al. Rhesus macaques are more susceptible to progressive tuberculosis than cynomolgus macaques: A quantitative comparison. Infection and Immunity. 2018;86(2).

3 A Computational Model Tracks Whole-Lung *Mycobacterium tuberculosis* Infection and Predicts Factors that Inhibit Dissemination

This chapter is a published work:
Wessler T*, Joslyn LR*, Borish HJ, Gideon HP, Flynn JL, Kirschner DE, Linderman JJ. A computational model tracks whole-lung *Mycobacterium tuberculosis* infection and predicts factors that inhibit dissemination. PLoS computational biology. 2020 May 20;16(5):e1007280. (*indicates co-first authorship)

3.1 Introduction

Tuberculosis (TB) kills more individuals per year than any other infectious disease and treatment remains a global challenge (1). Only a small fraction (5–10%) of those infected with *Mycobacterium tuberculosis* (Mtb) develop active symptomatic disease (2), while the remainder control but do not eliminate the infection, which is termed latent TB (LTBI). A hallmark of Mtb infection is the presence of lung granulomas (lesions), collections of immune cells that surround Mtb in an effort to contain and control an infection. Multiple granulomas can be present in humans and non-human primates (NHPs). In NHPs, each granuloma is initiated by a single bacillus (3). Of key importance is that each granuloma within an individual has its own independent trajectory behavior. For example, the immune response in some granulomas eliminates all bacteria, resulting in sterilization. In other granulomas, immune cells only contain Mtb growth, resulting in stable granulomas that may persist for decades (4). If Mtb growth is not contained, however, granulomas can grow and/or spread, allowing for dissemination of bacteria across the lungs leading to the formation of new granulomas, spread to the airways resulting in transmission of infection through aerosolized bacteria, and possibly death of the host if not treated. Understanding the collective behavior of granulomas within lungs leading to dissemination events is critical to the ultimate goal of controlling the global TB epidemic.

It is difficult to experimentally address specific mechanisms operating within lungs that drive different granuloma outcomes in primates, although it is known through interventional studies that certain factors, such as TNF, CD4+ T cells, and CD8+ T cells are important in controlling early and established Mtb infection (5–8). As a complementary approach, mathematical

modeling can generate hypotheses that can then be tested experimentally. Several mathematical and computational models for Mtb infection have been developed to explore the contributions of the innate and adaptive immune responses to granuloma formation and function (9–20). These models are informed by studies in humans and in animal models of infection, especially NHPs, rabbits, pigs, and mice (21). In particular, *GranSim*, our computational model that allows simulation of the formation and function of a single granuloma using a hybrid agent-based model framework, has offered strategies for drug treatment and vaccine development (12,14,22–24). *GranSim*, which considers thousands of cells and bacteria as "agents" in the simulation and tracks diffusion of multiple immune mediators (e.g., cytokines), is computationally intensive, limiting our ability to simultaneously simulate multiple granulomas present in an entire lung during infection. In contrast, Prats et al. (18) utilized a bubble model to demonstrate the importance of local inflammation, dissemination, and coalescence of lesions as key factors leading to active TB, but did not specifically model events at the granuloma scale. However, following the formation of individual granulomas, the dissemination of those granulomas across the lungs over time, and, importantly, tracking events at the granuloma scale could provide an important window into infection dynamics and could lead to new insights for prevention or treatment.

In order to study the formation of new granulomas after initial establishment of infection, referred to as dissemination, the evolution of individual granulomas must be captured over time. Recently, research on Mtb-infected NHPs provided data on disseminating granulomas (25). Of all animal models used to study Mtb infection, NHPs are most relevant to human TB disease because they recapitulate the full spectrum of clinical outcomes and pathologies seen in humans (26). From PET CT imaging, the emergence of new granulomas was tracked and recorded. The authors genetically matched Mtb barcodes, assigned each inoculation Mtb a unique barcode ID, and associated each granuloma identified in the temporal PET CT images with the Mtb barcodes inside that granuloma (Figure 3.1). By identifying Mtb barcodes that were present in multiple granulomas, they were able to distinguish disseminating from non-disseminating granulomas. When identifying multiple bacterial barcodes within a single granuloma, it is surmised a merger of granulomas took place. While Martin et al. showed these distinctions, the mechanisms that

lead to granuloma clustering or dissemination remain unanswered. We address these open questions using a hybrid computational-mathematical modeling framework.

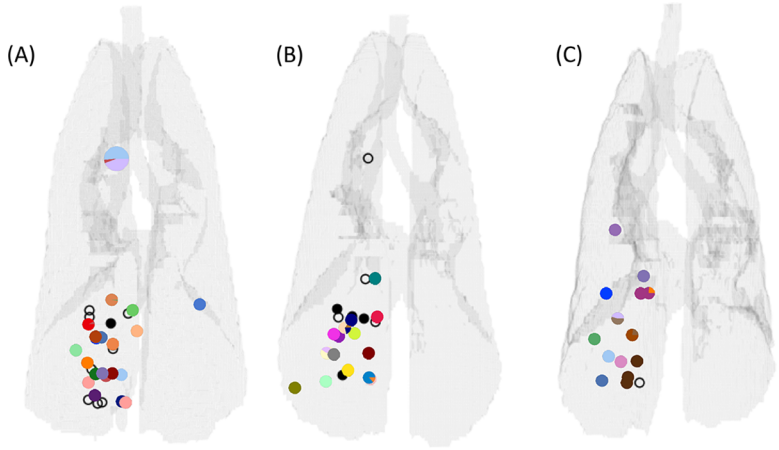

Figure 3.1 Three NHP lung maps illustrating the position of pulmonary granulomas and thoracic lymph nodes
Gray outlines denote the extent of the lungs, bronchial tubes, and trachea. Small markers superimposed on the outlines represent the positions of pulmonary granulomas, while larger markers denote lymph nodes. Colors denote unique barcode tags. Some samples had more than one barcode tag present, and often these were doublet granulomas (i.e., two granulomas too close in proximity to distinguish at necropsy) and so are marked with a pie chart showing the relative abundance of each barcode tag. The black markers represent pulmonary granulomas for which no barcode tags were found. Filled black markers are granulomas which grew bacteria upon plating but barcodes could not be determined for technical reasons, while open markers are granulomas that did not grow bacteria upon plating (sterile). Data previously published in Martin et al. (25)

Herein, we develop a novel multi-scale hybrid model, *MultiGran*, to track Mtb infection at the scale of the entire lung, including capturing multiple granulomas and their individual outcomes as well as the formation of new granulomas. *MultiGran* is an agent-based model that follows cells, cytokines, and bacterial populations across multiple lung granulomas throughout the course of infection. Each granuloma is now formulated as a single agent, and each agent contains within it a system of non-linear ordinary differential equations (ODEs) that capture individual granuloma dynamics. *MultiGran* follows the steps observed through the course of Mtb infection: (1) initial granuloma establishment with Mtb that have been virtually barcoded and placed within the lung environment, (2) granuloma development across time, (3) the possibility of granuloma dissemination with barcoded bacteria moving to a new location, and (4) granuloma merging by granulomas that have formed close together and whose individual boundaries are indistinguishable, or those that grow in size and thus merge into a granuloma cluster (that may have multiple barcoded bacteria IDs). We use *MultiGran* to address three outstanding questions

about dissemination: what mechanisms are consistent with granuloma dissemination and merging patterns seen *in vivo*? What is the likelihood of a granuloma to disseminate? Can we predict factors that lead to dissemination?

3.2 Methods

3.2.1 Animals and Experimental Dataset

All animal care, necropsy procedures, and experimental protocols and procedures are fully described in the published version of this chapter. Briefly, experimental data specifically for this study were obtained from seven cynomolgus macaques, infected with low dose Mtb (~10 CFU) as previously described (27–29). Necropsy was performed as previously described (28-30). For bacterial burden, each granuloma homogenate was plated, and the CFU were enumerated 21 days later to determine the number of bacilli in each granuloma (27,29).

To calibrate the individual granuloma computational model, we used excised granulomas from macaques that were infected for 3 weeks (n=2), 5 weeks (n=2), 7 weeks (n=2) and 9 weeks (n=1). In addition, an animal without Mtb infection was also included in this study as a control. To obtain accurate cell number measurements, enzymatic digestion was performed on excised granulomas. The single cell suspension obtained by enzymatic digestion was processed for bacterial burden and cell numbers enumeration (27). Single cell suspensions of individual granulomas were stained with cell surface antibodies to enumerate T cells (CD3) and macrophages (CD11b) for flow cytometry analysis.

In addition, bacterial burden data of 623 granulomas from 38 NHP that were controls in other studies (previously published (20,27,31–33) and ongoing studies) at University of Pittsburgh (Flynn Lab) were included for evaluation. The timing of infection depended on the particular study (Table of CFU values and tables of cell counts located at http://malthus.micro.med.umich.edu/lab/movies/MultiGran/ Table: gran-cfu-cyno-size) and ranged from 4-17 weeks post Mtb infection.

3.2.2 Non-human primate lung lattice data

To create a virtual lung that replicates an NHP lung, we used a CT scan of an uninfected NHP to model the 3-dimensional lung space. Binary images mapping the cross section of the lungs were created for each CT slice by segmentation of CT image values below -320 Houndsfield units. The individual slices were then stacked into an array, and a polygon mesh outlining the lung volume was generated using the marching_cubes_classic function in the open source Python scikit-image package (v 0.14.1, (34)).

3.2.3 Identifying granuloma distributions in non-human primate lungs

To allow us to test whether the distribution of granulomas in our virtual lungs matched that observed in NHP lungs, we refer to the distribution of granulomas arising from barcoded bacteria derived from our previously published data in Martin et al. (25). In that study, four cynomolgus macaques were infected with 11+/- 5 CFU barcoded Mtb Erdman. Barcoded libraries were generated where each bacterium has a different random 7-mer along with one of three 75-mer identifier tags inserted into the bacterial chromosome. This process created roughly 50,000 bacteria that are able to be uniquely identified by the random 7-mer tag with very small (< 2%) risk of duplication in an infection of <50 CFU (See Figure 1 in Martin et al. (25)). The animals were necropsied between 15 and 20 weeks post-infection. Animals were imaged at monthly intervals (or more frequently) to identify timing of granuloma establishment. Pulmonary granulomas were excised during necropsy, and their three-dimensional positions were recorded via matching to PET/CT imaging. Homogenates from excised pulmonary granulomas and infected thoracic lymph nodes were plated, scraped, and sequenced to identify the specific barcode(s) present in each granuloma. Matching the x, y, and z coordinates recorded for each granuloma with its determined barcode content led to a three-dimensional map of the locations of each barcode throughout the pulmonary space. Bacterial burden for each granuloma was determined by counting colonies on the plates.

Three of the four maps are shown in Figure 1 (the fourth was already presented in the original paper (25)). Lung outlines were calculated from terminal scans of each NHP by the process of creating a polygon mesh described above. Small markers represent pulmonary granulomas, while

larger markers denote lymph nodes. Each color represents a unique barcode tag. Some samples had more than one barcode tag present, and often these were doublet granulomas (i.e., two granulomas too close in proximity to distinguish at necropsy) and so are marked with a pie chart showing the relative abundance of each barcode tag. The black markers represent pulmonary granulomas for which no barcode tags were found. Filled black markers are granulomas which grew bacteria upon plating but for which barcodes could not be determined, while open markers are granulomas that did not grow bacteria upon plating (sterile); in this study, only CFU+ granulomas were available for barcode determination.

3.2.4 Model Overview

MultiGran is a novel multi-scale, hybrid agent-based model that describes the formation, function, and dissemination of lung granulomas containing Mtb (Figure 3.2). It uses sampling of nonhomogeneous Poisson processes; rule-based agent placement; parameter randomization; solving systems of non-linear ODEs; and post-process agent groupings to perform *in silico* experiments that track the progress of infection in an individual host. Each granuloma (agent) is placed stochastically within the boundary of the lung environment based on a set of rules. Within each agent, a system of ODEs is linked internally and solved simultaneously to update concentrations of cells, cytokines, and bacterial burdens within each granuloma at every time step. Additionally, within every time step, each granuloma is given the opportunity to disseminate locally and non-locally. Local dissemination involves a new granuloma being initialized nearby, while non-local dissemination allows initialization anywhere within the lung environment. At the lung scale, the model tracks the development, location, and quantity of granulomas, and determines whether each granuloma is either alone or a member of a larger granuloma cluster. At the granuloma scale, dissemination-event decisions, rules for granuloma formation, and concentrations of all granuloma components are tracked and defined. As is occasionally done when a flexible agent size is needed (35), our agents (granulomas) are placed on a continuous grid. Agents are spherical with dynamically-changing sizes, and granuloma clustering depends on the geometry and position of each of the agents.

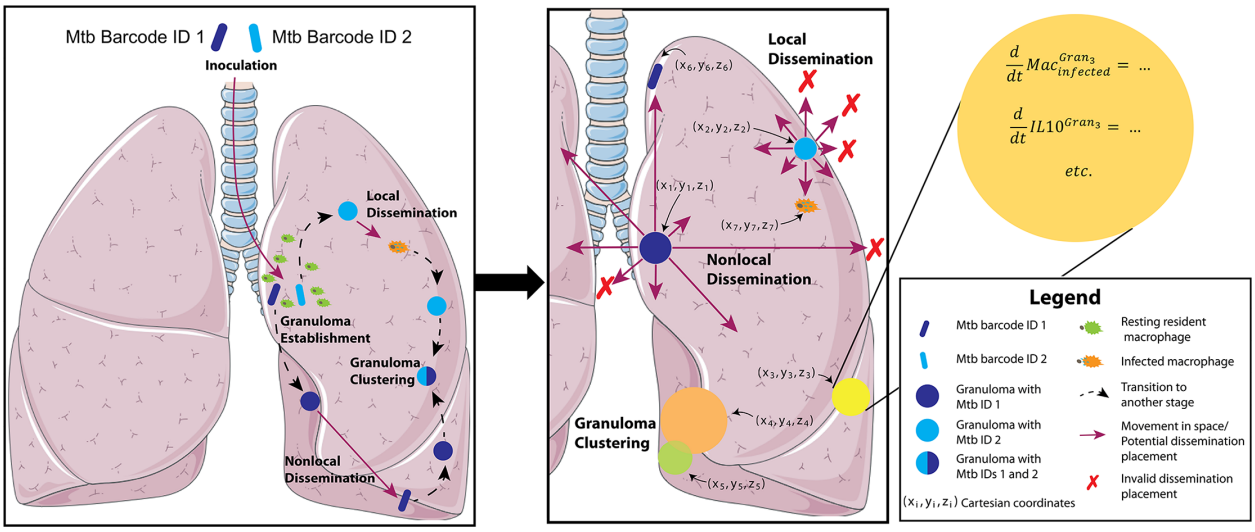

Figure 3.2 Process of Mtb infection and rules for granuloma dissemination and location within *MultiGran*

A non-human primate is inoculated with Mtb, here tracked using different "barcodes" or IDs. These Mtb are taken up by resident macrophages, initiating an innate immune response. This response includes the secretion of various cytokines and chemokines that help prime and/or recruit other immune cells to the site of the infection, resulting in the formation of lung granulomas. The dynamics within each granuloma are governed by systems of ordinary differential equations. Occasionally, as a granuloma develops, it may disseminate—either locally or non-locally. In local dissemination, an Mtb-infected macrophage moves to another nearby location within the same lung lobe. In non-local dissemination, a free extracellular Mtb reaches the airways or is carried to a draining lymph node and then deposited at a site not necessarily near the original location; i.e., in a different lung lobe. The (x,y,z) positions of disseminated granulomas depend on the method of dissemination (i.e., local or nonlocal) and the position of the parent granuloma. Granuloma clusters can form when granulomas develop near each other and may grow into each other, or when one granuloma forms immediately adjacent to the original granuloma via local dissemination (3). Granuloma clusters may contain more than one Mtb ID. Lung image adapted from Servier Medical Art.

Each *in silico* experiment using *MultiGran* is designed to replicate an *in vivo* experiment. To replicate the studies by Martin et al. (25), our simulated NHP is infected with roughly 19 uniquely-identified (barcoded) Mtb that are randomly placed in a localized region of the lungs, similar to the typical inoculation process in the NHP experiments. Each Mtb is assumed to be immediately taken up by a resident lung macrophage, forming a single, unique new granuloma (25). Each granuloma evolves independently. Whenever a granuloma is formed, it is initialized with parameter values that represent several characteristics that ultimately influence its future behavior, as well as the emergent outcomes of the system as a whole.

3.2.5 Simulation Environment

Code is written in MATLAB, with Bash script for submission to run on computer clusters. ODEs are solved using MATLAB's ode15s with the NonNegative option for all terms, and we define the start and end time interval to be the size of the agent time step. To avoid complications with the random number generator seed being reset with the initialization of each MATLAB instance, the Bash script executes code that generates a randomized seed list for the simulation to use. The website http://malthus.micro.med.umich.edu/lab/movies/MultiGran/ has pseudocode and implementation descriptions, as well as simulation videos.

3.2.6 Granuloma Establishment

A granuloma is initialized when Mtb is deposited into the lung environment. Based on our previous publications (3,25), we assume that each Mtb creates one granuloma (3,36). The granulomas established during inoculation (Figure B.1– Case 1) are referred to as "founder" granulomas and are considered first-generation granulomas; all other granulomas that may emerge throughout the simulation originate from these founders.

Granulomas are agents, so at initialization we assign parameter values to each granuloma and its infecting Mtb, as well as counts and concentrations of all cell types and cytokines. Every granuloma is assigned unique identification markers. These include being given a unique individual granuloma ID *IndivGranID(i)*, which is assigned in chronological order of initialization i=1,2,…N (where N is the total number of granulomas), as well as the individual granuloma ID of its parent, so the lineage of each of the founder Mtb can be tracked throughout the course of infection. Each granuloma is also given a position on a continuous grid.

3.2.7 Granuloma Development

The development of each individual granuloma "agent" is captured by a set of ODEs with 16 equations for 16 state variables capturing bacterial, T cell, macrophage and cytokine dynamics (see Table B.1 Equations for complete term-by-term description of the model). ODE model formulations build on our previous work (37–39) describing cells and levels of cytokines in a whole lung. The equations have been re-calibrated to NHP granuloma data (see section on Experimental dataset) to represent an individual granuloma (see section Model Calibration), and

have been updated in several ways. First, we increased the role of IL-10, including it as a factor for downregulating macrophage activation and TNF-α production by activated macrophages, as well as allowing infected macrophages to produce IL-10, based on NHP data (40–42). The other set of changes relates to intra- and extra-cellular Mtb to be consistent with recent findings on Mtb growth within macrophages (43–45). Rather than releasing the entire carrying capacity of bacteria at the occurrence of each death of an infected macrophage, the amount of intracellular Mtb within an average infected macrophage is released (with the exception of a bursting infected macrophage, in which case the maximum amount of Mtb is released). Furthermore, only a fraction of intracellular Mtb released during the natural death of an infected macrophage survives to become an extracellular Mtb. The expression for intracellular Mtb replication was also changed along with the addition of an expression for the natural slow death of intracellular Mtb for model stability. We record granuloma sterilization when the count of Mtb drops below 0.5.

3.2.8 Granuloma Dissemination

While the mechanisms behind dissemination are not yet well-understood (25), we have created rules such that the emergent outcomes are consistent with experiments (Figure B.1). We define a probability function for likelihood of a dissemination event, which we make dependent on the bacterial load (CFU) of the granuloma. We selected CFU because the data presented by Lin et al. (3) indicates that granuloma carrying capacity has a limit (approximately 10^5). Because NHP granulomas rarely exceed this limit (3,28), there is likely a link between granuloma CFU and dissemination. Because Mtb is by itself non-motile, we consider two routes of dissemination: 1) Mtb conveyance within an infected macrophage and 2) a single Mtb flowing through lung airways or deposited via a draining lymph node (LN). From these, we incorporated two types of dissemination events: local and non-local, the probabilities of each event being independent, and in the unlikely event that multiple dissemination events occur in the same time step, the order of events is randomized.

When a granuloma disseminates locally (Figure B.1– Case 3), an infected macrophage carrying intracellular Mtb is assumed to move from the parent granuloma position to a new position nearby. We assume the distance between the parent granuloma and a new position likely follows

a normal distribution with respect to parent location and we calibrated the mean and variance of this location using the data presented in Martin et al. (25). In Martin et al., the authors compute distances of each granuloma and granuloma clusters that they could identify via PET/CT, rather than every individual granuloma regardless of size and cluster affiliation. We also assume that a pre-determined quantity of T cells moves with an infected macrophage. After this dissemination event, the parent and daughter granulomas evolve independently from each other. When a granuloma disseminates non-locally (Figure B.1– Case 2), an extracellular Mtb is simulated as if entering airways (or via a LN) and deposited with equal likelihood anywhere within the lungs, where it is immediately taken up by a macrophage. Figure B.1-- Case 2 represents three realizations of trial coordinates wherein the trial coordinates represented by the red arrow do not satisfy our criteria, but the two black arrows would be acceptable placements for a bacterium in non-local dissemination.

We created two dissemination event probabilities describing local and non-local dissemination. In both, λ is the maximum probability of dissemination and is scaled by a Michaelis-Menten fraction, using a value of CFU at which the probability is half of the maximum value.

Equation 1 $$Prob_{Local}(t) = \lambda_{Local} \frac{CFU(t)}{CFU(t)+CFU_{half}^{Local}}$$

Equation 2 $$Prob_{Nonlocal}(t) = \lambda_{Nonlocal} \frac{CFU(t)}{CFU(t)+CFU_{half}^{Nonlocal}}$$

3.2.9 Granuloma Merging

Experiments demonstrate that a subset of granulomas contain a more than one Mtb barcode (25). Following inoculation or dissemination events, individual granulomas may merge, or are sufficiently close to each other, to form clusters. We identify granuloma clusters and their members when needed for plotting and computing statistics but allow them to evolve independently. Briefly, our algorithm evaluates all intersections of granulomas, and combines groups of granulomas that intersect in 3D space. These grouped granulomas are the granuloma clusters. A granuloma cluster may contain only descendants of a single founder Mtb ID, or may contain descendants of multiple founder Mtb IDs.

3.2.10 Model Calibration

An effective strategy for calibration of a complex system such as our multiscale model is evaluating the model's ability (and model parameters) to reproduce multiple scenarios and datasets (46–48), reducing the likelihood of overfitting parameters to a single dataset. Herein, we have built our multi-scale model of granuloma formation and dissemination using a priori biological knowledge and utilized multiple datasets, across multiple scales from unique experiments, to calibrate and validate our model parameters. Table 1 displays the multiple distinct datasets that we used to calibrate and validate this multi-scale model. First, we identified the parameter space of the individual granuloma ODE model that best represents the individual granuloma datasets (CFU and cell counts). See Figure 3.3 for an example of our workflow. To determine an initial, wide range of parameter values to test, we examined experimental values from literature, previous ODE models of a single granuloma formation (37–39), and values from *GranSim* (14,16,19,22,37–40,49). We then used a Latin Hypercube Sampling (LHS) algorithm (50) to sample this multi-dimensional parameter space 500 times. This initial wide range of simulations did not match the NHP data. We then narrowed the initial ranges and resampled the space in an iterative process until, out of the 500 simulations, ninety percent of the runs fell within the bounds of our experimental data on CFU, T cell counts, and macrophages within individual NHP granulomas. Figure 3.3 shows how we identify simulations that satisfy our criteria and isolate the parameters of those simulations to narrow parameter space. The parameter ranges for the calibrated model runs are in Table B.2, and represent the parameter space that we sampled in order to create the granulomas for our biorepository of 200 virtual monkey lungs and perform global sensitivity analysis techniques on.

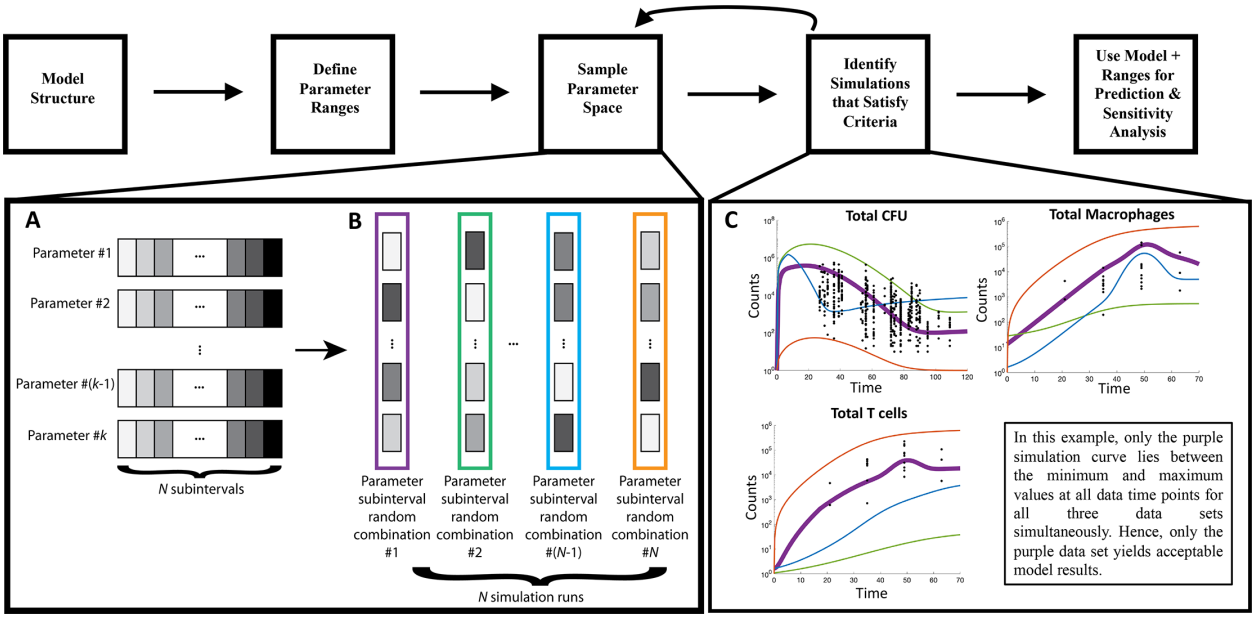

Figure 3.3 *MultiGran* calibration process
The model structure for the single granuloma ODE model and the broad parameter ranges (S1 Table) were based on previously published models and experimental data (14,16,19,22,37–40,49). We sample from the initial parameter space using a Latin Hypercube Sampling (LHS) process. LHS divides each of the *k* varied parameters into *N* subintervals (A), randomly selects a value from each subinterval, and randomly groups *k* values (one for each parameter) to create *N* parameter sets (B). We next identify simulations that satisfy all our criteria (C). Here, only the purple simulation curve (parameter set #1) has satisfied the criteria of passing within the minimum and maximum value at each timepoint for each of our three datasets simultaneously. Note that in a single LHS run, many simulations may satisfy all criteria, but for simplicity we have shown only a single one (purple curve). By inspecting values from parameter sets that pass all criteria, we are able to narrow each of the *k* broader parameter ranges. We iterate performing an LHS simulation followed by narrowing the *k* parameter ranges based on passing all of the criteria until 90% of the 500 simulations fall within the bounds of our experimental data on CFU, T cell counts, and macrophages within individual NHP granulomas.

Next, we identified the dissemination parameter space of *MultiGran* that matched the NHP whole lung outcome datasets (previously published (20,25,27,31–33) and ongoing studies). We again utilized LHS to sample this space and identify baseline parameter ranges that match the data (Table B.4). Figure 3.3 explains our workflow for calibrating the single-granuloma ODE model, which was similar to the approach for calibrating the lung-level dissemination equations. This calibrated parameter space was sampled to create a biorepository of *in silico* lungs to be used in Results. The entire repository of 200 virtual NHP CFU trends are displayed at http://malthus.micro.med.umich.edu/lab/movies/MultiGran/.

3.2.11 Sensitivity Analysis

We then used Partial Rank Correlation Coefficient (PRCC), a global sensitivity analysis index (50), to identify significant correlations between single-granuloma ODE model parameter changes and variation in whole lung outputs. We excluded the dissemination parameters from our multi-scale PRCC analysis because they are phenomenological in nature and we are interested in identifying the mechanistic events that occur at the granuloma scale and lead to dissemination, a whole lung outcome.

Table 3.1 Distinct datasets used to calibrate, validate and inform predictions in *MultiGran*
We calibrated our single-granuloma model, and then calibrated parameters specific for dissemination at the whole-lung level, prior to validation and predictions of individual NHP outcomes.

Dataset	Use	Model (scale)
Experimental values from literature, parameter values from previous ODE models of a single granuloma formation (37–39), and values from *GranSim* (14,16,19,22,37–40,49).	Initial sampling of entire single-granuloma parameter space	Single-granuloma ODE model (granuloma-level)
CFU/Granuloma Dataset Includes 623 granulomas from 38 NHPs	Calibration	Single-granuloma ODE model (granuloma-level)
Individual Granuloma Cell Count Dataset Includes 26 granulomas from 7 NHPs including total T cell counts and macrophage counts	Calibration	Single-granuloma ODE model (granuloma-level)
Granuloma Location Data Mean and variance of granuloma dissemination presented in Martin et al. (25)	Initial sampling of entire dissemination parameter space	*MultiGran* model (lung-level)
Whole Lung Outcome Measures Four outcomes - (1) number of Mtb at time of inoculation (2) number of granulomas at necropsy (3) the percentage of Mtb barcodes found in multiple granulomas and (4) the percentage of granulomas containing multiple Mtb barcodes	Calibration of dissemination parameters	*MultiGran* model (lung-level)

Spread of Infection Outcome Measures Including 38 NHP and the location of 623 granulomas across both lungs	Model validation	*MultiGran* model (lung-level)
Individual NHP CFU/granuloma Individual CFU/granuloma for a single NHP	Model prediction	*MultiGran* predictions about dissemination (multi-scale)

3.2.12 Linking Cellular Scale and Tissue Time Scales

We link the cell and cytokine scale events in the ODE model (single granuloma) with the tissue scale ABM (multiple granulomas) to form the multi-scale *MultiGran* model (Figure 2). Linking of timescales is important for proper model design (51). We use an ABM time-step of 1 day. At each ABM time-step, dissemination events can occur. After each ABM time step, the system of ODEs is solved for each granuloma to update the states of all host cells, cytokines and Mtb populations over the next 24 hours. We run the ODEs using adaptive time steps for 1 agent iteration, for each granuloma, before proceeding to the next agent time step, as dissemination events at the agent time step depend on the dynamically-changing state of ODEs. Additionally, the ODE state variable concentrations can be affected by the occurrence of a dissemination event.

3.3 Results

3.3.1 Simulated individual granulomas recapitulate *in vivo* primate granuloma dynamics

We calibrated our single-granuloma model, comprised of a system of non-linear ODEs, to data derived from NHP studies. We compared bacterial load (CFU), T cell counts, and macrophage counts over time per granuloma. Our CFU dataset consists of 623 granulomas from 38 NHPs (previously published (20,27,31–33) and ongoing studies). T cell and macrophage counts, as well as additional CFU, were derived from a separate, new dataset of 26 granulomas from 7 Mtb-infected NHPs and baseline data from one uninfected macaque (see Methods). The data from these 7 NHPs capture the timing of the immune system during early events in infection

(granulomas from all NHPs were collected between 3-9 weeks post infection) and were imperative for proper calibration of the model.

The single-granuloma model contains many parameters to represent various mechanisms that are part of innate and adaptive immune responses to Mtb infection, but we include few assumptions about the relative roles of each of these mechanisms; rather, we define equations and allow the relative influence of each mechanism emerge during calibration. We identify ranges of parameter values (Table B.2) that replicate CFU peaks at approximately 35 days and subsequent control of CFU after day 100 post-infection (Figure 3.4A), macrophage dynamics (Figure 3.4B), and T-cell dynamics (Figure 3.4C). These dynamics reflect the initial inability of the innate immune system to control Mtb replication, the eventual control provided by T cells that arrive from the lymph node around day 28, and the stabilization of Mtb counts around day 100. When isolating a suitable parameter range, we identified ranges that matched these overall trends and recapitulated the spread of granuloma outcomes outlined by the NHP datasets. Likely, our spread captures a fuller range of individual granuloma dynamics than a sample from a limited number of NHP can achieve.

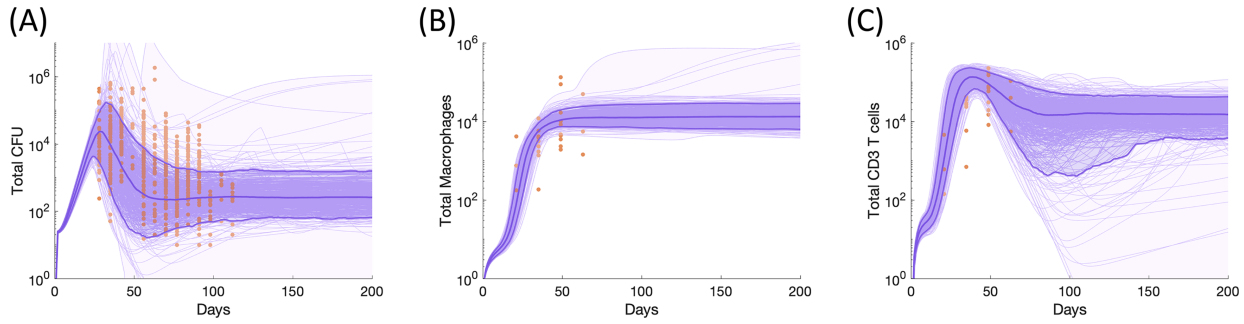

Figure 3.4 Bacteria, macrophage and T-cell dynamics within an individual granuloma
Individual NHP granuloma bacteria (A), macrophages (B), and CD3+ T cells (C) shown as orange points across time. Each individual point represents data from a single NHP granuloma. Purple lines indicate simulation outputs from 500 simulations that match NHP data. Light purple shading shows the minimum and maximum of simulation runs, darker purple shading represents the 5th to 95th percentiles of the simulations, and dark purple lines represent the 5th, 50th, and 95th percentiles of simulations. Parameter ranges are listed in Table B.2.

3.3.2 *MultiGran* simulates the appearance of granulomas throughout the lung, as seen *in vivo*

By employing the calibrated single-granuloma model (Figure 3.4) within our *MultiGran* framework, we can now simulate the spread of infection within the lung. We inoculate with 16 to 21 individual bacteria, mimicking the protocol of Martin et al. (25), placing them within an inoculation region within one of the lower lung lobes, as is done in the NHP inoculations via bronchoscope (see Methods). Each initial granuloma in an NHP arises from a single bacterium in an inoculation event (25). Therefore, we initially establish 16-21 granulomas. A sample simulation at the time-point of 250 days post-infection is shown in Figure 3.5. The blue lung mesh represents the dataset derived from NHPs for (x,y,z) coordinates of a lung. Placed on this mesh are simulation results – individual granulomas ("agents" in the model) and their location, size, and bacterial origin (barcode). Note that, as in the NHP images of Figure 3.1, infection is primarily within the inoculation region – but that 7 granulomas disseminated non-locally to the opposite lung. In this simulation, one granuloma cluster was found that contained more than one Mtb barcode, as is shown in the pie chart. Movies of disease progression using this 3D visualization are available on the website http://malthus.micro.med.umich.edu/lab/movies/MultiGran/.

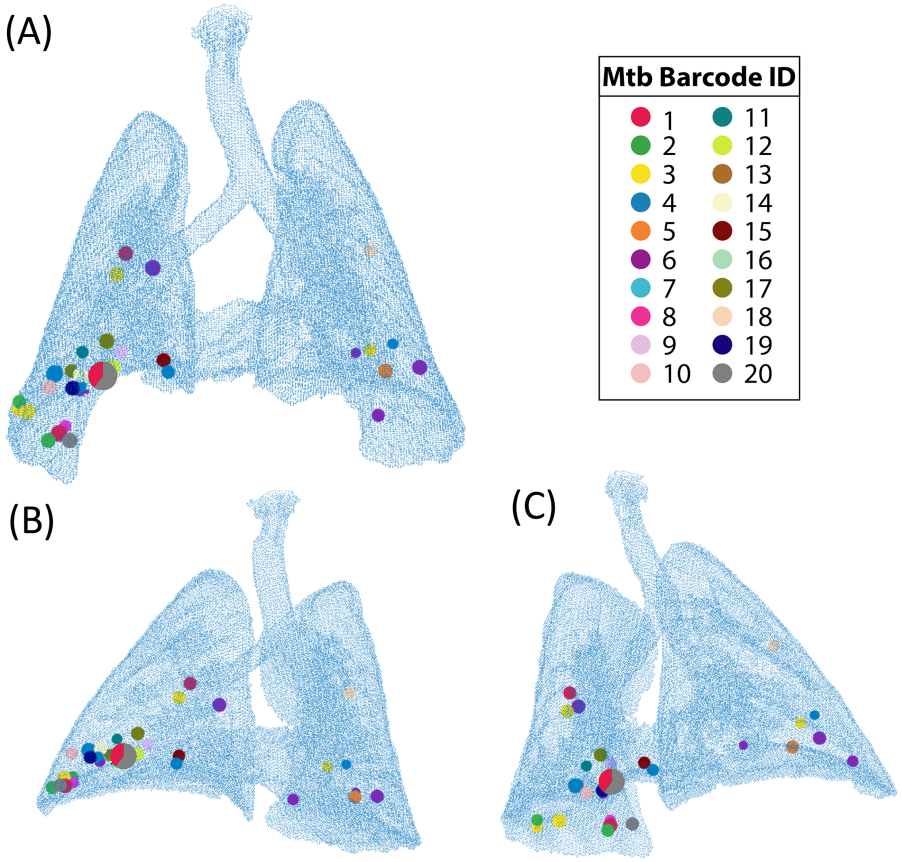

Figure 3.5 *MultiGran in silico* infection in a non-human primate lung
A single *in silico* simulation at 250 days post infection from three angles (A-anterior view, B&C-opposite posterior-lateral views), plotted over a data grid taken from PET/CT images of a single NHP. Granulomas are located within the lung in 3D space. Each circle of a single color represents a granuloma or granuloma cluster with a single Mtb barcode ID. The circle shown as a pie chart represents a granuloma cluster with two unique Mtb barcode IDs; each color represents the relative proportion of CFU of each ID compared to the total CFU of the granuloma cluster, while the overall size of the circle is proportional to the size of the cluster. Inoculation was in the lower right lung (bottom left in each image). Granulomas found in the upper right lung and the left lung result from non-local dissemination within the simulation.

3.3.3 Simulations are consistent with *in vivo* infection and predict dissemination likelihood rates

MultiGran allows both local and non-local dissemination of bacteria to initiate new granulomas, tracks the origin (Mtb ID) of each granuloma, and allows for merging of nearby granulomas to form a cluster. Each granuloma has a unique parameter set chosen from the ranges in Table B.2 according to an LHS design. To determine what leads to different dissemination patterns *in vivo*, we use our dataset consisting of four NHPs in that were inoculated with uniquely identifiable Mtb (Figure 3.1; Martin et al. (25)). Outcome measures from these experiments include: (1) the number of Mtb at time of inoculation (16-21 Mtb), (2) the number of granuloma (or granuloma

clusters) at necropsy (17-28 granulomas), (3) the percentage of Mtb barcodes found in multiple granulomas (12.5 - 68.4%), and (4) the percentage of granulomas containing multiple Mtb barcodes (~10-20%). We calibrated *MultiGran* dissemination dynamics to this dataset by varying the seven dissemination parameters (S3 Table). Our whole lung simulations and the NHP dataset are shown in Figure 3.6. Notice that the simulations capture the full heterogeneity of the *in vivo* results across each NHP. Additionally, the experimental data are from only four NHPs, while our simulations represent a larger, more diverse set of possible outcomes.

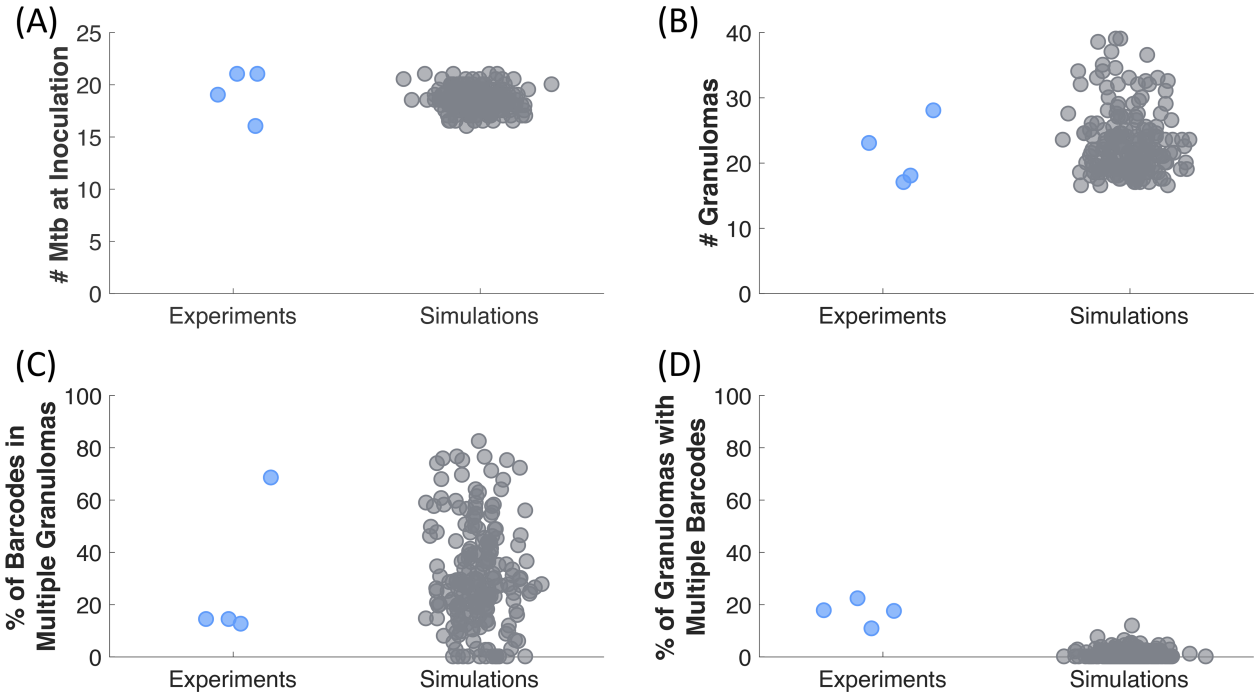

Figure 3.6 *MultiGran* recapitulates non-human primate dissemination outcomes
Martin et al. (25) infected 4 NHP with 16-21 different Mtb barcodes (A), and after 120 days the NHP immune system formed 16-28 non-sterilized granuloma clusters (B). We replicated these experiments by simulating 200 NHP, which started with 16-21 different Mtb. Of the 16-21 Mtb in NHP, 10%-70% were found in multiple granuloma clusters, meaning at least 10%-70% of Mtb were disseminating. Similar to the NHP data, our simulations have 0%-90% of Mtb barcodes disseminated to multiple granuloma clusters (C). Within the NHP experiments, of the 16-28 non-sterilized granuloma clusters, 10%-25% had multiple Mtb IDs within them, meaning at least 10%-25% of observed granulomas are clusters involving multiple sources of Mtb infection. Our 200 *MultiGran* simulations demonstrate a similar range of granuloma clusters with multiple Mtb barcodes (D). Simulations are shown in gray whereas NHP experiment outcomes are shown in blue. Each point represents a single NHP or in silico simulated granuloma.

To more directly test for non-local dissemination events, we validate our simulations against a second dataset of 38 NHPs (Figure 3.7). Within this NHP dataset, we identified the lung that contained the most granulomas for each NHP, and termed this lung the more-populated lung.

Next, we calculated the percentage of granulomas that resided in the more-populated lung out of the total number of granulomas across both lungs. We found that the 38 NHPs exhibited a range of 52%-100% of granulomas in the lung that was more-populated. Results from the same simulations used to create Figure 3.6 give a range ~54%-100%, providing additional support for the model in its ability to capture the range of data offered by NHP experiments. As this result is a validation step of our model, if *MultiGran* could not exhibit a similar range of granulomas across both lungs, the employed approach would have invalidated the model.

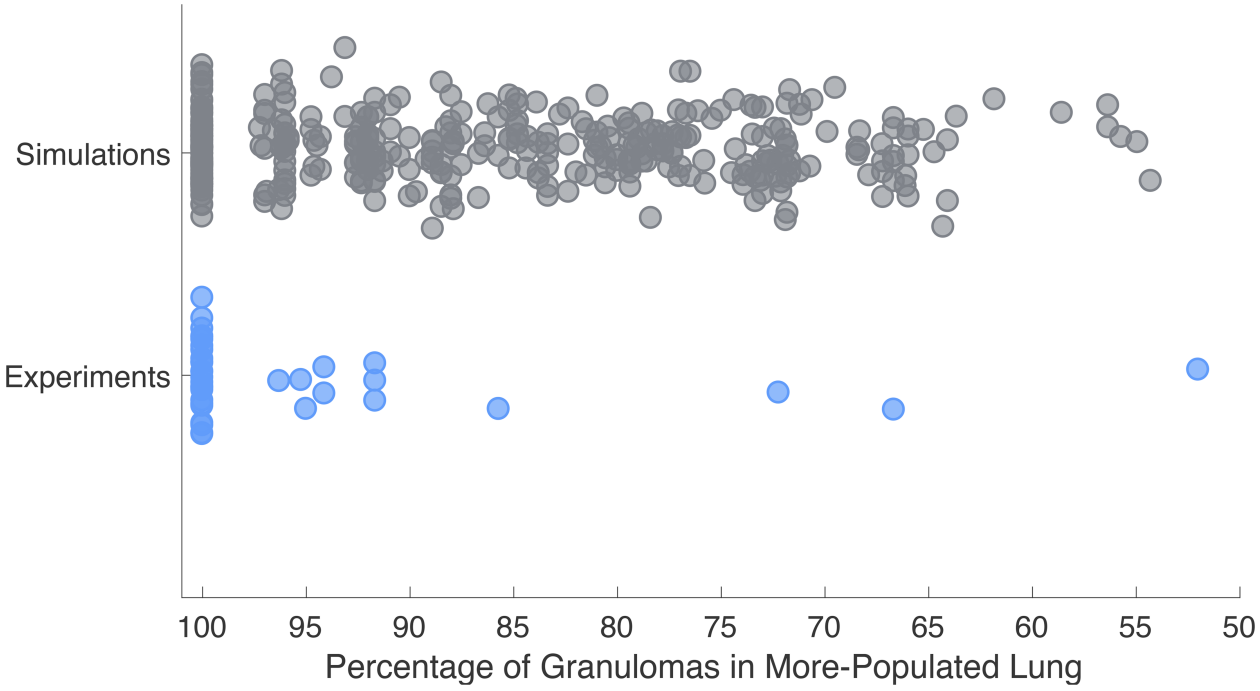

Figure 3.7 *MultiGran* recapitulates spread of infection data
At necropsy of 38 NHP experiments, we identified the lung that contained the most granulomas for each NHP. Next, we calculated the percentage of granulomas that resided in the more-populated lung out of the total number of granulomas. We found that 52-100% of granulomas formed resided within the more-populated lung. Blue dots represent each NHP experiment. We ran 200 in silico simulations that capture a similar range to the NHP spread of infection from lung to lung, ranging from 54.3% to 100%. Gray dots represent each simulated lung.

When examining *in vivo* data, the total number of dissemination events may be undercounted due to sterilization and granuloma clustering. In contrast, our model is able to count every dissemination event, and thereby provides a predicted frequency of local and non-local dissemination. We found that, on average, the rate of dissemination is about 1/24 dissemination events per granuloma per month for simulations run out to 250 days. Most dissemination occurs

earlier in the infection, as noted in Martin, et al. (25). Further, *MultiGran* predicts that local dissemination events occur about twice as frequently as non-local dissemination events.

3.3.4 *MultiGran* simulations match individual NHP infections

From our repository of 200 *MultiGran* simulated lungs, we isolated the five simulations that yielded the closest match to the median values of Mtb inoculation (20), the median number of granulomas at necropsy (20.5), the median percentage of Mtb barcodes that were found in multiple granulomas (14.3%), and the median percentage of granulomas that contained multiple Mtb barcodes (17.5%) across the four NHP from Martin et al. (25).

These five simulations represent the best matches to the NHP used in Martin et al. (25). We compare two of these simulations to the CFU/granuloma at necropsy from NHP:179-14 (Figure 3.8A & Figure 3.8C). Both lung simulations display satisfactory matches to the NHP CFU data; both simulations cover the spread of the experimental data while lying within the bounds of the dataset. However, while both simulations match the CFU data at 17 weeks, we are able to predict what could have happened beyond the necropsy date by running the simulation for a longer time period. Shown are two distinct possible outcomes with the same parameter set: note they diverge when predicting later dissemination events. Figure 3.8B shows one simulation predicts bacterial control across all the granulomas within that simulation. Figure 3.8D shows another outcome. Here, a single granuloma within the lung exhibits uncontrolled bacterial growth leading to dissemination and there is also formation of new granulomas via both local and non-local dissemination (at days 145, 166, and 193). These simulations suggest that NHP:179-14 was either containing the bacteria (i.e., LTBI) (our prediction in Figure 3.8B) or could have had a subclinical infection that was on the edge of leading to multiple dissemination events (our prediction in Figure 3.8D). Simulations that match the other three NHP are shown on our website, and reveal similar trends and predictions. Additionally, the entire repository of 200 virtual NHP CFU trends are displayed at:
http://malthus.micro.med.umich.edu/lab/movies/MultiGran/.

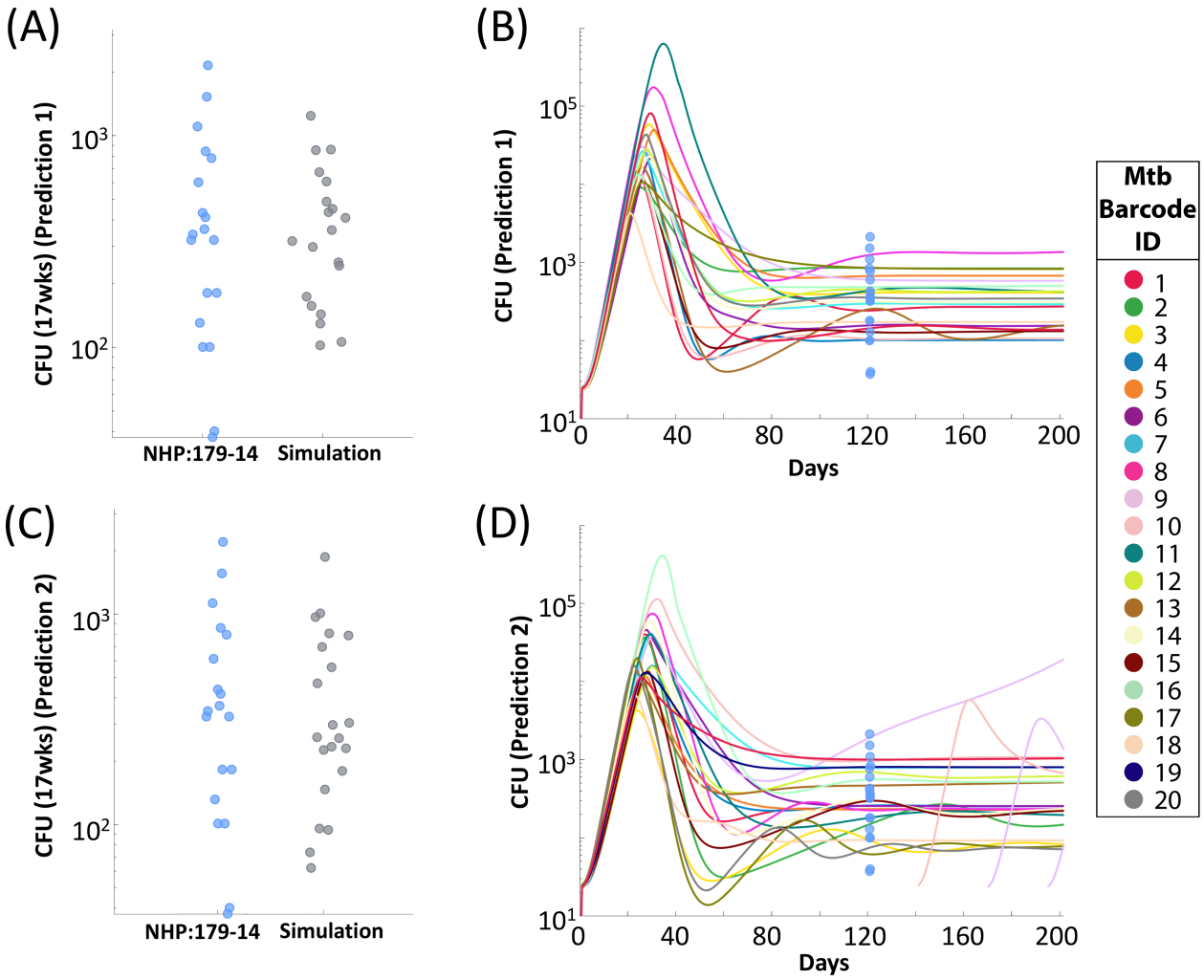

Figure 3.8 *MultiGran* matches individual NHP granuloma dynamics and predicts CFU burden across time

We compared the CFU/granuloma at necropsy for NHP:179-14 (A&C) to two separate simulations that matched these outcomes. Blue dots represent single-granuloma values taken from NHP:179-14; gray dots represent simulation values at comparable timepoints. Simulation predictions diverged after 17 weeks. One simulation predicted stability – i.e., granuloma containment of bacteria (B). The other simulation (D) predicted uncontrolled growth of bacteria within one granuloma, leading to dissemination and the formation of other granulomas across time. Each line in (B&D) represents one granuloma realization within *MultiGran* across time. Blue dots represent NHP:179 granuloma CFU values. Simulation behavior to the right of the blue dots should be considered a prediction. In D), the two disseminating granulomas arise after the provided experimental data and represent predictions of dissemination events occurring around day 130 and day 165 (colored peach and purple respectively).

3.3.5 Sensitivity analysis reveals important mechanisms responsible for dissemination

To predict the mechanisms that lead to dissemination events within lungs, we perform global sensitivity analysis using our repository of 200 *MultiGran* simulated lungs on four whole-lung outcomes of interest: the number of dissemination events, the total number of granuloma clusters at the end of the simulation, the percentage of granuloma clusters that contain multiple barcodes, and the percentage of granulomas that occupy the initially inoculated lung at the end of the simulation. We quantify the contributions of each model parameters to the outcomes of interest by calculating partial rank correlation coefficients (PRCC) at the end of the simulation (250 days). This analysis provides information about the contribution of each model parameter within our parameter space that was calibrated to multiple NHP datasets across cellular, granuloma, and whole-lung datasets. Our analysis reveals one parameter as the main driver of these four whole lung outcomes (Table 3.2). Parameter *CD8MultiFunc* describes the multi-functional nature of CD8+T cells, i.e., the amount of overlap of cytotoxic function and cytokine expression in CD8+ T cells. While the single-granuloma model was designed to be agnostic prior to calibration about the primary drivers behind bacterial killing and Mtb containment, we found that *CD8MultiFunc* is significantly correlated with each of the four outcomes. If *CD8MultiFunc* is increased so that a greater proportion of CD8+ T cells exhibits multi-functionality, then a larger percentage of granulomas will reside within a single lung (less non-local dissemination) and there will be fewer dissemination events and fewer granulomas overall. CD8+ T cells are a key host cell in a functional immune response to Mtb infection, and if the subpopulation that can perform multiple roles within the complex microenvironment of a granuloma increased, it would certainly benefit the host.

If we exclude parameter *CD8MultiFun* from the analysis, we reveal secondary contributions of other parameters to the whole lung outcomes (Table 3.2). These 12 parameters represent both adaptive and innate immune dynamics: we found both the adaptive and innate immune system were associated with non-local and local dissemination events. Notably, the role of macrophage-bacteria interactions is found to be important. *k18* represents the base rate of killing of extracellular bacteria by macrophages. If this rate is high, there are fewer dissemination events and fewer granulomas across the simulation. Additionally, *k17* represents the maximum bursting rate of infected macrophages. This parameter is positively correlated with the number of dissemination events and the number of granulomas across a simulation. If bursting occurs at a

high rate within a granuloma, our model predicts that a granuloma is more likely to disseminate both locally and non-locally. Taken together, these two parameters identify an important role for macrophage dynamics within the granuloma: if macrophages cannot adequately respond to Mtb, the likelihood of dissemination increases. Altogether, the results of this analysis represent a multi-scale impact: events governing cell function at the cellular scale impact local and non-local dissemination outcomes across the lungs and predict the difference between dissemination and control across the lung environment.

Table 3.2 Sensitivity analysis reveals global drivers of dissemination outcomes
PRCCs are shown for each parameter, showing a significant impact on each of the 4 *MultiGran* whole lung simulation outcomes at the end of the simulation. **Excluding parameter *CD8MultiFunc*, the overlap of cytotoxic function and cytokine expression in CD8+ T cells, 12 other parameters were also identified as having a significant impact on each of 4 *MultiGran* whole lung simulation outcomes at the end of the simulation. All PRCCs shown are significant to $p < .05$.

Parameter Name	Parameter Description	Number of Dissemination Events	Number of Granulomas and Clusters	Percentage of Granulomas with Multiple Barcodes	Percentage of Granulomas in More-Populated Lung
CD8MultiFunc **	overlap of cytotoxic function and cytokine expression in CD8+ T cells	-0.39	-0.38	-0.14	0.32
k18	Extracellular bacteria killed by macrophages	-0.11	-0.11	-0.041	0.11
nuI10	decay rate of IL-10 cytokine	-0.088	-0.087	-0.068	0.089
Sr1b	TNF based recruitment of primed CD4+ T cells	-0.075	-0.074	-0.044	0.06
k6	rate of differentiation from primed to Th1 CD4+ T cells	-0.084	-0.073	-0.047	0.071
s12	cell production of IL-12	-0.058	-0.056	-0.025	0.056
w	contribution of intracellular bacteria to resting macrophage activation	-0.037	-0.04	-0.021	0.04
s2	half-saturation of IL-4	-0.024	-0.021	-0.025	0.02
Sr3b	TNF based recruitment of Th2 CD4+ T cells	-0.036	-0.033	-0.021	0.025
alpha30	TNF production by infected macrophages	0.032	0.028	0.022	-0.037
nuTg	IFNg induced apoptosis of Th1 CD4+ T cells	0.057	0.055	0.037	-0.04

s4b	half-saturation of TNF on local resting macrophage recruitment	0.042	0.043	0.04	-0.043
k17	max rate of infected macrophages bursting	0.14	0.14	0.076	-0.12

3.4 Discussion

Tuberculosis is a complex and heterogeneous disease with a spectrum of outcomes, and the myriad of mechanisms that influence outcomes of initial infection are poorly defined. Our data in NHP models, and bolstered by data in humans, support the notion that each individual granuloma in a host is independent and dynamic, in terms of immunologic composition and function, ability to kill or restrain Mtb bacilli, and risk for dissemination or reactivation (52,53). However, it can be challenging in NHP models to determine the full range of host mechanisms that play a role in initial containment and prevention of dissemination, both of which are essential to limiting development of active TB. In the pursuit of a better understanding of the collective behavior of lung granulomas in individuals infected with Mtb, we performed a systems biology approach pairing NHP experiments and computational/mathematical modeling. Specifically, we explored events that lead to dissemination and new granuloma formation, and several studies have recently explored this biological phenomenon (25,36,54,55). In particular, the barcoding technique introduced by Martin et al. showed that dissemination varies widely among macaques despite initial infection conditions being similar, and that in individual macaques, each granuloma had a different dissemination risk, from no dissemination by most granulomas, even though these granulomas were CFU+, to multiple dissemination events from a single granuloma. The barcoding analysis provided critical new information about bacterial spread within the lung. However, identifying mechanisms that leading to granuloma dissemination, which is linked to development of active TB (36), is important in designing more effective vaccines and therapeutics against TB. Systems biology approaches can address these mechanisms and more generally contribute to our still limited understanding of Mtb infection dynamics.

In this work, we combine experimental data from NHPs with a novel multi-scale, hybrid agent-based model of granuloma formation, function and dissemination within the lung, called

MultiGran. We calibrate and validate *MultiGran* against multiple distinct NHP datasets that span cellular, bacterial, granuloma, and whole-lung scales. This calibration and validation allowed us to make predictions about dissemination within Mtb infected lungs. We report that the likelihood of local dissemination is approximately two times greater than non-local dissemination, which supports the *in vivo* data reported in Martin, et al. (25), and we used sensitivity analysis techniques to identify that dissemination is intertwined with the role of CD8+ T cells in granulomas. Specifically, we predict that the functionality of CD8+ T cells is critically important: if a greater percentage of CD8+ T cells can perform dual functions of cytokine expression (IFN-γ, TNF, and IL-10) and cytotoxicity, then the likelihood of dissemination significantly decreases.

The role of CD8+ T cell multi-functionality within the granuloma is controversial (for reviews of CD8+ T cells in TB, see (38,56). While the majority of T cells within a granuloma are single cytokine producers (27), multifunctional CD8+ T cells have been demonstrated in the blood of Mtb-infected humans and the proliferation and response rate of these cells differed between active and latent infection (57,58). Together, these studies and our current work suggest a need for increased focus on this specific cell type to evaluate the potential that CD8+ multifunctional T cells may offer.

Using *MultiGran*, we were able to match to granuloma population data coming from multiple monkeys (Figures 6 & 7) and granulomas (Figure 4). we were also able to match experimental data from a single NHP (Figure 8). In the era of precision medicine (59), the ability of *MultiGran* to match to individual data could help predict, in real time, whether the granulomas within that individual are likely to disseminate. This could happen when paired with PET/CT images of individually lung granulomas. However, more realistically, this provides an impetus for identifying biomarkers that are associated with granulomas at risk of dissemination, which could be more widely used to identify persons at risk of developing active TB following infection.

There are a few limitations of our study and model. First, the driving dissemination probability rules are somewhat phenomenological. Our goal in this first study was to rely on as few assumptions as possible; the only granuloma characteristic that is explicitly used in the

dissemination rules is the total bacterial burden. As a consequence, the model allows for even a stable, mature granuloma to disseminate (with small probability). We addressed this by allowing T cells to leave the parent granuloma to travel to a daughter granuloma in a local dissemination event, expecting this to sterilize new granulomas. Surprisingly, this was largely ineffective. Instead, it is more likely that the lung parenchyma in infected individuals has increased numbers of Mtb-specific T cells and possibly activated macrophages, so that new granulomas form in a completely different immune environment, compared to the initial granulomas that form in an immunologically naïve environment. This notion is supported by our data in NHP models demonstrating that primary ongoing infection protects against reinfection (32). *MultiGran* could be refined to test this in future iterations. Second, we restrict dissemination to be within the boundary of the lungs, but the actual environment within the lungs is very complicated and also could include airways and blood. Third, while we acknowledge thoracic lymph nodes as a source of non-local dissemination, and include adaptive immune cell recruitment in our ODE model, we currently do not explicitly model lymph node compartments. In future work, we plan to address the role of lymph nodes in Mtb infection and dissemination. Finally, while *MultiGran* was developed based on extensive NHP and human data, it does not contain all the various cell types and mechanisms in the complex environment of the granuloma, primarily because the functions and importance of certain cell types and factors remain obscure. As data become available, *MultiGran* can evolve to include additional factors for mechanistic test. Potentially, other modeling techniques might be better suited to answer specific questions surrounding granuloma dissemination. For example, if one was interested in exactly the path an infected macrophage might take when escaping the granuloma and initiating local dissemination, a spatial model at the site of infection, such as *GranSim* (60), could be more appropriate. However, such a modeling approach necessitates a loss of total lung-level dynamics that were critical to address our questions about dissemination events (both local and non-local) across NHP lungs.

In summary, we utilized a systems biology approach that combined computational modeling and NHP datasets to better understand mechanisms of granuloma dissemination. We present *MultiGran*, the first multi-scale model of granuloma dissemination and formation, that was calibrated and validated to NHP data and we make predictions about the rate of dissemination and the role of specific immune cells in granuloma dissemination. In particular, we discovered

roles for multifunctional CD8+ T cells and macrophage dynamics in preventing local and non-local dissemination within the lungs. Altogether, we argue that *MultiGran*, together with NHP experimental approaches, offers great potential to understand and predict dissemination events within Mtb infected lungs.

3.5 References

1. WHO. WHO Global tuberculosis report 2016. World Heal Organ Press. 2016. doi:ISBN 978 92 4 156539 4
2. Houben RMGJ, Esmail H, Emery JC, Joslyn LR, McQuaid CF, Menzies NA, et al. Spotting the old foe—revisiting the case definition for TB. Lancet Respir Med. 2019;7: 199–201. doi:10.1016/S2213-2600(19)30038-4
3. Lin PL, Ford CB, Coleman MT, Myers AJ, Gawande R, Ioerger T, et al. Sterilization of granulomas is common in active and latent tuberculosis despite within-host variability in bacterial killing. Nat Med. 2014;20: 75–79. doi:10.1038/nm.3412
4. Gideon HP, Flynn JL. Latent tuberculosis: What the host "sees"? Immunol Res. 2011;50: 202–212. doi:10.1007/s12026-011-8229-7
5. Lin PL, Myers A, Smith L, Bigbee C, Bigbee M, Fuhrman C, et al. Tumor necrosis factor neutralization results in disseminated disease in acute and latent *Mycobacterium tuberculosis* infection with normal granuloma structure in a cynomolgus macaque model. Arthritis Rheum. 2010;62: 340–350. doi:10.1002/art.27271
6. Diedrich CR, Mattila JT, Klein E, Janssen C, Phuah J, Sturgeon TJ, et al. Reactivation of latent tuberculosis in cynomolgus macaques infected with SIV is associated with early peripheral T cell depletion and not virus load. PLoS One. 2010;5. doi:10.1371/journal.pone.0009611
7. Mattila JT, Diedrich CR, Lin PL, Phuah J, Flynn JL. Simian Immunodeficiency Virus-Induced Changes in T Cell Cytokine Responses in Cynomolgus Macaques with Latent *Mycobacterium tuberculosis* Infection Are Associated with Timing of Reactivation . J Immunol. 2011;186: 3527–3537. doi:10.4049/jimmunol.1003773
8. Chen CY, Huang D, Wang RC, Shen L, Zeng G, Yao S, et al. A critical role for CD8 T cells in a nonhuman primate model of tuberculosis. PLoS Pathog. 2009;5. doi:10.1371/journal.ppat.1000392
9. Sershen CL, Plimpton SJ, May EE. Oxygen Modulates the Effectiveness of Granuloma Mediated Host Response to *Mycobacterium tuberculosis*: A Multiscale Computational Biology Approach. Front Cell Infect Microbiol. 2016. doi:10.3389/fcimb.2016.00006
10. Gough M, May E. An *in silico* model of the effects of Vitamin D3 on mycobacterium infected macrophage. Proceedings of the Annual International Conference of the IEEE Engineering in Medicine and Biology Society, EMBS. 2016. doi:10.1109/EMBC.2016.7590980
11. Linderman JJ, Kirschner DE. *In silico* models of M. Tuberculosis infection provide a route to new therapies. Drug Discov Today Dis Model. 2015;15: 37–41. doi:10.1016/j.ddmod.2014.02.006
12. Kirschner D, Pienaar E, Marino S, Linderman JJ. A review of computational and mathematical modeling contributions to our understanding of *Mycobacterium tuberculosis* within-host infection and treatment. Curr Opin Syst Biol. 2017;3: 170–185. doi:10.1016/j.coisb.2017.05.014
13. Hao W, Schlesinger LS, Friedman A. Modeling granulomas in response to infection in the lung. PLoS One. 2016;11. doi:10.1371/journal.pone.0148738
14. Warsinske HC, Pienaar E, Linderman JJ, Mattila JT, Kirschner DE. Deletion of TGF-β1 increases bacterial clearance by cytotoxic t cells in a tuberculosis granuloma model. Front Immunol. 2017;8. doi:10.3389/fimmu.2017.01843

15. Linderman JJ, Cilfone NA, Pienaar E, Gong C, Kirschner DE. A multi-scale approach to designing therapeutics for tuberculosis. Integr Biol (United Kingdom). 2015;7: 591–609. doi:10.1039/c4ib00295d
16. Cilfone NA, Perry CR, Kirschner DE, Linderman JJ. Multi-Scale Modeling Predicts a Balance of Tumor Necrosis Factor-α and Interleukin-10 Controls the Granuloma Environment during *Mycobacterium tuberculosis* Infection. PLoS One. 2013;8. doi:10.1371/journal.pone.0068680
17. Fallahi-Sichani M, Kirschner DE, Linderman JJ. NF-??B signaling dynamics play a key role in infection control in tuberculosis. Front Physiol. 2012;3 JUN. doi:10.3389/fphys.2012.00170
18. Prats C, Vilaplana C, Valls J, Marzo E, Cardona PJ, López D. Local inflammation, dissemination and coalescence of lesions are key for the progression toward active tuberculosis: The bubble model. Front Microbiol. 2016;7. doi:10.3389/fmicb.2016.00033
19. Marino S, Linderman JJ, Kirschner DE. A multifaceted approach to modeling the immune response in tuberculosis. Wiley Interdiscip Rev Syst Biol Med. 2011;3: 479–489. doi:10.1002/wsbm.131
20. Marino S, Gideon HP, Gong C, Mankad S, McCrone JT, Lin PL, et al. Computational and Empirical Studies Predict *Mycobacterium tuberculosis*-Specific T Cells as a Biomarker for Infection Outcome. PLoS Comput Biol. 2016;12. doi:10.1371/journal.pcbi.1004804
21. Flynn JL, Tsenova L, Izzo A, Kaplan G. Experimental Animal Models of Tuberculosis. Handbook of Tuberculosis. 2017. pp. 389–426. doi:10.1002/9783527611614.ch32
22. Wong EA, Joslyn L, Grant NL, Klein E, Lin PL, Kirschner DE, et al. Low Levels of T Cell Exhaustion in Tuberculous Lung Granulomas. Infect Immun. 2018;86. doi:10.1128/iai.00426-18
23. Pienaar E, Linderman JJ, Kirschner DE. Emergence and selection of isoniazid and rifampin resistance in tuberculosis granulomas. PLoS One. 2018;13. doi:10.1371/journal.pone.0196322
24. Sarathy J, Blanc L, Alvarez-Cabrera N, O'Brien P, Dias-Freedman I, Mina M, et al. Fluoroquinolone Efficacy against Tuberculosis Is Driven by Penetration into Lesions and Activity against Resident Bacterial Populations. Antimicrob Agents Chemother. 2019;63. doi:10.1128/aac.02516-18
25. Martin CJ, Cadena AM, Leung VW, Lin PL, Maiello P, Hicks N, et al. Digitally Barcoding *Mycobacterium tuberculosis* Reveals *In vivo* Infection Dynamics in the Macaque Model of Tuberculosis . MBio. 2017;8. doi:10.1128/mbio.00312-17
26. Flynn JL, Gideon HP, Mattila JT, Lin P ling. Immunology studies in non-human primate models of tuberculosis. Immunol Rev. 2015;264: 60–73. doi:10.1111/imr.12258
27. Gideon HP, Phuah JY, Myers AJ, Bryson BD, Rodgers MA, Coleman MT, et al. Variability in Tuberculosis Granuloma T Cell Responses Exists, but a Balance of Pro- and Anti-inflammatory Cytokines Is Associated with Sterilization. PLoS Pathog. 2015;11: 1–28. doi:10.1371/journal.ppat.1004603
28. Lin PL, Rodgers M, Smith L, Bigbee M, Myers A, Bigbee C, et al. Quantitative comparison of active and latent tuberculosis in the cynomolgus macaque model. Infect Immun. 2009;77: 4631–4642. doi:10.1128/IAI.00592-09
29. Lin PL, Pawar S, Myers A, Pegu A, Fuhrman C, Reinhart TA, et al. Early events in *Mycobacterium tuberculosis* infection in cynomolgus macaques. Infect Immun. 2006. doi:10.1128/IAI.00064-06

30. Lin PL, Coleman T, Carney JPJ, Lopresti BJ, Tomko J, Fillmore D, et al. Radiologic Responses in Cynomolgus Macaques for Assessing Tuberculosis Chemotherapy Regimens. Antimicrob Agents Chemother. 2013;57: 4237–4244. doi:10.1128/AAC.00277-13
31. Phuah J, Lin PL, Flynn JL, Chan J, Hendricks MR, Maiello P, et al. Effects of B Cell Depletion on Early *Mycobacterium tuberculosis* Infection in Cynomolgus Macaques. Infect Immun. 2016;84: 1301–1311. doi:10.1128/iai.00083-16
32. Cadena AM, Hopkins FF, Maiello P, Carey AF, Wong EA, Martin CJ, et al. Concurrent infection with *Mycobacterium tuberculosis* confers robust protection against secondary infection in macaques. PLoS Pathog. 2018;14. doi:10.1371/journal.ppat.1007305
33. Darrah PA, DiFazio RM, Maiello P, Gideon HP, Myers AJ, Rodgers MA, et al. Boosting BCG with proteins or rAd5 does not enhance protection against tuberculosis in rhesus macaques. npj Vaccines. 2019;4. doi:10.1038/s41541-019-0113-9
34. van der Walt S, Schönberger JL, Nunez-Iglesias J, Boulogne F, Warner JD, Yager N, et al. scikit-image: image processing in Python. PeerJ. 2014;2: e453. doi:10.7717/peerj.453
35. Wiktorski T. Spark. Adv Inf Knowl Process. 2019; 85–97. doi:10.1007/978-3-030-04603-3_9
36. Coleman MT, Maiello P, Tomko J, Frye LJ, Fillmore D, Janssen C, et al. Early changes by 18Fluorodeoxyglucose positron emission tomography coregistered with computed tomography predict outcome after *Mycobacterium tuberculosis* infection in cynomolgus macaques. Infect Immun. 2014;82: 2400–2404. doi:10.1128/IAI.01599-13
37. Wigginton JE, Kirschner D. A Model to Predict Cell-Mediated Immune Regulatory Mechanisms During Human Infection with *Mycobacterium tuberculosis*. J Immunol. 2001;166: 1951–1967. doi:10.4049/jimmunol.166.3.1951
38. Sud D, Bigbee C, Flynn JL, Kirschner DE. Contribution of CD8+ T Cells to Control of *Mycobacterium tuberculosis* Infection. J Immunol. 2014;176: 4296–4314. doi:10.4049/jimmunol.176.7.4296
39. Guzzetta G, Kirschner D. The Roles of Immune Memory and Aging in Protective Immunity and Endogenous Reactivation of Tuberculosis. PLoS One. 2013;8. doi:10.1371/journal.pone.0060425
40. Cilfone NA, Ford CB, Marino S, Mattila JT, Gideon HP, Flynn JL, et al. Computational Modeling Predicts IL-10 Control of Lesion Sterilization by Balancing Early Host Immunity–Mediated Antimicrobial Responses with Caseation during *Mycobacterium tuberculosis* Infection . J Immunol. 2015;194: 664–677. doi:10.4049/jimmunol.1400734
41. Marino S, Myers A, Flynn JL, Kirschner DE. TNF and IL-10 are major factors in modulation of the phagocytic cell environment in lung and lymph node in tuberculosis: A next-generation two-compartmental model. J Theor Biol. 2010;265: 586–598. doi:10.1016/j.jtbi.2010.05.012
42. Redford PS, Murray PJ, O'Garra A. The role of IL-10 in immune regulation during M. tuberculosis infection. Mucosal Immunol. 2011;4: 261–270. doi:10.1038/mi.2011.7
43. Mahamed D, Boulle M, Ganga Y, Mc Arthur C, Skroch S, Oom L, et al. Intracellular growth of *Mycobacterium tuberculosis* after macrophage cell death leads to serial killing of host cells. Elife. 2017;6. doi:10.7554/eLife.22028
44. Huang L, Nazarova E V., Tan S, Liu Y, Russell DG. Growth of *Mycobacterium tuberculosis in vivo* segregates with host macrophage metabolism and ontogeny . J Exp Med. 2018;215: 1135–1152. doi:10.1084/jem.20172020

45. Hoal-Van Helden EG, Hon D, Lewis LA, Beyers N, Van Helden PD. Mycobacterial growth in human macrophages: Variation according to donor, inoculum and bacterial strain. Cell Biol Int. 2001;25: 71–81. doi:10.1006/cbir.2000.0679
46. Read MN, Alden K, Rose LM, Timmis J. Automated multi-objective calibration of biological agent-based simulations. J R Soc Interface. 2016;13. doi:10.1098/rsif.2016.0543
47. Read MN, Alden K, Timmis J, Andrews PS. Strategies for calibrating models of biology. Brief Bioinform. 2018. doi:10.1093/bib/bby092
48. Menzies NA, Soeteman DI, Pandya A, Kim JJ. Bayesian Methods for Calibrating Health Policy Models: A Tutorial. Pharmacoeconomics. 2017;35: 613–624. doi:10.1007/s40273-017-0494-4
49. Fallahi-Sichani M, El-Kebir M, Marino S, Kirschner DE, Linderman JJ. Multiscale Computational Modeling Reveals a Critical Role for TNF- Receptor 1 Dynamics in Tuberculosis Granuloma Formation. J Immunol. 2011;186: 3472–3483. doi:10.4049/jimmunol.1003299
50. Marino S, Hogue IB, Ray CJ, Kirschner DE. A methodology for performing global uncertainty and sensitivity analysis in systems biology. Journal of Theoretical Biology. 2008. pp. 178–196. doi:10.1016/j.jtbi.2008.04.011
51. Cilfone NA, Kirschner DE, Linderman JJ. Strategies for Efficient Numerical Implementation of Hybrid Multi-scale Agent-Based Models to Describe Biological Systems. Cellular and Molecular Bioengineering. 2015. pp. 119–136. doi:10.1007/s12195-014-0363-6

52. Cadena AM, Fortune SM, Flynn JL. Heterogeneity in tuberculosis. Nat Rev Immunol. 2017;17: 691–702. doi:10.1038/nri.2017.69
53. Cadena AM, Flynn JL, Fortune SM. The importance of first impressions: Early events in *Mycobacterium tuberculosis* infection influence outcome. mBio. 2016. doi:10.1128/mBio.00342-16
54. Lin PL, Maiello P, Gideon HP, Coleman MT, Cadena AM, Rodgers MA, et al. PET CT Identifies Reactivation Risk in Cynomolgus Macaques with Latent M. tuberculosis. PLoS Pathog. 2016;12: e1005739. doi:10.1371/journal.ppat.1005739
55. Maiello P, DiFazio RM, Cadena AM, Rodgers MA, Lin PL, Scanga CA, et al. Rhesus macaques are more susceptible to progressive tuberculosis than cynomolgus macaques: A quantitative comparison. Infect Immun. 2018;86. doi:10.1128/IAI.00505-17
56. Lin PL, Flynn JL. CD8 T cells and *Mycobacterium tuberculosis* infection. Semin Immunopathol. 2015;37: 239–249. doi:10.1007/s00281-015-0490-8
57. Rozot V, Vigano S, Mazza-Stalder J, Idrizi E, Day CL, Perreau M, et al. *Mycobacterium tuberculosis*-specific CD8+ T cells are functionally and phenotypically different between latent infection and active disease. Eur J Immunol. 2013;43: 1568–1577. doi:10.1002/eji.201243262
58. Commandeur S, Lin MY, van Meijgaarden KE, Friggen AH, Franken KLMC, Drijfhout JW, et al. Double- and monofunctional CD4 + and CD8 + T-cell responses to *Mycobacterium tuberculosis* DosR antigens and peptides in long-term latently infected individuals. Eur J Immunol. 2011;41: 2925–2936. doi:10.1002/eji.201141602
59. Collins FS, Varmus H. A new initiative on precision medicine. N Engl J Med. 2015;372: 793–5. doi:10.1056/NEJMp1500523
60. Segovia-Juarez JL, Ganguli S, Kirschner D. Identifying control mechanisms of granuloma formation during M. tuberculosis infection using an agent-based model. J Theor Biol. 2004;231: 357–376. doi:10.1016/j.jtbi.2004.06.031

4 Integrating Non-Human Primate, Human, and Mathematical Studies to Determine the Influence of BCG Timing on H56 Vaccine Outcomes

This chapter is a published work:
Joslyn LR, Pienaar E, DiFazio RM, Suliman S, Kagina BM, Flynn JL, Scriba TJ, Linderman JJ, Kirschner DE. Integrating non-human primate, human, and mathematical studies to determine the influence of BCG timing on H56 vaccine outcomes. Frontiers in microbiology. 2018 Aug 17;9:1734.

4.1 Introduction

Among infectious diseases, tuberculosis (TB) remains the leading cause of death due to a single agent. Its infectious agent, *Mycobacterium tuberculosis* (Mtb), kills approximately three individuals per minute (1). Additionally, in 2015, there were an estimated 480,000 incident cases of multi-drug resistant TB. The morbidity and mortality due to tuberculosis, including drug resistant strains, require renewed investment and research for an effective vaccine.
While Bacillus Calmette-Guérin (BCG) is widely used to prevent TB disease in infants, its efficacy amongst the adult population is highly variable (2–7). Originally developed in the early 1900s, the first clinical trials for BCG began in France in the 1920s and proved its efficacy in children (8). By 1973, BCG was compulsory for South Africa (9) and emerged as the most widely used of all vaccines, due to ease of testing for vaccination via the tuberculin skin test. However, BCG efficacy fails to protect both infants and adults; with protection varying from 0-80% (8,10). Thus, the search for a more effective vaccine continues.

Improved management of the TB epidemic could stem from vaccinations that prevent infection, active disease, or reactivation from latent infection, or ameliorate active infections. Currently, more than 13 TB vaccine candidates have entered clinical trials (11,12). These candidates include attenuated versions of Mtb, mycobacterial whole cell vaccines, viral vectored vaccines, and subunit vaccines (13).

Subunit vaccination strategies emerged when the Mtb genome was sequenced in 1998 (14). One such promising subunit vaccine candidate is H56 formulated with adjuvant IC31. H56 is a multistage vaccine composed of three antigens: ESAT6, Ag85B, and Rv2660c (15). ESAT6 and Ag85B are early secreted antigens that have been used before as individual vaccine antigens (16–20). Ag85B is an antigen that is present in both BCG and H56 vaccine formulations. Both Ag85B and ESAT6 have been shown to be highly immunogenic antigens that are targeted by T cell populations (21,22). Rv2660c was included in the vaccine because of its association with T cell responses from LTBI (Latent Tuberculosis Infection) individuals and its expression under starvation or hypoxic conditions, although its function has not yet been determined (23–25). Finally, all three antigens are thought to play a role in a variety of methods that mycobacteria likely employs to survive the intracellular environment (23,26–29).

Common formulations of the H56 vaccine include the adjuvants IC31 and Cationic Adjuvant Formulation (CAF01). Human clinical trials used the IC31 adjuvant, a two-component adjuvant that includes the KLK peptide (an anti-microbial peptide) and oligodeoxynocleotide (a Toll-like receptor nine agonist) (30). IC-31 was used in an NHP study that showed H56 limited reactivation of clinical latent TB (23), while CAF01 has been used in NHP studies herein. CAF01 is composed primarily of DDA (liposomes prepared in dimethyl dioctadecyl ammonium) and TDB (a component of the mycobacterial cell wall, trehalose dimycolate) (31). Both adjuvants support a Th1 CD4 T cell response (30,31).

While H56 represents a new vaccine candidate, it also provides an opportunity for a case study. Before evaluating the success of a vaccine via challenge, can we compare vaccine immunogenicity in humans and NHPs to further characterize the inherent differences between each species? Furthermore, can we utilize antigen specificity to explore the impact and role of prior BCG vaccination on H56 immunogenicity?

We use a systems biology approach employing mathematical modeling to relate pre-exposure vaccination dynamics in humans and non-human primates. We describe T-cell responses in lymph nodes and blood using a 2-compartment mathematical model, demonstrate the impact of BCG timing on subsequent H56 vaccination, and reveal basic mechanisms that dictate vaccine

outcomes in NHPs and humans. We propose that timing of BCG vaccination and inherent differences between species could play an important role in the immune responses to the H56 vaccine candidate. Having this knowledge could improve the vaccine pipeline.

4.2 Methods

4.2.1 Non-Human Primate Data Collection and Analysis

Full animal and experimental protocols are described in the published version of this chapter. Briefly, eight cynomolgus macaques were primed with 0.1 mL BCG Danish intramuscularly followed by two doses of the vaccine H56 (Ag85B-ESAT6-Rv2660c; 50 μg) mixed with CAF01 (625 μg dimethyldioctadecyl-ammonium (DDA) and 125 μg trehalose-6,6-dibehenate (TDB)) at weeks 10 and 14 after BCG priming. Timing and doses of vaccination are based on previous studies by our collaborators and others in the field who perform protein-based boosting of BCG in macaques (16,23). ELISPOT for IFN-γ was performed to identify antigen-specific T-cell responses to the ESAT6 and Ag85B antigens at various time points following vaccination (Figure 4.1).

Figure 4.1 shows the timeline of experimental protocol, with blood draw events for NHP studies (bottom timeline). We represent the data from NHPs in a manner consistent with the standardization of the phase I clinical trial data provided by Luabeya et al. Like Luabeya et al., we analyzed the antigen specific T cell response for CD4+ effector (CD27-CD45+), effector memory (CD27-CD45-), and central memory (CD27+CD45-) subtypes. ESAT6- or Ag85B-specific cellular concentrations were calculated. Finally, we converted the antigen-specific responses for each T-cell subtype to represent a percentage of total CD4+ T cells in blood.

4.2.2 Phase I Clinical Trial Data Collection and Analysis

For model calibration, we used data described previously (30). Briefly, the data is from the first in-human phase I clinical trial of candidate TB vaccine, H56 in IC31 adjuvant. The authors tested the safety and immunogenicity of H56:IC31 in adults with or without Mtb infection. Across 112 days, eight individuals without evidence of Mtb infection were injected with 3 doses

of H56 (50 μg H56, 500 nmol IC31) at 56 day intervals. Blood was drawn from individuals on days 0, 14, 56, 70, 112, 126 and 210. Antigen-specific T-cell responses were isolated and collected at each sample collection time point. Every individual in the study received BCG vaccination as a child (approximately 30 years prior to this study). Figure 4.1 shows the timeline of experimental protocol for the human trial (top timeline).

We standardized the results of Luabeya et al. in a manner that allows for eventual comparison to NHP data. The study revealed that the H56 vaccine does not induce a robust CD8+ T cell response. Therefore, we focused all data analysis, model calibration, and results on individual subtypes of the CD4+ T cell response to vaccination. That is, we examined effector (CD45RA+ CCR7–), effector memory (CD45RA–CCR7–), central memory (CD45RA–CCR7+), and total CD4+ T cell populations. Luabeya et al. also discovered that a dose of 50 μg of H56 was not optimal; however, we have selected the 50 μg dataset so that we can directly compare human responses to the NHP studies described above.

For each T cell subtype, we normalized the response by subtracting the number of unstimulated, cytokine-producing T cells from the quantity of T cells that produced cytokines in response to antigen. We converted this metric to represent a percentage of the total number of CD4+ T cells. This calculation was performed for responses to both the ESAT6 and Ag85B antigens.
Note that the adjuvants used in these two studies (NHP and human) are different and could contribute significantly to the results observed. In this work, we do not examine adjuvant differences but focus instead on the impact of BCG timing and differences in T cell responses between species. See below for further discussion of how we indirectly capture adjuvants.

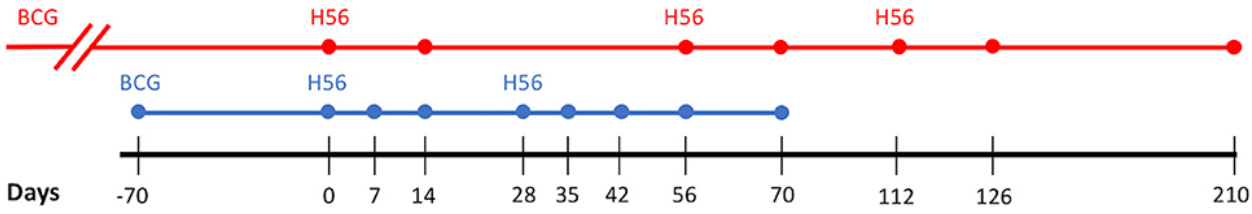

Figure 4.1 Vaccination Experimental Protocol.
Comparison of the Human (red) and Non-Human Primate (blue) study protocols. Dots along the respective timelines represent blood sample data collection time points. BCG, Bacillus Calmette–Guerin; H56, vaccination with H56 and adjuvant (IC31 in Human, CAF01 in Non-Human Primate).

4.2.3 Mathematical Model

In recent studies (32–35), we captured lymph node and blood dynamics in response to Mtb infection using a mathematical model. We used a compartmentalized system of 16 non-linear, autonomous ordinary differential equations (ODEs) to track specific and non-specific CD4+ effector, effector memory, and central memory T cell responses. In these previous works we represent Mtb-specific T-cells as a generic class of antigen-specific cells; thus, it was simple to retool this class of cells and track them as ESAT6- or Ag85B-specific. We assume that all antigen-specific T cells are equally immune responsive. Figure 4.2 displays the model schematic, Appendix C details the system of ODEs, and Table C.1 gives the list of all parameters, definitions, and values.

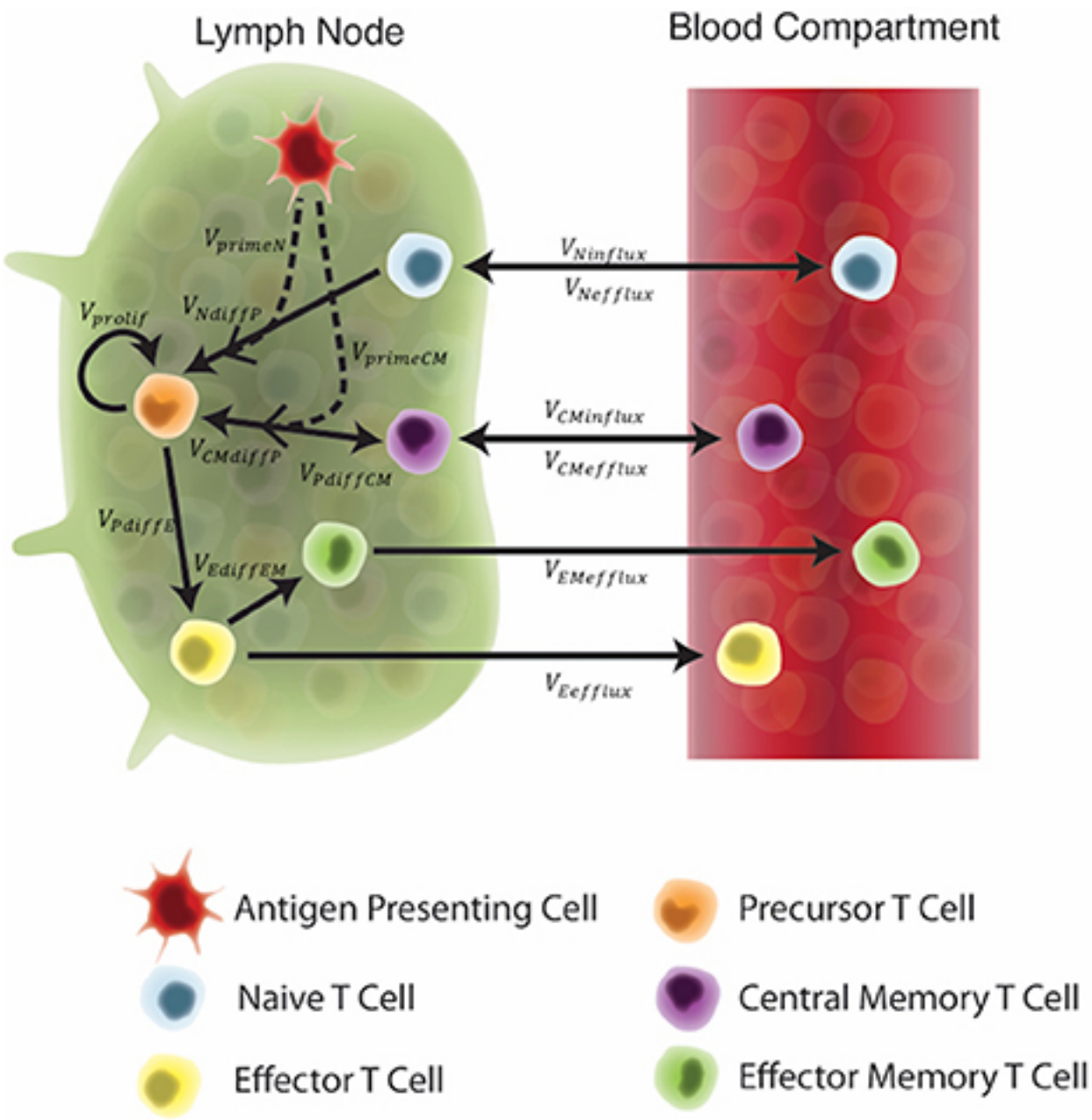

Figure 4.2 Schematic of the two-compartment model.
Each equation represents a concentration of a particular cell type, as outlined in the legend. These concentrations are dependent on other cell concentrations and interactions (as shown by arrows) between cells or compartments. Arrow labels are defined in greater detail in Appendix C. Briefly, V_{primeN} and $V_{primeCM}$ represents the impact of APCs on naïve and central memory cell recruitment. V_{NdiffP} and $V_{CMdiffP}$ shows the transformation of naïve and central memory T cells to the precursor T cell population. V_{prolif}, V_{PdiffE}, $V_{PdiffCM}$, and $V_{EdiffEM}$ represents precursor proliferation and differentiation to effector, central memory and effector memory cell types, respectively. Finally, influx and efflux rates between LN and blood are shown as $V_{Ninflux}$, $V_{CMinflux}$, $V_{CMefflux}$, $V_{Eefflux}$, and $V_{EMefflux}$.

Our key assumption is that the *in silico*, exogenous introduction of antigen loaded, antigen-presenting cells (APCs) will act as a reasonable proxy for vaccination. This is valid for two reasons: First, it is well known that vaccine peptides are presented to T cells by APCs. Second, while we did not mechanistically model the impact of an adjuvant in this study, this assumption indirectly evaluates the impact of an adjuvant on T-cell responses. APCs require adjuvant to properly process and present vaccine peptides (36). Therefore, to account for variability in individual response to an adjuvant and to represent variability across adjuvants (IC31 versus CAF01), the quantity of APCs pulsed during vaccination events was assigned to a single quantity within a range of values. Thus, we simulated vaccination events by pulsing the APC equation in the system of ODEs at a time point equal to the day of H56 vaccination, according to each experimental protocol.

The non-linear ODE model system was implemented and solved in Matlab (R2016b v 9.1). Experimental and simulation data cleaning, visualization, and post-processing was performed in R (R version 3.4.0, RStudio version 1.0.143) using ggplot2 (37), plyr (38), and tidyr (39) packages. See Appendix C for equations and model parameters.

4.2.4 Model Calibration and Sensitivity Analysis

We first sought to define the parameter space that best represents each "immunogenicity dataspace" to calibrate to the human and NHP datasets (see Appendix C for a description of several important terms for this section of our work). The parameter space was identified by a two-step process. First, for each immunogenicity space, we ran 1500 simulations with a 50% range around the baseline parameters outlined in our previous model construction (shown in (32)). A Latin hypercube sampling (LHS) algorithm was used to sample the multi-dimensional parameter space (40) . This wide range of simulations yielded multiple candidates of baseline parameters that might best represent each immunogenicity dataspace. In the second step, we simulated 500 runs (sampling parameters in approximately 20% range) around these candidates' baseline values, again using LHS to sample the parameter space. We accepted the candidate parameter sets if all 500 runs fulfilled two criteria: (1) the simulations' minimum and maximum run must remain within the immunogenicity dataspace. That is, all simulations from the parameter ranges needed to remain within the logarithmic scale of the data. (2) the median

simulation run across all 500 runs must cross the interquartile range of the majority of experimental time points (4 of 7 for human data, 4 of 8 for NHP data). This ensured that our model mimics at least the majority of both experimentally-determined dynamics. Appendix C displays the parameter range values after calibration to each immunogenicity dataspace.
We quantify the importance of each host mechanism involved in vaccination dynamics by finding correlations between model parameters and outputs. Correlations between specific model outputs and parameters were determined by using Partial Rank Correlation Coefficient (PRCC), where -1 denotes a perfect negative correlation between a model output and parameter (+1 denotes a perfect positive correlation between model output and parameter). Marino et al. completed a review of the statistical tests available to access significance of PRCC (40). PRCC results performed a dual role: not only do they reveal the relationship between model outcomes and parameters, they also inform calibration of the model to the immunogenicity dataspace. As the model is tuned, manipulations to the more sensitive parameters ameliorate model fitting according to the criteria above.

Since our model provides measurements in the form of cell counts in lymph node and cells/mm^3 in the blood, we performed post-processing of the simulations to ensure that units matched those provided by the H56 vaccination data (See Appendix C for details).

4.2.5 Parameter Space Visualization

We utilized radar charts to illustrate parameter range comparisons between species and the impact of BCG on cellular responses. Radar charts are a graphical visualization of multivariate data across multiple axis. In this work, we plotted radar charts using R's radarchart function in the fmsb package (41). Each axis represents a parameter of interest in our ODE model. Points near the center of each axis represent a lower value for that parameter whereas points near the outer edges of each axis represent larger values. To compare parameter ranges across species, we calculate the minimum and maximum for each axis on the charts as the minimum and maximum value for each parameter across all species and antigen-specific fits (see Appendix C). To compare the impact of BCG memory on the H56 immune response, we created the human radar charts with a minimum and maximum for each axis defined by the minimum and

maximum parameter value across human model fits to ESAT6 or Ag85B. We created the NHP radar charts by displaying the parameter ranges within the minimum and maximum values across NHP model fits to either antigen.

4.3 Results

4.3.1 Humans and non-human primates exhibit different T-cell responses to ESAT6 following H56 vaccination

In response to H56 vaccination, humans and NHPs showed large variability within and across species. While some of this variability can be attributed to the different experimental protocols used (Figure 4.1), the magnitudes of responses between species still differ. Several differences in the magnitude and timing of response across species are notable (Figure 4.3). The total response of CD4+ ESAT6+ T cells in NHPs is larger and more variable than the response in humans. For example, an F test to compare variances between the two species at day 14 reveals a significant difference (p-value = 0.0003; variance of NHPs was approximately 25 times greater than the humans). Day 14 is the final day that protocols follow the same timelines. Therefore we selected day 14 for this statistical test in order to exclude variability due to different experimental protocols.

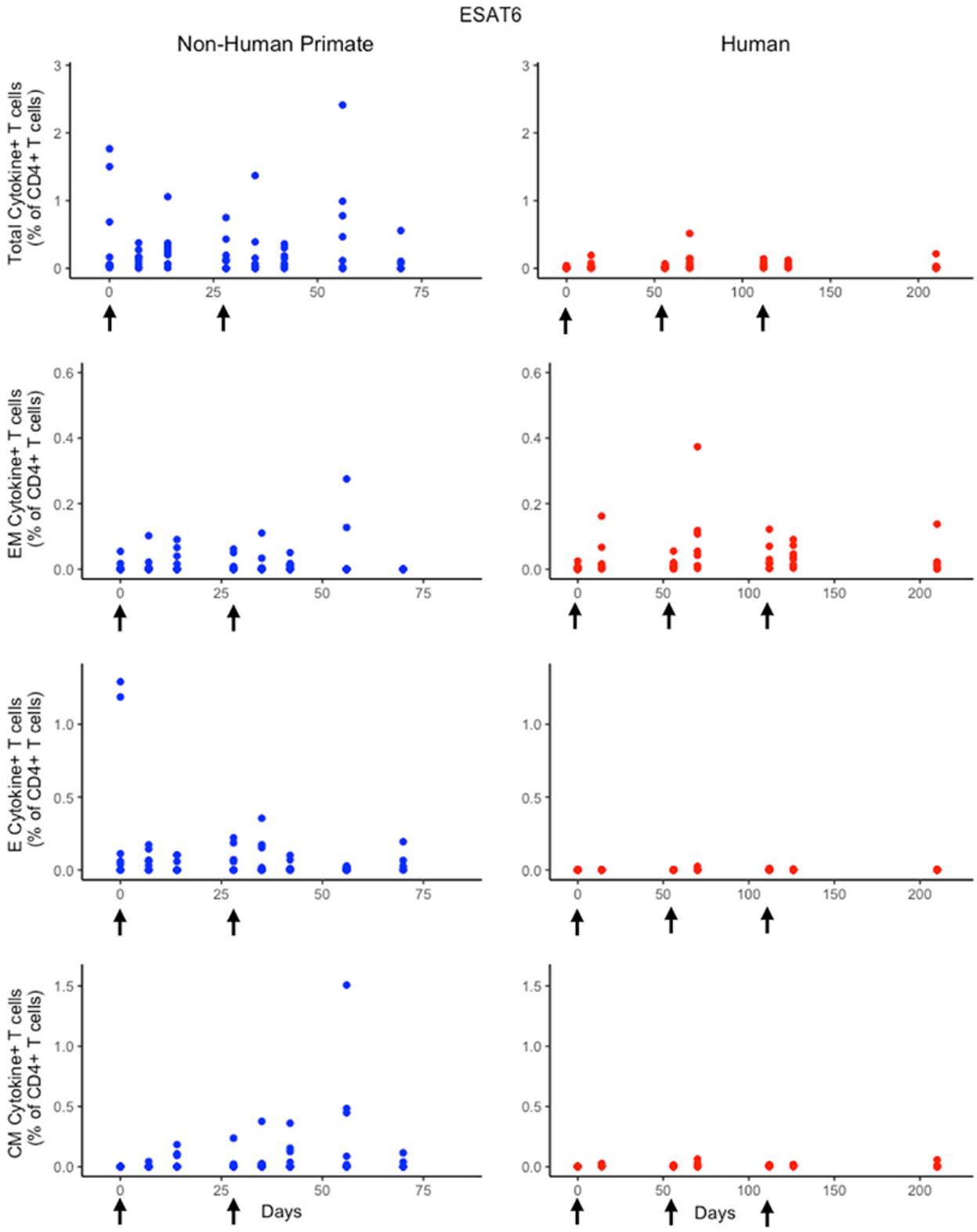

Figure 4.3 Experimental data show different responses to ESAT6 antigen following H56 vaccination

The percentage of blood CD4+ T cells that respond to ESAT6 by producing cytokines (cytokine+) is divided by the total number of CD4+ T cells in the blood. T cell subtypes are also shown. Each time point shows the responses of

all 8 human (red) or all 8 NHPs (blue) subjects. Note that it can be difficult to perceive 8 individual dots–if the subject's responses are similar or the same, as individual dots overlap. For ease of comparison, we have placed both panels of data on the same y-axis. Arrows represent vaccination timepoints.

Furthermore, the magnitude of effector and central memory population responses is larger in NHPs than humans. Between species, the effector memory subpopulation responses are most similar. The major contributors to the total NHP CD4+ ESAT6+ T-cell response are the effector T cell population during early timepoints and the central memory T cell population at later timepoints. The human response is dominated by effector memory T cells. Interestingly, some data suggest that the dose of H56 used in this study may also have contributed to this exaggerated memory T cell response; current thinking will pursue at least a 10-fold lower dose.

4.3.2 A single mathematical model describes both human and NHP T-cell responses to ESAT6

Statistically, we have shown that there is a difference in NHP and human responses to ESAT6. However, statistical analysis could not answer the following questions: 1) Are the data for both humans and NHPs consistent with the same mechanisms for mounting an immune response? 2) If those mechanisms are the same, can the rates of proliferation and differentiation alone be responsible for the differences we observe in ESAT immunogenicity? These questions require a method that can address the dynamics of priming, proliferation, and differentiation that are intrinsic to the development of an immune response. In Methods, we present a mathematical model that describes T cell priming, proliferation, and differentiation in response to APCs in the blood and LN of primates. Here, we hypothesize that this mathematical model can capture both human and NHP T cell responses to ESAT6; however, it will require the use of different sets of parameter values. In Figure 4.4, experimental data from Figure 4.3 were replotted as box and whisker plots (blue – NHP, red – human) and simulation curves are shown by the cloud and median lines (blue and red, respectively).

ESAT6

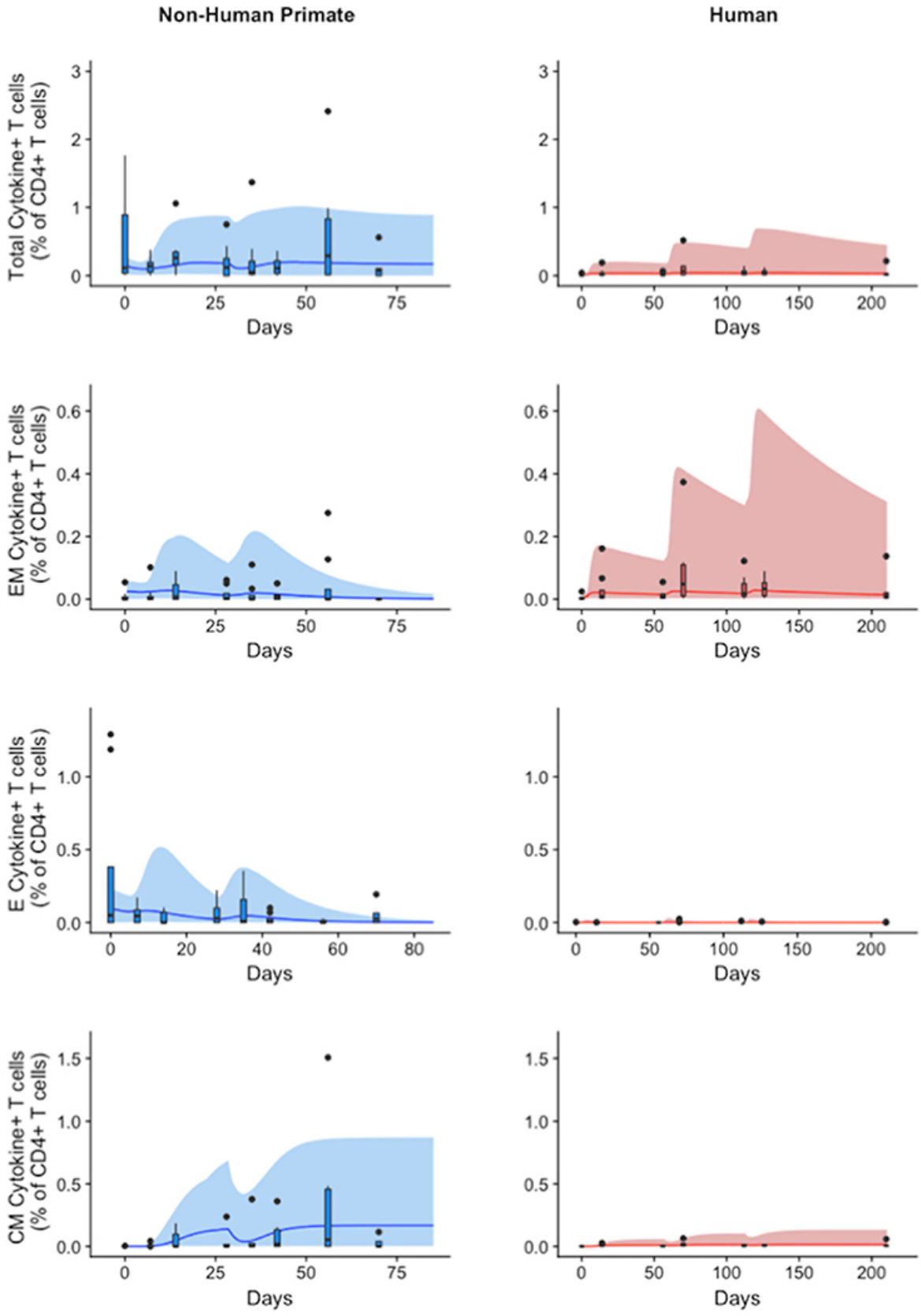
Non-Human Primate
Human
Total Cytokine+ T cells (% of CD4+ T cells)
EM Cytokine+ T cells (% of CD4+ T cells)
E Cytokine+ T cells (% of CD4+ T cells)
CM Cytokine+ T cells (% of CD4+ T cells)
Days

Figure 4.4 Model captures diverse response of both NHP and humans to ESAT6 antigen following H56 vaccination

The percentage of blood CD4+ T cells that respond to ESAT6 by producing cytokines (cytokine+) is divided by the total number of CD4+ T cells in the blood. T cell subtypes are also shown. Each time point shows the responses of all 8 human (red) or all 8 NHPs (blue) subjects using a box and whisker plot. These box and whisker plots provided a guide for the boundaries of immunogenicity dataspace. Whiskers were created by extending from the edge of the box to the data point that is the closest but does not exceed 1.5 times the interquartile range (defined as the distance between the first and third quartiles) from the edge of the box. Any experimental points beyond the edge of the whisker are deemed as outliers and plotted as black points. Simulation data are displayed as a blue or red cloud that outline the min and max of 500 runs for NHP or human calibrations, respectively. The blue or red line represents the median of those simulations. Our goal when calibrating to cell levels in blood of both species was to ensure that in silico simulations fell reasonably within these dataspaces, as outlined in Methods. Parameter ranges used to generate the simulation curves are shown in Appendix C.

NHP simulation data recapitulates the variability in the experimental data by capturing the dynamics of the experimental data. In particular, the median simulation line demonstrates how the model captures the general behavior of the data, by traveling through the interquartile range of at least 4 of the 8 timepoints for each subpopulation of T cells. The human simulations capture the clinical data– our maximum and minimum simulations include nearly all of the outlying data points across the subpopulations of T cells. A visual comparison of these parameter ranges is displayed in Appendix C. Altogether, we demonstrate that our model captures the ESAT6 immunogenicity dataspace of both NHPs and humans – suggesting that the mechanisms of generating a primary immune response are the same for both NHPs and humans.

4.3.3 Sensitivity analysis reveals both similar and distinct outcome drivers across species in response to ESAT6

Having calibrated our model to both ESAT6 human and ESAT6 NHP immunogenicity dataspaces, we next used these two model fits to ask questions about important processes within the CD4+ T cell response. In particular, we wanted to better understand the dual roles of proliferation and differentiation that drive immune response magnitude and timing following vaccination in both species. To investigate these processes, we performed uncertainty and sensitivity analysis on 3 outcomes (ESAT6-specific central memory, effector, and effector memory T cell subtypes) of our model. Table 4.1highlights processes (i.e. parameters) found to be significantly associated with changes in T cell response subpopulations for each species. For both species, uncertainty and sensitivity analysis support a key role for priming and proliferation within lymph nodes. This is not a novel concept, but rather acts as a proper control

for the utility of our model, as it is accepted that priming and proliferation within the lymph node underlies immunogenicity of a vaccine (42). Specifically, uncertainty and sensitivity analysis revealed a crucial role for CD4+ T cell precursor proliferation rates (k4) within the lymph node compartment. The significant, positive association between precursor T cell proliferation rates and 3 different T cell subtypes in the blood represents an inter-compartmental effect – not only does the parameter influence the dynamics within its own compartment (lymph node), it drives the dynamics of the compartment yielding experimentally validated results (blood).

There were also modest differences in the mechanisms driving model fits for NHP and humans, (Table 4.1). For example, only the human dataset showed significant negative correlations between cellular responses in the blood and the half-saturation values of precursor proliferation and differentiation in the lymph node (represented as 'likelihood of proliferation and differentiation' in Table 4.1). We predict that humans and NHPs are generally alike in response to ESAT6, but proliferation and differentiation in humans is not quite as easily triggered as proliferation and differentiation in the NHP. This could be in part due to the influence of humans regularly exposed to many and diverse environmental factors.

Table 4.1 Parameters with significant PRCCs for ESAT6 immune response outcomes.
One row displays humans, the other displays NHPs. Columns list the 3 model outcomes of interest – ESAT6-specific central memory, effector and effector memory T cell phenotypes. These outcomes were selected for analysis because the model was calibrated to their dataspace. Each table cell contains a general description of significant (i.e., $p < 10^{-3}$) parameters with respect to each output of the model.

ESAT6	Central Memory	Effector	Effector Memory
NHP	central memory reactivation rate; precursor proliferation and differentiation into central memory cells; APC and precursor death rates	precursor proliferation and differentiation into effector cells; effector, APC, and precursor death rates	precursor proliferation and differentiation into effector cells; APC and precursor death rates
Human	Likelihood of proliferation; precursor proliferation and differentiation to central memory; central memory recruitment; APC, and precursor death rates;	Likelihood of proliferation and differentiation; Naïve T cell recruitment; Precursor proliferation and differentiation to Effector; effector differentiation to effector Memory; effector Lymph efflux; effector, APC, and precursor death rates;	Likelihood of proliferation and differentiation; precursor proliferation; effector memory, APC, and precursor death rates;

4.3.4 Humans and non-human primates exhibit different T-cell responses to Ag85B following H56 vaccination

While the immunological response between humans and NHPs to the ESAT6 antigen in H56 vaccination can be attributed to intrinsic similarities and differences between species, the response to the Ag85B antigen offers an opportunity to investigate the role of prior BCG vaccination on H56 immunogenicity (Figure 4.5). When we compare magnitude and timing of responses across species, several differences emerge. As observed for responses to ESAT6, the total response of CD4+ Ag85B+ T cells in NHPs is higher and more variable than the response in humans. For example, an F test to compare variances for the central memory T cell population at day 14 revealed a significant difference (p-value = 3.984e-06; variance in NHPs is about 96 times greater than humans). While the magnitude of effector and central memory subpopulation responses were larger in NHPs, it appeared that humans had a larger effector memory subpopulation response.

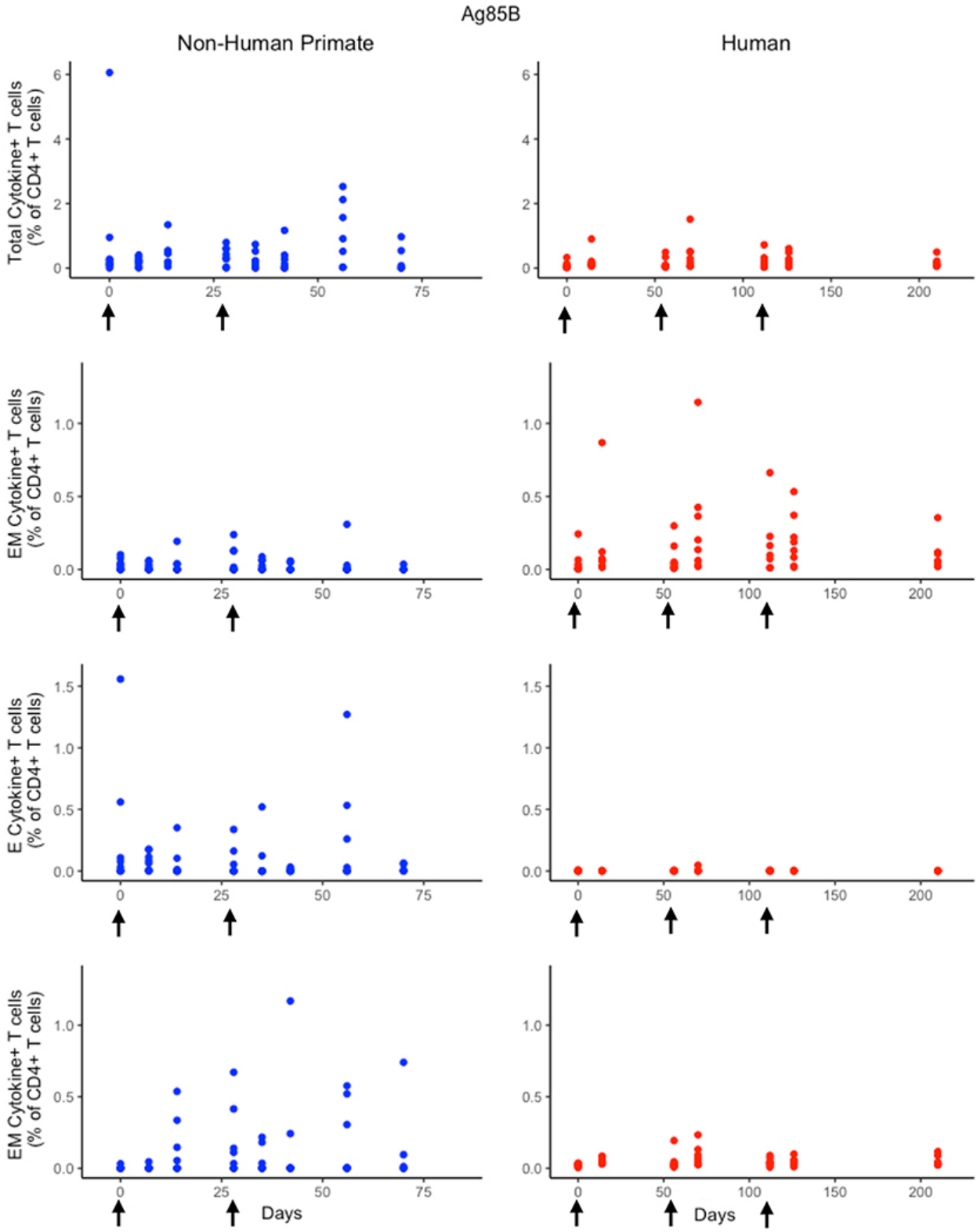

Figure 4.5 Human and NHP experimental data show different responses to Ag85B antigen following H56 vaccination

The percentage of blood CD4+ T cells that respond to Ag85B by producing cytokines (cytokine+) is divided by the total number of CD4+ T cells in the blood. T cell subtypes are also shown. Each time point shows the responses of

all 8 human (red) or all 8 NHPs (blue) subjects (some responses overlap, so it might be difficult to see 8 distinct dots). For comparison, we placed both panels of data on the same y-axis. Arrows represent vaccination timepoints.

4.3.5 A single mathematical model describes NHP and human T-cell responses to Ag85B

Using statistical analysis, we have revealed a difference between species in immune response to Ag85B. However, statistical analysis cannot answer the following questions: 1) what is the impact of different BCG timing on H56 response? 2) is the influence of BCG prime on H56 immune response the same for both species – i.e., do the two species possess a similar secondary response to an antigen? To mechanistically understand the role and timing of BCG prime on H56 vaccination, we require a mathematical modeling approach to predict dynamics of the different T cell responses to Ag85B. As with ESAT6, we tested whether our mathematical model can capture the Ag85B immunogenicity dataspace for both NHPs and humans (Figure 4.6). Our simulation data mimic the variability in the NHP experimental data by tracking most outlier points and whiskers. For example, simulations reflect a contraction of the central memory population and follow expected logic – a percentage of central memory cell populations will reactivate and become precursor T cells in the LN. Thus, the percentage of central memory T cells should contract within blood.

Ag85b

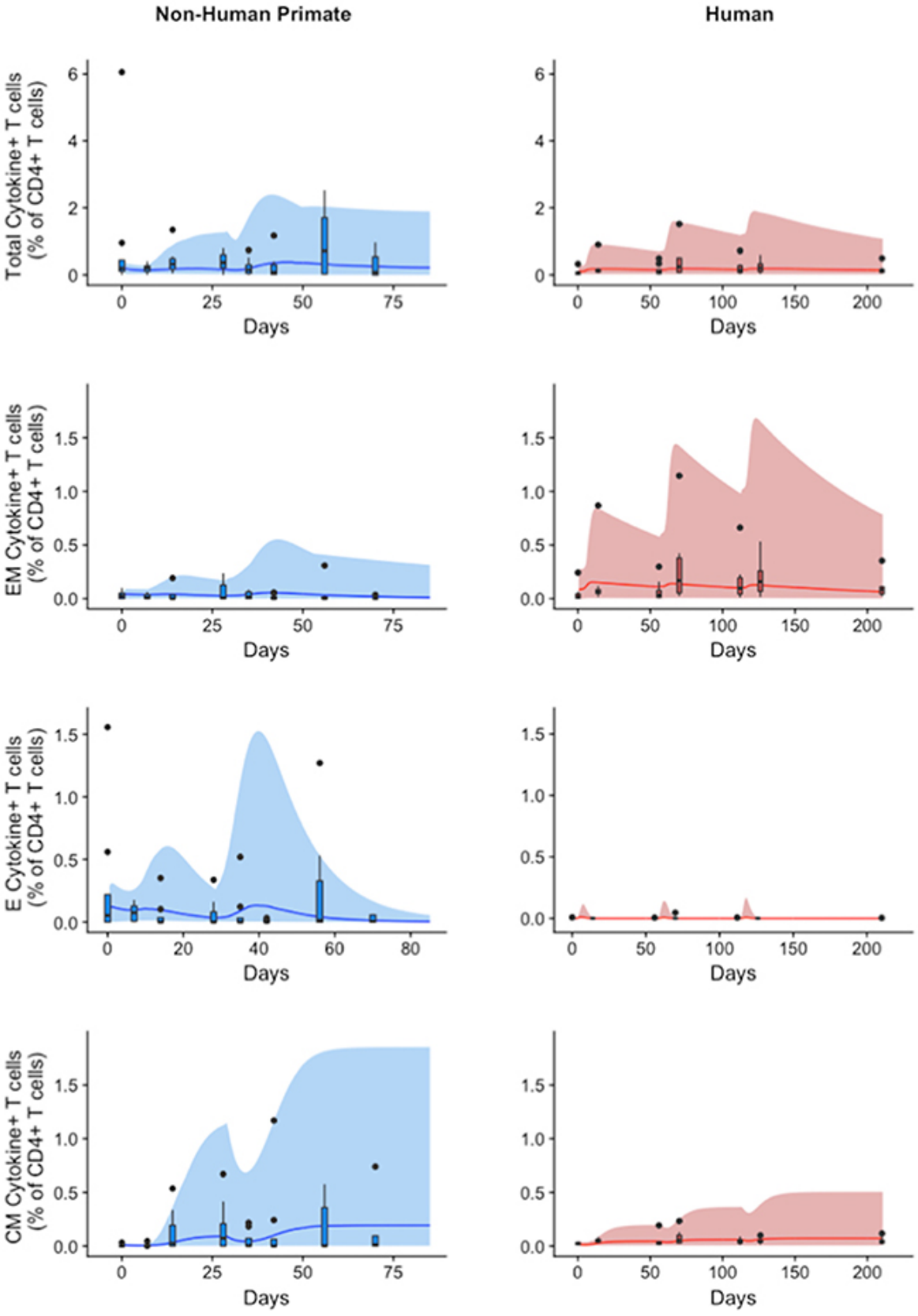
Non-Human Primate
Human
Total Cytokine+ T cells (% of CD4+ T cells)
EM Cytokine+ T cells (% of CD4+ T cells)
E Cytokine+ T cells (% of CD4+ T cells)
CM Cytokine+ T cells (% of CD4+ T cells)
Days

Figure 4.6 Model can fit diverse responses of both NHP and Humans to Ag85B antigen following H56 vaccination

The percentage of blood CD4+ T cells that respond to Ag85B by producing cytokines (cytokine+) is divided by the total number of CD4+ T cells in the blood. T cell subtypes are also shown. Each time point shows the responses of all 8 human (red) or all 8 NHPs (blue) subjects as a box and whisker plot. Whiskers were created in the same manner as the ESAT6 datasets. Simulation data are displayed as a blue or red cloud that outline the min and max of 500 runs for NHP or human calibrations, respectively. The blue or red line represents the median of those simulations and demonstrates that the model captures the general behavior of the data, by traveling through the interquartile range of at least 4 of the 8 timepoints for each subpopulation of T cells. Exact parameters ranges used to generate the simulation curves for NHP and human CD4+Ag85B+ T cells are shown in Table C.1.

The human simulations also capture the variability of the human dataset as well as the general trends, as shown by the median red line. A visual comparison between the parameter ranges is displayed in Figure C.1 and Table C.2 using radar charts. Altogether, we show that our mathematical model can capture the Ag85B immunogenicity dataspace of NHPs and humans with species-specific parameter ranges.

4.3.6 Differences in BCG timing between humans and NHPs is captured by initial conditions

Throughout our calibration process, we were aware of the potential for the timing of BCG priming events to influence the immune response of each species to Ag85B (as NHPs received BCG vaccination 70 days before H56 vaccination and humans received their BCG vaccination roughly 30 years before the clinical trial began -- see Methods and Figure 4.1). Instead of explicitly modeling a BCG vaccination event 70 days or 30 years prior to H56 vaccination, we varied initial concentrations of memory cell types in the LN and blood as a proxy for these BCG vaccinations. The initial cell concentrations represent the value of memory antigen-specific T cells within the system. That is, these T cells, prior to vaccination with H56, were specific for the Ag85B antigen. The initial condition values that led to the best model fits for both NHP and human T cell response are shown in Table 4.2 Initial conditions represent the difference in BCG timing between experimental protocols. Note that the abbreviated time between BCG and H56 vaccinations for NHPs meant that many precursor CD4+ T cells were present in the LN; this population may well have waned in humans who were vaccinated many years (to decades) prior. As a portion of these precursor T cells differentiate into central memory T cells and effector T cells, the BCG vaccination event enabled the model to recapitulate the immunogenicity

dataspaces for these two T cell subpopulations and could also explain the larger NHP response to the vaccine.

Table 4.2 Initial conditions represent the difference in BCG timing between experimental protocols

The disparity between initial condition values that preceded the NHP response and those corresponding values for the human response represent the impact of prior presentation of Ag85B via BCG on the system. ***** signifies that NHP experimental protocol did not give the NHPs a second boost of H56 vaccination

		ESAT6		Ag85b	
		NHP	Human	NHP	Human
Initial Condition of Cell Type	**Units**	**Range of Values**	**Range of Values**	**Range of Values**	**Range of Values**
Naïve CD4+ specific Blood T cells	cell/mm3	[0.1,0.25]	[0.07, 0.6]	[0.17,0.37]	[0.04,0.27]
Effector CD4+ specific Blood T cells	cell/mm3	[0.001,1.5]	0	[0.001,2.5]	0
Central Memory CD4+ specific Blood T cells	cell/mm3	[0.0015,0.006]	[0.00002, 0.03]	[0.002,0.2]	[0.02,0.3]
Effector Memory CD4+ specific Blood T cells	cell/mm3	[0.001,0.5]	[0.003, 0.15]	[0.003, 0.9]	[0.0016,2.6]
Naïve CD4+ nonspecific Blood T cells	cell/mm3	[160,240]	[100,600]	[241,361]	[59,272]
Effector CD4+ nonspecific Blood T cells	cell/mm3	[200,800]	[530,110]	[445, 670]	[358,875]
Central Memory CD4+ nonspecific Blood T cells	cell/mm3	[1,3]	[0.009,10]	[1,100]	[10,100]
Effector Memory CD4+ nonspecific Blood T cells	cell/mm3	[1,150]	[1,22]	[1,300]	[0.3,370]
Naïve CD4+ specific LN T cells	cell count	[91957, 322492]	[8255,111806]	[144500,546200]	[5000,5720]
Precursor CD4+ specific LN T cells	cell count	0	0	[6770, 10150]	0
Effector CD4+ specific LN T cells	cell count	0	0	[22,34]	0
Central Memory CD4+ specific LN T cells	cell count	[1295,7878]	[3.4, 5046]	[2377,285871]	[3132, 59431]
Effector Memory CD4+ specific LN T cells	cell count	0	0	[828,1241]	0
Naïve CD4+ nonspecific LN T cells	cell count	[123430594,355639025]	[11839508, 122029962]	[177300481, 535316901]	[7865162, 53811216]

Central Memory CD4+ nonspecific LN T cells	cell count	[775507,4253381]		[1229, 1895598]	[1219316, 134489106]	[1401106, 19893946]
APC (Prime Vaccination of H56)	cell count	[150,800]		[200,500]	[350,500]	[500,1000]
APC (Boost Vaccination 1 of H56)	cell count	[50, 150]		[200,500]	[250,500]	[400,600]
APC (Boost Vaccination 2 of H56)	cell count	******	******	[200,500]	****** ******	[400,600]

4.3.7 Sensitivity analysis reveals both similar and distinct outcome drivers across species in magnitude of T-cell responses to Ag85B antigen

We performed uncertainty and sensitivity analysis on the same 3 model outcomes as the ESAT6 response analysis to identify important processes in CD4+ T cell response to Ag85B in each species. We identified factors, such as CD4+ central memory cell recruitment, to be significantly associated with changes in T cell response subpopulations (Table 4.3). Uncertainty and sensitivity analysis also revealed a crucial role for CD4+ Precursor proliferation and half-saturation rates within the lymph node compartment (Table 4.3).

Table 4.3 Significant PRCCs for Ag85B immune response outcomes
One row represents humans, the other represents NHPs. Columns list the 3 model outcomes of interest – Ag85B-specific central memory, effector and effector memory T cell phenotypes. These outcomes were selected for analysis because the model was calibrated to their dataspace. Each table cell contains a general description of significant (i.e., $p < 10^{-3}$) parameters with respect to outputs of the model

Ag85B	Central Memory	Effector	Effector Memory
NHP	central memory reactivation rate; Likelihood of differentiation; precursor proliferation and differentiation into central memory cells; APC and precursor death rates	Likelihood of differentiation; precursor proliferation and differentiation into effector cells; effector, APC, and precursor death rates	precursor proliferation and differentiation into effector cells; APC and precursor death rates
Human	Likelihood of proliferation; precursor proliferation and differentiation into central memory; central memory recruitment rate; APC and precursor death rates	Likelihood of proliferation and differentiation; naïve T cell recruitment; precursor proliferation and differentiation to effector; effector differentiation to effector memory; effector Lymph efflux; effector, APC, and precursor death rates	Likelihood of proliferation; precursor Proliferation; effector memory, APC, and precursor death rates

Modest differences also exist in the mechanisms driving model fits for NHP and human (see Table C.1). In addition to the stark differences in initial conditions (from BCG timing), uncertainty and sensitivity analysis predicts that in NHPs, central memory reactivation rates were significantly associated with the total CD4+Ag85B+ response outcome. The importance of reactivation in the central memory population supports not only the role of BCG memory in this system, but could indirectly explain the late increase in Ag85B+ effector cells around day 56 (as the central memory cells that reactivate become precursor cells that, in turn, can become effector cells). Overall, the human and NHP Ag85B responses differ in values of initial conditions, central memory reactivation, and T cell differentiation. Despite these differences, like the ESAT6 response, we predict that the Ag85B response in NHPs and humans are generally alike – this similarity hints at a general secondary response that is conserved across species.

4.3.8 Secondary response to Ag85B antigen is characterized by the upregulation of differentiation to central memory phenotype

If we consider the T cell response of NHP and humans to ESAT6 as the epitome of each species' primary response to an antigen in vaccination, then we can view the parameter values that recapitulate the Ag85B response (a secondary response to the same antigen) as a BCG-induced modification to the parameter values that captured the ESAT6 response. For NHPs (blue) and humans (red), three parameters (k5, k6, k7) are represented on each axis of the radar charts for ESAT6 and Ag85B (Figure 4.7). Notice that, for each species, the radar charts include the maximum value for each parameter across the ESAT6 and Ag85B response fits. In the ESAT6 radar charts, both NHPs and humans skew toward the differentiation of effector and effector memory T cell phenotypes. As neither species has encountered ESAT6 prior to H56 vaccination, the relatively high rates of differentiation to effector and effector memory T cell phenotypes constitute a primary response that may be conserved across species.

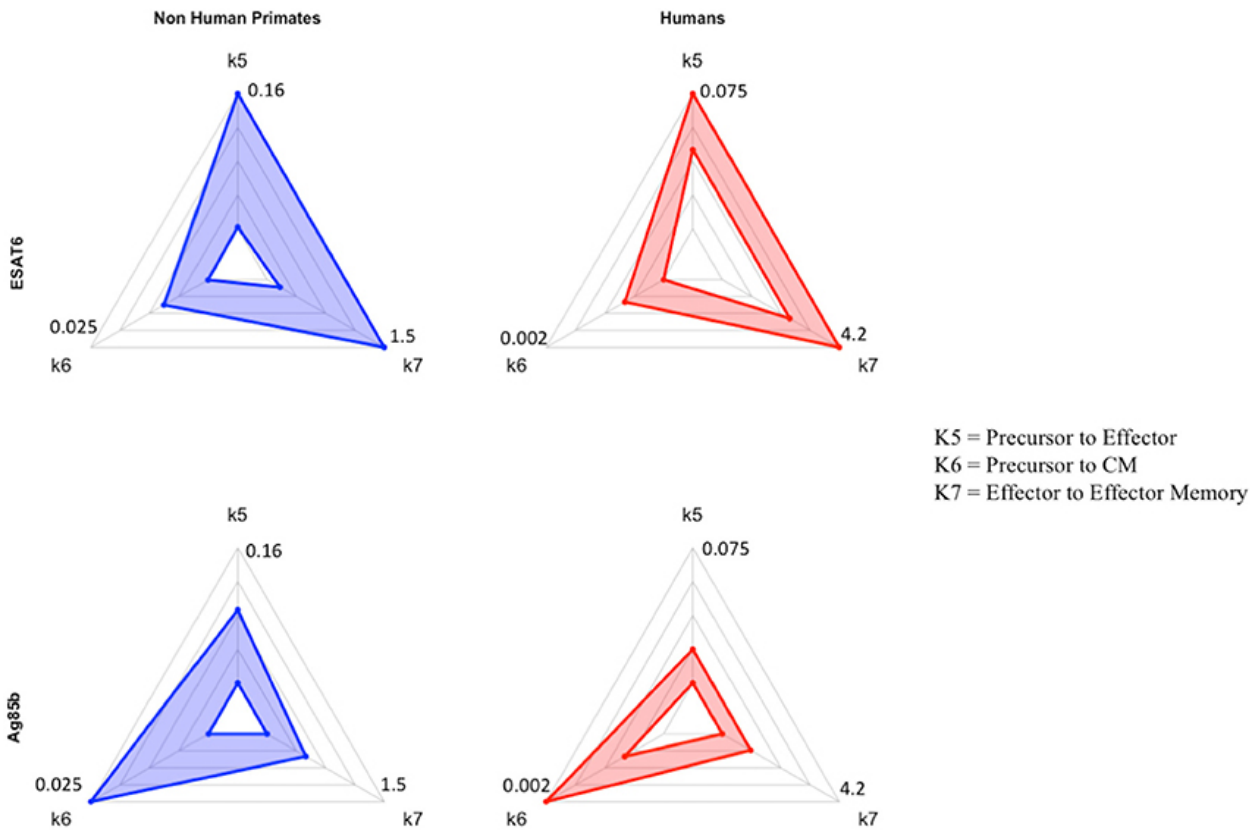

Figure 4.7 Radar charts reveal impact of immunological memory in response to Ag85B
We display 4 radar charts (see Appendix C and Methods) that visually represent the parameter space for several key parameters (as identified by PRCC) in model fits for both species and antigens. Each chart includes the maximum value of each parameter (for each species) on the diagrams. The top chart shows the parameter ranges that fit the ESAT6 immunogenicity dataspace. The bottom radar chart displays the parameter ranges that fit the Ag85B immunogenicity dataspace. These parameters were picked as they represent T-cell differentiation rates to central memory (k6), effector (k5), and effector memory (k7) T cell phenotypes. Each parameter space is represented by a blue (NHP) or red (human) band, which represents the min and max parameter value for each model fit. Table C.1 shows the numerical values of the parameter ranges. To directly compare the impact of BCG memory on the H56 immune response, we created the Human radar charts with a minimum and maximum for each axis defined by the minimum and maximum parameter value across Human model fits to ESAT6 or Ag85B. We created the NHP radar charts by displaying the parameter ranges within the min and maximum values across NHP model fits to either antigen. Viewers should not compare the charts from left to right, as the human charts display a parameter range that is wholly distinct from that of the non-human primates. For each species, the maximum values for each parameter are displayed at the edges of the radar charts.

Ag85B is an antigen that was first presented in BCG vaccination; if we compare the dynamics of ESAT6 responses to the dynamics of Ag85B responses, we can predict the BCG-induced modifications to T-cell differentiation during secondary responses to the same antigen. In the Ag85B radar charts, both species' ranges for differentiation to effector and effector memory become relatively smaller than the ranges that fit the ESAT6 response. Further, the ranges for the parameter that captures differentiation to a central memory phenotype grow larger relative to

the ranges shown in ESAT6 response. We speculate that this change in response is conserved across species – upon secondary response to the same antigen, both species' precursor T-cell populations upregulate the production of a central memory phenotype during differentiation.

4.4 Discussion

In the pursuit of a vaccine that can confer long-term, consistent immunity against TB, H56 is one new vaccine candidate. However, the role of prior BCG vaccination on H56 immunogenicity is unclear. In addition, the differences between NHP – a useful model animal for vaccine studies - and human responses to H56 has not been explicitly characterized. Identifying the influence of BCG on H56 vaccination and characterizing the species-specific responses to H56 will better facilitate our understanding of H56 immunogenicity and could potentially pave the way for more effective therapies. In addition, we strive to elaborate how computational modeling can assist with vaccine development and testing.

In this work, we used a systems biology approach that utilized mathematical modeling to explore both NHP and human response datasets to H56. We calibrated our two-compartment mathematical model to the ESAT6 and Ag85B immunogenicity dataspaces for both NHPs and humans. This calibration allowed us to study pre-exposure vaccination dynamics such as antigen presentation, T cell priming, and differentiation in both the lymph node and blood. Specifically, we utilized antigen specificity to draw our main conclusion: BCG similarly influences H56 immunogenicity in both NHPs and humans by upregulating differentiation to the central memory phenotype in the Ag85B-specific CD4+ T cell response. While Lin et al. found that H56 boosts the effects of BCG and prevents reactivation of latent infection (23), to our knowledge no one has documented the direct impact of prior BCG on H56 immunogenicity.

Using mathematical modeling, we were also able to isolate the impact of BCG timing differences on H56 immunogenicity. We discovered that the narrow window between BCG prime and H56 vaccination in NHPs promotes a larger quantity of antigen-specific cells that reside in the lymph node prior to H56 vaccination. Calibration to the Ag85B immunogenicity dataspace for NHPs revealed a much larger initial number of precursor T cells in the lymph node than the number of

initial precursor cells that were required for calibration to the human data. The difference in timing of BCG for the NHP experimental protocol (70 days prior to H56 vaccination) and human experimental protocol (up to decades before H56) explains the necessary differences required in model initial conditions to capture these events. Experimental assessment of vaccines in NHPs preclude the administration of BCG years prior to boosting with a subunit vaccine, due to costs. However, our data indicate that the timing of BCG and booster vaccines strongly influence the subsequent immune responses. Whether this also affects protection conferred by a vaccine remains to be tested.

Using uncertainty and sensitivity analysis, we found that each species' response to H56 vaccination was generally similar. While each species resides in a separate parameter space, the general dynamics dictating the H56 immune response was quite similar. This finding contrasts with previous findings that show the immune response of monkeys and humans to SIV or HIV (respectively) differs (43,44), however, like many others in the field of TB research, we conclude that NHPs are a good model for human responses (45–48). However, one consistent difference between NHP and human response were observed. Unlike the NHP response, the humans' central memory, effector, and effector memory T cell phenotypes was significantly negatively correlated with the half-saturation values of proliferation and differentiation in both the ESAT6 and Ag85B immunogenicity dataspaces. As the half-saturation values in our model measure the affinity (or likelihood) of a cell to proliferate or differentiate upon priming, our findings suggest that humans differ from NHPs in the ability of T cells to quickly react to H56 vaccination antigens within lymph nodes. Perhaps presentation of these antigens to T cells is not as effective in humans as it is in NHPs. We indirectly modeled adjuvant impact on vaccination (see Methods); however, a more mechanistic approach may be necessary to elucidate these species-specific differences in antigen uptake and presentation.

Furthermore, uncertainty and sensitivity analysis revealed an intriguing result regarding the human experimental protocol. Throughout our analysis, the number of APCs that entered the system via vaccinations (prime or boost events) was significantly, positively, associated with cellular responses in the blood. However, our analysis also showed that the number of APCs that entered the system as a result of the second boosting event (third H56 vaccination event) for

humans did not significantly impact the number of central memory T cells within the blood compartment. This result agrees with the previous finding that 50 ug of H56 is too high of a dose (30), resulting in large effector responses that may be suboptimal for long-term memory. As one major goal of any vaccination is to provide long lasting immunity in the form of immunological memory, our computational analysis has revealed that the third dose was likely redundant and that optimization of dose using computational predictions could have potentially improved outcomes, especially prior to the clinical trial. In the future our systems biology approach together with virtual clinical trials could help investigate these issues and assist in improving the vaccine pipeline.

One potential limitation of this study is that our current model represents the complex processes of proliferation, differentiation, and reactivation rates as a single parameter with a range of values. We believe this suffices since our goal was to identify the role of BCG in H56 vaccination response across humans and NHPs. However, future investigations into the processes dictating proliferation, differentiation, or reactivation could create a more detailed mathematical model including those details. In fact, the field of T-cell memory and the exact mechanisms of reactivation have been extensively studied (49–52). Conversely, phenomenological modeling has provided insights for T cell expansion (44,53,54). Future work could discuss the benefits of mechanistic or phenomenological models when addressing distinct questions about proliferation, differentiation, or reactivation.

In summary, we used a systems biology approach that combined NHP and human datasets with mathematical modeling to better understand the differences between NHP and human immune response to H56 vaccination. Specifically, we showed that each primate species had a similar response to H56, identified the role of BCG timing on H56 vaccination, and discovered that BCG similarly influences H56 immunogenicity in humans and NHPs.

Beyond the scope of this paper, we could have characterized other comparisons between humans and NHPs. For example, future studies could identify the species-specific differences during TB infection, identify the adaptive immune response differences to other antigens, or capture the dissimilarities of each species' innate immune response to adjuvant. Further, future studies

could also model the cellular dynamics following H56 vaccination before, during, or after TB infection in an effort to evaluate the potential success of this vaccine candidate. We argue that a systems biology approach that melds mathematical modeling together with experimental and clinical studies has the greatest potential to discover, predict, and evaluate new vaccination strategies that could end the TB epidemic.

4.5 References

1. WHO. WHO Global tuberculosis report 2016 [Internet]. World Health Organization Press. 2016. Available from: http://www.who.int/tb/publications/global_report/en/
2. Fine PEM. Variation in protection by BCG: implications of and for heterologous immunity. The Lancet. 1995;346(8986):1339–45.
3. Sterne JAC, Rodrigues LC, Guedes IN. Does the efficacy of BCG decline with time since vaccination? International Journal of Tuberculosis and Lung Disease. 1998;2(3):200–7.
4. Lanckriet C, Lévy-bruhl D, Bingono E, Siopathis RM, Guérin N. Efficacy of BCG vaccination of the newborn: Evaluation by a follow-up study of contacts in Bangui. International Journal of Epidemiology. 1995;24(5):1042–9.
5. S.K. M, V. A, A. R, N. S. Does B.C.G. vaccination prevent or postpone the occurrence of tuberculous meningitis? Vol. 63, Indian Journal of Pediatrics. 1996. p. 659–64.
6. Colditz GA, Berkey CS, Mosteller F, Brewer TF, Wilson ME, Burdick E, et al. The efficacy of bacillus Calmette-Guérin vaccination of newborns and infants in the prevention of tuberculosis: meta-analyses of the published literature. Pediatrics. 1995;96(1 Pt 1):29–35.
7. Zodpey SP, Shrikhande SN, Maldhure BR, Vasudeo ND, Kulkarni SW. Effectiveness of Bacillus Calmette Guerin (BCG) vaccination in the prevention of childhood pulmonary tuberculosis : A case control study in Nagpur, India. Southeast Asian Journal of Tropical Medicine and Public Health. 1998;29(2):285–8.
8. Andersen P, Doherty TM. Opinion: The success and failure of BCG — implications for a novel tuberculosis vaccine. Nature Reviews Microbiology. 2005;3(8):656–62.
9. Fourie PB. BCG vaccination and the EPI. South African Medical Journal. 1987;72(5):323–6.
10. Tameris MD, Hatherill M, Landry BS, Scriba TJ, Snowden MA, Lockhart S, et al. Safety and efficacy of MVA85A, a new tuberculosis vaccine, in infants previously vaccinated with BCG: A randomised, placebo-controlled phase 2b trial. The Lancet. 2013;381(9871):1021–8.
11. Evans TG, Schrager L, Thole J. Status of vaccine research and development of vaccines for tuberculosis. Vaccine. 2016;34(26):2911–4.
12. Gonzalo-Asensio J, Dessislava M, Carlos M, Aguilo N. MTBVAC: Attenuating the Human Pathogen of Tuberculosis (TB) Toward a Promising Vaccine against the TB Epidemic. Frontiers in Immunology. 2017;8:1803.
13. Ahsan MJ. Recent advances in the development of vaccines for tuberculosis. Therapeutic Advances in Vaccines. 2015;3(3):66–75.
14. Cole ST, Brosch R, Parkhill J, Garnier T, Churcher C, Harris D, et al. Deciphering the biology of *Mycobacterium tuberculosis* from the complete genome sequence. Nature. 1998;393(6685):537–44.
15. Aagaard C, Hoang T, Dietrich J, Cardona P-J, Izzo A, Dolganov G, et al. A multistage tuberculosis vaccine that confers efficient protection before and after exposure. Nature Medicine. 2011;17(2):189–94.
16. Langermans JAM, Doherty TM, Vervenne RAW, Van Der Laan T, Lyashchenko K, Greenwald R, et al. Protection of macaques against *Mycobacterium tuberculosis* infection by a subunit vaccine based on a fusion protein of antigen 85B and ESAT-6. Vaccine. 2005;23(21):2740–50.

17. Olsen AW, Van Pinxteren LAH, Okkels LM, Rasmussen PB, Andersen P. Protection of mice with a tuberculosis subunit vaccine based on a fusion protein of antigen 85B and ESAT-6. Infection and Immunity. 2001;69(5):2773–8.
18. Olsen AW, Williams A, Okkels LM, Hatch G, Andersen P. Protective effect of a tuberculosis subunit vaccine based on a fusion of antigen 85B and ESAT-6 in the aerosol guinea pig model. Infection and Immunity. 2004;72(10):6148–50.
19. Brandt L, Elhay M, Rosenkrands I, Lindblad EB, Andersen P. ESAT-6 subunit vaccination against *Mycobacterium tuberculosis*. Infection and Immunity. 2000;68(2):791–5.
20. Horwitz MA, Lee BW, Dillon BJ, Harth G. Protective immunity against tuberculosis induced by vaccination with major extracellular proteins of *Mycobacterium tuberculosis*. Proceedings of the National Academy of Sciences of the United States of America. 1995;92(5):1530–4.
21. Mustafa AS, Shaban FA, Abal AT, Al-Attiyah R, Wiker HG, Lundin KEA, et al. Identification and HLA restriction of naturally derived Th1-cell epitopes from the secreted *Mycobacterium tuberculosis* antigen 85B recognized by antigen-specific human CD4+ T-cell lines. Infection and Immunity. 2000;68(7):3933–40.
22. Mustafa a S, Oftung F, Amoudy H a, Madi NM, Abal a T, Shaban F, et al. Multiple epitopes from the *Mycobacterium tuberculosis* ESAT-6 antigen are recognized by antigen-specific human T cell lines. Clinical infectious diseases : an official publication of the Infectious Diseases Society of America. 2000;30 Suppl 3:S201-5.
23. Lin PL, Dietrich J, Tan E, Abalos RM, Burgos J, Bigbee C, et al. The multistage vaccine H56 boosts the effects of BCG to protect cynomolgus macaques against active tuberculosis and reactivation of latent *Mycobacterium tuberculosis* infection. Journal of Clinical Investigation. 2012;122(1):303–14.
24. Govender L, Abel B, Hughes EJ, Scriba TJ, Kagina BMN, de Kock M, et al. Higher human CD4 T cell response to novel *Mycobacterium tuberculosis* latency associated antigens Rv2660 and Rv2659 in latent infection compared with tuberculosis disease. Vaccine. 2010;29(1):51–7.
25. Betts JC, Lukey PT, Robb LC, McAdam RA, Duncan K. Evaluation of a nutrient starvation model of *Mycobacterium tuberculosis* persistence by gene and protein expression profiling. Molecular Microbiology. 2002;43(3):717–31.
26. Rohde KH, Veiga DFT, Caldwell S, Balázsi G, Russell DG. Linking the transcriptional profiles and the physiological states of *Mycobacterium tuberculosis* during an extended intracellular infection. PLoS Pathogens. 2012;8(6).
27. Wilkinson RJ, DesJardin LE, Islam N, Gibson BM, Andrew Kanost R, Wilkinson KA, et al. An increase in expression of a *Mycobacterium tuberculosis* mycolyl transferase gene (fbpB) occurs early after infection of human monocytes. Molecular Microbiology. 2001;39(3):813–21.
28. Ronning DR, Klabunde T, Besra GS, Vissa VD, Belisle JT, Sacchettini JC. Crystal structure of the secreted form of antigen 85C reveals potential targets for mycobacterial drugs and vaccines. Nature structural biology. 2000;7(2):141–6.
29. Ganguly N, Giang PH, Gupta C, Basu SK, Siddiqui I, Salunke DM, et al. *Mycobacterium tuberculosis* secretory proteins CFP-10, ESAT-6 and the CFP10:ESAT6 complex inhibit lipopolysaccharide-induced NF-kappaB transactivation by downregulation of reactive oxidative species (ROS) production. Immunology and cell biology. 2008;86(1):98–106.

30. Luabeya AKK, Kagina BMN, Tameris MD, Geldenhuys H, Hoff ST, Shi Z, et al. First-in-human trial of the post-exposure tuberculosis vaccine H56: IC31 in *Mycobacterium tuberculosis* infected and non-infected healthy adults. Vaccine. 2015;33(33):4130–40.
31. Agger EM. Novel adjuvant formulations for delivery of anti-tuberculosis vaccine candidates. Vol. 102, Advanced Drug Delivery Reviews. 2016. p. 73–82.
32. Marino S, Kirschner D. A Multi-Compartment Hybrid Computational Model Predicts Key Roles for Dendritic Cells in Tuberculosis Infection. Computation. 2016;4(4):39.
33. Marino S, Gideon HP, Gong C, Mankad S, McCrone JT, Lin PL, et al. Computational and Empirical Studies Predict *Mycobacterium tuberculosis*-Specific T Cells as a Biomarker for Infection Outcome. PLoS Computational Biology. 2016;12(4).
34. Gong C, Linderman JJ, Kirschner D. Harnessing the heterogeneity of T cell differentiation fate to fine-tune generation of effector and memory T cells. Frontiers in Immunology. 2014;5(FEB).
35. Ziraldo C, Gong C, Kirschner DE, Linderman JJ. Strategic priming with multiple antigens can yield memory cell phenotypes optimized for infection with *Mycobacterium tuberculosis*: A computational study. Frontiers in Microbiology. 2016;6(JAN).
36. Kamath AT, Valenti MP, Rochat AF, Agger EM, Lingnau K, von Gabain A, et al. Protective anti-mycobacterial T cell responses through exquisite *in vivo* activation of vaccine-targeted dendritic cells. European Journal of Immunology. 2008;38(5):1247–56.
37. Wickham H. ggplot2: Elegant Graphics for Data Analysis. Springer-Verlag New York; 2009.
38. Wickham H. The Split-Apply-Combine Strategy for Data Analysis. Journal of Statistical Software. 2011;40(1):1–29.
39. Wickham H, Henry L. tidyr: Easily Tidy Data with “spread()” and “gather()” Functions. R package; 2017.
40. Marino S, Hogue IB, Ray CJ, Kirschner DE. A methodology for performing global uncertainty and sensitivity analysis in systems biology. Vol. 254, Journal of Theoretical Biology. 2008. p. 178–96.
41. Nakazawa M. fmsb: Functions for Medical Statistics Book with some Demographic Data. R package; 2017.
42. Moliva JI, Turner J, Torrelles JB. Immune responses to bacillus Calmette-Guérin vaccination: Why do they fail to protect against *Mycobacterium tuberculosis*? Vol. 8, Frontiers in Immunology. 2017.
43. Yang Y, Ganusov V V. Defining kinetic properties of HIV-specific CD8⁺ T-cell responses in acute infection. bioRxiv. 2017 Jan 1;
44. Davenport MP, Ribeiro RM, Perelson AS. Kinetics of virus-specific CD8+ T cells and the control of human immunodeficiency virus infection. Journal of virology. 2004;78(18):10096–103.
45. Kaushal D, Mehra S, Didier PJ, Lackner AA. The non-human primate model of tuberculosis. Vol. 41, Journal of Medical Primatology. 2012. p. 191–201.
46. Flynn JL, Gideon HP, Mattila JT, Lin P ling. Immunology studies in non-human primate models of tuberculosis. Immunological Reviews. 2015;264(1):60–73.
47. Scanga CA, Flynn JL. Modeling tuberculosis in nonhuman primates. Cold Spring Harbor Perspectives in Medicine. 2014;4(12).
48. Pena JC, Ho WZ. Monkey models of tuberculosis: Lessons learned. Vol. 83, Infection and Immunity. 2015. p. 852–62.

49. Youngblood B, Hale JS, Kissick HT, Ahn E, Xu X, Wieland A, et al. Effector CD8 T cells dedifferentiate into long-lived memory cells. Nature. 2017 Dec 13;552:404.
50. Akondy RS, Fitch M, Edupuganti S, Yang S, Kissick HT, Li KW, et al. Origin and differentiation of human memory CD8 T cells after vaccination. Nature. 2017 Dec 13;552:362.
51. MacLeod MKL, Kappler JW, Marrack P. Memory CD4 T cells: generation, reactivation and re-assignment. Immunology. 2010 May 11;130(1):10–5.
52. Harrington LE, Janowski KM, Oliver JR, Zajac AJ, Weaver CT. Memory CD4 T cells emerge from effector T-cell progenitors. Nature. 2008 Mar 5;452:356.
53. Akondy RS, Johnson PLF, Nakaya HI, Edupuganti S, Mulligan MJ, Lawson B, et al. Initial viral load determines the magnitude of the human CD8 T cell response to yellow fever vaccination. Proceedings of the National Academy of Sciences of the United States of America. 2015;112(10):3050–5.
54. Antia R, Ganusov V V., Ahmed R. The role of models in understanding CD8+ T-cell memory. Nature Reviews Immunology. 2005;5(2):101–11.

5 A Host-Scale Model Distinguishes Infection Outcomes in Tuberculosis

5.1 Introduction

Even during the COVID-19 pandemic, tuberculosis (TB) continues to be a global threat. Approximately 25% of the world is infected with *Mycobacterium tuberculosis* (Mtb) and 5-10% of those currently infected will progress to develop symptomatic clinical disease (1). TB patients are often classified as having latent tuberculosis (LTBI) or active TB. LTBI is an asymptomatic state of infection with typically low levels of Mtb present. Active TB cases exhibit clinical symptoms including fever, weight loss, night sweats, and coughing typically with high levels of Mtb present. While patients are categorized within these binary states, recent work has shown that TB manifests as a spectrum of clinical and infection outcomes within humans and non-human primates (NHPs) (2–5). Latently-infected individuals can undergo reactivation events and therefore act as a potential reservoir for disease transmission (6,7). Much remains unknown about the biology that drives clinical outcomes in TB (i.e., latent or active) for each individual patient. It is critical to understand events that lead to latent or active TB in order to develop effective vaccines and host-directed therapies.

The hallmark of TB is the formation of lung granulomas, which are organized immune structures that surround Mtb and Mtb-infected cells within lungs of infected hosts (8). NHP data have shown that a single mycobacterium is sufficient to begin the formation of a granuloma and that each granuloma has a unique trajectory (9,10). Granulomas are composed of bacteria and various immune cells, such as macrophages and T cells (primarily CD4+ and CD8+ T cells, although other unconventional T cell phenotypes are also present, reviewed in (11)). Other cells such as neutrophils, fibroblasts and dendritic cells are also present. T cells have well-known critical functions against Mtb (12–14), but unlike other infections, T cells are slow to enter the site of infection within lungs, arriving approximately one month after primary infection (15). Lung-draining lymph nodes (LN) serve as the sites for initiating and generating an adaptive immune response against most pulmonary infections, including Mtb. However, delays in LN T-cell priming, activation, and trafficking through blood to lungs is characteristic of the adaptive

immune response in Mtb (16,17) and is thought to be key in allowing Mtb to establish infection within lungs (15). The delay is thought to arise from slowly growing mycobacteria in the lungs, delaying the signals for adaptive immunity (18).

While studies at the granuloma scale have elucidated important features about how individual granulomas control infection, it is difficult to experimentally identify specific immune mechanisms within lung granulomas and LNs that drive clinical outcomes of TB at a whole-host scale. Specific factors such as CD4+ T cells, CD8+ T cells and TNFα are important in controlling established Mtb infection (12,19,20). NHP studies have also shown active TB individuals harbor significantly more bacteria than LTBI individuals (21) but these studies have been unable to relate individual granuloma outcomes to whole-host clinical outcomes, in part because the fate of individual granulomas vary within a single host (9).

Data from sites of infection (lung granulomas) in humans are generally unavailable. Consequently, it is not known whether numbers of immune cells in the blood reflect ongoing events during infection within human lungs (22). This has limited the ability to use blood as a predictive measure for infection progression or diagnosis. However, recent association studies suggest ratios of antigen-specific CD4+ and CD8+ T cells within the blood of Mtb-infected hosts may help delineate LTBI from active TB (23,24). Conversely, NHP studies have shown that T-cell responses in the blood do not consistently reflect T-cell responses in granulomas (25,26).

Mathematical and computational modeling offer complementary approaches to experimental studies. Models have the power to simultaneously track multiple immune cell populations across multiple compartments, explore mechanisms of action related to immunological phenomenon, and predict timing of major immune events. In TB (27), modeling has been used to explore bacterial behavior in relation to the granuloma environment (28), drug-dynamics within granulomas (29,30) and immune cell interactions and cytokines within a lung model (31–33). Additionally, pseudo whole-host models have been developed to begin to investigate biomarkers in TB (26) and drug dynamics across a host (34). Mathematical and computational modeling is a unique tool that could serve to bridge events occurring within a host to whole-host level TB outcomes (i.e. LTBI vs active TB).

Here we develop a novel whole-host scale modeling framework that captures key elements of the immune response to Mtb within three physiological compartments - LNs, blood and lungs of infected individuals. Beginning with our whole lung framework originally called MultiGran, each granuloma is formulated as an individual 'agent' in an agent-based model that contains a sub-model tracking immune cells, cytokines, and bacterial populations for each granuloma (previously presented in Chapter 3 and (35)). We extend this framework to capture dynamics of a whole host by linking it with a two-compartment model representing immune cell dynamics occurring within LNs and blood (previously presented in Chapter 4 and (36,37)). Together, this new model platform, called *HostSim*, represents a whole-host framework for tracking Mtb infection dynamics within a single host across long time scales (days to months to years). We calibrate and validate the model using multiple datasets from published NHP studies. We use *HostSim* to answer two outstanding questions surrounding whole-host outcomes in TB: 1) what are the mechanisms within a host that drive clinical outcomes in TB at the whole-host scale? 2) is there a relationship between counts of blood immune cells and clinical outcomes at the whole-host scale? We use *HostSim* to relate immune responses in blood to the sites of infection within lungs and utilize sensitivity analysis to predict factors that lead to clinical outcomes of TB.

5.2 Methods

5.2.1 *HostSim* model overview

Our novel multi-scale whole-host scale model, *HostSim*, tracks Mtb infection across three separate physiological compartments (Figure 5.1). We describe the formation, function and dissemination of multiple granulomas that represent distinct sites of infection developing within a whole-lung model. We additionally describe the initiation of adaptive immunity within a LN compartment after receiving signals from antigen presenting cells migrating from lungs. Finally, we track immune cell counts within a blood compartment that acts as a bridge between LN to lungs. *HostSim* uses rule-based agent placement, parameter randomization, solves non-linear systems of ODEs, performs post-processing agent groupings, and utilizes rule-based linking between scales to perform *in silico* simulations of a single host.

Our model is called *HostSim* as we consider a simulation of an entire primate host during Mtb infection; however, our *in silico* "hosts" are comprised solely of lungs, LN and blood. These

three physiological compartments comprise the majority of dynamics that occur during pulmonary TB (38,39). Other organs and body system are also involved during extrapulmonary TB, including liver, brain, and other extrapulmonary sites. We believe that focusing this study on pulmonary TB is without loss of generality, and that adding in those other body sites would serve to fine tune our predictions to other clinical outcomes of TB.

Each virtual host includes multiple granulomas with separate parameter values, and a single parameter set for the LN and blood. The assumption that granulomas within the same host have separate parameter values is supported broadly by both modeling and experimental studies that have shown each granuloma within a host evolves independently (9,10,25,26,29,35,40,41).

5.2.2 Modeling multiple lung granulomas across time – *MultiGran*

In a recent study, we built a novel hybrid agent-based model that describes the development of multiple lung granulomas known as *MultiGran* (35). In this model, each granuloma acts as an agent, placed stochastically within the boundary of a 3-dimensional lung environment (Figure 5.1A). To create this 'virtual lung' we used a CT scan from an uninfected NHP (35) as the three-dimensional lung architecture upon which multiple granulomas develop across time (translating the x,y,z coordinates from a CT scan to our computer model). Our previous study provides further detail about lung architecture (35). Simulations begin with inoculation of multiple bacteria into the lung environment. A granuloma is initialized when each Mtb is placed within the lung environment, as NHP studies have shown that each Mtb bacterium can form a unique granuloma (9,10).

Briefly, the development of each individual granuloma "agent" is captured by a system of ODEs that tracks bacterial, macrophage, T cell, and cytokine dynamics. To describe the role of the innate immune response within a granuloma, we track resting, infected and activated macrophages as well intracellular and extracellular bacterial populations. To capture the impact of the adaptive immune system, we track primed CD4+ and CD8+ T cell populations. Primed CD4+ T cells can differentiate into effector Th1 or Th2 populations and primed CD8+ T cell populations can differentiate into cytotoxic or cytokine producing CD8+ T cell populations. Recruitment of T cells from the blood compartment to granulomas is described in greater detail below. We additionally track concentrations of pro- and anti- inflammatory cytokines within

each granuloma, including IFN-γ, TNF-α, IL-10, IL-4 and IL-12. *MultiGran* originally only included the primed and differentiated T cell populations described above; but we now include effector memory T cells to be consistent with experiments that have shown effector memory T cells are present within the granuloma environment (42–44). Thus, we expanded the set of ODEs representing each single granuloma in *MultiGran* (35) to include CD4+ and CD8+ effector memory T cell subpopulations. Briefly, we assume effector memory cells are recruited from the blood to granulomas according to the inflammatory profiles of granulomas (see Linking models section below for further detail). Once at the site of the granuloma, effector memory cells differentiate into T cells that exhibit effector functions (44–46).

Granulomas within *MultiGran* can sterilize bacteria, control bacterial growth over time, or exhibit uncontrolled bacterial growth. Granulomas can also disseminate, spreading bacteria locally or non-locally (Figure 5.1A). Local dissemination events initialize a new granuloma near the disseminating granuloma whereas non-local dissemination initializes a new granuloma randomly within the lung environment. Model equations and details are in the Appendix D and includes the list of all parameters, definitions, and ranges.

5.2.3 Lymph node and blood models

In previous work, we captured lung-draining lymph node (LN) and blood cellular dynamics following Mtb infection or vaccination using a two-compartment mathematical model (26,37,47). Briefly, we track Mtb-specific and Mtb-non-specific CD4+ and CD8+ naïve, effector, effector memory, and central memory T cell responses using a compartmentalized system of 31 non-linear ODEs (Figure 5.1B). We represent Mtb-specific T cells as a generic class of antigen-specific cells across time. In the LN, T cells are tracked as counts across time, whereas in the blood, the cells are tracked as a concentration (cells/μL) because experimental data on blood T cells is often presented as a concentration. The Appendix D gives the list of all parameters, definitions, and ranges for the blood and LN models.

5.2.4 Creating the multiscale model: Linking the lung model (*MultiGran)* and the lymph node model

T-cell priming, proliferation and differentiation begins in the LN when an antigen-presenting cell (APC) travels from lungs to LN and interacts with a Mtb-specific T cells. In mice, this process

does not begin until 9-13 days after inoculation (16,39), but serial positron emission tomography coupled with computed tomography scans (PET-CT) in NHP studies have shown that LNs do not become metabolically active until 2-4 weeks post-infection (38,48,49). Wolf et al. showed that the migration of cells to LN is transient (39), and NHP PET-CT studies revealed that LNs do not increase metabolic activity following 8-12 weeks post-infection during latent infection (48).

We mirror this biological phenomenon in a coarse-grained manner within *HostSim* (Figure 2C). As infection progresses within *HostSim*, we allow infected macrophages within granulomas to act as a proxy for APCs that migrate to the LN beginning ~1-4 weeks post-infection. This assumption is supported by experimental studies and previous modeling has made similar assumptions (35,50,51). We represent the percentage (5-25%) of infected macrophages which will act as APCs and migrate to the lymph node as a parameter. This range emerged from calibration but is validated by experiments that show only a small fraction of cells can traffic to the LN (50–52). The main migration of cells to the LN ceases ~7-14 weeks post-infection, consistent with the NHP PET-CT data (48). However, as TB is a chronic disease, we include stochastic events where a small percentage of cells randomly migrate to the LN in low levels every few days. All processes that link lung and LN compartments are events guided by parameters whose initial ranges were estimated from both mouse (16,39) and NHP data (38,48,49). For example, even though we model a single LN compartment, approximately five lung draining lymph nodes are involved in NHP and human Mtb infection (49), so we scale all LN T cell counts by a multiple of five when they enter the blood compartment, as done previously (26,36,37).

5.2.5 Creating the multiscale model: Linking the blood model to the lung model (*MultiGran*)

We also coarse-grain the process of T-cell lung-homing and migration to the sites of granulomas. In *HostSim*, there are three types of blood T cells that are recruited to the granuloma: Mtb-specific effector T cells, Mtb-specific effector memory T cells, and non-specific T-cells. Note, once blood Mtb-specific effector T cells arrive in the granuloma, they are considered primed T cells. Recruitment occurs for both CD4+ and CD8+ T cell lineages.

Each cell type is recruited to each granuloma according to inflammatory signals within our granuloma model. These include counts of activated and infected macrophages, and levels of the pro-inflammatory cytokine TNF, consistent with experimental data and previously presented models (25,36,53–56). We calculate the number of Mtb-specific effector T cells that will be recruited from the blood to the i^{th} granuloma, $granuloma_i$, per time step according to the following equation, as outlined in our previous modeling work (33,35,57):

$$granuloma_i Recruit = \alpha_{1a}(granuloma_i M_A + w_2 granuloma_i M_I) + Sr_{1b}\left(\frac{granuloma_i TNF_\alpha}{granuloma_i TNF_\alpha + f_8 granuloma_i IL_{10} + s_{4b2}}\right)$$

Where $\alpha_{1a}, w_2, Sr_{1b}, f_8, s_{4b2}$ are granuloma-specific parameters (see Table D.1 for details). Effector Memory T cells are recruited similarly to each granuloma, but recruitment is performed proportional to the level of TNF-α within the granuloma (see Effector Memory T cell granuloma equations in Appendix D). We assume different mechanisms of recruitment between these T cell phenotypes arises due to known differences in migration of effector memory and effector T cells to non-lymphoid sites, such as the lung (reviewed in (58)). Altogether, numbers of macrophage and inflammatory cytokine levels act as a proxy within our model for chemotactic and adhesion molecules acting within a granuloma that attract T cells to the site. We perform this recruitment for each granuloma at every timestep within the model – once per 24 hours. At each timestep we update the blood cell levels by subtracting the summed granuloma recruitment for each cell type, according to the following general form:

$$BloodCell = BloodConcentration * scaleToCount$$

$$BloodCell = BloodCell - \sum_{i=1}^{n=number\ of\ granulomas} granuloma_i Recruit$$

$$BloodConcentration = BloodCell * scaleToConcentration$$

where blood cell concentrations (cells/μL) are converted to blood cell numbers prior to entering the granulomas. The parameter $scaleToCount$ = 3.6x10^5, is a well-established value in the literature that represents the volume of blood in μL (26,36,37,59). This parameter is used to scale cells when they traffic between the blood and the lung or LN compartments. The value of

$scaleToCount$ is the inverse of $scaleToConcentration$. This type of volumetric scaling is standard in compartmental modeling (60).

During very early timesteps following inoculation, granulomas may occasionally attempt to recruit more Mtb-specific T cells than are physically available within the blood compartment. Should this happen, recruitment cell counts are obtained by normalizing the corresponding blood concentrations, such that the magnitude of cell recruitment is proportional to the blood concentration. In general, our assumption that more inflammatory granulomas are able to recruit larger quantities of T cells is consistent with previously presented models and experimental data (25,26,33,41,53).

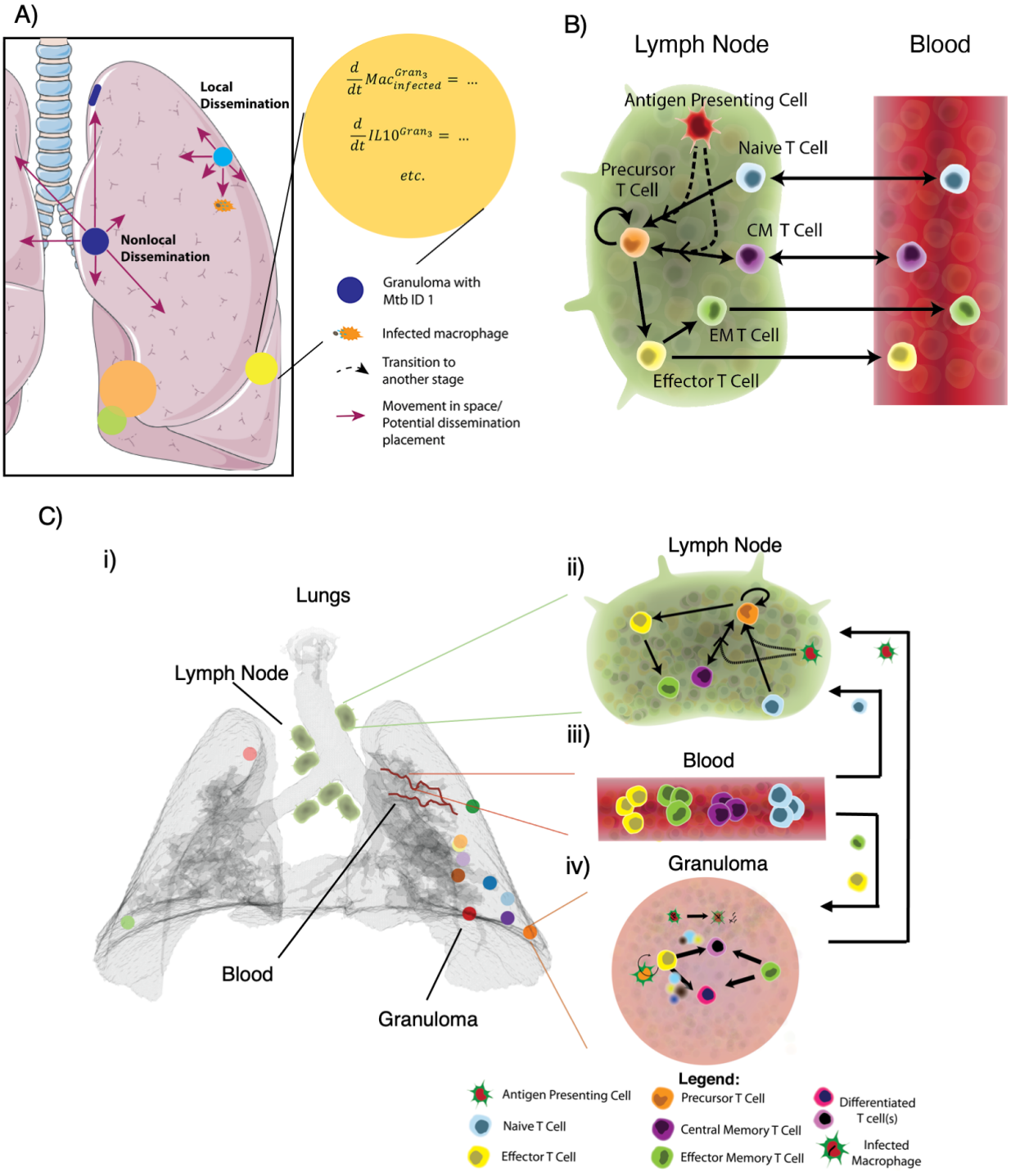

Figure 5.1 *HostSim* multiscale modeling framework
(A) Multiple lung granuloma (*MultiGran*) model conceptual framework. Adapted from Figure 2 in (35), and Chapter 3. B) The blood and lymph node (LN) model that tracks multiple T cell phenotypes across LN and blood compartments. Adapted from Figure 2 in (37) and Chapter 4. C) i) HostSim model schematic showing lungs (gray), separate granulomas (various colored circles), lung draining lymph nodes (green near trachea), and conceptual lung vasculature (red curves). (ii) APCs travel from lung granulomas to lymph nodes to initiate T cell priming,

proliferation and differentiation. T cells travel from lymph nodes into (iii) blood and re-enter lung granuloma environments (iv) continuously over time to participate in bacterial killing and containment within the granuloma.

5.2.6 Calibrating *HostSim* to multiple datasets

After construction of *HostSim*, we calibrated the model to estimate model parameter values. An effective strategy to calibrate a complex, multi-scale and multi-compartment system is to calibrate to multiple datasets, thereby reducing the likelihood of parameter overfitting (61). We utilized our previously published protocol for calibrating complex systems to biological data, *CaliPro* (62), to generate a range of calibrated parameter values.

Using *CaliPro*, we simultaneously calibrated to biological datasets across multiple biological scales. We calibrated the single granuloma ODE model to previously published T cell and macrophage datasets from 28 NHP granulomas across 70 days and a bacterial CFU dataset for 623 granulomas from 38 NHPs across 120 days (25,26,63,64). At the whole-host scale, we calibrated the lymph node and blood compartment to a previously published T cell dataset from 26 NHPs across 200 days (26). Each time point within these data sets includes multiple data points, such that the experimental data illustrates a heterogenous range of potential outcomes (Figure 5.2 B, C & D).

We determined initial parameter ranges for each model parameter based on experimental values from literature, as well as previous single granuloma ODE models, previous lymph node and blood ODE models, and our previous work in modeling multiple granulomas (33,37,57,65). In this modeling framework, some of the parameter values are constrained (such as rates of bacterial killing or cellular death rates) and were not as widely varied as others. We utilized a Latin hypercube sampling (LHS) scheme to sample 500 times within the initial parameter space, thereby creating 500 unique simulations of *HostSim* (i.e. generating 500 unique virtual hosts). We then use *CaliPro* to refine and resample this wide initial parameter space in an iterative manner.

CaliPro requires users to explicitly define a pass set – this is an automated criterion for which the model simulations can be considered calibrated. We specify a pass set as the simulations that fall within the range bounded by an order of magnitude on either side of the minimum and maximum experimental data point for every time point across each of the experimental

outcomes. The experimental data range includes over four orders of magnitude (Figure 5.2 B), therefore our pass set definition was selected since it encapsulates the general behavior of the experimental datasets we are using for calibration and will not remove simulations that are within the same order of magnitude as experimental data points. Additionally, we know that the long-term behavior of bacterial numbers in granulomas are fairly stable without intervention (9), and thus we set an upper bound at 36000 bacteria for days 90-200 as a specific criterion for calibration of this outcome. If the simulation value for bacterial numbers eclipses this bound within those days, the simulation does not belong to the pass set, even if the granuloma T cells and macrophages all lie within the bounds of the experimental data. In an iterative manner, *CaliPro* redefines the parameter ranges for each parameter according to the pass set simulations and reruns the model, comparing against the experimental data until calibration is considered complete (a pre-defined user input). For *HostSim*, calibration was considered complete when 90% of simulations belonged to the pass set. Table D.1 lists the calibrated parameter ranges for each varied parameter.

5.2.7 Establishing criteria for clinical classifications in *HostSim*

To explore the range of possible host-scale outcomes in *HostSim*, we sample from our calibrated parameter space and generate a virtual population of 500 unique hosts. Each individual simulation begins with an inoculation dose of 10 CFU, stochastically placed within the lower left lung lobe to seed the formation of 10 unique granulomas. We start each simulation with 10 CFU to be consistent with the inoculation of NHPs, which inoculate ~10 CFU to begin experiments (71).

Each virtual host in the population is simulated for 200 days. At 200 days, we delineate clinical classifications across the population of 500 virtual hosts according to the total lung CFU per host. We calculate the total lung CFU by summing the individual granuloma CFU for all granulomas within a host at each time point. We use the following cutoffs for clinical classification: TB eliminators: total lung CFU<1; Active TB cases: total lung CFU > 10^5; LTBI: all other virtual hosts. We establish the threshold between active TB cases and LTBI cases in *HostSim* to be consistent with NHP studies that show that total bacterial burden in active TB cases is significantly higher than that of LTBI monkeys, although the same study did show a small number of active cases with a bacterial burden similar to that of latent NHPs (see

Discussion and (21) for more detail). Finally, we select 200 days (~7 months) post-infection for clinical classification in order to be consistent with NHP studies that classify animals 6-8 months following infection (67).

In the dose inoculation studies, we use the same virtual population of 500 hosts, but run 25 separate virtual experiments and vary the inoculation dose from 1-25 CFU. Thus, depending on the study, hosts begin the simulation with 1 to 25 unique granulomas. At the conclusion of the simulation – day 200 – we use the same thresholds of total lung CFU for determining clinical classifications across all hosts.

5.2.8 Uncertainty and sensitivity analysis

We quantify the importance of host-scale and granuloma-scale mechanisms involved in infection outcomes using statistical techniques known as uncertainty and sensitivity analysis. As mentioned above, we efficiently sample our multi-dimensional calibrated parameter space using LHS algorithms to generate 500 individual virtual hosts. We then determine correlations between model outputs and parameter values by using Partial Rank Correlation Coefficient (PRCC), a common method for determining correlation-based sensitivity (68).

Sensitivity analyses of multiscale models can be difficult (69). 'All-in-one' sensitivity analyses are one method for exploring relationships between model parameters and outcomes by treating the full model as a black box and varying all parameters. In particular, 'all-in-one' sensitivity analyses are not always sufficient for understanding relationships between model parameters and outcomes, especially when a model is sufficiently complex and composed of multiple compartments or sub-models, as is the case with *HostSim*. As reviewed in (70), an 'all-in-one' sensitivity analysis can be paired with an intra-compartmental model approach to provide comprehensive understanding of the model behavior across scales.

We present results from two separate sensitivity analyses in the Results Section. First, we vary parameters across the whole-host scale and granuloma-scale physiological compartments to create 500 unique virtual hosts. Each virtual host in this population includes multiple granulomas with separate parameter values. We perform an 'all-in-one' sensitivity analysis across these 500

virtual hosts to identify significant associations between parameters and whole-host clinical outcomes in TB (i.e., LTBI or active TB cases).

Next, to perform an intra-compartmental analysis, we select two representative hosts – one host that was classified as an active TB host and one that was classified as a TB eliminator according to their total lung CFU at day 200. For each representative host, we rerun the simulation 500 times, varying only granuloma-scale parameters while fixing the blood and LN parameters (Figure D.1 displays granuloma CFU trajectories of each set of 500 simulations). From each set of simulations, we calculate PRCC values to identify associations between granuloma-scale parameters and granuloma CFU at day 200. We performed False Discovery Rate test corrections (71) on all reported significant parameters.

5.2.9 Pro- and anti- inflammatory profiles of *HostSim granulomas*

We present a unitless measure that represents the ratio of pro- and anti- inflammatory cytokines for granulomas within *HostSim*. Cytokine units in *HostSim* granulomas are picograms per microliter, a measure that is consistent with previously published models of cytokine levels in granulomas (33,57,72). However, to investigate relative ratios of pro- and anti- inflammatory cytokines within each *HostSim* granuloma, we calculated the common logarithm (logarithm with base 10) of the IL-10, TNF-α and IFN-γ cytokines and plotted these values in a 3-dimensional scatterplot. This allows for a comparison of granuloma inflammatory profiles, across orders of magnitudes of cytokine concentrations within the granuloma environment.

5.2.10 Model analysis tools and simulation environment

Model code and preliminary data analyses are written in MATLAB (R2020a). We solve the systems of ODEs using MATLAB's ode15s stiff solver, using a timestep of one day. At the end of each timestep, we perform cell recruitment and update granuloma cell, cytokine, and bacterial states as well as lymph node and blood cell concentrations. A single *in silico* individual simulation across 200 days of infection time can be performed on a 2-core laptop in approximately 5 minutes. We wrote bash scripts to submit multiple runs of *HostSim* on compute clusters. We perform post-processing statistical analysis, graphing and movie rendering within MATLAB (R2020a).

5.3 Results

5.3.1 *HostSim* recapitulates *in vivo* granuloma-scale and host-scale dynamics

We calibrate *HostSim* to published datasets from NHPs across multiple scales following a single primary infection event. We utilized *CaliPro*, our protocol to define and perform calibration for computational models (62). *CaliPro* identifies a parameter space where each varied parameter has a range of values that correspond to a range of outcomes that match experimental datasets. For this work, the experimental data come from published NHP studies (10,25,35,64). Our *HostSim* website shows calibration datasets and references for each dataset (http://malthus.micro.med.umich.edu/lab/movies/HostSim/).

When sampling parameter sets within our calibrated parameter ranges, *HostSim* matches both the range of experimental outcomes and the dynamics outlined by datasets of primary Mtb infection derived from published NHP studies (Figure 5.2). At the granuloma scale, *in silico* granulomas from *HostSim* simulations are able to replicate NHP granuloma CFU, T cell and macrophage dynamics across time (Figure 5.2B, experimental data from previously published NHP studies (10,25,35,64)). Granuloma CFU peaks at approximately 35 days as macrophage and T cell counts increase. Following the peak, CFU, macrophage and T-cell counts correspondingly stabilize across time. At the host scale, *in silico* blood cell counts replicate NHP blood CD4+ and CD8+ T cell data across time (26). Following infection, there is a slight peak in overall effector and effector memory T-cell types that precedes a growing number of central memory CD4+ and CD8+ T cells. (Figure 5.2 C&D). Across multiple scales, *HostSim* presents a 'virtual host' model of the immune response to Mtb infection.

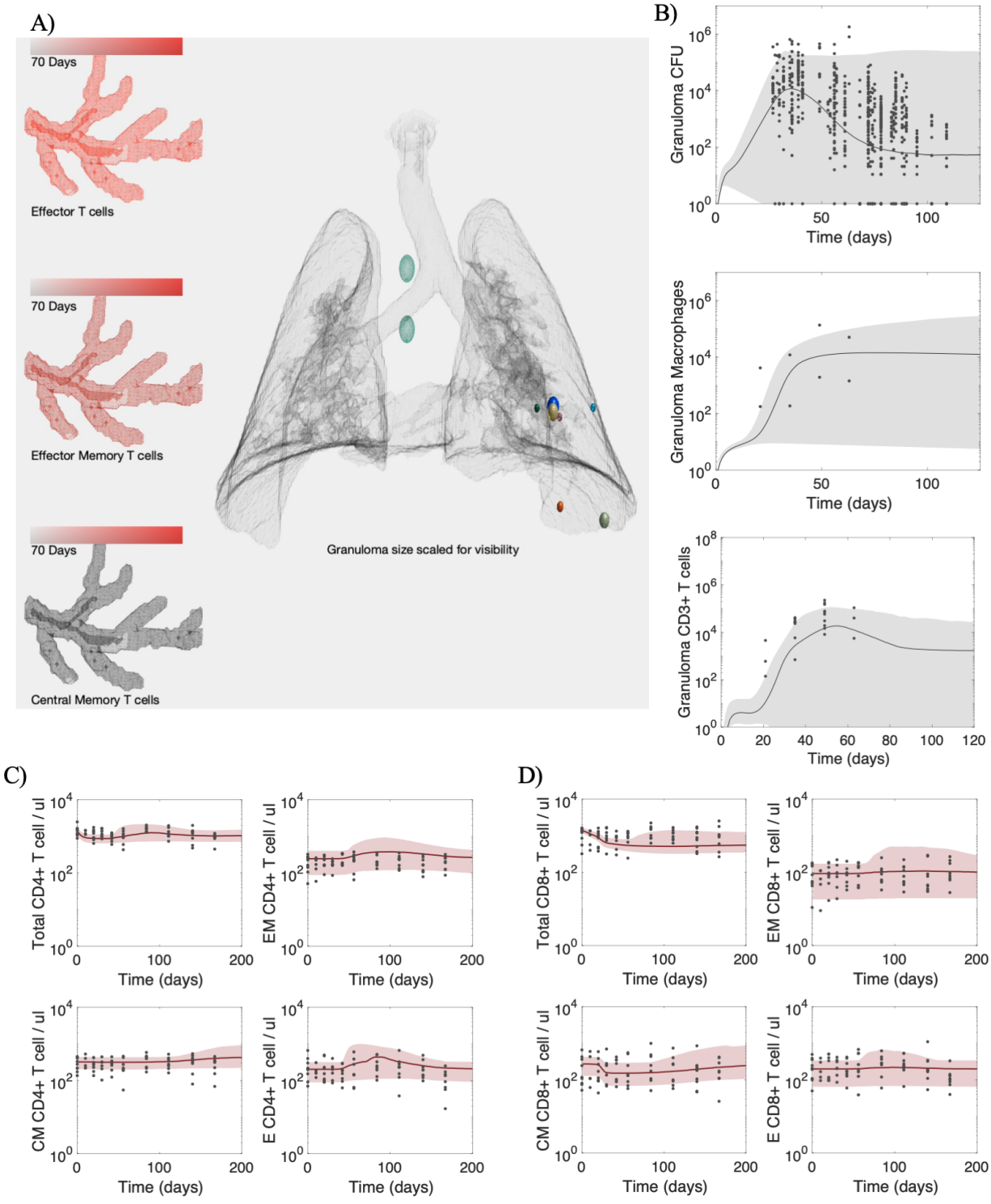

Figure 5.2 Calibrated *HostSim* recapitulates dynamics of Mtb infection at both granuloma-scale and host-scale.

(A) Snapshot of *HostSim* time-lapse video showing virtual lungs, granulomas, lung draining lymph nodes, and blood cell concentrations for three cell types. Mtb-specific effector, effector memory and central memory T cells numbers within blood are qualitatively captured by a color change across time, from black (very few cells in the blood) to

bright red (representing the maximum number of cells of that blood type across the simulation). At day 70, Mtb-specific effector T cells numbers peak, Mtb-specific effector memory T cells are continuing to grow in magnitude, and Mtb-specific central memory T cells have not yet started to differentiate in large numbers. Full time courses can be found at http://malthus.micro.med.umich.edu/lab/movies/HostSim/. *HostSim* was calibrated to published datasets from NHPs on (B) lung granuloma CFU, macrophage and T cell granuloma numbers from previous studies (26); (C) blood CD4+ T cell data and (D) blood CD8+ T cell data from both simulation and NHP following a single infection event in NHP studies (25,26,63,64). Published NHP study data is shown as black dots across the graphs. For direct comparison, we display simulation data as a gray (granuloma outcomes) or red (blood outcomes) cloud that outlines the 1st and 99th percentile across 500 host simulations. Gray and red lines represent the medians of those simulations. Simulations shown until day 200 post-infection. In A) granulomas are scaled by a factor of 10 for ease of visibility in lung environment.

5.3.2 Emergent *HostSim* behavior across a virtual population matches spectrum of tuberculosis

Humans present a spectrum of clinical outcomes in TB, including (but not limited to) complete elimination of infection, latent infection, and active TB disease (3). Work in NHPs have shown that total bacterial burden is associated with clinical outcomes. Specifically, total bacterial burden in active TB cases is significantly higher than that of LTBI monkeys (21). *HostSim* exhibits similarly heterogenous host-scale outcomes.

To explore the range of host-scale outcomes virtual hosts, we sample from our calibrated parameter space to generate a virtual population of 500 unique hosts. Each simulation begins with an inoculation dose of 10 CFU (selected to be consistent with inoculation of NHPs (71)), thereby starting the formation of 10 individual granulomas within the lung environment. Simulations run for 200 days. We calculate the total lung CFU by summing the individual granuloma CFU for all granulomas within a host.

Across our virtual population of 500 virtual hosts, the total lung CFU per host spans several orders of magnitude, from 0 CFU (infection elimination) to 10^6 CFU (Figure 5.3A). We delineate our virtual population into 3 groups according to their total lung CFU at day 200, analogous to the clinical classifications of NHPs 6-8 months following primary infection (67). We use the following cutoffs for classification: TB eliminators: total lung CFU<1; Active TB cases: total lung CFU > 10^5; LTBI: all other virtual hosts. Across our 500 virtual hosts, there are 24 TB eliminators, 110 active TB cases, and 366 LTBI individuals. Snapshots from representative simulations of these diverse outcomes are displayed in Figure 5.3D, E & F.

After classifying the virtual hosts by total lung CFU, we looked at two additional statistics. First, the number of sterilized granulomas across the three different clinical classifications (Figure 5.3B). Our model predicts that ~75% of active TB cases include at least one sterile granuloma. This finding is validated by a previously published NHP dataset, which showed 11 out of 13 active monkeys had at least a single sterilized granuloma (9).

Second, we looked at the number hosts which have individual granulomas with a high bacterial burden (defined as granulomas with $5x10^4$ CFU or higher; Figure 5.3C). As expected, all TB eliminators and the majority of LTBI virtual hosts do not contain a granuloma with a high bacterial burden. However, we see approximately 8% of our LTBI classified hosts include one high CFU granuloma. These cases indicate that our model may have the potential to capture incident or subclinical TB and may explain the spectrum nature of TB disease these individuals could be more likely to reactivate or progress to active disease (5).

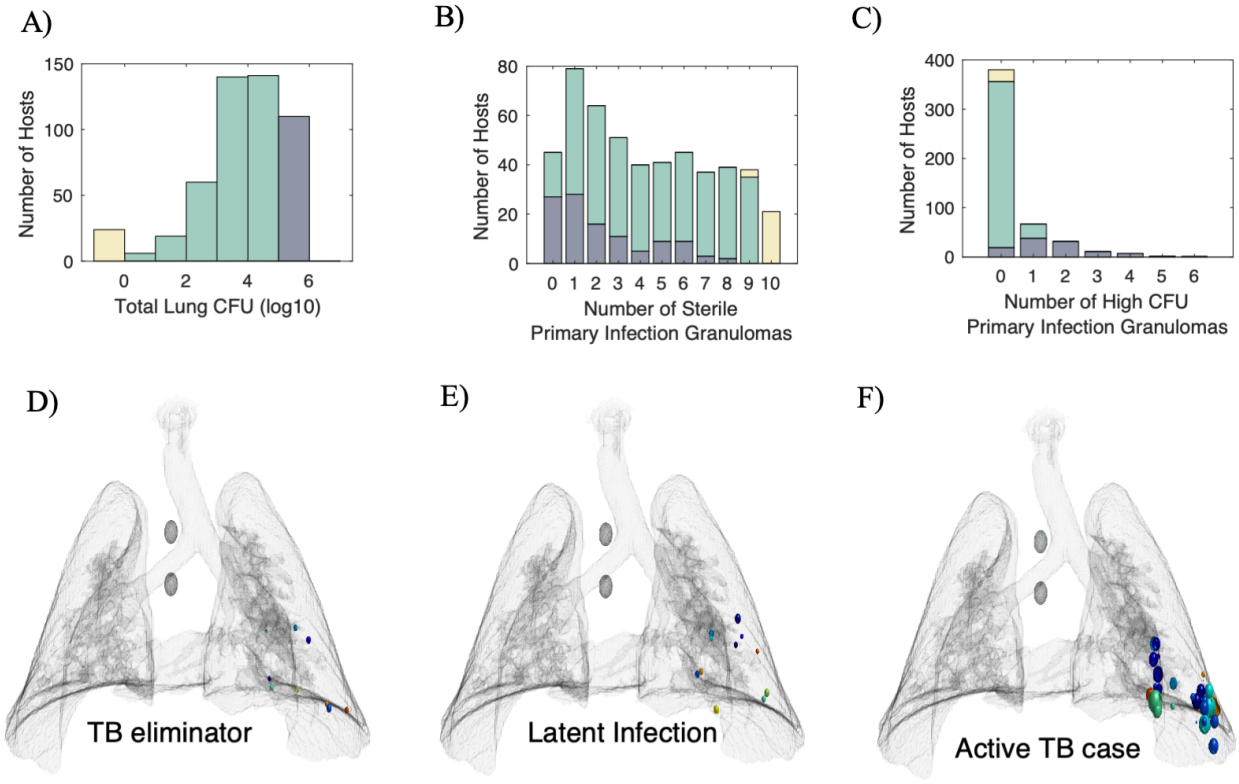

Figure 5.3 HostSim exhibits a spectrum of whole-host outcomes across a population of 500 virtual hosts.
(A) Histogram displaying the total lung CFU per host at day 200 across our virtual population of 500 hosts. We delineate the virtual population into three groups: TB eliminator (yellow), LTBI (green), or active TB cases (dark blue) according to the total Lung CFU. (B) Stacked bar chart displaying the number of sterile granulomas per host across TB eliminator, LTBI, or active TB cases. (C) Stacked bar chart displaying the number of high CFU

granulomas per host across TB eliminator, LTBI, or active TB cases. (D, E, F) *HostSim* time-lapse video snapshots display virtual lung architecture and granuloma locations for representative TB eliminator, LTBI and active TB cases at day 200 post-infection.

5.3.3 Infection outcomes of virtual hosts are dose dependent

In humans, a relationship between inoculation dose and severity of clinical disease has been hypothesized (73–75). To explore this in our virtual hosts, we performed a set of inoculation dose experiments using *HostSim*. We reran our virtual population of 500 hosts through 25 simulated experiments. For each experiment we re-simulated the 500 virtual hosts with identical random seeds and parameter sets, and only varied dose inoculum. We varied dose inoculum from 1 to 25 CFU. Figure 5.4 displays the total lung CFU and clinical classification of those 500 hosts at day 200 following each of the 25 experiments.

As dose inoculum increases, the median lung CFU for the population of 500 hosts (at day 200 post-infection) increases; however, the model predicts a range of outcomes across the population for each inoculation dose (Figure 5.4A). For example, among the 500 hosts inoculated with 25 CFU, a few hosts had low levels of CFU within the lung (CFU <100). Conversely, after a dose inoculum of 1 CFU, some hosts still exhibited considerable infection, with total lung CFU > 10^5.

For each of the 25 dose experiments, clinical classifications of the virtual hosts based on the total lung CFU at 200 days post-infection are shown in Figure 5.4B. We delineated the virtual population into three groups, as above, where TB eliminators have a total lung CFU<1, active TB cases have a total lung CFU > 10^5 and all other hosts are classified as LTBI. After an inoculum of 25 CFU, ~55% of the simulations are classified as LTBI and ~45% are classified active TB cases at day 200 (Figure 5.4B). Thus, *HostSim* predictions agree with human association studies (73–75) suggesting TB disease severity is dose dependent.

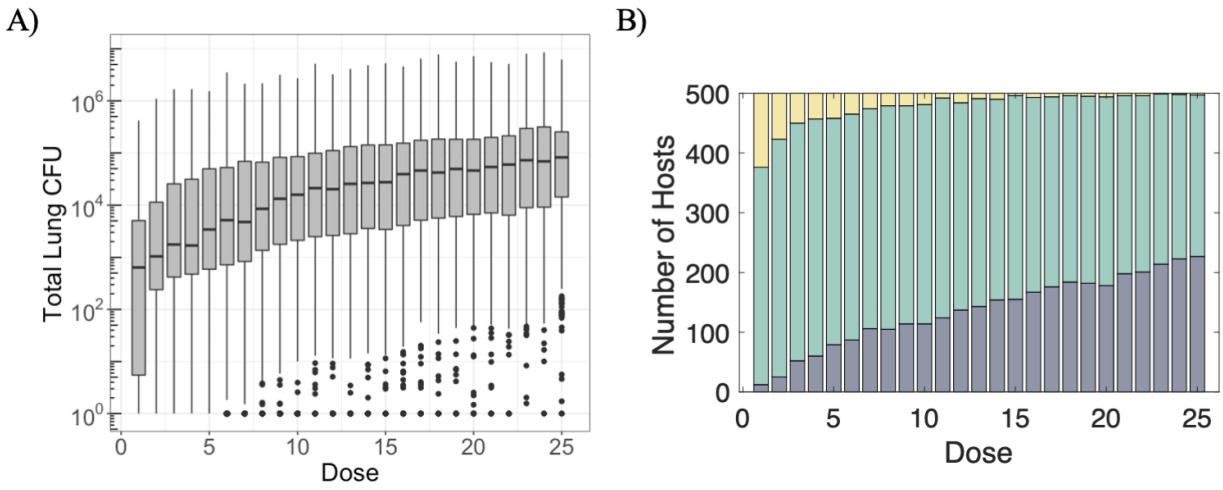

Figure 5.4 Infection outcomes at day 200 post-infection across a population of 500 virtual hosts are dose dependent.
(A) Distribution of total lung CFU per host among the virtual population for the 25 inoculation dose experiments. Total lung CFU is calculated by summing CFU across all granulomas in a single host. (B) Stacked bar charts display the classification of virtual hosts based on total lung CFU per host for the 25 inoculation dose experiments. Bar chart colors are the same as Figure 3 - TB eliminators (yellow), active TB cases (dark blue) or LTBI (green).

5.3.4 The fate of individual granulomas is heterogeneous within hosts

In both human and NHP studies, individual granulomas within a single host can present a heterogeneous array of morphological, pathological, and immunological outcomes (40,76–78). In NHP studies, even granulomas within active TB monkeys can exhibit sterilization (9,21,79). Similarly, within individual hosts across our virtual population of 500 hosts, we identify a range of granuloma-scale outcomes, from total sterilization to uncontrolled growth. Figure 5.5 displays the individual granuloma CFU trajectories from five representative hosts ranging across different clinical cohort classifications: TB eliminator, LTBI and active TB cases, respectively. Within-host variation is apparent in all hosts, but we highlight that host #5 has both sterilized and disseminating granulomas present. Dissemination occurs when bacteria escape one granuloma and seed the formation of another granuloma elsewhere in the lung environment. Dissemination granulomas can be identified when a new CFU trajectory begins at any timepoint after the initial infection (c.f. Figure 5.5B host #5). However, dissemination does not only occur in active TB hosts; we also note a dissemination event occurred in host #3 (Figure 5.5B), a virtual host that is still classified as LTBI according to our established criteria outlined in Figure 3A and Methods.

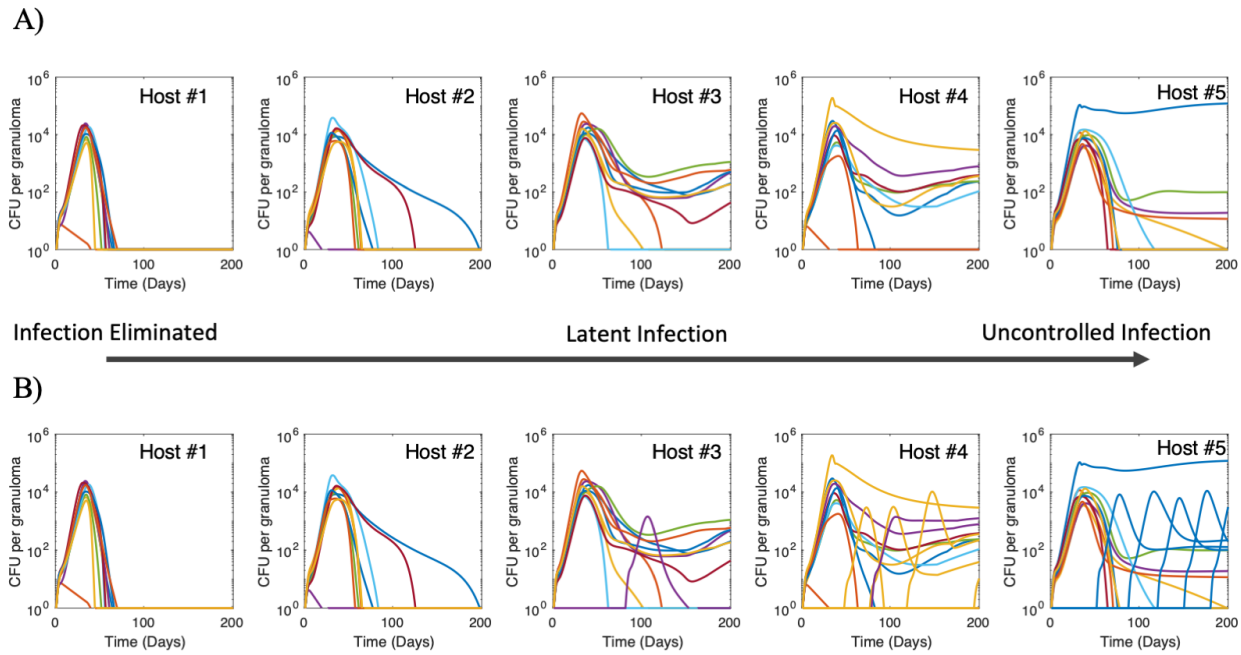

Figure 5.5 *HostSim* exhibits spectrum of granuloma-scale outcomes within hosts.
500 virtual hosts were simulated to create our population, as shown in Figure 3. We identified 5 representative hosts that exhibited a spectrum of whole-host outcomes (elimination, control and uncontrolled infection outcomes). Each graph is an individual host – the same five hosts are shown in (A) and (B). Each line represents the CFU in a single granuloma within the host over time. Sterilization of an individual granuloma can be seen when CFU reaches 0 at any timepoint post-infection. Dissemination occurs when a new line begins at any timepoint after the initial infection. Dissemination granuloma CFU trajectories are colored to match the granuloma from which they disseminated. (A) Individual granuloma CFU trajectories for primary infection granulomas within the 5 representative virtual hosts. B) Primary infection and dissemination granuloma CFU trajectories across the same 5 virtual hosts. Note that in the far-right of panel B), one granuloma (blue CFU trajectory) incurred multiple dissemination events, spurring the formation of multiple new granulomas across time. Each color is a separate granuloma within each host, except dissemination granulomas which are colored to match the granuloma from which they disseminated.

For the majority of hosts across our virtual population, the fate of the primary infection granulomas is sufficient to delineate the clinical cohort classification at day 200. Out of the 500 *in silico* hosts, only 8 hosts (~2%) are reclassified as active TB cases when considering both primary infection granuloma and disseminating granuloma bacterial burdens. That is, the outcomes of dissemination granulomas are not necessary to classify clinical cohorts within *HostSim*. This prediction suggests that the fate of clinical outcomes is determined at early stages of infection, even prior to dissemination events that occur after inoculation.

5.3.5 Early events across multiple scales during infection are predictive of TB clinical classification

Early events in Mtb infection are thought to impact late-stage clinical outcomes (13,15,67,80) however, this is a difficult relationship to investigate clinically or experimentally. Once an animal is necropsied there is no way to know a priori if that animal would have progressed to active or latent infection. *HostSim* provides a tool through which we can relate early events within the lungs and LNs to clinical classifications (TB eliminators, LTBI, or active TB) determined months later across our virtual population of hosts. In *HostSim*, we predict that mechanisms operating at early stages across multiple scales impact clinical classifications. At the host scale, we investigate relationships between blood and lung immune cell counts. Additionally, we stratify lung T-cell counts by clinical classifications. At the granuloma scale, we examine the ratio of pro- and anti- inflammatory cytokines within the granuloma.

First, we asked whether there is a relationship between levels of immune cells in the blood and within the lung. Figure 5.6A shows an association between lung levels and blood levels of T cells at day 50 for four separate T cell phenotypes (Mtb-specific CD4+ effector, effector memory and Mtb-specific CD8+ effector, effector memory) across the 500 virtual hosts. Day 50 was selected as it is typically the height of effector-expansion within in the model, timing that is supported by the NHP granuloma and blood T cell datasets (c.f. Figure 5.2). Each datapoint is colored according to the simulations' clinical outcomes at day 200. Note that there is a relationship between numbers of lung and blood CD4+ effector T cells and CD8+ effector T cells ($r = 0.5$, $p < 0.01$ and $r = 0.61$, $p < 0.01$, respectively). However, by day 200 (Figure 5.6B), the time point we use for clinical classification, this relationship between blood and lung is less clear ($r = 0.3$, $p < 0.01$ and $r = 0.14$, $p < 0.01$; for CD4+ and CD8+ effector T cells, respectively).

Second, we identify the fold-change difference of numbers of lung T cells between days 30 and 40 post-infection as indicative of clinical classification 160 simulation days later (Figure 5.6C). Across the four Mtb-specific T cell phenotypes that are recruited into the lung (Mtb-specific CD4+ effector, effector memory and Mtb-specific CD8+ effector, effector memory), virtual hosts that are classified as TB eliminators typically had a larger fold-change difference between days 30 and 40 than did virtual hosts that are classified as active TB or LTBI cases at day 200

(Table D.2 shows Vargha and Delaney's A measure for effect size comparisons across all clinical outcomes). Specifically, the median fold change between days 30 and 40 of numbers of Mtb-specific CD8+ effector memory T cells in TB eliminator virtual hosts is approximately 10x larger than that of active TB virtual hosts. We observe a similar difference between LTBI and active TB virtual hosts for numbers of Mtb-specific CD4+ effector T cells. These results suggest that numbers of these cell types have a crucial and early role that impacts clinical classifications made over 150 days later.

Finally, the cytokine profile of granulomas at early time points is indicative of downstream clinical classifications. Figure 5.6D shows a three-dimensional scatterplot of pro- and anti-inflammatory cytokine concentrations (pg/mL of IFN-γ, TNF-a, and IL-10) of every granuloma at day 60 across the 500 virtual hosts. Each granuloma data point is colored according to the classification of the host within which the granuloma resides. Note that a cluster emerges wherein granulomas with high levels of IFN-γ, low levels of TNF-α, and low levels of IL-10 are indicative of granulomas that are destined to be within active hosts. By day 200 (Figure 5.6E), this cluster cannot be as easily separated from the other simulations, suggesting that the dynamic balance of pro- and anti-inflammatory cytokines across time (81) could obscure this finding for granulomas sampled at later timepoints.

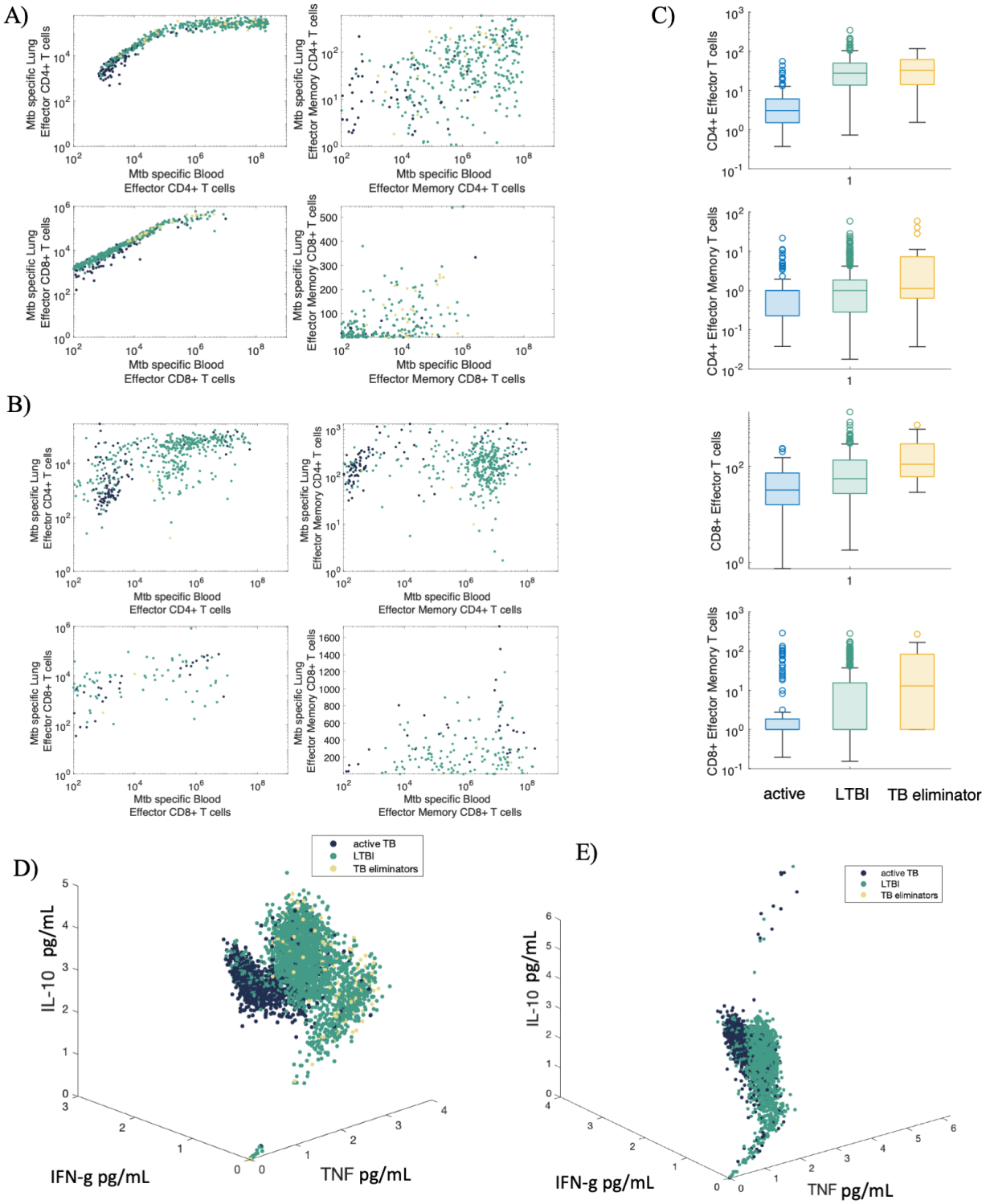

Figure 5.6 Early events at granuloma-scale and host-scale can predict clinical classifications across a population of 500 virtual hosts.

Scatterplots display blood (x-axis) and lung (y-axis) cell counts for Mtb-specific effector and effector memory CD4+ and CD8+ T cells at day 50 (A) and day 200 (B). C) The fold change in numbers of lung T-cells between day 30 and day 40, grouped by clinical classifications at day 200. Each graph displays the fold change for a separate T

cell phenotype in the lung. All granulomas from 500 virtual hosts plotted according to relative concentration TNF, IFN-γ and IL-10 cytokine concentrations (pg/mL) on a log scale (see Methods) at day 60 (D) and day 200 (E) colored according to the classification of the host within which the granuloma resides. Across all plots, dark blue = active TB cases, green = LTBI, yellow = TB eliminators.

5.3.6 A multiscale sensitivity analysis reveals adaptive immunity drives clinical classification, but innate immunity impacts granuloma-scale outcomes

To investigate the mechanisms that drive host-scale clinical outcomes in *HostSim*, we perform an 'all-in-one' sensitivity analysis (described in Methods) on the clinical classifications across the 500 virtual hosts from our calibrated parameter space. Table 5.1 highlights parameters found to be significantly correlated ($p<0.05$) with each clinical classification from our PRCC analysis. We find that adaptive immune responses within the LN are the main drivers of whole-host clinical outcomes within our calibrated parameter space. Specifically, the differentiation and proliferation of T cells within LNs are significantly associated with clinical classification (i.e. active TB, LTBI or TB eliminator). The significant, positive association between T-cell proliferation in LN and clinical classification at the whole-host scale represents an inter-physiologic compartmental effect – not only does lymph node parameter influence T-cell counts within the lymph node, but it influences whole-host scale clinical outcomes as well. Further, both Mtb-specific CD4+ and Mtb-specific CD8+ T cell parameters in the lymph node impact whole-host outcomes, lending further support to emerging studies showing the importance of CD8+ T cells in TB (44,71,82).

To explore the drivers of granuloma-scale variation within a host, we perform an intra-compartmental sensitivity analyses (see Methods) focusing solely on which granuloma-scale parameters are associated with granuloma CFU at day 200. This allows us to identify how granuloma scale parameters may contribute to heterogenous granuloma CFU outcomes within a host when blood and LN parameters are held fixed (exact PRCC values are given in Appendix D). Table 5.1 lists mechanisms that we identified from both the adaptive and innate immune responses. Multiple parameters that dictate macrophage behavior were identified as key drivers of granuloma CFU. Additionally, adaptive immune response parameters were also associated with reduced granuloma CFU (i.e., Fas:FasL cell death in Table 1).

Altogether, the results from our 'all-in-one' sensitivity analysis as well as our intra-compartmental analyses show important roles for both adaptive and innate immune systems. Specifically, we predict that while the adaptive immune response in LNs drives host-scale clinical outcomes, the innate immune system plays an important role within a host by contributing to the heterogeneity of granuloma CFU outcomes seen within humans and NHPs.

Table 5.1 Parameters identified as significant from sensitivity analysis.
For each analysis, parameters shown here have a PRCC absolute value of $\rho > 0.1$ and p-value<0.05. Parameters listed as associated with clinical outcomes are the result of our 'all-in-one' sensitivity analysis. Clinical classifications were assigned a value of 0 (active TB case), 1 (LTBI) or 2 (TB eliminator) to calculate the PRCC value for each parameter. Parameters listed as associated with granuloma CFU were the result of our intra-compartment analysis. These parameters were significantly correlated with granuloma CFU at day 200. PRCC values are listed in Appendix D.

Parameters associated with clinical outcomes	Description for parameters from 'all-in-one' sensitivity analysis
LN_k13	Precursor CD8+ T cell proliferation within the lymph node
LN_k14	CD8+ T cell differentiation to CD8+ effector T cell in lymph node
LN_k4	Precursor CD4+ T cell proliferation within the lymph node
LN_k5	CD4+ T cell differentiation to CD4+ effector T cell in lymph node
Parameters associated with granuloma CFU	**Description for parameters from intra-compartment sensitivity analysis**
k2	Resting macrophage infection rate
c9	Likelihood of resting macrophages to phagocytize bacteria
N	Carrying capacity of intracellular bacteria within macrophages
k17	Max rate of infected macrophage death from intracellular bacteria
k18	Extracellular bacterial killing by resting macrophages
k14a	Fas:FasL induced apoptosis of MI
alpha11	IL-4 production from primed T cells

5.4 Discussion

Tuberculosis is a complex and heterogenous disease. At the host-scale, the disease can manifest clinically across a spectrum of classifications, including but not limited to TB eliminators, LTBI or active TB (3). Within a single host, individual granulomas are diverse in terms of morphology, immunology and bacterial burden. One of the most highly studied aspects of TB pathology is the granuloma, but the link between granuloma-scale outcomes and whole-host outcomes is still not clear. Even active TB cases can contain a non-uniform collection of granulomas, wherein a subset of granulomas can still sterilize bacteria despite a collective failure by the host to rid the body of disease (9). Using experimental studies alone, it can be challenging to identify the full

set of mechanisms responsible for such heterogeneous outcomes within and across hosts in TB. Mathematical and computational modeling approaches provide a unique tool that can address these mechanisms by linking events within a host to outcomes operating at the host-scale. In pursuit of a better understanding of the events that occur across multiple-scales and lead to clinical classifications in TB, we develop a novel multi-scale and multi-compartment model of whole-host Mtb infection called *HostSim*. We calibrate and validate *HostSim* against previously published, distinct NHP datasets that span cellular, bacterial, granuloma and whole-host scales and make predictions about events that may cause heterogeneous outcomes across multiple scales.

An effective weapon in the global public health battle against TB is identification of robust biomarkers for disease diagnosis and treatment. In TB, there have been many studies and debates regarding both the identification and usefulness of biomarkers (83–90). One barrier to identifying robust biomarkers is the variability in disease outcomes between, and within, hosts at a population scale. In this work, we have presented evidence for another relatively unconsidered barrier: biomarkers are transient in time by their very nature. In this work, we have predicted that the relationship between numbers of blood immune cells and numbers of cells within the lung may only be well-defined at early time points following infection. Months, or years later, when an individual might present to a clinic (91), blood immune cell levels may not accurately reflect events within the lung and therefore may not be a useful compartment to sample when delineating disease status or progression. This reflects a key *HostSim* prediction: recent efforts to identify events in the blood that may correlate with events in the lung (23,24) may not be generalizable to every time point for every patient. This prediction is consistent with a recent NHP study that shows blood T-cell responses do not consistently reflect T-cell responses within granulomas (25). These findings are more broadly supported by the idea of a dynamically balanced immune response that occurs across time during chronic infections (81).

In TB animal studies, experimentalists are often unable to know a priori if animals necropsied at early time points were destined to be classified as active or latent (67). Using our virtual population of 500 hosts, we were able to show that early events at both the granuloma-scale and host-scale can be predictive of clinical classifications ~150 days later. These predictions are

potentially useful for experimentalists, who can use analogous experimental techniques (such as serial intravascular staining (92), or IHC cytokine staining of granulomas (93)) to make educated predictions about downstream clinical classifications. Further, these *HostSim* predictions contribute to a growing body of evidence that suggests early immune events matter in TB (15,80,94).

As the primary intracellular niche for Mtb during both early and chronic stages of infection, macrophages play a central role in TB pathology (95). Recent experimental work has identified Bacille Calmette Guérin (BCG), the only licensed TB vaccine, as a potentially potent innate immune response stimulator by educating macrophage progenitors (96,97). In this work, we used sensitivity analysis techniques to show that parameters governing interactions between Mtb and macrophages at the granuloma-scale are important contributors to the heterogenous granuloma outcomes within a host. Together, these studies and our predictions suggest that macrophages could be viable targets for future therapeutic interventions in TB. This follows as macrophages are crucial cells that sit at the intersection of adaptive and innate immune responses against Mtb.

There are a few limitations to our study and model. First, while we call *HostSim* a whole-host model of Mtb infection, we only represent three physiologically unique compartments (lung, lung-draining lymph nodes and blood). Some of the most progressive forms of TB include extrapulmonary disease (98). As it is beyond the scope of this work, we do not capture the dynamics of extrapulmonary disease with this model, though future work could focus on the dissemination of bacteria into the lymph node as an initial step to model extrapulmonary disease. Second, while *HostSim* has been developed based on previous modeling efforts and extensive NHP datasets, it does not include all the various cell types present within the granuloma environment (i.e. neutrophils (99) or fibroblasts (100)). These cells were not included here primarily because datasets were not as readily available or mechanistic functions of these cells within granulomas are not as well characterized. The *HostSim* modeling framework is flexible and can include these cell types in the future as more becomes known about their role in granulomas. This limitation extends to the lymph node and blood models as well, where we do not capture the events of every cell type involved in Mtb infection (i.e., B cells in the lymph

node). Finally, *HostSim* does not capture symptoms of TB disease such as coughing or weight loss. Accordingly, we assumed total lung bacterial burden can be used as a proxy for clinical classifications of TB. This assumption is not without precedent. Antibiotic studies in TB frequently use sputum-based assays as a proxy for drug efficacy and assessment of treatment progression in humans (101). Further, NHP studies have shown that total bacterial burden in active TB cases is significantly higher than that of LTBI monkeys, although the same study did show a small number of active cases with a bacterial burden similar to that of latent NHPs (21). Thus, our cut-off for active TB cases (total lung CFU>10^5) in *HostSim* virtual hosts is unable to capture individuals that may have symptomatic TB but relatively low bacterial burdens. However, as more data become available regarding the relationship between symptomatic TB and bacterial burden, future work can integrate those findings into our *HostSim* framework, perhaps by incorporating a bronchoalveolar lavage (BAL) compartment, for direct comparison to sputum samples.

In conclusion, we utilized a computational modeling framework to better understand the relationship between within-host dynamics and clinical outcomes in TB. We present *HostSim*: the first whole-host model to track events across granuloma- and host- scales. Using *HostSim*, we make predictions about relationships between immune cell counts in the blood and lungs and the role of adaptive and innate immune cells in granuloma-scale and host-scale outcomes. In particular, we predict that adaptive immunity generated in lymph nodes drives clinical classifications across hosts in TB, but that innate immunity can drive heterogeneous granuloma outcomes within a single host. We posit that *HostSim* offers potential as a computational tool that can be used in concert with experimental approaches to understand and predict events about various aspects of TB disease and therapeutics.

5.5 References

1. WHO. WHO Global Tuberculosis Report 2019. World Health Organization Press. 2019.
2. Lin PL, Flynn JL. The End of the Binary Era: Revisiting the Spectrum of Tuberculosis. The Journal of Immunology. 2018;201(9):2541–8.
3. Barry CE, Boshoff HI, Dartois V, Dick T, Ehrt S, Flynn JA, et al. The spectrum of latent tuberculosis: Rethinking the biology and intervention strategies. Vol. 7, Nature Reviews Microbiology. 2009. p. 845–55.
4. Williams CM, Abdulwhhab M, Birring SS, de Kock E, Garton NJ, Townsend E, et al. Exhaled *Mycobacterium tuberculosis* output and detection of subclinical disease by face-mask sampling: prospective observational studies. The Lancet Infectious Diseases. 2020;20(5):607–17.
5. Drain PK, Bajema KL, Dowdy D, Dheda K, Naidoo K, Schumacher SG, et al. Incipient and subclinical tuberculosis: a clinical review of early stages and progression of infection. Clinical microbiology reviews. 2018;31(4).
6. Flynn JL, Chan J. Tuberculosis: latency and reactivation. Infection and immunity [Internet]. 2001 Jul;69(7):4195–201. Available from: https://pubmed.ncbi.nlm.nih.gov/11401954
7. Dye C, Scheele S, Pathania V, Raviglione MC. Global burden of tuberculosis: estimated incidence, prevalence, and mortality by country. Jama. 1999;282(7):677–86.
8. Flynn JL, Gideon HP, Mattila JT, Lin P ling. Immunology studies in non-human primate models of tuberculosis. Immunological Reviews. 2015;264(1):60–73.
9. Lin PL, Ford CB, Coleman MT, Myers AJ, Gawande R, Ioerger T, et al. Sterilization of granulomas is common in active and latent tuberculosis despite within-host variability in bacterial killing. Nature Medicine. 2014;20(1):75–9.
10. Martin CJ, Cadena AM, Leung VW, Lin PL, Maiello P, Hicks N, et al. Digitally Barcoding *Mycobacterium tuberculosis* Reveals *In vivo* Infection Dynamics in the Macaque Model of Tuberculosis . mBio. 2017;8(3).
11. Joosten SA, Ottenhoff THM, Lewinsohn DM, Hoft DF, Moody DB, Seshadri C, et al. Harnessing donor unrestricted T-cells for new vaccines against tuberculosis. Vaccine [Internet]. 2019/04/27. 2019 May 21;37(23):3022–30. Available from: https://pubmed.ncbi.nlm.nih.gov/31040086
12. Diedrich CR, Mattila JT, Klein E, Janssen C, Phuah J, Sturgeon TJ, et al. Reactivation of latent tuberculosis in cynomolgus macaques infected with SIV is associated with early peripheral T cell depletion and not virus load. PLoS ONE. 2010;5(3).
13. Yao S, Huang D, Chen CY, Halliday L, Wang RC, Chen ZW. CD4 + T Cells Contain Early Extrapulmonary Tuberculosis (TB) Dissemination and Rapid TB Progression and Sustain Multieffector Functions of CD8 + T and CD3 − Lymphocytes: Mechanisms of CD4 + T Cell Immunity . The Journal of Immunology. 2014;192(5):2120–32.
14. Sakai S, Mayer-Barber KD, Barber DL. Defining features of protective CD4 T cell responses to *Mycobacterium tuberculosis*. Vol. 29, Current Opinion in Immunology. 2014. p. 137–42.
15. Cadena AM, Flynn JL, Fortune SM. The importance of first impressions: Early events in *Mycobacterium tuberculosis* infection influence outcome. Vol. 7, mBio. 2016.
16. Reiley WW, Calayag MD, Wittmer ST, Huntington JL, Pearl JE, Fountain JJ, et al. ESAT-6-specific CD4 T cell responses to aerosol *Mycobacterium tuberculosis* infection are initiated in the mediastinal lymph nodes. Proceedings of the National Academy of Sciences of the United States of America. 2008;105(31):10961–6.

17. Gallegos AM, Pamer EG, Glickman MS. Delayed protection by ESAT-6-specific effector CD4+ T cells after airborne M. tuberculosis infection. Journal of Experimental Medicine. 2008;205(10):2359–68.
18. Matzinger P. The evolution of the danger theory. Interview by Lauren Constable, Commissioning Editor. Expert review of clinical immunology [Internet]. 2012 May;8(4):311–7. Available from: https://pubmed.ncbi.nlm.nih.gov/22607177
19. Lin PL, Myers A, Smith L, Bigbee C, Bigbee M, Fuhrman C, et al. Tumor necrosis factor neutralization results in disseminated disease in acute and latent *Mycobacterium tuberculosis* infection with normal granuloma structure in a cynomolgus macaque model. Arthritis and Rheumatism. 2010;62(2):340–50.
20. Mattila JT, Diedrich CR, Lin PL, Phuah J, Flynn JL. Simian Immunodeficiency Virus-Induced Changes in T Cell Cytokine Responses in Cynomolgus Macaques with Latent *Mycobacterium tuberculosis* Infection Are Associated with Timing of Reactivation . The Journal of Immunology. 2011;186(6):3527–37.
21. Lin PL, Rodgers M, Smith L, Bigbee M, Myers A, Bigbee C, et al. Quantitative comparison of active and latent tuberculosis in the cynomolgus macaque model. Infection and Immunity. 2009;77(10):4631–42.
22. Willis JCD, Lord GM. Immune biomarkers: the promises and pitfalls of personalized medicine. Nature Reviews Immunology [Internet]. 2015;15(5):323–9. Available from: https://doi.org/10.1038/nri3820
23. Mpande CAM, Musvosvi M, Rozot V, Mosito B, Reid TD, Schreuder C, et al. *Mycobacterium tuberculosis*-specific T cell activation identifies individuals at high risk of tuberculosis disease. medRxiv [Internet]. 2020 Jan 1;2020.06.26.20135665. Available from: http://medrxiv.org/content/early/2020/06/29/2020.06.26.20135665.abstract
24. Rozot V, Vigano S, Mazza-Stalder J, Idrizi E, Day CL, Perreau M, et al. *Mycobacterium tuberculosis*-specific CD8+ T cells are functionally and phenotypically different between latent infection and active disease. European Journal of Immunology. 2013;43(6):1568–77.
25. Gideon HP, Phuah JY, Myers AJ, Bryson BD, Rodgers MA, Coleman MT, et al. Variability in Tuberculosis Granuloma T Cell Responses Exists, but a Balance of Pro- and Anti-inflammatory Cytokines Is Associated with Sterilization. PLoS Pathogens. 2015;11(1):1–28.
26. Marino S, Gideon HP, Gong C, Mankad S, McCrone JT, Lin PL, et al. Computational and Empirical Studies Predict *Mycobacterium tuberculosis*-Specific T Cells as a Biomarker for Infection Outcome. PLoS Computational Biology. 2016;12(4).
27. Kirschner D, Pienaar E, Marino S, Linderman JJ. A review of computational and mathematical modeling contributions to our understanding of *Mycobacterium tuberculosis* within-host infection and treatment. Current Opinion in Systems Biology [Internet]. 2017;3:170–85. Available from: http://linkinghub.elsevier.com/retrieve/pii/S2452310016300117
28. Sershen CL, Plimpton SJ, May EE. Oxygen modulates the effectiveness of granuloma mediated host response to *Mycobacterium tuberculosis*: A multiscale computational biology approach. Frontiers in Cellular and Infection Microbiology. 2016;6(FEB).
29. Cicchese JM, Dartois V, Kirschner DE, Linderman JJ. Both Pharmacokinetic Variability and Granuloma Heterogeneity Impact the Ability of the First-Line Antibiotics to Sterilize Tuberculosis Granulomas [Internet]. Vol. 11, Frontiers in Pharmacology . 2020. p. 333. Available from: https://www.frontiersin.org/article/10.3389/fphar.2020.00333
30. Pienaar E, Sarathy J, Prideaux B, Dietzold J, Dartois V, Kirschner DE, et al. Comparing efficacies of moxifloxacin, levofloxacin and gatifloxacin in tuberculosis granulomas using a

multi-scale systems pharmacology approach. PLoS computational biology. 2017;13(8):e1005650.
31. Pitcher M, Bowness R, Dobson S, Eftimie R, Gillespie S. Modelling the effects of environmental heterogeneity within the lung on the tuberculosis life-cycle. Journal of Theoretical Biology [Internet]. 2019;110381. Available from: http://www.sciencedirect.com/science/article/pii/S0022519320302368
32. Català M, Bechini J, Tenesa M, Pérez R, Moya M, Vilaplana C, et al. Modelling the dynamics of tuberculosis lesions in a virtual lung: Role of the bronchial tree in endogenous reinfection. PLoS Computational Biology. 2020;16(5).
33. Wigginton JE, Kirschner D. A Model to Predict Cell-Mediated Immune Regulatory Mechanisms During Human Infection with *Mycobacterium tuberculosis*. The Journal of Immunology. 2001;166(3):1951–67.
34. Bartelink IH, Zhang N, Keizer RJ, Strydom N, Converse PJ, Dooley KE, et al. New Paradigm for Translational Modeling to Predict Long-term Tuberculosis Treatment Response. Clinical and Translational Science. 2017;10(5):366–79.
35. Wessler T, Joslyn LR, Borish HJ, Gideon HP, Flynn JL, Kirschner DE, et al. A computational model tracks whole-lung *Mycobacterium tuberculosis* infection and predicts factors that inhibit dissemination. PLOS Computational Biology [Internet]. 2020 May 20;16(5):e1007280. Available from: https://doi.org/10.1371/journal.pcbi.1007280
36. Marino S, Kirschner D. A Multi-Compartment Hybrid Computational Model Predicts Key Roles for Dendritic Cells in Tuberculosis Infection. Computation [Internet]. 2016;4(4):39. Available from: http://www.mdpi.com/2079-3197/4/4/39
37. Joslyn LR, Pienaar E, DiFazio RM, Suliman S, Kagina BM, Flynn JAL, et al. Integrating non-human primate, human, and mathematical studies to determine the influence of BCG timing on H56 vaccine outcomes. Frontiers in Microbiology. 2018;9(AUG).
38. Ganchua SKC, White AG, Klein EC, Flynn JL. Lymph nodes—The neglected battlefield in tuberculosis. PLOS Pathogens [Internet]. 2020 Aug 13;16(8):e1008632-. Available from: https://doi.org/10.1371/journal.ppat.1008632
39. Wolf AJ, Desvignes L, Linas B, Banaiee N, Tamura T, Takatsu K, et al. Initiation of the adaptive immune response to *Mycobacterium tuberculosis* depends on antigen production in the local lymph node, not the lungs. The Journal of experimental medicine [Internet]. 2007/12/24. 2008 Jan 21;205(1):105–15. Available from: https://pubmed.ncbi.nlm.nih.gov/18158321
40. Cadena AM, Fortune SM, Flynn JL. Heterogeneity in tuberculosis. Nature Reviews Immunology. 2017;17(11):691–702.
41. Segovia-Juarez JL, Ganguli S, Kirschner D. Identifying control mechanisms of granuloma formation during M. tuberculosis infection using an agent-based model. Journal of Theoretical Biology. 2004;231(3):357–76.
42. Kaufmann SHE. Tuberculosis: back on the immunologists' agenda. Immunity. 2006;24(4):351–7.
43. Moguche AO, Shafiani S, Clemons C, Larson RP, Dinh C, Higdon LE, et al. ICOS and Bcl6-dependent pathways maintain a CD4 T cell population with memory-like properties during tuberculosis. Journal of Experimental Medicine [Internet]. 2015 Apr 27;212(5):715–28. Available from: https://doi.org/10.1084/jem.20141518
44. Prezzemolo T, Guggino G, la Manna MP, di Liberto D di, Dieli F, Caccamo N. Functional signatures of human CD4 and CD8 T cell responses to *Mycobacterium tuberculosis*. Vol. 5, Frontiers in Immunology. 2014.

45. Martin MD, Badovinac VP. Defining Memory CD8 T Cell. Frontiers in Immunology [Internet]. 2018;9:2692. Available from: https://www.frontiersin.org/article/10.3389/fimmu.2018.02692
46. du Bruyn E, Ruzive S, Lindestam Arlehamn CS, Sette A, Sher A, Barber DL, et al. *Mycobacterium tuberculosis*-specific CD4 T cells expressing CD153 inversely associate with bacterial load and disease severity in human tuberculosis. Mucosal Immunology [Internet]. 2020; Available from: https://doi.org/10.1038/s41385-020-0322-6
47. Marino S, Kirschner D. A Multi-Compartment Hybrid Computational Model Predicts Key Roles for Dendritic Cells in Tuberculosis Infection. Computation [Internet]. 2016;4(4):39. Available from: http://www.mdpi.com/2079-3197/4/4/39
48. Coleman MT, Maiello P, Tomko J, Frye LJ, Fillmore D, Janssen C, et al. Early changes by 18Fluorodeoxyglucose positron emission tomography coregistered with computed tomography predict outcome after *Mycobacterium tuberculosis* infection in cynomolgus macaques. Infection and Immunity. 2014;82(6):2400–4.
49. Ganchua SKC, Cadena AM, Maiello P, Gideon HP, Myers AJ, Junecko BF, et al. Lymph nodes are sites of prolonged bacterial persistence during *Mycobacterium tuberculosis* infection in macaques. PLOS Pathogens [Internet]. 2018 Nov 1;14(11):e1007337-. Available from: https://doi.org/10.1371/journal.ppat.1007337
50. Flynn JL, Chan J, Lin PL. Macrophages and control of granulomatous inflammation in tuberculosis. Mucosal immunology [Internet]. 2011/03/23. 2011 May;4(3):271–8. Available from: https://pubmed.ncbi.nlm.nih.gov/21430653
51. Giacomini E, Iona E, Ferroni L, Miettinen M, Fattorini L, Orefici G, et al. Infection of Human Macrophages and Dendritic Cells with *Mycobacterium tuberculosis* Induces a Differential Cytokine Gene Expression That Modulates T Cell Response. The Journal of Immunology [Internet]. 2001 Jun 15;166(12):7033. Available from: http://www.jimmunol.org/content/166/12/7033.abstract
52. Marino S, Pawar S, Fuller CL, Reinhart TA, Flynn JL, Kirschner DE. Dendritic Cell Trafficking and Antigen Presentation in the Human Immune Response to *Mycobacterium tuberculosis* . The Journal of Immunology. 2004;173(1):494–506.
53. Allie N, Grivennikov SI, Keeton R, Hsu N-J, Bourigault M-L, Court N, et al. Prominent role for T cell-derived Tumour Necrosis Factor for sustained control of *Mycobacterium tuberculosis* infection. Scientific Reports [Internet]. 2013;3(1):1809. Available from: https://doi.org/10.1038/srep01809
54. Marino S, Kirschner DE. The human immune response to *Mycobacterium tuberculosis* in lung and lymph node. Journal of Theoretical Biology [Internet]. 2004;227(4):463–86. Available from: https://www.sciencedirect.com/science/article/pii/S0022519303004429
55. Sallin MA, Kauffman KD, Riou C, du Bruyn E, Foreman TW, Sakai S, et al. Host resistance to pulmonary *Mycobacterium tuberculosis* infection requires CD153 expression. Nature Microbiology [Internet]. 2018;3(11):1198–205. Available from: https://doi.org/10.1038/s41564-018-0231-6
56. Cohen SB, Urdahl KB. Going beyond gamma for TB protection. Nature Microbiology [Internet]. 2018;3(11):1194–5. Available from: https://doi.org/10.1038/s41564-018-0266-8
57. Sud D, Bigbee C, Flynn JL, Kirschner DE. Contribution of CD8+ T Cells to Control of *Mycobacterium tuberculosis* Infection. The Journal of Immunology. 2014;176(7):4296–314.

58. Woodland DL, Kohlmeier JE. Migration, maintenance and recall of memory T cells in peripheral tissues. Nature Reviews Immunology [Internet]. 2009;9(3):153–61. Available from: https://doi.org/10.1038/nri2496
59. Gong C, Linderman JJ, Kirschner D. Harnessing the heterogeneity of T cell differentiation fate to fine-tune generation of effector and memory T cells. Frontiers in Immunology. 2014;5(FEB).
60. Jacquez JA. Compartmental analysis in biology and medicine. 1972;
61. Read MN, Alden K, Timmis J, Andrews PS. Strategies for calibrating models of biology. Briefings in Bioinformatics. 2018;
62. Joslyn LR, Kirschner DE, Linderman JJ. *CaliPro*: A Calibration Protocol That Utilizes Parameter Density Estimation to Explore Parameter Space and Calibrate Complex Biological Models. Cellular and Molecular Bioengineering. 2020;
63. Cadena AM, Hopkins FF, Maiello P, Carey AF, Wong EA, Martin CJ, et al. Concurrent infection with *Mycobacterium tuberculosis* confers robust protection against secondary infection in macaques. PLoS Pathogens. 2018;14(10).
64. Darrah PA, DiFazio RM, Maiello P, Gideon HP, Myers AJ, Rodgers MA, et al. Boosting BCG with proteins or rAd5 does not enhance protection against tuberculosis in rhesus macaques. npj Vaccines. 2019;4(1).
65. Wessler T, Joslyn LR, Borish HJ, Gideon HP, Flynn JL, Kirschner DE, et al. A computational model tracks whole-lung *Mycobacterium tuberculosis* infection and predicts factors that inhibit dissemination. bioRxiv [Internet]. 2019 Jan 1;713701. Available from: http://biorxiv.org/content/early/2019/07/24/713701.abstract
66. Gideon HP, Hughes TK, Wadsworth MH, Tu AA, Gierahn TM, Hopkins FF, et al. Single-cell profiling of tuberculosis lung granulomas reveals functional lymphocyte signatures of bacterial control. bioRxiv [Internet]. 2020 Jan 1;2020.10.24.352492. Available from: http://biorxiv.org/content/early/2020/10/26/2020.10.24.352492.abstract
67. Scanga CA, Flynn JL. Modeling tuberculosis in nonhuman primates. Cold Spring Harbor Perspectives in Medicine. 2014;4(12).
68. Marino S, Hogue IB, Ray CJ, Kirschner DE. A methodology for performing global uncertainty and sensitivity analysis in systems biology. Vol. 254, Journal of Theoretical Biology. 2008. p. 178–96.
69. Saltelli A, Aleksankina K, Becker W, Fennell P, Ferretti F, Holst N, et al. Why so many published sensitivity analyses are false: A systematic review of sensitivity analysis practices. Environmental Modelling & Software [Internet]. 2019;114:29–39. Available from: https://www.sciencedirect.com/science/article/pii/S1364815218302822
70. Renardy M, Hult C, Evans S, Linderman JJ, Kirschner DE. Global sensitivity analysis of biological multiscale models. Current Opinion in Biomedical Engineering [Internet]. 2019;11:109–16. Available from: https://www.sciencedirect.com/science/article/pii/S2468451119300479
71. Benjamini Y, Hochberg Y. Controlling the false discovery rate: a practical and powerful approach to multiple testing. Journal of the Royal statistical society: series B (Methodological). 1995;57(1):289–300.
72. Cilfone NA, Ford CB, Marino S, Mattila JT, Gideon HP, Flynn JL, et al. Computational Modeling Predicts IL-10 Control of Lesion Sterilization by Balancing Early Host Immunity–Mediated Antimicrobial Responses with Caseation during *Mycobacterium tuberculosis* Infection . The Journal of Immunology. 2015;194(2):664–77.

73. Fennelly KP, Jones-López EC. Quantity and Quality of Inhaled Dose Predicts Immunopathology in Tuberculosis. Frontiers in immunology [Internet]. 2015 Jun 29;6:313. Available from: https://pubmed.ncbi.nlm.nih.gov/26175730
74. Horsburgh CR, Rubin EJ. Latent Tuberculosis Infection in the United States. New England Journal of Medicine [Internet]. 2011 Apr 13;364(15):1441–8. Available from: https://doi.org/10.1056/NEJMcp1005750
75. Koch R. The etiology of tuberculosis. Mittheilungen aus dem Kaiserlichen Gesundheitsamte. 1884;2:1–88.
76. Lenaerts A, Barry 3rd CE, Dartois V. Heterogeneity in tuberculosis pathology, microenvironments and therapeutic responses. Immunological reviews [Internet]. 2015 Mar;264(1):288–307. Available from: https://pubmed.ncbi.nlm.nih.gov/25703567
77. Subbian S, Tsenova L, Kim M-J, Wainwright HC, Visser A, Bandyopadhyay N, et al. Lesion-Specific Immune Response in Granulomas of Patients with Pulmonary Tuberculosis: A Pilot Study. PloS one [Internet]. 2015 Jul 2;10(7):e0132249–e0132249. Available from: https://pubmed.ncbi.nlm.nih.gov/26133981
78. Lieberman TD, Wilson D, Misra R, Xiong LL, Moodley P, Cohen T, et al. Genomic diversity in autopsy samples reveals within-host dissemination of HIV-associated *Mycobacterium tuberculosis*. Nature medicine [Internet]. 2016/10/31. 2016 Dec;22(12):1470–4. Available from: https://pubmed.ncbi.nlm.nih.gov/27798613
79. Maiello P, DiFazio RM, Cadena AM, Rodgers MA, Lin PL, Scanga CA, et al. Rhesus macaques are more susceptible to progressive tuberculosis than cynomolgus macaques: A quantitative comparison. Infection and Immunity. 2018;86(2).
80. Lin PL, Pawar S, Myers A, Pegu A, Fuhrman C, Reinhart TA, et al. Early events in *Mycobacterium tuberculosis* infection in cynomolgus macaques. Infection and Immunity. 2006;
81. Cicchese JM, Evans S, Hult C, Joslyn LR, Wessler T, Millar JA, et al. Dynamic balance of pro- and anti-inflammatory signals controls disease and limits pathology. Immunological Reviews. 2018;285(1):147–67.
82. Lin PL, Flynn JL. CD8 T cells and *Mycobacterium tuberculosis* infection. Seminars in Immunopathology [Internet]. 2015;37(3):239–49. Available from: http://link.springer.com/10.1007/s00281-015-0490-8
83. MacLean E, Broger T, Yerlikaya S, Fernandez-Carballo BL, Pai M, Denkinger CM. A systematic review of biomarkers to detect active tuberculosis. Nature microbiology. 2019;4(5):748–58.
84. Goletti D, Lee M, Wang J, Walter N, Ottenhoff THM. Update on tuberculosis biomarkers: from correlates of risk, to correlates of active disease and of cure from disease. Respirology. 2018;23(5):455–66.
85. Weiner 3rd J, Parida SK, Maertzdorf J, Black GF, Repsilber D, Telaar A, et al. Biomarkers of inflammation, immunosuppression and stress with active disease are revealed by metabolomic profiling of tuberculosis patients. PloS one. 2012;7(7):e40221.
86. Wallis RS, Kim P, Cole S, Hanna D, Andrade BB, Maeurer M, et al. Tuberculosis biomarkers discovery: developments, needs, and challenges. The Lancet infectious diseases. 2013;13(4):362–72.
87. Sutherland JS, Hill PC, Adetifa IM, de Jong BC, Donkor S, Joosten SA, et al. Identification of probable early-onset biomarkers for tuberculosis disease progression. PloS one. 2011;6(9):e25230.

88. Sester U, Fousse M, Dirks J, Mack U, Prasse A, Singh M, et al. Whole-blood flow-cytometric analysis of antigen-specific CD4 T-cell cytokine profiles distinguishes active tuberculosis from non-active states. PloS one. 2011;6(3):e17813.
89. Whitworth HS, Aranday-Cortes E, Lalvani A. Biomarkers of tuberculosis: a research roadmap. Biomarkers in medicine. 2013;7(3):349–62.
90. Walzl G, Ronacher K, Hanekom W, Scriba TJ, Zumla A. Immunological biomarkers of tuberculosis. Nature Reviews Immunology. 2011;11(5):343–54.
91. Rossitto S, Spagnolo P. The timing from tuberculosis infection to cavitation. Rassegna di Patologia dell'Apparato Respiratorio. 2020;35:29–37.
92. Potter EL, Gideon HP, Tkachev V, Fabozzi G, Chassiakos A, Petrovas C, et al. Measurement of leukocyte trafficking kinetics in macaques by serial intravascular staining. Science Translational Medicine [Internet]. 2021 Jan 13;13(576):eabb4582. Available from: http://stm.sciencemag.org/content/13/576/eabb4582.abstract
93. Gideon HP, Phuah J, Junecko BA, Mattila JT. Neutrophils express pro- and anti-inflammatory cytokines in granulomas from *Mycobacterium tuberculosis*-infected cynomolgus macaques. Mucosal Immunology [Internet]. 2019;12(6):1370–81. Available from: https://doi.org/10.1038/s41385-019-0195-8
94. Thacker V v, Dhar N, Sharma K, Barrile R, Karalis K, McKinney JD. A lung-on-chip model of early *Mycobacterium tuberculosis* infection reveals an essential role for alveolar epithelial cells in controlling bacterial growth. Stallings CL, Garrett WS, Shiloh MU, editors. eLife [Internet]. 2020;9:e59961. Available from: https://doi.org/10.7554/eLife.59961
95. Liu CH, Liu H, Ge B. Innate immunity in tuberculosis: host defense vs pathogen evasion. Cellular & Molecular Immunology [Internet]. 2017;14(12):963–75. Available from: https://doi.org/10.1038/cmi.2017.88
96. Kaufmann E, Sanz J, Dunn JL, Khan N, Mendonça LE, Pacis A, et al. BCG Educates Hematopoietic Stem Cells to Generate Protective Innate Immunity against Tuberculosis. Cell [Internet]. 2018;172(1):176-190.e19. Available from: https://www.sciencedirect.com/science/article/pii/S0092867417315118
97. Bickett TE, McLean J, Creissen E, Izzo L, Hagan C, Izzo AJ, et al. Characterizing the BCG Induced Macrophage and Neutrophil Mechanisms for Defense Against *Mycobacterium tuberculosis*. Frontiers in Immunology [Internet]. 2020;11:1202. Available from: https://www.frontiersin.org/article/10.3389/fimmu.2020.01202
98. Lee JY. Diagnosis and treatment of extrapulmonary tuberculosis. Tuberculosis and respiratory diseases [Internet]. 2015/04/02. 2015 Apr;78(2):47–55. Available from: https://pubmed.ncbi.nlm.nih.gov/25861336
99. Cardona P-J. The key role of exudative lesions and their encapsulation: lessons learned from the pathology of human pulmonary tuberculosis. Frontiers in microbiology [Internet]. 2015 Jun 16;6:612. Available from: https://pubmed.ncbi.nlm.nih.gov/26136741
100. Evans S, Butler JR, Mattila JT, Kirschner DE. Systems biology predicts that fibrosis in tuberculous granulomas may arise through macrophage-to-myofibroblast transformation. PLOS Computational Biology [Internet]. 2021 Dec 28;16(12):e1008520-. Available from: https://doi.org/10.1371/journal.pcbi.1008520
101. Rockwood N, du Bruyn E, Morris T, Wilkinson RJ. Assessment of treatment response in tuberculosis. Expert review of respiratory medicine [Internet]. 2016/03/31. 2016 Jun;10(6):643–54. Available from: https://pubmed.ncbi.nlm.nih.gov/27030924

6 Mediators of Concomitant Immunity in *Mycobacterium tuberculosis* Infection

6.1 Introduction

The human immune system responds extremely well to invasion and infection by most pathogens. After a first encounter (primary infection), the immune response leaves behind a memory immune response that is typically protective against a second infection event (reinfection) at a later date. It is well-documented that primary infection with some pathogens confers protection against secondary infection, even with a primary infection that is persistent (1–5). This later phenomenon, known as concomitant immunity, was first described in Stedman's medical dictionary as "infection-immunity" (6). Formally, concomitant immunity is "the paradoxical immune status in which resistance to reinfection coincides with the persistence of the original infection" (7,8).

Concomitant immunity is thought to be pathogen-dependent and thereby mediated by different immune modalities depending on infection type. For example, persistent infection with lymphocytic choriomeningitis virus (LCMV) promotes a greater accumulation of effector-like memory T cells at nonlymphoid sites (9). On the other hand, a study of infection with Leishmania major found that CD4+ regulatory T cells were key mediators of concomitant immunity during persistent infection (7) and it was recently found that if these CD4+ effector T cells are not sustained, concomitant immunity against reinfection is inadequate (10). Across multiple types of parasitic infection, separate and distinct cellular and antibody immune responses develop that are consistent with acquisition of concomitant immunity (1–5). Thus, both cellular mediators and longevity of concomitant immunity are both likely pathogen-dependent.

In tuberculosis (TB), which remains the worldwide leading cause of death by infectious agent even during the COVID-19 pandemic, it is unclear if primary infection confers enduring protection against reinfection during a persistent infection with M. tuberculosis (Mtb). The hallmark of TB, a primarily pulmonary disease, is the formation of lung granulomas: organized

immune cellular structures that surround Mtb (11). Granulomas are composed of various immune cells, including macrophages and T cells (primarily CD4+ and CD8+ T cells, although other unconventional T cell phenotypes are also present, reviewed in (12)). T cells have well-known critical functions against Mtb (13–17), but unlike other infections, T cells arrive approximately one month after primary infection (18). The delays in lymph node T-cell priming, activation, and trafficking through blood to lungs is characteristic of Mtb infection (19,20) and is thought to arise due to a lack of 'danger' signals (21) at early stages of infection during Mtb growth in the lungs (18).

Concomitant immunity against Mtb appears to provide at least limited protection against reinfection. Observational cohort studies from natural infection case studies suggest that individuals with latent TB had a 35 - 80% lower risk of progression to active TB after reinfection compared to uninfected individuals (22–26). Further, other studies in mice suggest that concomitant immunity is not fully protective against secondary infection with Mtb, but that bacterial burden from a secondary infection is reduced when compared to primary infection (27,28). Recently, Cadena et al. showed that in non-human primates (NHP) concomitant immunity was robust against a secondary infection with Mtb (29). However, due to the inherent constraints of NHP studies, Cadena et al. were only able to show reduction of bacterial burden at a single time point, and therefore were unable to test mechanisms driving concomitant immunity or predict the potential longevity of a concomitant immune response in TB. Based on the observation that Mtb-specific T cells resided in uninvolved lung tissue prior to reinfection, Cadena et al. did hypothesize that resident memory T cells prevent the establishment of reinfection.

Resident memory T cells (TRM) are a relatively newfound cell that may drive concomitant immunity in TB. The defining feature of TRMs is their permanent residence within nonlymphoid tissues and inability to circulate through the blood stream and lymphatics (30). These cells act as a sentinel against future infection and have been shown to be protective against various infectious diseases, including influenza, herpes simplex virus, and human immunodeficiency virus (reviewed in (30)). Further, skin TRM cells have been shown to provide concomitant immunity in the case of cutaneous leishmaniasis (31). Relatively few

studies have examined TRMs in the context of TB (32). However, mucosal administration of the BCG vaccine in mice, as well as adoptive transfer of CD8+ TRMs in mice, have demonstrated enhanced protection against Mtb, presumably through the ability of CD8+ TRM to respond quickly following infection (33). TRMs develop during the adaptive immune response to primary infection in TB and may play a role in concomitant immunity as they have been identified within uninvolved lung tissue of infected hosts (29). However, experimental studies have so far been unable to identify their exact role in concomitant immunity against Mtb. Further, the longevity of this cell population in the lung has not been well-characterized in NHPs or humans.

As a complementary approach, mathematical and computational modeling can predict the mechanism and timing of major immune events beyond the timeline of experimental studies. In TB, modeling has been used to explore various aspects of granuloma formation (34,35), drug-dynamics (36,37), and immune cell and cytokine dynamics within lung granulomas (34,38–40). The advantages of a modeling approach are well-suited to answer outstanding questions about reinfection and the potential longevity of TRM cell populations in the human lung.

To investigate questions surrounding concomitant immunity during Mtb infection, we utilize *HostSim*, our whole-host modeling framework that captures key elements of TB pathology across lungs, lymph nodes and blood in infected individuals. We have previously calibrated and validated the model using multiple datasets derived from published NHP studies and have shown the ability of this model to capture heterogeneous host-scale clinical outcomes such as infection clearance, control (LTBI) or active disease (Chapter 5). We now use the *HostSim* framework to address three outstanding questions about concomitant immunity in TB: Do TRMs mediate concomitant immunity in Mtb? Can we predict if and when concomitant immunity will wane in Mtb infection? Further, can we predict the lifespan of TRMs in human lung tissue?

6.2 Methods

6.2.1 Including resident memory T cells to the *HostSim* modeling framework

In Chapter 5, we present *HostSim*, a whole host modeling framework of Mtb infection. Briefly, *HostSim* tracks the development of multiple lung granulomas, as well as immune cell trafficking to the lymph node and from the blood. Within each lung granuloma, we capture the dynamics of

various immune cells across time, including macrophages and T cells, as well as pro-inflammatory and anti-inflammatory cytokines. Within the lymph node and blood, we track Mtb-specific T-cell priming, proliferation, differentiation and migration to forming lung granulomas. Chapter 5 includes full model details as well as calibration of this model to primary infection dynamics. Additionally, it shows how we delineate TB clinical outcomes across a virtual host population. Briefly, we identify TB eliminators, whose total lung CFU<1, active TB cases, whose total lung CFU >10^5, and LTBI, all other virtual hosts. Figure E.1 displays the breakdown of each clinical classification following primary infection, wherein across 500 virtual hosts, 110 are classified as active TB cases, 366 are classified as LTBI cases, and 24 are classified as TB eliminators.

6.2.2 Resident memory T cell (TRM) lifespan in the lungs

The lifespan of lung TRM in humans is largely unknown, but there is evidence that TRM populations are not as stable in the lung environment as they are in the skin or other locations (41,42). Further, one study estimated lung TRM persistence in mice (43). Morris et al used an exponential decay function to model the longevity of TRM populations across time and assumed no influx to the lung TRM population:

$$T_{RM} = T_{RM}(0)e^{d_{TRM}t}$$

where d_{TRM} is the death rate of TRM. By calibrating to mice lung TRM datasets, Morris et al. determined d_{TRM} = 0.03 cells/day, or a lifespan of about 33 days (where lifespan is calculated as $1/d_{TRM}$). As they note, human lung TRMs are less well-studied, primarily due to inability to sample healthy lung tissue. In our parallel virtual host reinfection studies (see below), we utilize this TRM longevity function to inform the initial conditions of TRMs (Figure 1). Additionally, we explore the death rate value to predict lifespan of these cell types in primates.

6.2.3 Simulating TRM during reinfection

In this chapter, we use *HostSim* to explore reinfection at various timepoints. We expanded the set of granuloma ordinary differential equations in *HostSim* to include an equation for TRMs to be present during reinfection scenarios (Figure 6.1) since TRMs have been hypothesized to play a role in preventing the establishment of reinfection with Mtb (29).

We have two key assumptions about the roles of TRMs during reinfection. First, TRMs have been shown to kill pathogens upon re-encounter very quickly, presumably by rapidly activating macrophages to kill their intracellular bacteria (29,30,33). Therefore, we assume that TRMs in *HostSim* assist macrophages in killing intracellular bacteria at a rate proportional to bacteria, macrophage, and TRM counts within the granuloma (see supplement for full intercellular Mtb equation).

Second, Mtb specific TRMs have been identified in uninvolved lung tissue during primary infection (29). Thus, we assume TRMs would be present at very early stages prior to granuloma formation upon reinfection. To identify how many TRMs might be present, we matched the reinfection CFU dynamics from the NHP study at the reinfection timepoint (day 112) and use 1 to 10 TRM as initial conditions (see Figure 6.3). However, when we perform the parallel virtual reinfection studies (see below), we change the initial condition of the TRM population to reflect the lifespan of this cell population (see TRM lifespan section above).

Reinfection studies within *HostSim* involve re-inoculating our virtual hosts with 10 CFU at the reinfection timepoint which seeds 10 unique new granulomas within the lung environment (Figure 6.1). Each reinfection granuloma begins with one intracellular bacterium, one infected macrophage and between 1 and 10 TRM as initial conditions.

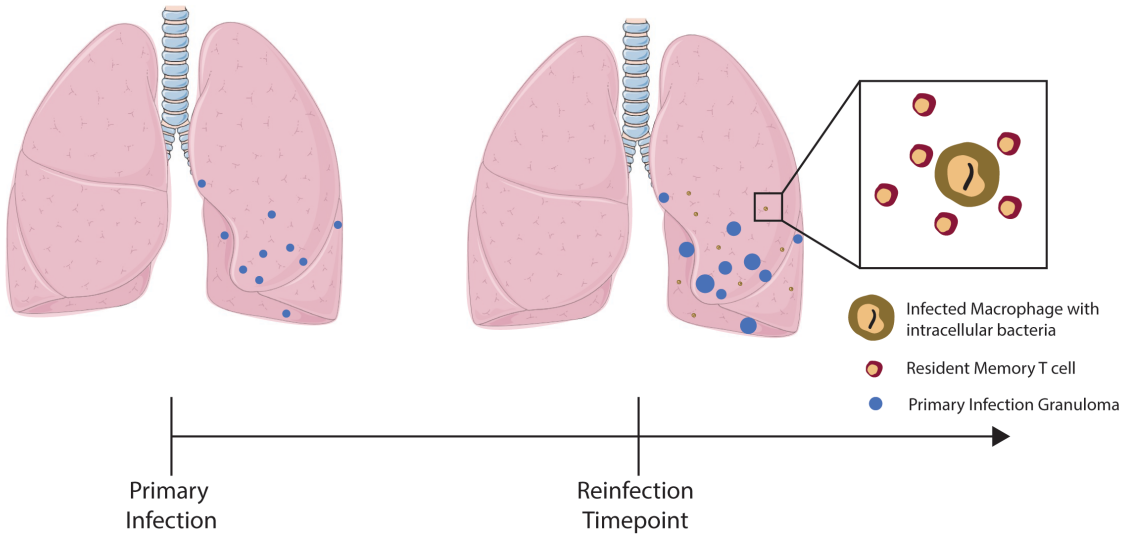

Figure 6.1 Resident memory T cells impact establishment of reinfection.
Primary infection begins with the inoculation of 10 CFU. At the reinfection timepoint, which varies from study to study, virtual hosts are re-inoculated with 10 CFU. TRMs may or may not be present during reinfection depending on the TRM lifespan and the reinfection timepoint.

6.2.4 Parallel virtual host reinfection studies

In order to predict the lifespan of TRMs in the lung, we perform several parallel virtual host studies. Figure 6.2 demonstrates the experimental protocol for three sets of 21 reinfection studies. Each reinfection study consists of the same 500 individual *HostSim* simulations run for 500 virtual hosts over approximately a 7-year timeframe (2,500 total days) differing only in the time of reinfection. Study 1 begins with a reinfection timepoint at day 112 (the reinfection timepoint used in the NHP dataset from Cadena et al. (29)) and each subsequent study has a reinfection time point occurring 100 days after the previous study.

The 21 reinfection studies are each simulated three times, varying the death rate of TRMs between each set. The first death rate, 0.03 cells/day, is the predicted death rate of TRM in mice from Morris et al (43). The second, 0.0012 cells/day, was calculated based on allometric scaling, as humans live ~25x longer than mice (44). The third death rate selected was 0.0001 cells/day, a rate similar to that observed for central memory T cell populations, which are known to persist for decades (45).

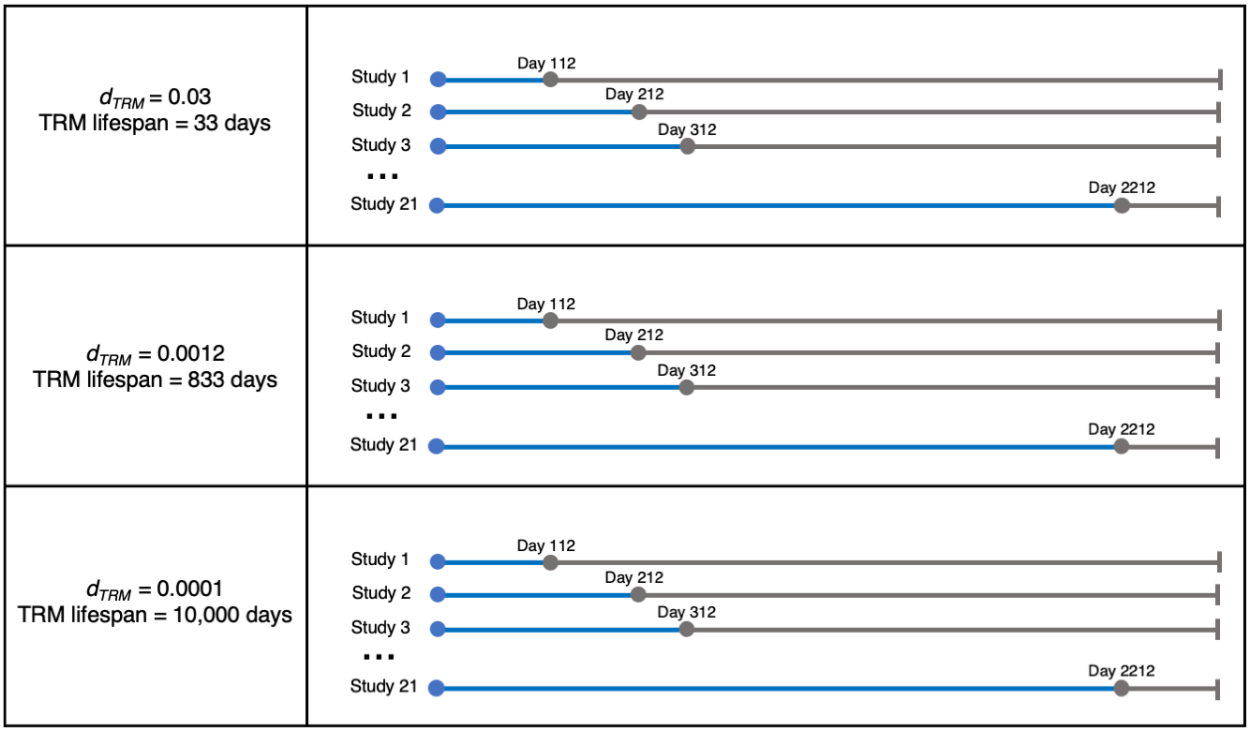

Figure 6.2 Parallel virtual host reinfection study protocol.
The experimental protocol for our *HostSim* reinfection studies. We performed 3 sets of 21 separate reinfection studies on 500 virtual hosts, where the only difference between studies was timing of Mtb reinfection with a low dose of 10 CFU. Reinfection time points shown as gray dots on the timeline. We assigned a different death rate of TRM (d_{TRM}) for each of 3 sets of reinfection studies. In total, we perform 63 reinfection studies where the same 500 hosts are simulated for 2500 days (approx. 7 years).

6.2.5 Calculating the reduced risk of active TB following reinfection compared to primary infection

Studies from the pre-antibiotic era of TB tracked the percentage of nursing students that contracted active TB disease (22). Upon entering nursing school, students were stratified into two groups: those that had a positive Tuberculin Skin Test (TST), indicating previous exposure to Mtb, and those that had a negative TST, indicating no previous exposure to Mtb. A meta-analysis of these studies showed that individuals with a TST+ upon entering nursing school were at a 79% reduced risk of developing active TB compared to TST- individuals (22). Assuming that all nurses had similar exposure to infectious TB patients, these studies are strong evidence of a protective concomitant immune response against reinfection. Figure E.2 shows the data from these studies – note that studies with a longer period of observation (closer to 5 years) saw greater percentages of active TB cases among the TST+ population compared to those where students were observed for two years or less. Although this association is not statistically

significant, the greater percentage of active TB cases during longer studies suggests a potentially waning protection from concomitant immunity.

Using *HostSim*, we can estimate the reduced risk of developing active TB from reinfection for virtual hosts. We do this by simulating a virtual population of hosts and comparing 1) the fraction of virtual hosts which develop active TB from primary infection and 2) the fraction of virtual hosts which develop active TB from reinfection. These two fractions are analogous to the TST- and TST+ groups in the meta-analysis of nursing students, respectively (22). We previously determined this first fraction in Chapter 5 (see Figure E.1) where we showed 110 out of a virtual population 500 hosts will develop active TB (total lung CFU>10^5 at day 200 post-infection). We determine the second fraction during our reinfection studies by counting the number of hosts that have a total lung CFU > 10^5 at 200 days after reinfection. As an example, if 50 out of 500 virtual hosts develop active TB after reinfection, the risk reduction calculation would be as follows:

$$\frac{observed - expected}{expected} = \frac{\substack{fraction\ of\ active\ hosts \\ following\ reinfection} - \substack{fraction\ of\ active\ hosts \\ following\ primary\ infection}}{\substack{fraction\ of\ active\ hosts \\ following\ primary\ infection}} = \frac{\frac{50}{500} - \frac{110}{500}}{\frac{110}{500}}$$

resulting in a 54.5% reduced risk of developing active TB.

6.2.6 Model environment and analysis

Model code and preliminary data analysis is written in MATLAB (R2020b). ODEs are solved using MATLAB's ode15s stiff solver. Simulation for a single *in silico* individual across 200 days post-infection can be performed on an 8-core laptop in approximately 30 seconds. Bash scripts were written for submission to run on Great Lakes HPC Cluster at the University of Michigan for parallel virtual host reinfection studies. Post-processing statistical analysis and graphing was performed in MATLAB (R2020b).

6.3 Results

6.3.1 *HostSim* recapitulates *in vivo* granuloma and host-scale dynamics of reinfection

In NHPs, ongoing primary infection with Mtb confers protection against reinfection. This previously published dataset includes 8 NHPs that received a primary inoculation of barcoded Mtb and a secondary inoculation of separately barcoded Mtb 16 weeks later (29). Four weeks after the secondary inoculation, the animals were necropsied and granuloma bacterial loads from

both primary and secondary inoculation events were obtained. We performed 50 *HostSim* simulations following the same experimental protocol, for comparison to the *in vivo* granuloma CFU from primary infection and reinfection (Figure 6.3A).

Concurrent Mtb infection within *HostSim* limits the establishment of reinfection granulomas, matching what was observed in NHPs (29). We predict the vast majority of reinfection granulomas do not contain CFU at 28 days post-infection using *HostSim* (Figure 6.3D black data points). For 33 out of the 50 virtual hosts, reinfection was not established, as these hosts had total sterilization of all reinfection granulomas prior to day 28. This is consistent with the NHP study, that showed 5 of 8 monkeys had total sterilization of reinfection granulomas at this time point. If we rerun the 50 virtual hosts but knock-out TRM, we no longer match the NHP dataset. Intriguingly, reinfection granulomas in the knockout study still contained significantly less bacterial burden than primary infection granulomas (Figure 6.3D red data points). This suggests that while TRMs are the main drivers of a concomitant immune response, other immune cells may also impact the growth of bacteria within reinfection granulomas.

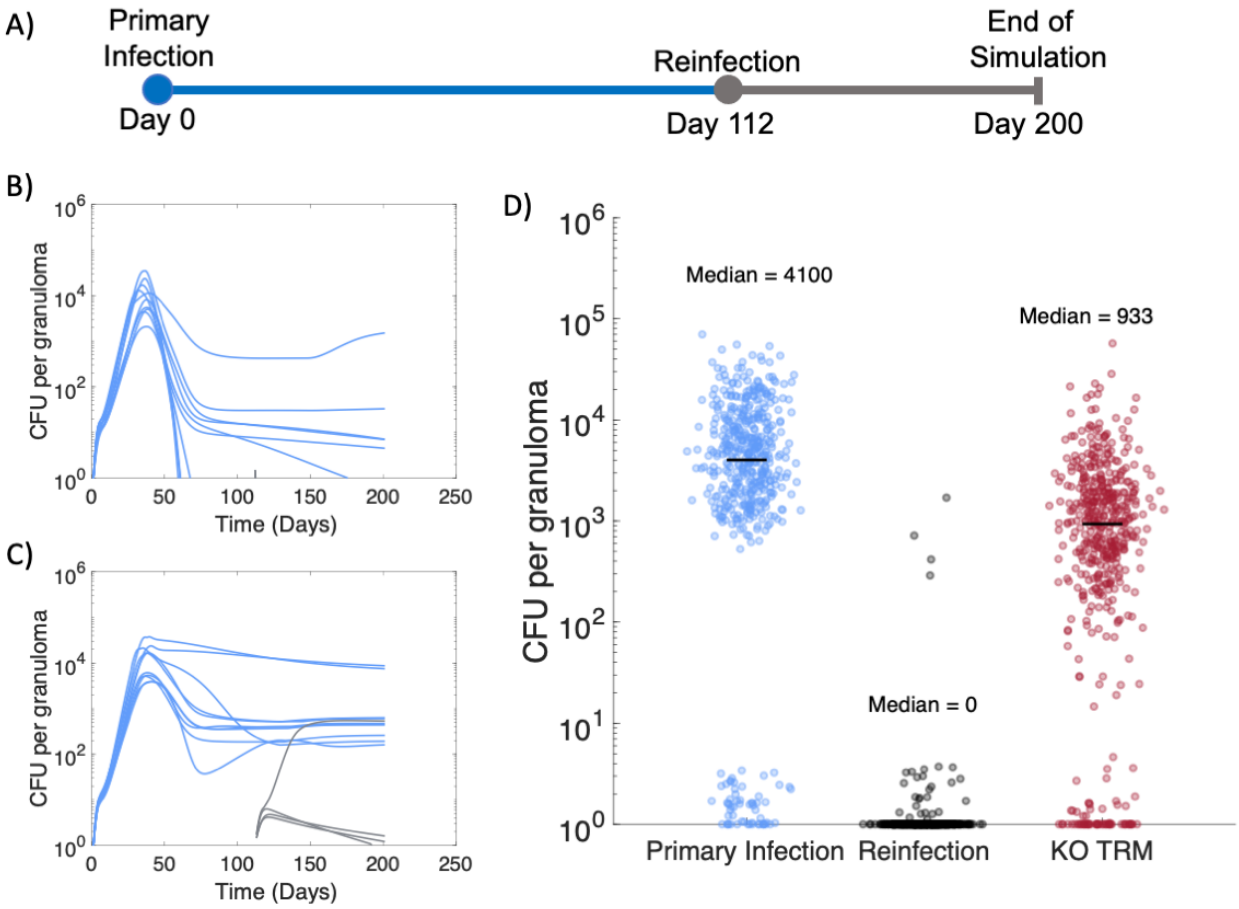

Figure 6.3 Reinfection in 50 virtual hosts matches dynamics of reinfection in NHPs.
(A) Experimental protocol for reinfection study. Primary infection (blue) with 10 CFU inoculum occurred at day 0 and reinfection (gray) with 10 CFU inoculum, matching the NHP study protocol (29). Granuloma CFU trajectories from two representative hosts shown in panel (B) & (C). (D) Across 50 virtual hosts, reinfection granulomas exhibit greater sterilization compared to primary infection granulomas 28 days post-infection, as previously shown in NHPs (29). We re-simulated the same 50 hosts but knocked-out the TRM cell population at reinfection (red data points). CFU per granuloma between KO TRM virtual hosts and the primary infection granuloma CFU was significantly different (Vargha and Delaney's A measure = 0.76).

6.3.2 Predicting the lifespan of TRMs and durability of concomitant immunity

While concomitant immunity is protective against reinfection at 112 days in NHPs, the durability of the concomitant immune response across time is not yet known (29). However, prospective cohort studies from the pre-antibiotic era of TB treatment predict that LTBI individuals had a 79% reduced risk of developing active TB following reinfection compared to uninfected individuals (22). These studies were observational, and it was not possible to determine the exact time point of reinfection. However, these studies provide an opportunity for a case study: we can use *HostSim* to predict the death rate of lung TRM – the main cellular mediators of concomitant immunity, as shown by *in silico* knock-out in Figure 6.3D.

We performed three sets of virtual reinfection studies using 500 virtual hosts (see Methods) to predict the death rates of lung TRM and measure the longevity of concomitant immunity in *HostSim*. Figure 6.2 shows the experimental protocols for the three sets of virtual reinfection studies. We alter the death rate of lung TRMs between the three sets of reinfection studies (See Methods).

In Figure 6.4, we display the breakdown of active TB (dark blue), LTBI (green) and TB eliminator (yellow) cases (as defined by the total lung bacterial burden [Figure E.1]) at day 200 post-reinfection for the 500 hosts across the 21 reinfection studies. When the lifespan of TRMs is set to previous estimates from Morris et al. in mice (d_{TRM} =0.03 cells/day) (43), concomitant immunity wanes quickly (Figure 6.4 A & D); by reinfection study 2 (reinfection 212 days after primary infection), there is a total loss of concomitant immunity against reinfection. In contrast, if the lifespan of TRM lasts for decades (d_{TRM} =0.0001 cells/day; Figure 6.4 C & F), then all of the hosts sterilize or control reinfection. Both of these TRM lifespans result in predictions inconsistent with the human cohort studies. Only when the lifespan of TRMs is ~25x longer than originally estimated by Morris et al. (d_{TRM} =0.0012 cells/day, calculated based on allometric scaling), does the reduced risk of active TB match that of the human cohort studies (Figure 6.4 B & E). Across the 21 reinfection studies in Figure 6.4 B, the average reduced risk of active TB is 77% following reinfection compared to uninfected virtual hosts. This is a prediction that is consistent with reduced risk estimates in humans. Thus, we predict that the lifespan of TRMs is approximately 2-3 years.

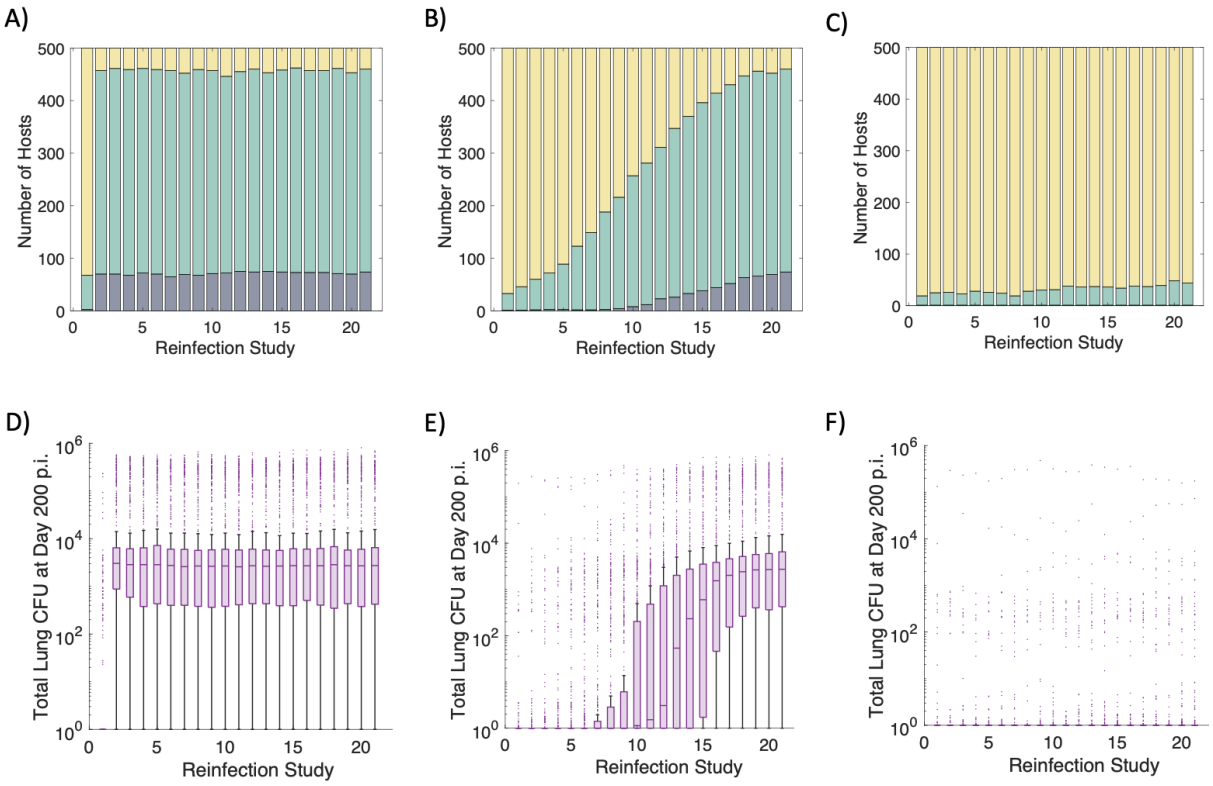

Figure 6.4 Clinical classifications and total lung CFU across three sets of virtual reinfection studies.
Clinical classifications for 500 virtual hosts across 21 separate reinfection studies when the lifespan of TRMs is varied from 33 days, 833 days, or 10,000 days (d_{TRM} = 0.03, 0.0012, or 0.0001 cells/day) (A, B, C, respectively). Each stacked bar chart shows the number of active TB (dark blue), LTBI (green) or TB eliminator (yellow) hosts for each reinfection study. Clinical classifications are determined according to total lung CFU 200 days after reinfection. Box-and-whisker plots show the distribution of total lung CFU across the 500 virtual hosts for each reinfection study when d_{TRM} = 0.03, 0.0012, or 0.0001 cells/day (D, E, F, respectively).

6.3.3 In the absence of TRMs, T-cell counts in the blood delineate active vs latent outcomes following reinfection

We have shown that concomitant immunity is intrinsically associated to TRM lifespan across time. Intriguingly, at reinfection timepoints after the majority of TRM cells have died, we still note an average reduction of 35% in active TB from reinfection compared to uninfected controls (Figure 4A, reinfection studies 2-21). We use this situation as a case study to identify mechanisms driving active and LTBI classification host outcomes during reinfection events that may occur after waning of TRMs populations.

In Figure 6.5, we focus on the first set of reinfection studies, when the life span of TRMs is 33 days (d_{TRM} = 0.03 cells/day), although results are consistent across sets of reinfection studies

(Figure E.3). In this set of reinfection studies, the TRM population is no longer present by a reinfection time point 212 days after primary infection (Figure 6.5A). For reinfection studies 2-21, we observed many virtual hosts still control infection, and are only classified as LTBI, even without the presence of TRM populations in the lung (Figure 6.4A). Further, we observed that virtual hosts who control reinfection (classified as LTBI) had higher counts of Mtb-specific effector (Figure 6.5B), effector memory (Figure 6.5C), and central memory (Figure 6.5D) T cells in the blood one day prior to reinfection compared to hosts that went on to develop active TB after reinfection. Thus, we predict that the numbers of Mtb-specific T cells in the blood prior to reinfection is a key factor for protection against active TB following reinfection in the absence of TRMs.

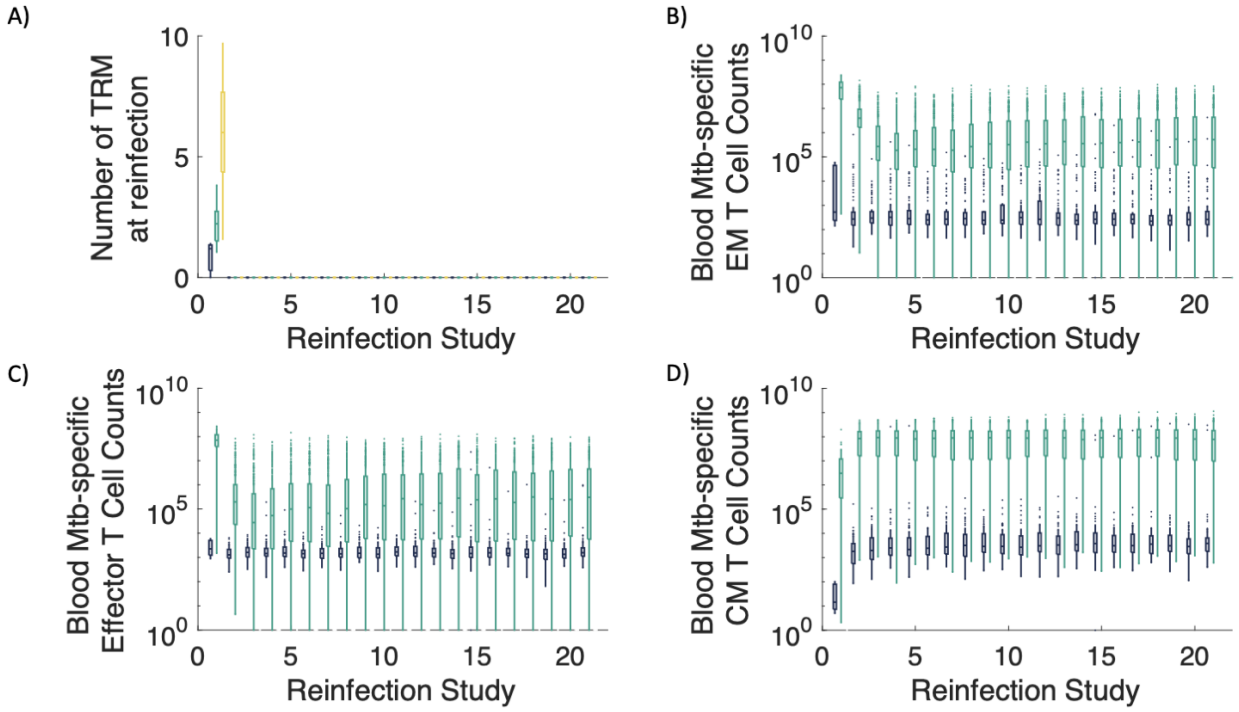

Figure 6.5 Mtb-specific T cells in blood from primary infection offer protection against active TB during reinfection in absence of TRM populations.
In our first set of reinfection studies, we set the lifespan of TRMs to be 33 days (d_{TRM} = 0.03 cells/day). (A) Accordingly, all TRM populations have died by day 212, the reinfection time point of reinfection study 2. Box-and-whisker plots show the distribution of Mtb-specific effector memory (EM), effector, and central memory (CM) T cell counts in the blood one day prior to the timepoint of reinfection for each reinfection study (B, C, D, respectively). We stratify the T-cell numbers according to a host's total lung CFU at a time point 200 days later. If the host was classified as an active TB case (total lung CFU>10^5), the box and whisker plot is dark blue. If the host was classified as an LTBI case (total lung CFU<10^5), the box and whisker plot is green. Note that the vast majority of LTBI hosts have larger numbers of Mtb-specific blood effector, effector memory and central memory T cells than that of their active TB case counterparts.

6.4 Discussion

Concomitant immunity is a special case of immune memory that is generated when a host is infected by the same pathogen while they are current fighting a primary infection by the same pathogen. Concomitant immunity does not provide a robust and enduring immune response against reinfection for all persistent pathogens (46). For example, during chronic HIV infection, reinfection has been shown to clinically arise as quickly as before one-year after primary infection (47). If a concomitant immune response is observed, then cellular-mediators and longevity of immunity appear to be pathogen-dependent, ranging from memory T cell mediated immunity in chronic LCMV to extremely short-lived immunity in parasitic infection (48,49). In TB, concomitant immunity against reinfection appears protective initially, but the longevity and cellular mediators of such a response are not yet known.

To address these uncertainties, we utilize *HostSim*, our novel mathematical and computational modeling tool that allows us to more directly investigate the cellular mechanisms that lead to concomitant immunity by relating events and dynamics within each host to population scale outcomes. A significant benefit of this *in silico* approach is that the group of 500 virtual individual *HostSim* simulations is identical across reinfection studies. Therefore, we can directly compare each reinfection study against the others. This allows us to build on the studies begun in NHP (29) and perform simulated studies impossible to do with *in vivo* experiments – even performing two separate reinfection experiments on different NHPs would require a large financial and resource commitment, and since NHPs are outbred animals there is substantial host-to-host variation that might complicate comparisons between reinfection studies.

Our predictions add support to growing evidence that primary Mtb infection does provide a concomitant immune response (29), but our studies predict that this protection is transient, waning ~3 years after primary infection, with a substantial loss of protection by 5 years post-infection (Figure 4B). Further, we predict that longevity of concomitant immunity against Mtb is intrinsically tied to the magnitude of numbers of TRM cells generated, as our studies indicate that these cells are key mediators of protection against reinfection.

As key players against reinfection, TRMs offer intriguing targets for vaccination. In fact, intravenously administered BCG was recently shown to provide a pool of lung resident memory T cells that exhibited protection against infection with Mtb in NHPs (50). The longevity of these cells has implications for vaccine design. In humans, the longevity of TRMs in the lungs is not yet known. In this work, we predict that in the context of an ongoing, persistent infection the lifespan ($1/d_{TRM}$) of TRMs in the lungs is 833 days, or approximately two years. To our knowledge, this is the first estimate of TRM lifespan human lungs.

Our findings suggest that if immunity can only be achieved through an antigen-specific TRM cell population, then a successful vaccine must extend the durability and longevity of this cell population, thereby toggling the properties of T cell memory across time. Preclinical trial results of a viral vector-based vaccine in TB suggests that this vaccine platform might provide the necessary antigen persistence for continuous stimulation toward a protective memory T cell pool across time (51). However, vaccine protection studies in NHPs have yet to be completed where the timing of infection was >1 year after vaccination (51).

In the absence of TRM populations, we still note limited protection against reinfection (Figure 3D and Figure 5). In our first set of reinfection studies, the average reduction of risk of developing active TB was 35% for reinfection studies 2-21 (the studies that included a reinfection timepoint after the loss of all lung TRMs). This percentage is consistent with estimates of protection from reinfection in a household contact study in Peru, that showed 3-35% protection against reinfection across an average interval of 3.5 years (26). Our works suggests that in lieu of TRMs, there are other mechanisms within the body to prevent uncontrolled reinfection and perhaps this is reflected in the study of Peruvian individuals. We posit that in order for individuals to develop active TB following reinfection, it requires a sufficiently poor adaptive immune response; wherein the magnitude of both TRMs and blood Mtb-specific T cells must be deficient.

In this study, we could not model every cell type present in both primary infection and reinfection granulomas. For example, unrestricted or unconventional T cells have not been considered in this work but could very well impact reinfection granuloma environments and have

important implications for vaccination (12). Therefore, these cell types (as well as others) could be considered in future work. Additionally, while natural TB case studies have shown protection against reinfection (22,25,26), patients who successfully complete TB drug treatment are at an increased risk of developing TB upon reinfection, with an incidence rate four times that of primary infection (48,49). We do not capture this population in the current study, although current work in our group is incorporating drug treatment into *HostSim* and could further investigate this phenomenon. Finally, we selected three values for d_{TRM} based on previous estimates and our hypotheses of lung TRM longevity, although many other death rates could have been tested through an optimization process using a surrogate model, as has been previously done by our group (52). In the current work, we used a virtual host framework of Mtb infection and reinfection and predict that concomitant immunity protects and wanes in accordance with the magnitude of TRM populations across time. However, even in the absence of TRM populations, the majority of hosts are able to control reinfection through blood Mtb-specific cells that were generated during primary infection.

6.5 References

1. Buck JC, de Leo GA, Sokolow SH. Concomitant Immunity and Worm Senescence May Drive Schistosomiasis Epidemiological Patterns: An Eco-Evolutionary Perspective. Frontiers in Immunology. 2020;11.
2. Miller HM, Gardiner ML. Passive immunity to infection with a larval tapeworm of the albino rat. Science. 1932;75(1940):270.
3. Mitchell GF. A Note on Concomitant Immunity in Host-Parasite Relationships: A Successfully Transplanted Concept from Tumor Immunology. Advances in Cancer Research. 1990;54(C):319–32.
4. Lightowlers MW. Fact or hypothesis: Concomitant immunity in taeniid cestode infections. Vol. 32, Parasite Immunology. 2010. p. 582–9.
5. MacDonald AJ, Turaga PSD, Harmon-Brown C, Tierney TJ, Bennett KE, McCarthy MC, et al. Differential cytokine and antibody responses to adult and larval stages of Onchocerca volvulus consistent with the development of concomitant immunity. Infection and Immunity. 2002;70(6):2796–804.
6. Stedman TL, editor. Stedman's medical dictionary for the health professions and nursing. Lippincott Williams & Wilkins; 2005.
7. Belkaid Y, Piccirillo CA, Mendez S, Shevach EM, Sacks DL. CD4+CD25+ regulatory T cells control Leishmania major persistence and immunity. Nature. 2002;420(6915):502–7.
8. Belkaid Y, Tamoutounour S. The influence of skin microorganisms on cutaneous immunity. Vol. 16, Nature Reviews Immunology. 2016. p. 353–66.
9. Beura LK, Anderson KG, Schenkel JM, Locquiao JJ, Fraser KA, Vezys V, et al. Lymphocytic choriomeningitis virus persistence promotes effector-like memory differentiation and enhances mucosal T cell distribution. Journal of leukocyte biology [Internet]. 2014/11/13. 2015 Feb;97(2):217–25. Available from: https://pubmed.ncbi.nlm.nih.gov/25395301
10. Peters NC, Pagán AJ, Lawyer PG, Hand TW, Henrique Roma E, Stamper LW, et al. Chronic Parasitic Infection Maintains High Frequencies of Short-Lived Ly6C+CD4+ Effector T Cells That Are Required for Protection against Re-infection. PLoS Pathogens. 2014;10(12).
11. Flynn JL, Gideon HP, Mattila JT, Lin P ling. Immunology studies in non-human primate models of tuberculosis. Immunological Reviews. 2015;264(1):60–73.
12. Joosten SA, Ottenhoff THM, Lewinsohn DM, Hoft DF, Moody DB, Seshadri C, et al. Harnessing donor unrestricted T-cells for new vaccines against tuberculosis. Vaccine [Internet]. 2019/04/27. 2019 May 21;37(23):3022–30. Available from: https://pubmed.ncbi.nlm.nih.gov/31040086
13. Mattila JT, Diedrich CR, Lin PL, Phuah J, Flynn JL. Simian Immunodeficiency Virus-Induced Changes in T Cell Cytokine Responses in Cynomolgus Macaques with Latent *Mycobacterium tuberculosis* Infection Are Associated with Timing of Reactivation . The Journal of Immunology. 2011;186(6):3527–37.
14. Diedrich CR, Mattila JT, Klein E, Janssen C, Phuah J, Sturgeon TJ, et al. Reactivation of latent tuberculosis in cynomolgus macaques infected with SIV is associated with early peripheral T cell depletion and not virus load. PLoS ONE. 2010;5(3).
15. Yao S, Huang D, Chen CY, Halliday L, Wang RC, Chen ZW. CD4 + T Cells Contain Early Extrapulmonary Tuberculosis (TB) Dissemination and Rapid TB Progression and Sustain Multieffector Functions of CD8 + T and CD3 − Lymphocytes: Mechanisms of CD4 + T Cell Immunity . The Journal of Immunology. 2014;192(5):2120–32.

16. Gideon HP, Phuah JY, Myers AJ, Bryson BD, Rodgers MA, Coleman MT, et al. Variability in Tuberculosis Granuloma T Cell Responses Exists, but a Balance of Pro- and Anti-inflammatory Cytokines Is Associated with Sterilization. PLoS Pathogens. 2015;11(1):1–28.
17. Chen CY, Huang D, Wang RC, Shen L, Zeng G, Yao S, et al. A critical role for CD8 T cells in a nonhuman primate model of tuberculosis. PLoS Pathogens. 2009;5(4).
18. Cadena AM, Flynn JL, Fortune SM. The importance of first impressions: Early events in *Mycobacterium tuberculosis* infection influence outcome. Vol. 7, mBio. 2016.
19. Reiley WW, Calayag MD, Wittmer ST, Huntington JL, Pearl JE, Fountain JJ, et al. ESAT-6-specific CD4 T cell responses to aerosol *Mycobacterium tuberculosis* infection are initiated in the mediastinal lymph nodes. Proceedings of the National Academy of Sciences of the United States of America. 2008;105(31):10961–6.
20. Gallegos AM, Pamer EG, Glickman MS. Delayed protection by ESAT-6-specific effector CD4+ T cells after airborne M. tuberculosis infection. Journal of Experimental Medicine. 2008;205(10):2359–68.
21. Matzinger P. The evolution of the danger theory. Interview by Lauren Constable, Commissioning Editor. Expert review of clinical immunology [Internet]. 2012 May;8(4):311–7. Available from: https://pubmed.ncbi.nlm.nih.gov/22607177
22. Andrews JR, Noubary F, Walensky RP, Cerda R, Losina E, Horsburgh CR. Risk of progression to active tuberculosis following reinfection with *Mycobacterium tuberculosis*. Clinical Infectious Diseases. 2012;54(6):784–91.
23. Clark M, Vynnycky E. The use of maximum likelihood methods to estimate the risk of tuberculous infection and disease in a Canadian First Nations population. International Journal of Epidemiology. 2004;33(3):477–84.
24. Vynnycky E, Fine PEM. The natural history of tuberculosis: The implications of age-dependent risks of disease and the role of reinfection. Epidemiology and Infection. 1997;119(2):183–201.
25. Sutherland I, Švandová E, Radhakrishna S. The development of clinical tuberculosis following infection with tubercle bacilli. 1. A theoretical model for the development of clinical tuberculosis following infection, linking from data on the risk of tuberculous infection and the incidence of clinic. Tubercle. 1982;63(4):255–68.
26. Brooks-Pollock E, Becerra MC, Goldstein E, Cohen T, Murray MB. Epidemiologic inference from the distribution of tuberculosis cases in households in Lima, Peru. Journal of Infectious Diseases. 2011;203(11):1582–9.
27. Henao-Tamayo M, Obregón-Henao A, Ordway DJ, Shang S, Duncan CG, Orme IM. A mouse model of tuberculosis reinfection. Tuberculosis. 2012;92(3):211–7.
28. Repique CJ, Li A, Collins FM, Morris SL. DNA immunization in a mouse model of latent tuberculosis: Effect of DNA vaccination on reactivation of disease and on reinfection with a secondary challenge. Infection and Immunity. 2002;70(7):3318–23.
29. Cadena AM, Hopkins FF, Maiello P, Carey AF, Wong EA, Martin CJ, et al. Concurrent infection with *Mycobacterium tuberculosis* confers robust protection against secondary infection in macaques. PLoS Pathogens. 2018;14(10).
30. Sasson SC, Gordon CL, Christo SN, Klenerman P, Mackay LK. Local heroes or villains: tissue-resident memory T cells in human health and disease. Cellular & Molecular Immunology [Internet]. 2020;17(2):113–22. Available from: https://doi.org/10.1038/s41423-019-0359-1

31. Scott P. Long-Lived Skin-Resident Memory T Cells Contribute to Concomitant Immunity in Cutaneous Leishmaniasis. Cold Spring Harbor Perspectives in Biology. 2020;12(10):a038059.
32. Ogongo P, Porterfield JZ, Leslie A. Lung Tissue Resident Memory T-Cells in the Immune Response to *Mycobacterium tuberculosis*. Frontiers in immunology [Internet]. 2019 May 3;10:992. Available from: https://pubmed.ncbi.nlm.nih.gov/31130965
33. Muruganandah V, Sathkumara HD, Navarro S, Kupz A. A Systematic Review: The Role of Resident Memory T Cells in Infectious Diseases and Their Relevance for Vaccine Development. Frontiers in immunology [Internet]. 2018 Jul 9;9:1574. Available from: https://pubmed.ncbi.nlm.nih.gov/30038624
34. Kirschner D, Pienaar E, Marino S, Linderman JJ. A review of computational and mathematical modeling contributions to our understanding of *Mycobacterium tuberculosis* within-host infection and treatment. Current Opinion in Systems Biology [Internet]. 2017;3:170–85. Available from: http://linkinghub.elsevier.com/retrieve/pii/S2452310016300117
35. Sershen CL, Plimpton SJ, May EE. Oxygen modulates the effectiveness of granuloma mediated host response to *Mycobacterium tuberculosis*: A multiscale computational biology approach. Frontiers in Cellular and Infection Microbiology. 2016;6(FEB).
36. Cicchese JM, Dartois V, Kirschner DE, Linderman JJ. Both Pharmacokinetic Variability and Granuloma Heterogeneity Impact the Ability of the First-Line Antibiotics to Sterilize Tuberculosis Granulomas [Internet]. Vol. 11, Frontiers in Pharmacology . 2020. p. 333. Available from: https://www.frontiersin.org/article/10.3389/fphar.2020.00333
37. Pienaar E, Sarathy J, Prideaux B, Dietzold J, Dartois V, Kirschner DE, et al. Comparing efficacies of moxifloxacin, levofloxacin and gatifloxacin in tuberculosis granulomas using a multi-scale systems pharmacology approach. PLoS computational biology. 2017;13(8):e1005650.
38. Pitcher M, Bowness R, Dobson S, Eftimie R, Gillespie S. Modelling the effects of environmental heterogeneity within the lung on the tuberculosis life-cycle. Journal of Theoretical Biology [Internet]. 2019;110381. Available from: http://www.sciencedirect.com/science/article/pii/S0022519320302368
39. Català M, Bechini J, Tenesa M, Pérez R, Moya M, Vilaplana C, et al. Modelling the dynamics of tuberculosis lesions in a virtual lung: Role of the bronchial tree in endogenous reinfection. PLoS Computational Biology. 2020;16(5).
40. Wigginton JE, Kirschner D. A Model to Predict Cell-Mediated Immune Regulatory Mechanisms During Human Infection with *Mycobacterium tuberculosis*. The Journal of Immunology. 2001;166(3):1951–67.
41. Takamura S, Kohlmeier JE. Establishment and maintenance of conventional and circulation-driven lung-resident memory CD8+ T cells following respiratory virus infections. Frontiers in immunology. 2019;10:733.
42. Slütter B, Van NB-B, Abboud G, Varga SM, Salek-Ardakani S, Harty JT. Dynamics of influenza-induced lung-resident memory T cells underlie waning heterosubtypic immunity. Science immunology. 2017;2(7).
43. Morris SE, Farber DL, Yates AJ. Tissue-Resident Memory T Cells in Mice and Humans: Towards a Quantitative Ecology. The Journal of Immunology [Internet]. 2019 Nov 15;203(10):2561. Available from: http://www.jimmunol.org/content/203/10/2561.abstract

44. Campbell DB. Can Allometric Interspecies Scaling be Used to Predict Human Kinetics? Drug Information Journal [Internet]. 1994 Jan 1;28(1):235–45. Available from: https://doi.org/10.1177/009286159402800130
45. de Boer RJ, Perelson AS. Quantifying T lymphocyte turnover. Journal of Theoretical Biology [Internet]. 2013;327:45–87. Available from: https://www.sciencedirect.com/science/article/pii/S0022519313000076
46. Ranjeva SL, Baskerville EB, Dukic V, Villa LL, Lazcano-Ponce E, Giuliano AR, et al. Recurring infection with ecologically distinct HPV types can explain high prevalence and diversity. Proceedings of the National Academy of Sciences of the United States of America. 2017;114(51).
47. Chohan B, Lavreys L, Rainwater SMJ, Overbaugh J. Evidence for frequent reinfection with human immunodeficiency virus type 1 of a different subtype. Journal of virology [Internet]. 2005 Aug;79(16):10701–8. Available from: https://pubmed.ncbi.nlm.nih.gov/16051862
48. Verver S, Warren RM, Beyers N, Richardson M, van der Spuy GD, Borgdorff MW, et al. Rate of reinfection tuberculosis after successful treatment is higher than rate of new tuberculosis. American Journal of Respiratory and Critical Care Medicine. 2005;171(12):1430–5.
49. Uys P, Brand H, Warren R, van der Spuy G, Hoal EG, An Helden PDV. The risk of tuberculosis reinfection soon after cure of a first disease episode is extremely high in a hyperendemic community. PLoS ONE. 2015;10(12).
50. Darrah PA, Zeppa JJ, Maiello P, Hackney JA, Wadsworth MH, Hughes TK, et al. Prevention of tuberculosis in macaques after intravenous BCG immunization. Nature. 2020;577(7788):95–102.
51. Hansen SG, Zak DE, Xu G, Ford JC, Marshall EE, Malouli D, et al. Prevention of tuberculosis in rhesus macaques by a cytomegalovirus-based vaccine. Nature Medicine. 2018;24(2):130–43.
52. Cicchese JM, Pienaar E, Kirschner DE, Linderman JJ. Applying Optimization Algorithms to Tuberculosis Antibiotic Treatment Regimens. Cellular and Molecular Bioengineering. 2017;10(6):523–35.

7 *CaliPro:* A Calibration Protocol that Utilizes Parameter Density Estimation to Explore Parameter Space and Calibrate Complex Biological Models

This chapter is a published work:

Joslyn, L.R., Kirschner, D., & Linderman, J. (2020). *CaliPro*: A Calibration Protocol That Utilizes Parameter Density Estimation to Explore Parameter Space and Calibrate Complex Biological Models. Cellular and Molecular Bioengineering, 1-17.

7.1 Abstract

Mathematical and computational modeling have a long history of uncovering mechanisms and making predictions for biological systems. However, to create a model that can provide relevant quantitative predictions, models must first be calibrated to recapitulate known biological data about that system. While many calibration approaches exist, current approaches may not be appropriate for complex biological models because: 1) many calibration approaches minimize an objective function in order to recapitulate only a single aspect of the experimental data (such as a median trend) or 2) Bayesian calibration techniques require specification of parameter priors and likelihoods to experimental data that cannot always be confidently assigned. Here, we develop *CaliPro*, an iterative, model-agnostic calibration protocol that utilizes parameter density estimation to refine parameter space and calibrate to temporal biological datasets. We illustrate the usefulness of *CaliPro* with four examples, spanning different model formulations, unique calibration datasets and diverse calibration goals. *CaliPro* can reduce time until calibration, reduce computational cost, and optimize model calibration.

7.2 Introduction

As part of a systems biology approach, mathematical and computational modeling can interrogate biological theories and provide context to better understand complex phenomena across multiple scales. In particular, the explosion of data from genomics, transcriptomics, proteomics and metabolomics coupled with the introduction of data from new cytometry and

imaging techniques have revealed an opportunity for systems modeling approaches to predict and reveal mechanistic relationships between various biological agents (1–13). However, before making useful predictions, a model must be able to replicate particular experimental outcomes and/or temporal dynamics of the related biological system.

Model calibration is the process of altering model inputs, e.g. initial conditions and parameters, until model outputs satisfy one or more biologically-related criteria. Often, these criteria include matching model outputs to experimental data across time. For simple models with relatively few parameters, calibration can be trivial. However, complex models often face a more difficult calibration process for three reasons. First, the number of parameters in these models can be large. Second, initial parameter estimates can be discovered via experimental studies (or other models) but still may contain a large degree of uncertainty. For example, if a parameter estimate is derived from multiple studies, estimates could vary greatly between them and a modeler will understandably have less confidence in the true value of this parameter. Third, some parameters are, by construction, intended to represent a group of biological processes. If a process(es) is modeled more phenomenologically, then parameter values may be very difficult, if not impossible, to measure directly via experiments.

A large body of work covers the calibration of complex models to biological data (see Read et al (14) for a thorough review of various calibration techniques in biological modeling). Popular calibration algorithms such as simulated annealing (15), genetic algorithms (16,17), gradient descent (18) and others (19,20) leverage the power of optimization schemes to refine parameter space in an iterative fashion. As Read et al. acknowledge, many, if not all, of these calibration techniques use a single metric (often called an 'objective function') to define the difference between experimental and simulated outcomes. The general aim is to minimize these differences across each iteration. However, not all models can or should be fit to experimental data through the minimization of a single metric for each outcome.

In fact, new experimental technologies (e.g., single-cell measurements, flow cytometry, advanced imaging) have allowed for the identification of greater biological variability, often across scales ranging from genomic to population-level information. In fact, many experimental

techniques now allow for the observation of greater biological variability. For example, at the genetic scale, advanced imaging techniques, single cell sequencing and mass cytometry have catalyzed the Human Cell Atlas Project (21), an effort to map the variability across every human cell type. Additionally, the introduction of functional assay screening (22) and targeted immunotherapy strategies (23) within cancer precision medicine have embraced heterogeneity across the population and provide a path toward patient-specific clinical therapies.
In response, mathematical and computational models have been built to address questions from fields as diverse as cell-signaling (24), wound healing (25), sepsis (26) and drug treatment in tuberculosis (27), among many others. As systems biology approaches attempt to reveal sources of variability, models must first be able to recapitulate biological variance and therefore should not be fit to a median trend line or a single metric. By calibrating to and thereby capturing a distribution of outcomes, modeling can assess and provide explanations of variability between individuals, species or other modelled biological agents.

Bayesian calibration approaches are a collection of calibration techniques that utilize Bayesian statistics to leverage information about the distribution of model outputs, information about the distribution of parameters and assumptions that relate model parameters to outputs (28–37). Sample Importance Resampling (SIR) is one example of a Bayesian calibration approach that draws a large number of parameter combinations from a prior parameter distribution, executes the model to create simulation outcomes, then uses outcomes to estimate a likelihood for each parameter set compared to the experimental data. The approach requires resampling from the original parameter space with replacement, where likelihood values are assigned as sampling weights (38). This approach, refined and modified over the years (30,39–41) has yielded success in calibrating models for which the distribution of both parameter values and experimental outcomes can be sufficiently derived from available data.

However, if the distribution of values within experimental datasets or model parameters cannot be approximated, Bayesian calibration approaches may not be the best strategy. Furthermore, some models should be calibrated with an emphasis on finding a robust parameter space – defined as a continuous region of parameter space wherein the vast majority of model runs will pass within the bounds of experimental data for the particular outcomes of interest – instead of a

single global optimum or a vast parameter space wherein some areas are weighted more than others. Finding a robust parameter space for a complex biological model is often a user-intensive process that, when performed manually, can take weeks due to a lack of automated protocols. Here, we describe a calibration protocol, *CaliPro*, that quickly identifies a robust parameter space where a range of distinct and biologically reasonable simulation results are represented when both model parameter and experimental data distributions cannot be approximated. We highlight the ability of *CaliPro* to identify a robust parameter space for multiple model types, including simple, complex, deterministic and stochastic biological models. We apply this approach to a variety of model types to show the flexibility of this protocol to calibrate different types of systems to multiple datasets.

7.3 Methods

7.3.1 Defining the appropriate use of *CaliPro*

Many traditional model-fitting techniques and strategies discover the global, or local, optimum within the outcome landscape. These techniques belong to a class of optimization procedures called metaheuristics (42). Unlike these procedures, *CaliPro* is an empirical approach that is not guaranteed to find the single global, or even local, optimum as it is commonly defined.

Both hill-climbing (a heuristic procedure (43)) and simulated annealing (a metaheuristics process (15)) algorithms will find the global optimum of a smooth, peaked landscape (Figure 7.1A&B) given ample time and computational resources. However, if a modeler wishes to fit to only the median of the data, they may potentially ignore important events that cause a higher or lower response. Models do have the potential to elucidate this behavior when properly calibrated to the entire range of experimental outcomes (44). If the modeler seeks to identify model simulations that fit within the range of the experimental data (blue simulation lines in Figure 7.1D), the outcome space (Figure 7.1C) becomes very difficult, if not impossible, for these algorithms to evaluate. As the model simulations either fall within the elevated region, or far below it, this binary classification of model simulations does not provide a heuristic or meta-heuristic process with enough information to estimate the next parameter combination decision. Figure 7.1C & D outlines one such theoretical case where *CaliPro* can calibrate the model, by embracing the

binary classification of model simulation outcomes and represent the full range of experimental outcomes.

We envision the use of *CaliPro* in situations such as those shown in Figure 7.1 but, more specifically, for calibration to meet three criteria: 1) the termination of model calibration is not a single parameter set that can recapitulate one aspect of the experimental dataspace (such as the median), but rather a set of parameter ranges that represent a continuous and robust parameter space able to recapitulate the broad range of outcomes captured within the experimental data. 2) The objective function cannot be easily defined as many model simulations may lie within the experimental dataspace and those that lie outside of that dataspace may not necessarily provide an optimization procedure with information for its next parameter choice. 3) The distribution of experimental outcomes is indistinguishable, or should not be approximated. *CaliPro* provides a method for which models with these criteria can be calibrated to experimental data that might encompass a broad range of outcomes but whose distribution might not be easily distinguished.

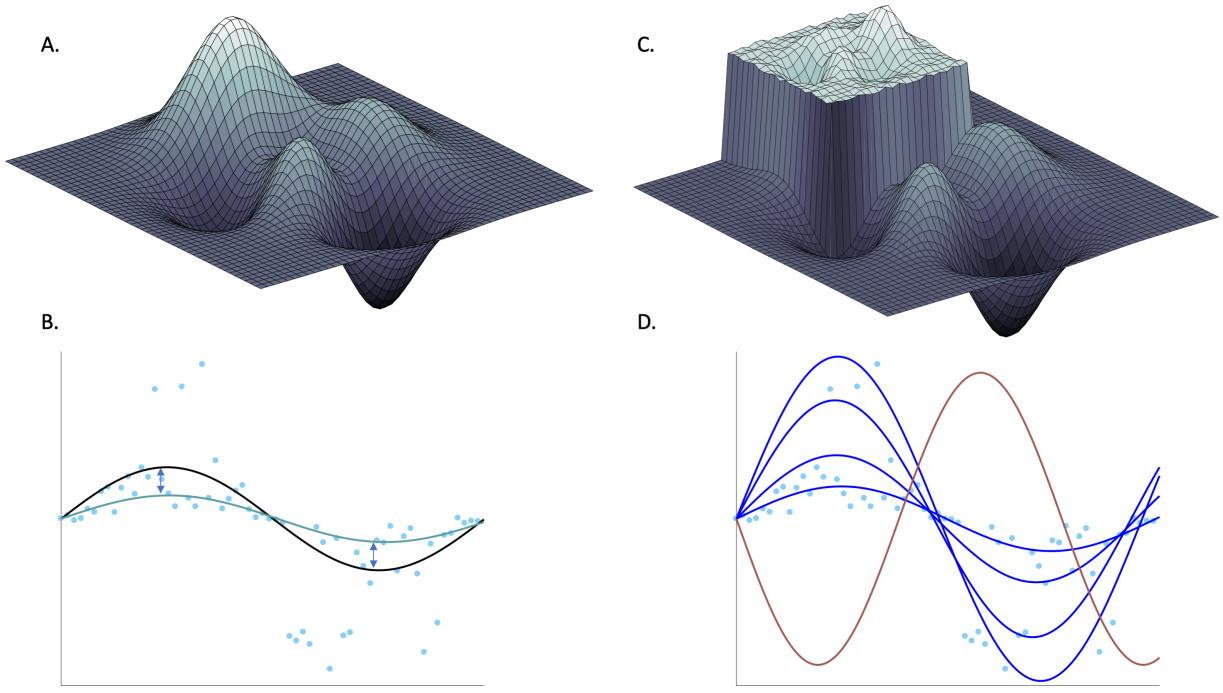

Figure 7.1 Calibrating a model to a range of plausible outcomes requires a new calibration approach

(Panel A& B) Panel A represents an example of a smooth model outcome landscape defined by a biologically relevant hypercube of parameter space. Each (x,y,z) point in this hypothetical 3D mapping of outcome space is defined by a single set of parameter inputs. B) The teal curve represents a single model outcome within the full

landscape in A), that is, the teal curve corresponds to a single (x,y,z) point in A). The blue dots are available experimental datasets, and the black curve represents a hypothetically known optimal for fitting the model to that experimental data (this corresponds to the white peak in A). Ultimately, in the situation outlined by Panel A&B, the modeler seeks to minimize the difference (shown as arrows) between the simulation and median line by defining an objective function and using either hill-climbing or simulated annealing (or another similar technique) to select the next parameter combination. (Panel C&D) If the optimal within outcome space is a set of simulations that encompass various aspects of the experimental data, the landscape in A) looks much more like the landscape in C). Here, the optimum is now an elevated region of space that may include many outcomes. Panel D) now includes a set of simulations (shown in royal blue) that reasonably recapitulate different aspects of the experimental data and each individual simulation maps to different points on the elevated region in C). One failed simulation (shown in red) does not reasonably portray the experimental data (light blue dots), and would map to the lower regions in outcome space in C).

7.3.2 General Overview of *CaliPro*

CaliPro is utilized following a model building process, when a modeler already has 1) a model in hand and 2) a series of datasets that exhibit behavior that the model is partially designed to replicate. Figure 7.2 displays the general overview process of *CaliPro*. Step 1 of Figure 7.2 shows the multiple data types that are input to *CaliPro*.

Determining initial parameter ranges can be a difficult process as even parameters discovered via experimental studies (or other models) may contain uncertainty as to their exact value(s). However, by examining multiple values from the literature, the modeler should assign the widest range that are biologically feasible, which includes all previous estimates that have been derived. It is also important to note that some parameters are fairly well-constrained, either biologically or by design, and are thus easier to assign an initial range. Following initial parameter range assignment, in Step 2 the modeler performs a stratified sampling of the parameter space using such algorithms as Latin Hyper-cube Sampling (LHS), Sobel sequences, Monte Carlo, etc. The model is then executed for each of the parameter combinations.

Step 3 in Figure 7.2, Model Evaluation, is a crucial step. If the experimental datasets for calibration at each timepoint can be approximated as a distribution (Gaussian, Poisson, or otherwise) we suggest following Bayesian calibration approaches by creating a likelihood to compare model parameters and simulation outcomes with the experimental data. Subsequently, there are many techniques to refine parameter space, including SIR. However, should the experimental data be uniform or indistinguishable, then we suggest specifying a pass set definition (

Appendix F - Box 1). This is a user-intensive step of *CaliPro*, as the pass set definition is entirely up to the modeler. Within *CaliPro* this model evaluation step can also be automated and defined computationally a priori. Model simulations that satisfy the pass set definition are gathered together into one matrix and thereby constitute a pass run set (
Appendix F - Box 1). All model runs that do not satisfy the pass set definition are placed within the fail run set (
Appendix F - Box 1).

Next, *CaliPro* creates two density plots for each parameter within the pass and fail parameter sets (
Appendix F - Box 1) to display the regions of parameter space that are more inhabited by the pass or fail run set (Step 4 in Figure 7.2). Once the density plots have been created, the initial parameter ranges can be refined using one of two methods (Step 4 in Figure 7.2, methods below). Following parameter range refinement, these parameters will be sampled again in an iterative fashion. Steps 2-4 will be repeated until the termination criteria (
Appendix F - Box 1) is met.

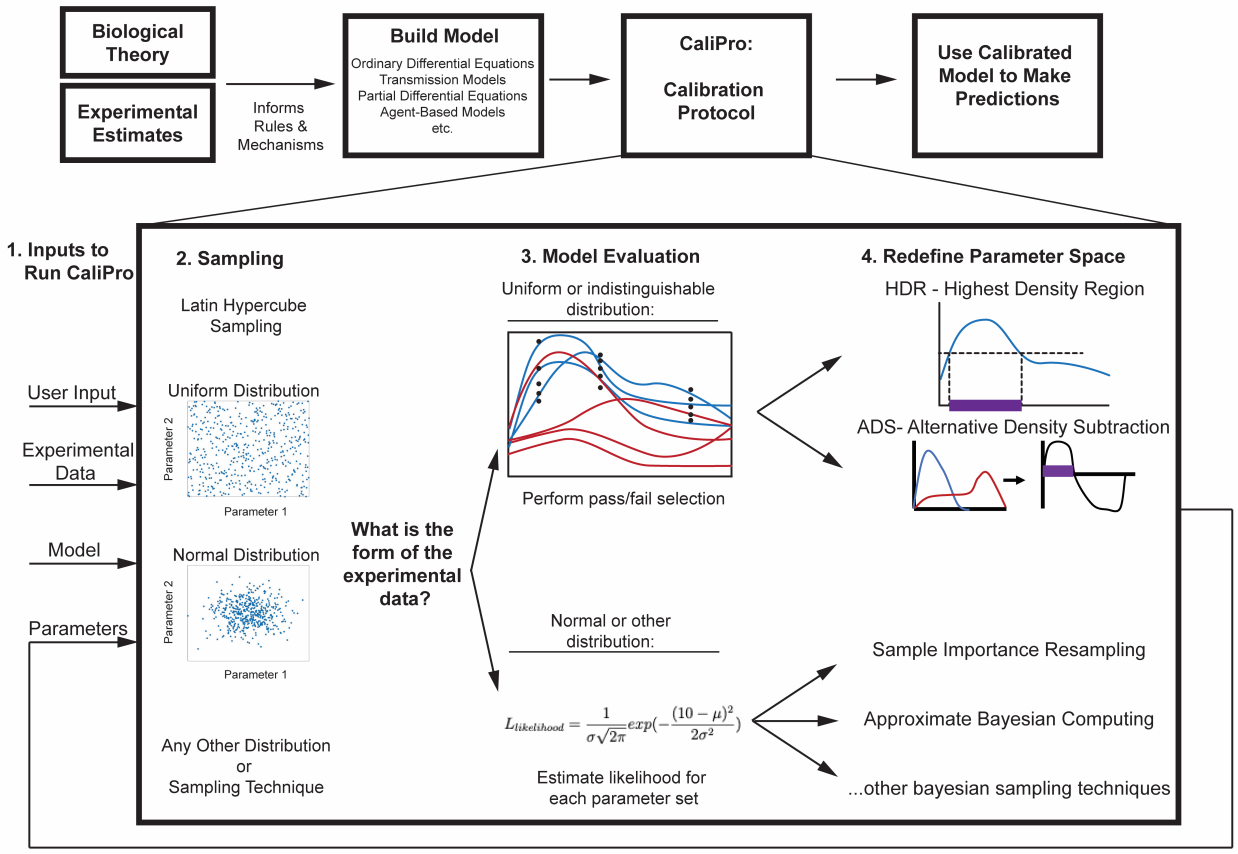

Figure 7.2 Overview of *CaliPro*

The model building process begins by incorporating biological theory and experimental estimates to inform rules, mechanisms, and model structure. Once the model is built, there is (an often prolonged) period of calibration, wherein the model outcomes and general behavior are compared to a set of experimental outcomes across time to identify the best fit. Here, we have provided a protocol, called *CaliPro*, for calibrating complex biological models. This begins with Step 1: Inputs. Several inputs including the experimental data, the model itself, and the model parameters – given as a range of initial values for each parameter. Step 2: Sampling. Here, we utilize an Latin Hyper-cube Sampling (LHS) scheme (See (64) for an in-depth review of LHS and uncertainty/sensitivity analysis) where each parameter is sampled uniformly or normally, but sampling could be performed using any sampling scheme (Sobel sequences, Monte Carlo, etc.). Step 3: Model Evaluation. At this stage in the calibration process, the modeler will execute the model for each of the parameter combinations created via sampling parameter space, and begin to evaluate the model by comparing it to the experimental data. If the form of the experimental data can be approximated by a likelihood, or the modeler is comfortable assigning a distribution to the experimental data, they should proceed with Bayesian calibration approaches such as Sample Importance Resampling, approximate Bayesian computing or other techniques. However, if the modeler cannot distinguish a distribution for experimental datasets, or if that distribution is uniform at each timepoint, then we suggest narrowing the parameter space via our *CaliPro* techniques. Still as part of the model evaluation in step 3, the modeler chooses a pass set definition (Appendix F - Box 1) to identify a subset of model simulations that they consider the pass run set (blue simulation lines). All other runs constitute the fail run set (red simulation lines). Step 4: Redefine Parameter Space. Transitioning from evaluating the model, the modeler creates two density plots for each parameter, one for the pass parameter set and the other for the fail parameter set (blue, red lines density plot lines, respectively) across the original parameter range (the x-axis) for each parameter. Like any other density plot, the y-axis represents the probability density function. If a modeler prefers, the y-axis could be transformed to become a percentage (normalized from 0 to 100). The modeler then narrows the parameter ranges using either Highest Density Region (HDR) or Alternative Density Subtraction (ADS) selection (see more on these approaches in methods). Each

parameter will be sampled again from this new parameter subrange (purple bounded region identified on the x-axis) at Step 2 in an iterative fashion. Steps 2-4 are repeated until the termination criteria (
Appendix F - Box 1) has been met. At this point, the modeler has a well-calibrated model.

7.3.3 Highest Density Region estimation to identify parameter subranges

Calculating the Highest Density Region (HDR) is one approach to summarize a probability distribution. HDR satisfies the following criteria: 1) the region that summarizes the probability distribution must occupy the smallest possible volume in the sample space and 2) every point within the region has a probability density larger than every point outside the region (45). HDR is defined by letting $f(x)$ be the density function of random parameter X. Then the $100(1-\alpha)\%$ HDR $R(f_\alpha)$, is the subset of the sample space of X such that $R(f_\alpha) = \{x: f(x) \geq f_\alpha\}$ where f_α is the largest constant such that $Pr\ Pr\left(X \in R(f_\alpha)\right) \geq 1-\alpha$ (45). A modeler specifies α, which represents the size of the region, as a percentage of the density function, $f(x)$.

We apply this method to the distribution created by the pass parameter set across a one-dimensional parameter space, for each parameter (Step 4 in Figure 7.2). When used within the *CaliPro* pipeline, HDR serves to refine parameter space by identifying subranges within each individual parameter range toward the region that has the highest density of simulations that satisfy the *pass set definition*. While HDR can identify several disjoint regions for multimodal distributions, within the *CaliPro* pipeline, if disjoint regions are identified, the parameter range for the next iteration will be bounded by the minimum value and the maximum value across the disjoint regions.

7.3.4 Alternative Density Subtraction to identify parameter subranges

Another option for narrowing the initial parameter range of each parameter is Alternative Density Subtraction (ADS). ADS leverages information from the probability density of both the pass parameter set and fail parameter set across each parameter range. ADS is defined by letting $p(x)$ be the density function of the pass parameter set for the random parameter X and by letting $d(x)$ be the density function of fail runs for the same random parameter X. Then ADS is the subset of the sample space of X such that $\{x: p(x) - d(x) \geq 0\}$.

When used within the *CaliPro* pipeline (Step 4 in Figure 7.2), ADS refines parameter space by identifying regions within each individual parameter range that have a higher density of simulations that satisfy the *pass set definition* than those that fail to satisfy the *pass set definition*. If disjoint regions are identified, the parameter range for the following iteration will be bounded by the minimum value and the maximum value across the disjoint regions.

7.3.5 Computational Platform

CaliPro can be implemented within any programming language. In the examples we list below, we have implemented *CaliPro* in R (version 3.5.3) and MATLAB (R2016) environments. R packages used include plyr, dplyr and tidyr for data organizing and reformatting. We used ggplot2 and scales for plotting and hdrcde to identify highest density regions when that option was exercised within *CaliPro*.

On our lab website (webpage address: http://malthus.micro.med.umich.edu/*CaliPro*), we provide a directory that includes all MATLAB scripts for running a fully automated version of *CaliPro*, including model execution of the predator-prey model example described below. We suggest modelers wishing to utilize the *CaliPro* framework use these scripts as a starting point for their own implementation. Additionally, all equations are listed in the Appendix F.

7.4 Results

To show how to apply *CaliPro*, we provide four examples of model formulations with datasets for calibration. We show that *CaliPro* is model agnostic and works well for these types of model structures: ordinary differential equations (ODEs) (deterministic, continuous) and agent-based models (stochastic, discrete). The number and type of experimental datasets will likely differ for potential *CaliPro* users: therefore, we also illustrate this diversity in our examples.

7.4.1 Example 1: *CaliPro* finds parameter ranges that satisfy a predator-prey test problem

We first test *CaliPro* using a classic ODE system of deterministic population dynamics: a predator-prey (or Lotka-Volterra) model. The Lotka-Volterra model is a two-equation model that was developed independently by Lotka (1925) and Volterra (1926) to represent predator-prey interactions across time and has been studied in thousands of papers since its first publication.

The model has two state variables (H(t) and L(t) as a vector of values corresponding to each time point) and several parameters that represent predator and prey interactions across time. H(t) represents the number of prey per time, L(t) represents the number of predators per time, α represents reproduction rate constant of prey, β is the rate constant of predation, σ is the death rate of predators and δ is the reproduction rate constant of predators:

$$\frac{dH}{dt} = \alpha H(t) - \beta H(t)L(t)$$

$$\frac{dL}{dt} = -\sigma L(t) + \delta H(t)L(t)$$

At this point, a modeler could calibrate this model to a single trend line for each of the two species using traditional calibration techniques (e.g. least square regression). However, we use this model to test whether *CaliPro* can identify a parameter space that satisfies a range of experimental outcomes. For simplicity, we built a small test problem using a synthetic experimental dataset that has a range of outcome values at each time point. To build this synthetic experimental dataset, we selected a narrow range of values for each of the four parameters in the model (Table 7.1– Synthetic Data Range). Then, we simulated the model 500 times, sampling from this narrow parameter space. The minimum and maximum value of those 500 simulations for 21 timepoints are shown as black data points in Figure 7.3 and make-up our synthetic experimental dataset. These synthetic experimental data points serve as the data for calibration within this test-case *CaliPro* example.

Beginning *CaliPro* to calibrate this model, we sample from our initial parameter range: a larger range of values for each parameter that encompass the smaller range used to create the synthetic experimental dataset (Table 7.1– First Iteration Range). Note that for the initial parameter range for beta, this . Figure 7.3(top row) shows the predator (gold) and prey (blue) outcomes following this initial sampling of parameter space. As part of the *CaliPro* process, we define a termination criterion that 90% of runs must belong to pass run set. Additionally, we outline a pass set definition where simulation values must fall within ranges bounded by two times the maximum experimental data point and one-half of the value of the minimum experimental data for both predator and prey populations for every time point. This pass set definition was selected because it encapsulates the synthetic experimental data while ensuring there are enough simulations within the pass run set to inform the next iteration. Altogether, a given model simulation must satisfy each of those criteria (above the minimum, but below the max for each of the 21 timepoints for each species) in order to belong within the pass run set. If even one simulation value does not reside within this range for one time point in one species, the simulation is designated as part of the fail run set. Following initial sampling, <1% of the 500 model simulations satisfy the pass set definition, so we narrow this parameter space using the HDR method with a coverage of 0.85 as described in Methods. The second iteration in Figure 7.3 reveals the results of sampling this parameter space, wherein ~35% of runs are now classified as part of pass run set.

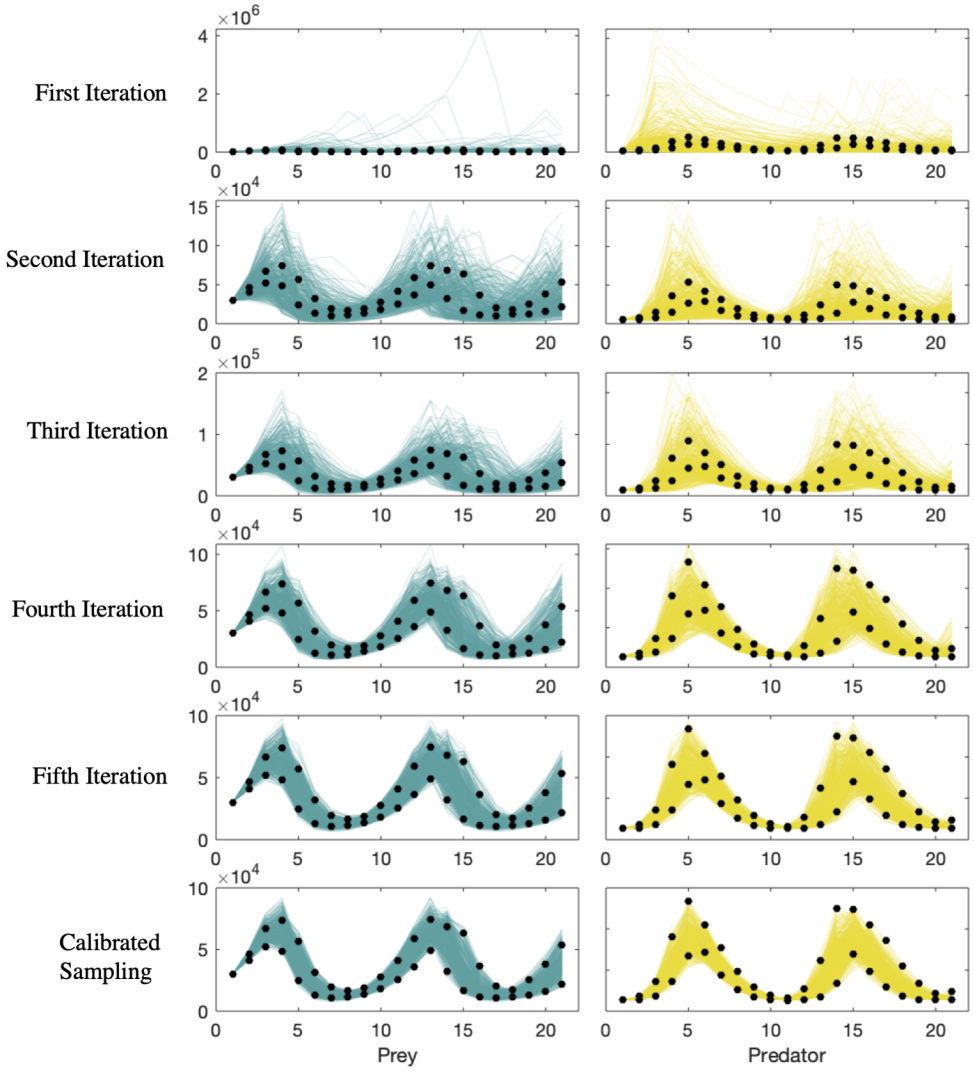

Figure 7.3 Example 1 - Predator-Prey Model: *CaliPro* identifies best fit parameter space using HDR

Prey (blue) and predator (gold) model simulation populations overlaid on synthetic experimental data (black data points) at each timepoint (minimum and maximum values shown). Termination criteria: 90% of runs must belong to pass run set. Pass set definition: (Iterations 1 & 2) Simulation values, at each timepoint, lie within the range bounded by two times the maximum experimental data point and half the value of the minimum experimental data point for each species. (Iterations 3-6) For each time point, the simulation value must fall within the 1.25 times the maximum experimental data point and the value of the minimum experimental data point divided by 1.25 for both predator and prey. In the final iteration, 98% of the 500 simulations belong to the pass run set, exceeding our termination criteria.

Now, there may be modeling instances wherein the termination criteria for *CaliPro* could be satisfied following the results of this second iteration, as the model outcomes do capture the full spread of experimental outcomes and generally capture the behavior of the experimental data across both predator and prey (Figure 7.3, second iteration). However, the goal is to identify a

more refined parameter space for this test problem as the range of outcomes is slightly too broad for our satisfaction.

We continue using *CaliPro* via iteration, but reformulate our pass set definition to be stricter than the previous iterations (see MATLAB files for automated implementation at http://malthus.micro.med.umich.edu/*CaliPro*) since our pass parameter set is sufficiently large. Now, we impose a new pass set definition specifying a narrower range for both predators and prey for every time point. We use HDR again to narrow the parameter space following iteration 2 and resample this space 500 times. Following the third iteration, 16% of the 500 model simulations satisfy the new pass set definition. We narrow and resample parameter space three more times before our termination criteria is met (see Figure 7.3). Out of 500 total model simulations at the final iteration, 98% of model simulations belong to the pass run set. Figure 7.3 shows model outcomes against the synthetic experimental dataset; and Figure 7.4 displays the iterative refining of the parameter space for each parameter in this model. We display the pass and fail parameter density plots for each parameter at each iteration in Figure 7.4. These parameter density plots reveal where, across the range of sampled values, the majority of simulations did or did not satisfy the pass set definition. For example, in the initial sampling of the δ parameter range in column 4 of Figure 7.4, the runs that satisfy the pass set definition clearly reside along the region bounded between 0 and 0.04. Through iteratively defining the next parameter range for sampling (the purple range band along a portion of the x-axis on each subplot in Figure 7.4), we satisfy our termination criterion that 90% of the runs satisfy the pass set definition by iteration 6. *CaliPro* is able to find a range of values for each parameter that satisfies our test problem of relatively simple predatory-prey dynamics (Table 7.1).

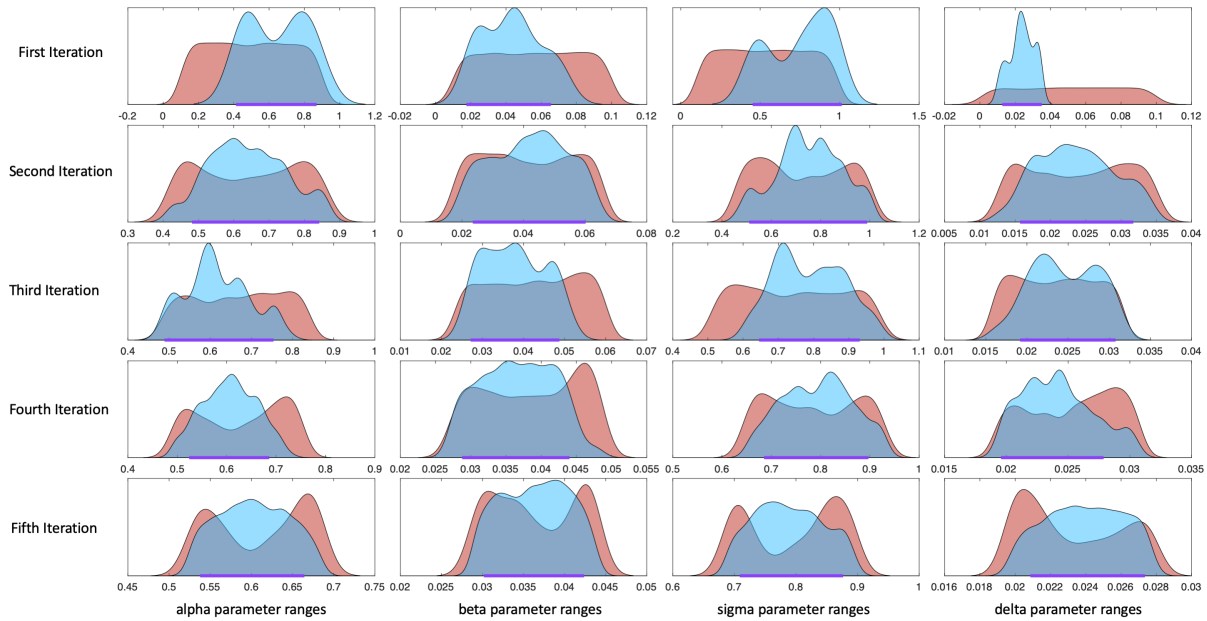

Figure 7.4 Example 1 - Parameter Density Plots at each *CaliPro* iteration
The density plots for pass (blue) and fail (red) parameter sets are shown for each parameter (columns) and at each iteration (rows). Ranges along the x-axis where the pass parameter density is larger than the fail parameter density suggest regions in parameter space where simulations are more likely to satisfy the pass set definition. The purple range band along the x-axis of each density plot denotes the region of parameter space identified by HDR (HDR coverage set at 0.85) that will become the parameter range for sampling in the next iteration. 6th iteration is not shown as sampling from the purple band along the x-axis in the fifth iteration results in a calibrated parameter space.

Table 7.1 Initial and Calibrated Parameter Ranges for the predator-prey test case problem
For each of the four parameters, the first iteration range was assigned to be much larger than the range of parameters used to create the synthetic dataset. Following five *CaliPro* iterations, the final sampling space was satisfactorily close to the synthetic data range, with 98% of model realizations lying with the minimum and maximum bounds of experimental datasets.

Parameters	Synthetic Data Range	First Iteration Range	*CaliPro* Final Range
alpha	0.5-0.7	0.1-0.9	0.53 – 0.66
beta	0.02-0.035	0.01-0.1	0.03 – 0.042
sigma	0.6-0.9	0.1- 0.99	0.7 - 0.88
delta	0.02-0.03	0.001-0.1	0.02 - 0.027

7.4.2 Example 2: *CaliPro* identifies parameter ranges for ODE granuloma lesion model within non-human primate lung

For a larger example, we apply *CaliPro* to a system of 16 non-linear ODEs (see Granuloma ODE Equations in

Appendix F) that capture bacterial, T cell, macrophage and cytokine dynamics within a single granuloma lesion that forms within a non-human primate (NHP) lung as an immune response to infection with *Mycobacterium tuberculosis* (46). As a roughly spherical mass of immune cells acting to contain bacteria to a local region within the lung, the granuloma is typically a few millimeters in size and is the hallmark of tuberculosis. We use *CaliPro* to explore parameter space of this more detailed non-linear ODE model with 108 parameters and identify parameter ranges that replicate NHP single granuloma experimental datasets.

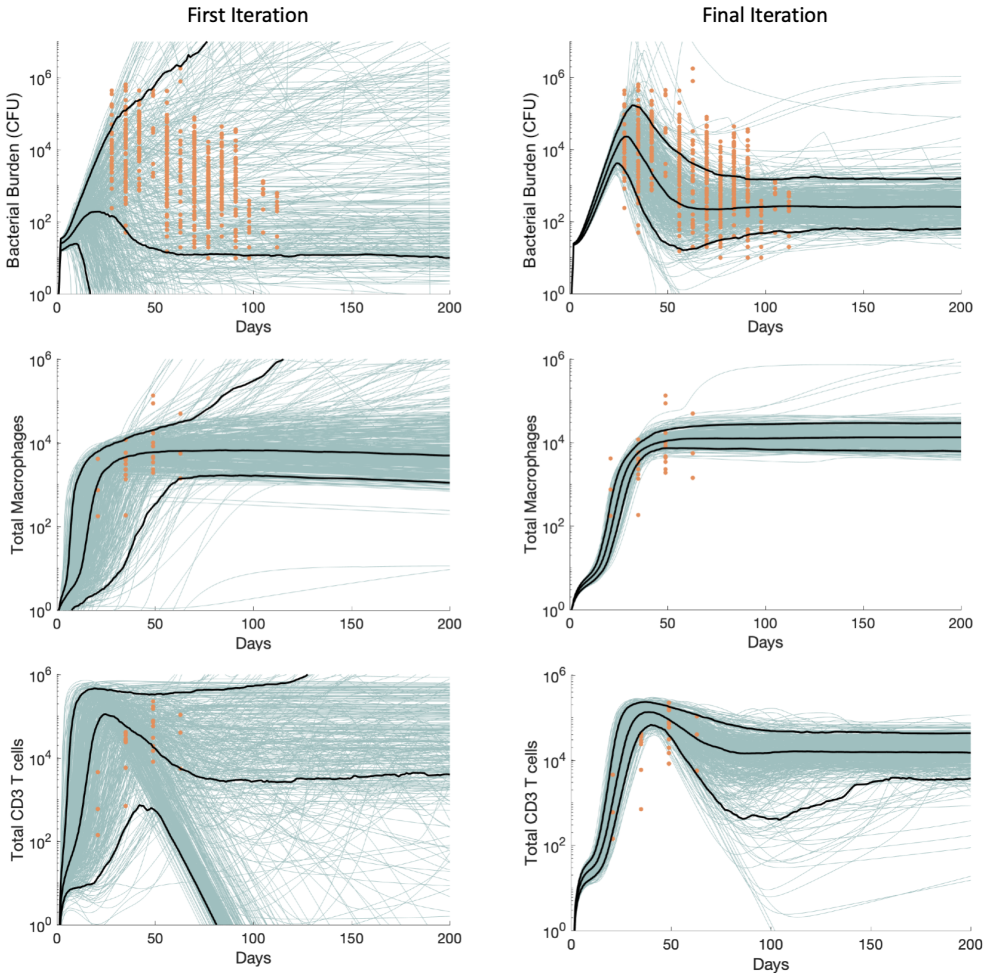

Figure 7.5 Example 2 - Single Granuloma ODE: *CaliPro* identifies calibrated parameter space using ADS

500 model simulations are shown (blue lines) overlaid on experimental data (orange data points) for bacterial numbers (Bacterial Burden), total numbers of CD3+ T cells and total numbers of macrophages. The 5th, 50th, and 95th percentiles of model simulations are shown as black lines. Termination criteria: 75% of runs must belong to

pass run set. Pass set definition: (All Iterations) Simulation values, at each timepoint, lie within the range bounded by an order of magnitude above the maximum experimental data point and an order of magnitude below the value of the minimum experimental data point for each experimental dataset. Additionally, for days 90-200, the simulation value for bacterial numbers cannot eclipse 36000. In the final iteration, 91% of the 500 simulations belong to the pass run set, exceeding our termination criteria.

Unlike Example 1 above, in this example we calibrate this system of ODEs to three separate experimental datasets, rather than a synthetic dataset, shown as orange data points across time in Figure 7.5. There are 628 data points in the bacterial burden dataset and 26 data points in the T cell and macrophage dataset. Each separate data point represents experimental data generated on outcomes from an individual NHP granuloma. Thus, while these datasets are not strictly temporal in nature, since the data are gathered at the time of NHP necropsy, the outcomes taken together can be treated as a single dataset, although it is a collection of data.

We begin the *CaliPro* process on this system by defining our initial parameter range of values for 80 of the 108 parameters in the model. We determined initial parameter ranges by examining experimental values from literature as well as other previous models (12,47–54). It is important to note that values of some parameters were fairly well-constrained (e.g. extensive data in the literature gives rates of bacterial killing) while others are less so. The remaining 28 parameters are death or decay rates, ratios or weights for scaling, or other parameters that are constrained by the biology and are therefore not varied. We specify the pass set definition such that the simulations must fall within the range bounded by an order of magnitude on either side of the minimum and maximum experimental data point for every time point across each of the three experimental outcomes. The experimental data range includes over four orders of magnitude, therefore our pass set definition was selected because it encapsulates the general behavior of the experimental datasets we are using for calibration, and will not remove simulations that are within the same order of magnitude as experimental data points. Additionally, we know that the long-term behavior of bacterial numbers in granulomas is fairly stable without intervention (55–57), so we set an upper bound at 36000 bacteria for days 90-200. If the simulation value for bacterial numbers eclipses this bound within those days, the simulation is immediately assigned as part of the fail run set. We sample this initial parameter space to create 500 model simulations and show the simulation outcomes overlaid with experimental data (Figure 7.5). Of this sampling, only 6.8% of the runs satisfy the pass set definition. We then use ADS to narrow the

parameter space and resample, finding that 46.8% of the runs satisfy the pass set definition during the second iteration. We iterate this process until the final iteration yields 91% of the total model runs belong to the pass run set, which is above our termination criterion of 75%. Additionally, the simulation outcomes are consistent with other information about this biological system: we know that bacterial levels of individual granulomas should peak prior to day 50, and should stabilize after day 100, whereas T cell and macrophage cell numbers should increase until they stabilize or drop around day 75 (55). Thus, *CaliPro* is able to simultaneously calibrate a complex, non-linear ODE system to a series of diverse experimental outcomes and calibration goals.

7.4.3 Example 3: *CaliPro* identifies continuous parameter space for a transmission model of infectious disease without assigning likelihoods or informative priors

In a review of Bayesian calibration approaches, Menzies et al. (28) present an ODE model of a generic sexually-transmitted disease that includes six state variables, representing non-susceptible, susceptible, early diseased, late diseased, treated, and dead populations. Eleven parameters govern the rates of transmission between these populations, and the model is evaluated for 30 years. See Menzies et al. for a model schematic and further model details (28). The equations for this model are available in
Appendix F.

Additionally, the authors present three sets of "calibration targets", or experimental datasets that are used to calibrate the model—disease prevalence, treatment volume, and average survival in years. Menzies et al. assign functions to approximate likelihoods of modeled outcomes to the original datasets and use an SIR technique to probe parameter space and calibrate the model to these targets (calibration technique and results recreated herein - Figure 7.6A). However, as Menzies et al. point out, care must be taken when deciding to approximate likelihoods, define summary statistics, or assign distributions to experimental outcomes (28). Additionally, we suggest that any approximations or estimations derived from low sample sizes may introduce unnecessary assumptions into the calibration process.

Therefore, in this example, we use *CaliPro* to calibrate their ODE model to the same calibration targets, but do not impose likelihoods nor assume any prior known distributions of the experimental datasets. Unlike Menzies et al., and in an effort to further test *CaliPro*, we set our initial parameter range to create a parameter space that is uninformative - we uniformly sampled each of the seven varied parameters according to an LHS scheme. These initial parameter ranges were assigned to the widest values that Menzies et al. selected when they sampled with normal (or beta) parameter distributions. We generated 500,000 samples within this uninformative parameter space.

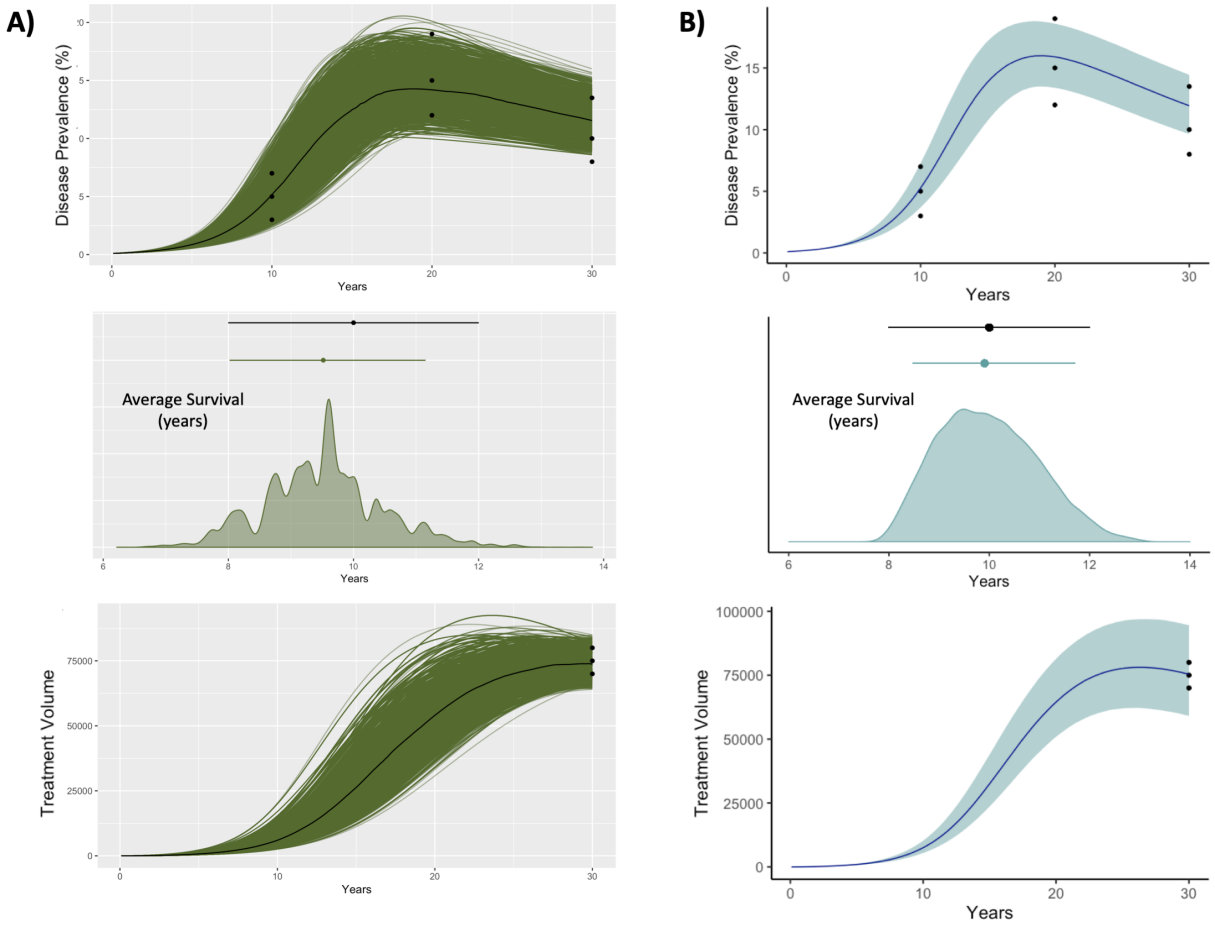

Figure 7.6 Example 3 - Disease transmission: SIR and *CaliPro* calibrations
A) We recreated the results of Menzies et al. (28) by using SIR to calibrate the ODE transmission model (individual model simulations shown as green lines and median trend line shown in black) to three experimental outcomes: disease prevalence, average survival (in years), and treatment volume. The average survival graph also shows the posterior distribution of average survival across all the parameter combinations. Experimental data are shown as black data points. B) Model simulation and experimental outcomes following *CaliPro* using HDR. The 5th - 95th percentile is represented by the blue region (50th percentile – dark blue line). Termination criteria: 75% of runs must belong to pass run set. Pass set definition: (Iterations 1-3) For each time point, simulation values lie within 1.25 times the maximum experimental data point and 0.75 times the value of the minimum experimental data point for all

calibration targets (Iteration 4) Changed the lower bound of pass set definition to be an exact match to the experimental data at each timepoint.

Of these samples, we outline a pass set definition as simulations that include average survival, treatment volume, and disease prevalence outcomes within the range bounded by 75% of the minimum and 125% of the maximum experimental data point for every experimental time point across each of the three outcomes. This pass set definition was selected because it encapsulates the general behavior of the calibration targets. Following each iteration, we refine parameter space by defining the new parameter ranges for each parameter using HDR with a coverage of 0.75 of the density created by the pass parameter set. After the first iteration, subsequent samplings generated 10,000 simulations (fewer samples were necessary to identify the pass run set). Following the third iteration, the distribution of the pass parameter set was trending toward the minimum values of the calibration target data for average survival time. Thus, we adjusted the lower bound of our pass set definition to be an exact match to the experimental data at each timepoint for the fourth iteration. After four iterations, 97% of model simulations satisfy the parameter set definition. Figure 7.6 shows the 95% confidence interval and median line of all the simulations in the calibrated parameter space. *CaliPro* is able to calibrate this model to the calibration targets outlined by Menzies et al. despite an uninformative prior and without assigning a likelihood function to the datasets. We propose that *CaliPro* is a useful calibration tool for a situation where the modeler is unable to assign priors or likelihoods (e.g. small sample sizes).

7.4.4 Example 4: *CaliPro* successfully calibrates stochastic models: using an agent-based model of granuloma outcomes as an example

While *CaliPro* displays a promising ability to identify robust parameter space for ODE models of varying complexity, stochastic models are notoriously difficult to calibrate (28). We posit that *CaliPro* is agnostic to model formulation and therefore unbothered by new complexities that stochastic models raise in traditional calibration settings. Thus, we apply *CaliPro* to a stochastic agent-based model of granuloma formation, *GranSim*.

GranSim is a two-dimensional hybrid agent-based model of granuloma formation during *Mycobacterium tuberculosis* infection. *GranSim* captures the environmental, cellular, and bacterial dynamics at the site of infection across molecular, cellular, and tissue-scale events. The spatial environment of this model is a 4 mm by 4 mm section of lung tissue. Agents (cells) populate this environment and constitute various immune cells as well as bacteria. The cells interact with one another across time according to rules that dictate movement, speed, proliferation, and change of phenotype. Chemokines and cytokines also exist on the lattice, but are represented as continuous values instead of individual agents, making the model a hybrid formulation. As an established model, *GranSim* has been modified and calibrated across 15 years extensively to data from the NHP model of tuberculosis (12,50–53,58–60) and see *GranSim* website for more details: http://malthus.micro.med.umich.edu/*GranSim*). Herein, we present a single calibration effort of this model using *CaliPro*.

Our data for single granuloma formation is the same as the experimental data we used to calibrate the granuloma ODE model (example 2). However, for this calibration, we use bacterial numbers as the primary measure to sort pass and fail simulations, then use the immune response metrics (T cell and macrophage counts) and visual confirmation of granuloma formation (via agent-based model snapshots) as validation measures. This adds a new spatial criterion that must be met in addition to the temporal dataset criteria.

For comparison, we select the initial parameter ranges to be the same as a previous manual calibration effort performed in the lab – where 52 of 131 parameters in *GranSim* are varied within reasonable bounds according to values from literature and previous versions of the model (12,50–52). We sampled this parameter space 1000 times according to an LHS scheme with three replicates each to create 3000 unique *in silico* granulomas (Figure 7.7). For the first iteration, we specified the pass set definition to include simulations where total bacterial numbers in the simulation were less than the maximum experimental value (36000) at day 85. This pass set definition was selected because we wanted to isolate the simulations whose bacterial values decreased after peaking near day 40. After the first iteration, 62% of the runs satisfy the pass set definition. We refine the parameter space using the ADS method and resample to create another set of 3000 granulomas. At iteration 2, we redefined our pass set definition so that simulations

must have less than 104 bacteria at day 175 – an additional criterion that was implemented so that simulation bacterial numbers remain stable across time. Of the 3000 simulations, 67.5% satisfy this new pass set definition. Again, we refined the parameter space using ADS, and resampled. However, this time 83% of simulations satisfy the pass set definition, eclipsing our preset termination criteria of 75%. As a validation step, we checked the immune response of these calibrated simulations to ensure the majority fell within the bounds created by the T cell and macrophage experimental data (Figure 7.7). NHP granulomas have a distinct formation and, while there is variation, there are generally well-accepted spatial structures (55,61). So, as a secondary validation step, we manually inspected screenshots of the agent-based model to ensure that they recapitulated known granuloma spatial characteristics. This introduces modeler bias, however, with most experimental studies, assumptions and decisions are necessary. We are currently working on a way to automate visual discrimination of both simulated and experimental granulomas. Thus, *CaliPro* is able to calibrate a complex, stochastic and discrete hybrid model to a set of diverse experimental outcomes, calibration goals, and validation datasets.

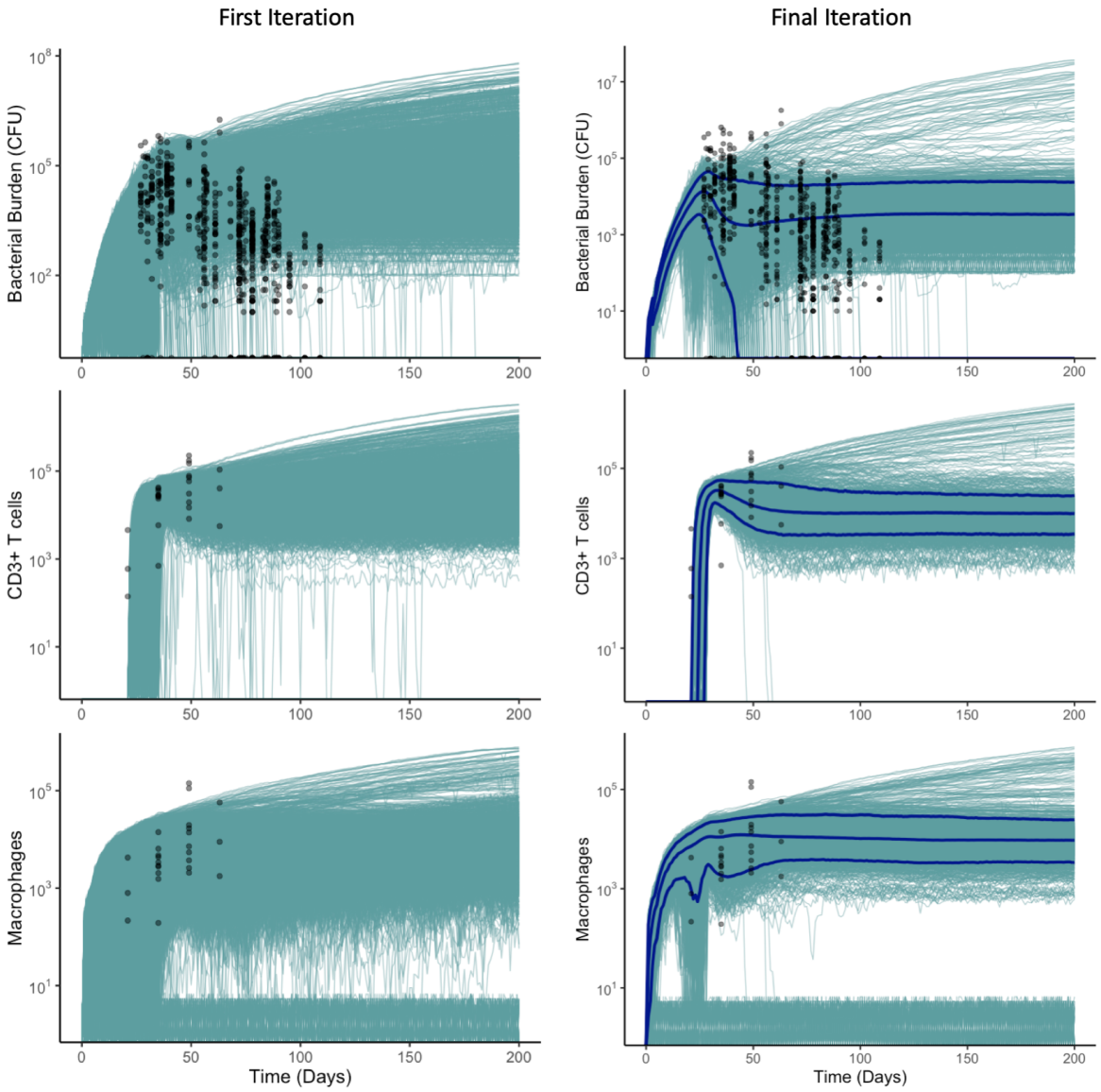

Figure 7.7 Example 4 - agent-based model: *CaliPro* finds calibrated parameter space using ADS.
Model simulations (blue lines) and experimental data (black data points representing total bacterial numbers, total Macrophage cell counts, and total CD3+ T cell counts) across time in days. The 5th, 50th, and 95th percentiles of model simulations are shown as dark blue lines for the final iteration. In simulations where bacterial burden sterilizes, the macrophage count drops below 10. Termination criteria: 75% of runs must belong to pass run set. Pass set definition: (Iteration 1) Simulations with total bacterial numbers less than the maximum experimental value (36000) at day 85. (Iteration 2 & 3) Simulations with total bacterial numbers less than 104 at day 175.

7.5 Discussion

Increasingly, mathematical and computational models are utilized to interrogate complex biological systems, provide context to understand interactions, and make predictions. Model

calibration is a crucial step that ensures models reasonably portray biological complexities in the real system and can thus make reliable inferences or predictions of future system state(s). However, traditional calibration approaches are not always appropriate for complex biological models due to one of two drawbacks: 1) many calibration approaches minimize an objective function in order to recapitulate only a single aspect of the experimental data (such as a median trend) or 2) Bayesian calibration techniques require specification of parameter priors and likelihoods of experimental data which cannot always be confidently assigned if there are low numbers of experimental samples or if distributions across samples are indistinguishable. As such, we have developed *CaliPro*, an iterative calibration protocol that utilizes parameter density estimation to refine model parameter spaces and to calibrate models to temporal biological datasets.

By assigning model simulations to a pass or fail run set upon each sampling of parameter space, *CaliPro* provides an automated framework through which the goals of calibration are clearly defined and standardized. Further, as the definition of pass vs. fail is a user-intensive step, the roles of both modelers' expertise and biologists' intuitions are more explicitly integrated into *CaliPro*. As such, specifying a pass set definition is perhaps the most crucial step in *CaliPro*. However, it can easily be defined by considering the acceptable criteria under which the modeler might be satisfied when calibration is considered complete. For example, there may be multiple calibration goals, as we outlined in Example 2, where model simulations must match the general dynamics outlined by the three separate experimental datasets. Additionally, by imposing an upper-bound for bacterial numbers at later time points, we explicitly integrated the intuition of the biology into the calibration process. We believe that *CaliPro*'s incorporation of explicit definitions of intuition are an important contribution of this method that is typically overlooked within other calibration procedures.

Relatedly, the modeler can toggle the pass set definition according to bounds defined by the datasets available. If the datasets are sparse or are estimated across a wide range of studies, then a modeler can assign a pass set definition that is more lenient. Conversely, if a modeler is certain that datasets represent an absolute maximum or minimum value that could ever be observed experimentally, then the modeler should define a very strict adherence to dataset(s). Like others

(44), we tend to subscribe to the notion that a model likely captures more biological variability than the heterogeneity observed from the naturally limited sample sizes procured from experimental datasets.

If *CaliPro* fails to identify a robust calibrated parameter space, the user should evaluate their input prior to attempting other methods of calibration. Primarily, we suggest evaluating the pass set definition. This is a crucial step within *CaliPro*, and as our results section shows, iteration successions do not require the same pass set definition. In general, we have found the number of *CaliPro* iterations should have an inverse relationship with the leniency of the pass set definition. Thus, the pass set definition should become more strictly aligned with the experimental datasets as *CaliPro* progresses through iterations.

The method of refining the model parameter space is another user input that can dictate the success of calibration. HDR more quickly narrows parameter space between iterations. If the range of experimental data is very narrow, HDR may be the correct choice (such as the predator-prey model and transmission ODE model examples). However, if the range of experimental data varies greatly within one time point, ADS might be the more appropriate choice. In general, we suggest that modelers use ADS as this method accounts for information from all aspects of parameter space (pass and fail sets) whereas HDR only includes information from a subset of space (only pass sets).

While we have shown that *CaliPro* works for both stochastic and deterministic models, *CaliPro* may not be the correct approach for every calibration situation. For example, there is a vast literature of calibration solutions targeted at recapitulating just one dynamic in a mathematically rigorous manner. Further, *CaliPro* is only able to identify a parameter space where system outcomes recapitulate the dynamics of the experimental dataset. In the predator-prey model (Example 1), it is well-known that the system can exhibit chaotic behavior (62). However, because the synthetic experimental dataset for that example does not exhibit this chaotic behavior, *CaliPro* does not identify a parameter space that captures that system behavior. More generally, when applying *CaliPro* to any modeling system, *CaliPro* is unlikely to find behavior

that exists outside the ranges of calibration datasets, and thus may "miss" potentially interesting behaviors that could be predictions of the model for other parameter ranges.

Additionally, if the modeler is comfortable specifying likelihood functions to relate the model and experimental datasets in-hand, we suggest employing one of the suites of Bayesian calibration approaches, such as SIR. Further, in our experience, calibrating agent-based models that exhibit oscillations (such as agent-based models of predator-prey dynamics) with *CaliPro* is a difficult task. Identifying the pass run set in such a situation is complicated as the timing of the oscillations may differ between model simulation and experimental data, resulting in a failed run even when frequency and peak-to-trough values of simulations and experiments are identical. For agent-based models that exhibit oscillations, one could perform a Fourier transform on simulation outcomes and compare to experimental data within the frequency domain to evaluate the model as one solution.

In addition to enabling models to reasonably approximate biological processes, we believe a great strength of *CaliPro* is the potential to extend beyond the calibration protocol itself. In particular, the parameter density plots (as we showed in Figure 4) that are created for the pass and fail parameter sets within every iteration provide a large amount of information to the modeler. In general, we advise using the parameter density plots as a quick and easy method to identify and focus on certain behavior in the model. For example, if a subset of runs exhibit interesting behavior near the end of a simulation, the modeler can consider this subset the pass run set and then compare the parameter densities of the pass parameter set to those of the fail parameter set – those that do not exhibit the behavior. Moreover, after the final iteration, when the model has been calibrated to the experimental datasets, a modeler could use the parameter density plots (Figure 4) in order to identify the ideal prior distribution of each parameter (instead of uniform or normal) for future model simulations. Finally, beyond the scope of this paper – but an important consideration for any calibration or modeling process – we believe the parameter density plots offer a possible method for identifying highly correlated parameters by isolating parameters whose density plots are near identical across model behavior (see (63) for an excellent framework to address parameter identifiability).

7.6 References

1. Qu Z, Garfinkel A, Weiss JN, Nivala M. Multi-scale modeling in biology: How to bridge the gaps between scales? Vol. 107, Progress in Biophysics and Molecular Biology. 2011. p. 21–31.
2. Schliess F, Hoehme S, Henkel SG, Ghallab A, Driesch D, Böttger J, et al. Integrated metabolic spatial-temporal model for the prediction of ammonia detoxification during liver damage and regeneration. Hepatology. 2014;60(6):2040–51.
3. Kuepfer L, Kerb R, Henney AM. Clinical translation in the virtual liver network. Vol. 3, CPT: Pharmacometrics and Systems Pharmacology. 2014.
4. Schwen LO, Schenk A, Kreutz C, Timmer J, Rodríguez MMB, Kuepfer L, et al. Representative sinusoids for hepatic four-scale pharmacokinetics simulations. PLoS ONE. 2015;10(7).
5. Cedersund G, Strålfors P. Putting the pieces together in diabetes research: Towards a hierarchical model of whole-body glucose homeostasis. European Journal of Pharmaceutical Sciences. 2009;36(1):91–104.
6. Nyman E, Brännmark C, Palmér R, Brugård J, Nyström FH, Strålfors P, et al. A hierarchical whole-body modeling approach elucidates the link between in vitro insulin signaling and *in vivo* glucose homeostasis. Journal of Biological Chemistry. 2011;286(29):26028–41.
7. Brännmark C, Nyman E, Fagerholm S, Bergenholm L, Ekstrand EM, Cedersund G, et al. Insulin signaling in type 2 diabetes: Experimental and modeling analyses reveal mechanisms of insulin resistance in human adipocytes. Journal of Biological Chemistry. 2013;288(14):9867–80.
8. Santoni D, Pedicini M, Castiglione F. Implementation of a regulatory gene network to simulate the TH1/2 differentiation in an agent-based model of hypersensitivity reactions. Bioinformatics. 2008;24(11):1374–80.
9. Palsson S, Hickling TP, Bradshaw-Pierce EL, Zager M, Jooss K, O'Brien PJ, et al. The development of a fully-integrated immune response model (FIRM) simulator of the immune response through integration of multiple subset models. BMC Systems Biology. 2013;7.
10. Castiglione F, Pappalardo F, Bianca C, Russo G, Motta S. Modeling biology spanning different scales: An open challenge. Vol. 2014, BioMed Research International. 2014.
11. Azhar N, Vodovotz Y. Innate immunity in disease: Insights from mathematical modeling and analysis. Advances in Experimental Medicine and Biology. 2014;844:227–43.
12. Warsinske HC, Pienaar E, Linderman JJ, Mattila JT, Kirschner DE. Deletion of TGF-β1 increases bacterial clearance by cytotoxic t cells in a tuberculosis granuloma model. Frontiers in Immunology. 2017;8(DEC).
13. Kitano H. Systems biology: A brief overview. Vol. 295, Science. 2002. p. 1662–4.
14. Read MN, Alden K, Timmis J, Andrews PS. Strategies for calibrating models of biology. Briefings in Bioinformatics. 2018;
15. Bohachevsky IO, Johnson ME, Stein ML. Generalized simulated annealing for function optimization. Technometrics. 1986;28(3):209–17.
16. Holland JH. Adaptation in natural and artificial systems : an introductory analysis with applications to biology, control, and artificial intelligence. Ann Arbor University of Michigan Press 1975. University of Michigan Press; 1975. viii, 183 p.
17. Wang QJ. The Genetic Algorithm and Its Application to Calibrating Conceptual Rainfall-Runoff Models. Water Resources Research. 1991;27(9):2467–71.

18. Bottou L. Large-Scale Machine Learning with Stochastic Gradient Descent. In: Proceedings of COMPSTAT'2010. 2010. p. 177–86.
19. Hogue TS, Sorooshian S, Gupta H, Holz A, Braatz D. A multistep automatic calibration scheme for river forecasting models. Journal of Hydrometeorology. 2000;1(6):524–42.
20. Gábor A, Banga JR. Robust and efficient parameter estimation in dynamic models of biological systems. BMC Systems Biology. 2015;9(1).
21. Regev A, Teichmann SA, Lander ES, Amit I, Benoist C, Birney E, et al. The human cell atlas. eLife. 2017;6.
22. Friedman AA, Letai A, Fisher DE, Flaherty KT. Precision medicine for cancer with next-generation functional diagnostics. Vol. 15, Nature Reviews Cancer. 2015. p. 747–56.
23. Deng X, Nakamura Y. Cancer Precision Medicine: From Cancer Screening to Drug Selection and Personalized Immunotherapy. Vol. 38, Trends in Pharmacological Sciences. 2017. p. 15–24.
24. Spinosa PC, Humphries BA, Mejia DL, Buschhaus JM, Linderman JJ, Luker GD, et al. Short-term cellular memory tunes the signaling responses of the chemokine receptor CXCR4. Science Signaling. 2019;12(588).
25. Rikard SM, Athey TL, Nelson AR, Christiansen SLM, Lee JJ, Holmes JW, et al. Multiscale Coupling of an Agent-Based Model of Tissue Fibrosis and a Logic-Based Model of Intracellular Signaling. Frontiers in Physiology. 2019;
26. Cockrell C, An G. Sepsis reconsidered: Identifying novel metrics for behavioral landscape characterization with a high-performance computing implementation of an agent-based model. Journal of Theoretical Biology. 2017;430:157–68.
27. Pienaar E, Sarathy J, Prideaux B, Dietzold J, Dartois V, Kirschner DE, et al. Comparing efficacies of moxifloxacin, levofloxacin and gatifloxacin in tuberculosis granulomas using a multi-scale systems pharmacology approach. PLoS computational biology. 2017;13(8):e1005650.
28. Menzies NA, Soeteman DI, Pandya A, Kim JJ. Bayesian Methods for Calibrating Health Policy Models: A Tutorial. PharmacoEconomics. 2017;35(6):613–24.
29. Ades AE, Sculpher M, Sutton A, Abrams K, Cooper N, Welton N, et al. Bayesian methods for evidence synthesis in cost-effectiveness analysis. Vol. 24, PharmacoEconomics. 2006. p. 1–19.
30. Raftery AE, Bao L. Estimating and Projecting Trends in HIV/AIDS Generalized Epidemics Using Incremental Mixture Importance Sampling. Biometrics. 2010;66(4):1162–73.
31. Whyte S, Walsh C, Chilcott J. Bayesian calibration of a natural history model with application to a population model for colorectal cancer. Vol. 31, Medical Decision Making. 2011. p. 625–41.
32. Rutter CM, Miglioretti DL, Savarino JE. Bayesian calibration of microsimulation models. Journal of the American Statistical Association. 2009;104(488):1338–50.
33. Lunn DJ, Thomas A, Best N, Spiegelhalter D. WinBUGS - A Bayesian modelling framework: Concepts, structure, and extensibility. Statistics and Computing. 2000;10(4):325–37.
34. Sunnåker M, Busetto AG, Numminen E, Corander J, Foll M, Dessimoz C. Approximate Bayesian Computation. PLoS Computational Biology. 2013;9(1).
35. Beaumont MA, Zhang W, Balding DJ. Approximate Bayesian computation in population genetics. Genetics. 2002;162(4):2025–35.
36. Cowles MK, Carlin BP. Markov Chain Monte Carlo Convergence Diagnostics: A Comparative Review. Journal of the American Statistical Association. 1996;91(434):883.

37. Farah M, Birrell P, Conti S, Angelis D De. Bayesian Emulation and Calibration of a Dynamic Epidemic Model for A/H1N1 Influenza. Journal of the American Statistical Association. 2014;109(508):1398–411.
38. Rubin DB. Using the SIR Algorithm to Simulate Posterior Distributions. Vol. 3, Bayesian Statistics. 1988. p. 395–402.
39. Rajaona H, Septier F, Armand P, Delignon Y, Olry C, Albergel A, et al. An adaptive Bayesian inference algorithm to estimate the parameters of a hazardous atmospheric release. Atmospheric Environment. 2015;122:748–62.
40. Steele RJ, Raftery AE, Emond MJ. Computing normalizing constants for finite mixture models via incremental mixture importance sampling (IMIS). Journal of Computational and Graphical Statistics. 2006;15(3):712–34.
41. Cornuet JM, Marin JM, Mira A, Robert CP. Adaptive Multiple Importance Sampling. Scandinavian Journal of Statistics. 2012;39(4):798–812.
42. Blum C, Roli A. Metaheuristics in Combinatorial Optimization: Overview and Conceptual Comparison. Vol. 35, ACM Computing Surveys. 2003. p. 268–308.
43. Brewka G. Artificial intelligence—a modern approach by Stuart Russell and Peter Norvig, Prentice Hall. Series in Artificial Intelligence, Englewood Cliffs, NJ. Vol. 11, The Knowledge Engineering Review. 1996. 78–79.
44. An G. The Crisis of Reproducibility, the Denominator Problem and the Scientific Role of Multi-scale Modeling. Bulletin of Mathematical Biology. 2018;80(12):3071–80.
45. Hyndman RJ. Computing and Graphing Highest Density Regions. American Statistician. 1996;50(2):120–6.
46. Wessler T, Joslyn LR, Borish HJ, Gideon HP, Flynn JL, Kirschner DE, et al. A computational model tracks whole-lung *Mycobacterium tuberculosis* infection and predicts factors that inhibit dissemination. PLOS Computational Biology. 2020 May 20;16(5):e1007280.
47. Wigginton JE, Kirschner D. A Model to Predict Cell-Mediated Immune Regulatory Mechanisms During Human Infection with *Mycobacterium tuberculosis*. The Journal of Immunology. 2001;166(3):1951–67.
48. Sud D, Bigbee C, Flynn JL, Kirschner DE. Contribution of CD8+ T Cells to Control of *Mycobacterium tuberculosis* Infection. The Journal of Immunology. 2014;176(7):4296–314.
49. Guzzetta G, Kirschner D. The Roles of Immune Memory and Aging in Protective Immunity and Endogenous Reactivation of Tuberculosis. PLoS ONE. 2013;8(4).
50. Wong EA, Joslyn L, Grant NL, Klein E, Lin PL, Kirschner DE, et al. Low Levels of T Cell Exhaustion in Tuberculous Lung Granulomas. Infection and Immunity. 2018;86(9).
51. Cilfone NA, Perry CR, Kirschner DE, Linderman JJ. Multi-Scale Modeling Predicts a Balance of Tumor Necrosis Factor-α and Interleukin-10 Controls the Granuloma Environment during *Mycobacterium tuberculosis* Infection. PLoS ONE. 2013;8(7).
52. Cilfone NA, Ford CB, Marino S, Mattila JT, Gideon HP, Flynn JL, et al. Computational Modeling Predicts IL-10 Control of Lesion Sterilization by Balancing Early Host Immunity–Mediated Antimicrobial Responses with Caseation during *Mycobacterium tuberculosis* Infection . The Journal of Immunology. 2015;194(2):664–77.
53. Fallahi-Sichani M, El-Kebir M, Marino S, Kirschner DE, Linderman JJ. Multiscale Computational Modeling Reveals a Critical Role for TNF- Receptor 1 Dynamics in Tuberculosis Granuloma Formation. The Journal of Immunology. 2011;186(6):3472–83.

54. Marino S, Linderman JJ, Kirschner DE. A multifaceted approach to modeling the immune response in tuberculosis. Wiley Interdisciplinary Reviews: Systems Biology and Medicine. 2011;3(4):479–89.
55. Lin PL, Ford CB, Coleman MT, Myers AJ, Gawande R, Ioerger T, et al. Sterilization of granulomas is common in active and latent tuberculosis despite within-host variability in bacterial killing. Nature Medicine. 2014;20(1):75–9.
56. Lin PL, Rodgers M, Smith L, Bigbee M, Myers A, Bigbee C, et al. Quantitative comparison of active and latent tuberculosis in the cynomolgus macaque model. Infection and Immunity. 2009;77(10):4631–42.
57. Lin PL, Flynn JL. Understanding Latent Tuberculosis: A Moving Target. The Journal of Immunology. 2010;185(1):15–22.
58. Marino S, Kirschner D. A Multi-Compartment Hybrid Computational Model Predicts Key Roles for Dendritic Cells in Tuberculosis Infection. Computation. 2016;4(4):39.
59. Marino S, Gideon HP, Gong C, Mankad S, McCrone JT, Lin PL, et al. Computational and Empirical Studies Predict *Mycobacterium tuberculosis*-Specific T Cells as a Biomarker for Infection Outcome. PLoS Computational Biology. 2016;12(4).
60. Segovia-Juarez JL, Ganguli S, Kirschner D. Identifying control mechanisms of granuloma formation during M. tuberculosis infection using an agent-based model. Journal of Theoretical Biology. 2004;231(3):357–76.
61. Cadena AM, Fortune SM, Flynn JL. Heterogeneity in tuberculosis. Nature Reviews Immunology. 2017;17(11):691–702.
62. Toro M, Aracil J. Chaotic behavior in predator-prey-food system dynamics models. Proceedings of the 1986 International Conference of the Systems Dynamics Society: System Dynamics: On the Move. . 1986. p. 353.
63. Eisenberg MC, Jain H V. A confidence building exercise in data and identifiability: Modeling cancer chemotherapy as a case study. Journal of Theoretical Biology. 2017;431:63–78.
64. Marino S, Hogue IB, Ray CJ, Kirschner DE. A methodology for performing global uncertainty and sensitivity analysis in systems biology. Vol. 254, Journal of Theoretical Biology. 2008. p. 178–96.

8 Conclusions and Future Directions

8.1 Summary

One quarter of the worldwide population is currently infected with *Mycobacterium tuberculosis* (Mtb), the causative agent of tuberculosis (TB) (1). In the context of the ongoing COVID-19 pandemic, TB still represents a significant global burden and is the second-leading cause of global morbidity from an infectious agent (2). The ultimate weapon against TB would be a highly efficacious vaccine. Despite considerable effort and multiple large-stage clinical trials across the past two decades (3,4), a clinically effective vaccine has remained elusive.

Identifying the various roles that T cells play in Mtb infection is critical to develop effective vaccines and host-directed therapies against TB. Experimental studies have proven invaluable in characterizing the fundamental functions of T cells during Mtb infection. However, the clinical failure of past vaccines developed using reductionist approaches suggests that a new approach is necessary to fully appreciate their role in TB.

In this dissertation, we used a computational and mathematical modeling approach to integrate datasets across multiple scales and better understand the role of T cells in controlling Mtb infection at both the granuloma and whole-host scale. We use computational modeling to compare T-cell responses between species following vaccination and utilized a model of granuloma formation to explain low levels of T cell exhaustion. Finally, we present a whole-host modeling framework that has implications for evaluating future vaccination or therapeutic strategies in TB. The major conclusions of this dissertation are listed below, organized by main findings.

8.1.1 The granuloma is a physical barrier that prevents T-cell exhaustion

T-cell functionality within a granuloma has been previously shown to be surprisingly low, wherein approximately 10% of T cells produce cytokines (5). One hypothesis for the observed lack of T-cell function is T-cell exhaustion. T-cell exhaustion is a type of T-cell dysfunction characterized by a loss of effector functions and caused by chronic antigen stimulation (6,7). In Chapter 2, we investigated the possibility of T-cell exhaustion within TB granulomas.

Despite the potential for chronic antigen stimulation within a granuloma, T cells in NHPs experiments did not exhibit phenotypic markers of T-cell exhaustion. Further, we used *GranSim*, a computational model of granuloma formation and function, to show that T-cell exhaustion is not present at high levels within *in silico* granuloma formation. We illustrate that chronic antigen stimulation, and therefore T-cell exhaustion, can only occur within the center of granulomas. We therefore predict that the structure of the granuloma itself prevents the potential of widespread T-cell exhaustion. This prediction suggests that the structure of the granuloma may also prevent T-cell function, as the majority of T cells are located at the outer-most layers of the granuloma, far from infected macrophages within the center of the granuloma. Other work in our lab supported this hypothesis (8).

8.1.2 Multi-functional CD8+ T cells prevent dissemination of bacteria throughout the lung

The majority of granulomas that form following Mtb infection contain bacteria to an isolated environment within the lung (9). However, some granulomas are unable to control Mtb growth, leading to bacterial escape and spread elsewhere within the lung environment. These bacteria seed the growth of new granulomas and are associated with poor TB outcomes for hosts (9). In Chapter 3, we built MultiGran, a novel whole-lung model of multiple granuloma formation in the lungs to track and predict rates of dissemination. We calibrate this multi-scale model to granuloma-scale datasets and then validate the model against whole-lung datasets. We perform sensitivity analysis to identify mechanisms that prevent dissemination events through the lungs across time. We predict that the relative percentage of granuloma CD8+ T cells that can exhibit both cytotoxic and cytokine-producing functions is negatively correlated to the number of dissemination events across time. This particular type of T-cell, known as a multi-functional CD8+ T cell, has been relatively understudied within TB literature (10). Our work suggests that

this cell requires further study and offers potential to prevent the worst forms of TB disease. We propose that future vaccination and therapeutic efforts should attempt to induce greater numbers of this particular cell type within granulomas.

8.1.3 Prior BCG vaccination impacts the T-cell response to current vaccines

The only licensed TB vaccine is not highly efficacious against adult forms of TB. The vaccine, called Bacillus Calmette-Guérin (BCG), is widely used at birth to prevent TB disease in infants and children, but its efficacy amongst the adult population varies from 0-80% (11,12). A highly efficacious vaccine would be the ultimate weapon against the TB global epidemic. However, TB vaccine candidates have failed to be highly effective during large-scale clinical trials. H56 is a TB vaccine in phase II clinical trials that was previously shown to be effective in NHP studies (13).

In Chapter 4, we use H56 as a case study to explore similarities and differences between human and NHP T-cell responses to vaccination. We calibrated a two-compartment lymph node and blood ordinary differential equation model to the NHP and human T-cell response to ESAT6 and Ag85B antigens following vaccination with BCG and H56. We demonstrate that NHP and human T-cell responses to the H56 vaccination were generally similar, with a few differences in rates of cell proliferation, differentiation and reactivation. We additionally show that the secondary response of both species to Ag85B (an antigen present in both BCG and H56 vaccines) upregulates differentiation to a central memory CD4+ T cell phenotype. This prediction indicates that prior BCG vaccination will influence future vaccination efforts: we suggest that the preclinical efficacy of any new TB vaccine candidates must be evaluated within the context of prior BCG vaccination, as the majority of the world has received BCG at birth (14).

8.1.4 A whole-host model describes the multiscale immune response to Mtb

In Chapter 5, we present a novel whole-host modeling platform. By linking the models developed and utilized in Chapter 3 and Chapter 4, we developed a multi-scale model that tracks the formation of multiple granulomas, dissemination events within the lungs, and the adaptive immune response to Mtb infection across the lymph nodes, blood, and granulomas within a virtual host. The model, called *HostSim*, was calibrated and validated against multiple NHP

datasets across granuloma and whole-host scales. *HostSim* has the potential to be used within multiple realms of TB research. As shown in this thesis, it can be used as a tool to investigate basic questions about the immune response following Mtb infection or reinfection. However, it has the potential to be used in epidemiological studies or as a tool to investigate therapeutics, antibiotic regimens, or vaccination strategies within a broader, personalized-medicine approach to TB care. These later applications are further discussed within the future directions of this chapter.

8.1.5 Biomarkers may be transient in TB

Clinically, TB patients are often placed within one of two binary classifications: latent tuberculosis or active tuberculosis. Latent tuberculosis (LTBI) cases are asymptomatic, potentially contagious individuals who harbor the bacteria yet show no outward signs of disease. Active TB cases exhibit the symptoms of TB disease (i.e. fever, night sweats, coughing, weight-loss, etc.). Much remains unknown about the biology that drives an individual towards LTBI or active TB outcomes, but many studies have attempted to identify biomarkers differentiating these two states (reviewed in (15–18)).

In Chapter 5, we demonstrate the utility of mathematical and computational modeling approaches to act as a bridge to better understand events within a host that lead to empirically evident whole-host outcomes (such as LTBI or active TB). We calibrate and validate *HostSim* to multiple datasets and find that early events in Mtb infection are predictive of clinical classifications over 100 days later. Importantly, we predict that the relationship between blood immune cell numbers and numbers of cells in the lung may only be well-defined at early timepoints following infection. When a patient presents in the clinic months or years later, cells in the blood may not reflect events occurring in the lung. As such, we predict that biomarkers in TB may not be generalizable to every patient, at every point in time.

8.1.6 Protection against reinfection is dependent on resident memory T cells that wane across time

Concomitant immunity is a paradoxical immune status wherein protection against pathogen re-encounter coincides with an inability to clear the persistent, primary infection (19). In TB,

concomitant immunity in NHPs is robust at relatively short timepoints between primary and reinfection (20). However, the mediators and longevity of a concomitant immune response in TB are unknown, although it is hypothesized that resident memory T cells (TRM) play a prominent role in preventing reinfection.

In Chapter 6, we perform multiple sets of virtual reinfection studies across a population of *HostSim* virtual hosts. We predict TRM are the main drivers of a concomitant immune response in TB. Further, we predict, for the first time, the lifespan of these cell populations in human lungs. We predict that protection against reinfection begins to wane with the loss of these cell populations across time (~3 years). However, in the absence of TRM, we still observed limited protection against active TB during reinfection, an outcome that was driven by high levels of circulating Mtb-specific T cells in the blood originating from primary infection.

8.1.7 *CaliPro* can calibrate complex models to diverse biological datasets

Calibrating mathematical and computational models to biological datasets can be a difficult task. In Chapter 6, we present a new protocol for calibrating complex models to multiple biological datasets across time. We demonstrate the utility of this protocol, called *CaliPro*, to quickly calibrate deterministic or stochastic models to a robust parameter space wherein the vast majority of model runs will satisfy user-provided criteria for calibration. We comment on crucial aspects of the calibration process, including formalizing a modeler's calibration goals within what we call the 'pass set definition'. We introduce a new method of refining and narrowing parameter space, called alternative density subtraction (ADS), which leverages information from both regions of parameter space where model runs match experimental data as well as regions of parameter space where model runs fail to match experimental data. Finally, we postulate that *CaliPro* could be extended further as an analysis tool to isolate intriguing model outcomes.

8.2 Future Directions

8.2.1 Future directions in T-cell biology and memory

The immune response to Mtb is T-cell dependent. Throughout this dissertation, we have incorporated known and hypothesized functions of the T-cell mediated adaptive immune response into various mathematical and computational models. As key takeaways, we have predicted the importance of two cell types, CD8+ multifunctional T cells and resident memory T cells, that could be further evaluated for therapeutic or vaccination efforts.

However, much still remains unknown about T-cell biology. In particular, there are two outstanding questions for T-cell biology in the context of Mtb infection. First, what are the mechanisms that cause a T cell to set up residency within the lung? Second, what are the characteristics of a memory T-cell pool across time? In Chapter 6, we model the establishment of resident memory T-cell populations in the lung phenomenologically due to a lack of evidence on how precisely T cells establish permanent residency in the lung (21–23). However, future work could test various mechanisms of residency by asking questions such as 'do TRMs differentiate from effector cells that enter the lung?' or 'are TRM truly a separate T cell with distinct functions or are they a type of highly specialized effector memory cell'? In order to model these scenarios, longitudinal datasets from cells in both lung and blood are required – datasets that are difficult to curate in NHPs or humans and can only be derived from parallel mice studies. However, as we showed in Chapter 6, even fundamental aspects of TRM biology (i.e., death rate) differ between primates and mice, limiting the utility of mice as an animal model for questions about TRM. In order to mechanistically model these cell populations, we need more experimental evidence of establishment in the lungs and the role(s) they play in clearing infection.

Textbook immunology teaches that there are distinct subsets of T-cell memory that are generated and maintained across time. However, recent work has suggested that T-cell memory subsets might not be independent. For example, in Sendai virus infection and lymphocytic choriomeningitis (LCMV) infection, the effector memory T-cell population plays a prominent role in executing a potent, effective recall response at earlier timepoints following primary infection, but the composition of the memory T-cell pool becomes primarily central memory at later timepoints (24,25). The paradigm of a dynamic memory T-cell pool has clear applications for vaccination, wherein vaccines may be protective shortly following vaccination, but could lose

efficacy across time if that efficacy is dependent on shorter lived memory cells or effector memory cell populations. Modeling T-cell memory across time could better inform vaccine dose administration (i.e., when to administer a second dose) based on this emerging work.

8.2.2 Future Directions for *GranSim*

In Chapter 2, we added a functionality to *GranSim* that allowed us to make predictions about T-cell exhaustion within tuberculosis lung granulomas. Herein, I make three suggestions that could extend the utility of *GranSim*, not only regarding T-cell dynamics during infection, but when addressing broader questions related to dissemination or contagiousness.

First, as shown in Chapter 2, the spatial structure of the granuloma is inherently related to the functionality of T cells. This prediction has been validated by other work within the lab that showed granuloma structure not only prevents T-cell exhaustion, but also can inhibit proper T cell function at the site of infection (8). However, *GranSim* does not track multi-functional T cells within the granuloma, and instead assigns a single function to T cells (IFN-γ producing T cells or cytotoxic T cells or regulatory T cells). In Chapter 4, we used a separate modeling framework to predict that multi-functional CD8+ T cells are crucial in preventing bacterial dissemination and escape from the granuloma environment. Modeling multi-functional T-cells within the spatial modality of *GranSim* could further validate this prediction. Furthermore, multifunctional CD8+ T cells have a relatively controversial role in TB and have been associated with both active TB, LTBI and vaccinated individuals (26–28). Exploring the role of multi-functional T cells within the spatial structure of a granuloma could potentially answer some long-standing questions within the field about this cell as a potential correlate of protection.

Second, airways and vasculature are important components of granuloma formation that provide physical constraints to collective lesion growth and cellular mobility. In particular, as Mtb is a non-motile bacterium, airways offer a conduit for Mtb to reseed elsewhere within the lungs (9) or for transmission of disease to other individuals (29). Additionally, bronchoalveolar lavage (BAL) fluid datasets could be used for calibration or validation of airway events in *GranSim*, as this is a type of dataset that can be acquired serially in either NHPs or humans (30). By isolating regions of the *GranSim* grid environment as airways, we could take a relatively easy first step

toward modeling how a granuloma may disseminate into the airways and further explore the complicated relationship between infection and infectiousness in TB.

Finally, in other work during my time in graduate school, we published a pipeline for identifying sub-structures within *in silico* and in vivo granulomas using topological data analysis and graphical information systems (GIS) (31). Briefly, we tested the ability of various machine learning algorithms to predict associations between granuloma structural patterns and uncontrolled or controlled bacterial growth outcomes (31). This pipeline could be extended for the comparison and integration of novel datasets within *GranSim*. In particular, spatial transcriptomics (32) is a new technique that could generate unique datasets for direct comparison with *GranSim*'s cellular location and structure datasets. Pairing spatial transcriptomics from slices of NHP granulomas, GIS, topological data analysis, and agent-based modeling could provide fundamental understanding about granuloma structure across time and could better inform antibiotic design.

8.2.3 Future Directions for *HostSim*

8.2.3.1 Improvements to dissemination in HostSim

In *HostSim*, we model dissemination events in a phenomenological way. Dissemination is modeled as a probability based on the bacterial burden of a granuloma. As currently modeled, the majority of dissemination events occur after day 50. However, its known that dissemination events can also occur quite early within infection (9), an outcome not well-described by these first versions of *HostSim*. One issue with capturing early dissemination is the lack of known, or even hypothesized, mechanisms that drive dissemination. Current, ongoing work within the lab using *GranSim* shows that neutrophils are a potential vehicle of local dissemination (unpublished). Neutrophils are cells that can respond at very early timepoints during infection, have the unique capacity for surviving within caseum, and are phagocytic cells that are unable to kill intracellular Mtb (33). Consequently, this cell type is potentially an early instigator of local dissemination events. Translating those studies from *GranSim* to model neutrophils within *HostSim* could provide greater insight into local dissemination events at early timepoints.

Non-local dissemination events in *HostSim* could be modeled more mechanistically in two ways. The first, and perhaps most straightforward solution, is to add greater anatomical structure to the lung architecture of *HostSim*. This added detail would not only provide physical structure to non-local dissemination but could lend greater insight into the relationship between individual granuloma outcomes and infectiousness during Mtb infection. MRI and CT scans of the lungs provide information about airway location and vasculature within lungs (34). By adding bronchial trees and airways, *HostSim* granuloma inoculation could become more mechanistic, and as granulomas develop, non-local dissemination could be an event triggered by granuloma growth into one of the airways. With this suggestion, I hypothesize that non-local dissemination events may be more related to granuloma location and size than granuloma CFU, although granuloma size and CFU are loosely associated (35).

Second, lymph nodes have been identified as a relatively neglected site of infection within TB (36), and are thought to be both an origin and terminus of bacterial dissemination (37). Modeling lymph node granuloma formation is a natural next step in *HostSim* that not only provides mechanisms for non-local dissemination, but also provides another whole-host outcome for *HostSim*: extrapulmonary TB. In Chapter 5, we note that *HostSim* only tracks three unique physiological compartments. Should we wish to capture some of the worst forms of TB (extrapulmonary TB), modeling bacteria within the lung-draining lymph node is a good first step.

8.2.3.2 Adding resolution to the blood compartment in *HostSim*

In Chapter 5, we showed that immune cell counts in the blood compartment can be transiently indicative of ongoing events within the lung and eventually drive clinical outcomes at the whole-host scale. While NHP studies have shown that the blood is not consistently reflective of events within the lungs, association studies in humans tell another story. In particular, many association studies attempt to delineate LTBI from active TB based on cytokine profiles within the blood (15–18,38–46). These studies often offer contradictory evidence about the role of various cytokines and desperately require mechanistic analysis to provide clarity about which biomarkers may be relevant in a patient-specific manner (40). Further, clinical trials of TB vaccine candidates often sample the blood at consistent time points in order to characterize cell function

and cytokine secretion within the blood (47). These studies are indicative of the never-ending search for biomarkers of infection progression and correlates of protection within TB.

Modeling cytokines within the blood compartment of *HostSim* would enable us to directly integrate this large set of human data into *HostSim*. In Chapter 3, we showed the utility of modeling as a translational tool to compare NHP and human responses to a vaccine. Modeling cytokines like TNF, IL-10, or IFN-γ would allow us to continue to use modeling in this capacity - as a tool to bridge the translational gap. Finally, we have previously published studies regarding the dynamic balance of pro-inflammatory and anti-inflammatory cytokines at the sites of infection during chronic disease (48). By modeling cytokine dynamics within the blood compartment, we could test the hypothesis that this dynamic balance is intrinsically systemic (40), and not necessarily isolated to the sites of infection in TB.

8.2.3.3 Integrating single cell sequencing datasets into *HostSim*

A constant challenge in modeling is the integration of novel datasets that may not be perfectly suited for a given modeling platform. As modelers, we are often forced to ask ourselves: should we transform the data (at some loss in resolution) in order to fit the conditions of the modeling framework or should we change the modeling technique? For example, in this dissertation, we used several different modeling techniques in order to answer the scientific question at hand. We used an agent-based model to answer questions about the spatial behavior of T cells in Chapter 2, then utilized a blood and lymph node model in Chapter 4 to answer questions about the magnitude and timing of T-cell response to TB vaccines, and finally, created whole-lung and whole-host models in order to answer questions at that scale in Chapter 3, Chapter 5 and Chapter 6. Each choice between model platforms depends on 1) the scientific question and 2) the available datasets to inform model development.

Recently, our experimental collaborators published single cell profiling data (scRNA-Seq) on lung granulomas (49). While spatial transcriptomics techniques offer comparisons to ABM platforms like *GranSim* (see above), single cell sequencing datasets offer excellent calibration targets for ODE models. Briefly, scRNA-Seq in this context provides counts, concentrations, or

percentages of cell types within a tissue sample at a given time point. Similarly, the outcomes of *HostSim* granuloma ODEs are cell counts across time. Therefore, we can directly compare ODE outcomes to the single cell data across multiple time points. This new data can be paired with our flow cytometry datasets that have been used for calibration with *CaliPro*, as discussed in Chapter 6. I should note that the proposal to integrate scRNA-Seq datasets as calibration targets is accompanied with a bit of caution. Interpreting single cell data in this manner requires an inherent assumption: gene expression is suggestive of cellular function within a granuloma.

8.2.3.4 Evaluating therapeutics using a virtual patient

In Chapter 5, we presented a first-of-its kind whole-host modeling framework that tracks the immune response across lymph nodes, blood and individual granulomas in lungs following Mtb infection. As shown in this dissertation, *HostSim* can be used to identify cellular mechanisms that prevent the worst forms of TB and could therefore be evaluated as new therapeutic targets (such as multifunctional CD8+ T cells). As a first step towards the development of a virtual tuberculosis patient, *HostSim* has the potential to evaluate therapeutic combinations or strategies against TB.

In Chapter 4, we utilized the blood and lymph node compartments of *HostSim* to compare NHP and human responses to a TB vaccine called H56. Our sensitivity analysis revealed the third H56 dose in humans was not significantly associated memory T cell counts across time. While the relationship between memory T cell counts and vaccine efficacy is yet to be explored, this result suggests that the H56 dose administration regimen was not optimized to maximize T-cell memory generation. Our analysis predicts that even a brute force comparison of multiple H56 dose regimens in *HostSim* prior to clinical trials would have led to the selection of a better H56 dose administration protocol. By employing a virtual clinical trial approach prior to the actual clinical trial, resources and trial time could have been saved while still maximizing memory T cell magnitude across time.

This idea to optimize vaccine dose administration is seldom mentioned within the literature. In total, only three papers have been published on the topic (50–52). The authors call this process immunostimulation/immunodynamics (IS/ID), analogous to the process of

pharmacokinetics/pharmacodynamics (PK/PD) that analyzes the effects of drug dose administration. In particular, the TB vaccination field would benefit enormously from an IS/ID approach paired with *HostSim* as TB vaccine clinical trials are notoriously non-standardized from trial to trial, and it is difficult to compare trial results statistically (47). We showed in Chapter 4 that mathematical modeling is a tool that has the flexibility to compare non-standard protocols and lend insight into different mechanisms that may drive outcomes across studies. Should we include cytokines in the blood compartment of *HostSim* (as suggested above), *HostSim* quickly becomes an *in silico* platform for directly comparing and analyzing TB vaccines across non-standardized protocols and could inform dose selection, timing of administration and clinical trial design. In ongoing lab work, antibiotic regimens are being integrated for comparison and evaluation within the *HostSim* framework.

8.2.4 Extending Model Development, Analysis and Calibration

8.2.4.1 *CaliPro* v2.0 – a generalized calibration suite

In Chapter 6, we demonstrate that *CaliPro* can calibrate simple, complex, deterministic or stochastic model formulations to biological datasets across time. *CaliPro* was intentionally conceived as a flexible calibration protocol such that the pass definition can be formalized in a manner fit for the modeler's calibration specifications.

Implementing a generalized coding framework for *CaliPro* would further extend this goal for a flexible calibration process. There are several ways I propose generalizing *CaliPro*. First, I suggest extending our methods of redefining parameter space (ADS or HDR) to a multi-variate method that incorporates densities from multiple parameters. Currently these methods are applied on a 1D space (for each parameter), but more information about parameter identifiability or parameter dependencies could be harnessed by performing these methods across the multidimensional parameter space.

Additionally, there are several ways that *CaliPro* could be generalized from a single calibration protocol to a become a suite of calibration tools. Depending on the situation, a modeler may want to optimize model outcomes to recapitulate a single median line of the experimental data.

Should that be the case, *CaliPro* could offer that utility by including popular gradient descent optimization algorithms to search parameter space. Additionally, there are many Bayesian calibration techniques that employ more rigorous statistical comparisons between model outcomes and experimental datasets than *CaliPro* currently does. If a modeler is comfortable with a potentially discontinuous parameter space, then they could instruct *CaliPro* to employ a method like Sample Importance Resampling. Further, *CaliPro* could then be used to directly compare different calibration techniques, as offering techniques such as Sample Importance Resampling alongside ADS/HDR methods allows for head-to-head comparison of methods. Perhaps more importantly, if multiple methods agree on the same parameter space, then the modeler can be even more confident in their model structure, parameter space, and modeling assumptions prior to making predictions specific to their biological system of interest.

8.2.4.2 Unifying machine learning and mechanistic modeling

Machine learning is a powerful tool within biomedical sciences. At minimum, machine learning algorithms provide a user with the ability to quickly derive patterns from datasets and use features within a dataset to predict outcomes of interest. However, if the data is incomplete, sparse, or cannot fully capture the relationships between features and outcomes, it can fail to provide useful insights. In precisely these circumstances, I suggest a hybrid approach wherein mechanistic modeling can be paired with machine learning, to 'fill in the gaps' and enhance the resolution of datasets by providing rules about known relationships for the biological problem at hand. Pairing machine learning and mechanistic modeling techniques, while rare, has provided a unique approach to resolve a set of problems within biomedical science (53).

Conversely, machine learning could also be used to coarse-grain a sub-model within the larger modeling framework. As mechanistic models grow larger and build towards the 'virtual patient', some aspects of the modeling platform must be coarse-grained due to computational expense (54). In this case, machine learning can offer a previously trained model that can quickly relate inputs from one scale to outputs at another scale and thereby coarse-grain the processes within scales that are not-of-interest. For example, in *GranSim* a large computational cost is the diffusion process of cytokines. If we trained a neural network (or other machine learning

algorithm) to a large dataset of diffusion values from previous *GranSim* runs, we may not need to run diffusion across every time step, for every simulation, as we do now. Instead, the neural network acts as a type of 'intelligent look-up table' that can quickly and accurately predict the values of cytokines across the grid space from time step to time step. A multiscale model of thrombus growth used a neural network in this manner to coarse grain platelet cell signaling (55). Of course, if the scientific question at-hand requires running diffusion (for example: how well do antibiotics diffuse through the granuloma?) other aspects of the model could instead be coarse-grained.

Despite the potential utility of this hybrid approach, it appears as though both machine learning and mechanistic modeling fields have developed in parallel. Even if researchers do not adopt a hybrid approach that combines machine learning and mechanistic modeling, I argue for greater crosstalk and communication between fields. Model interpretability is an example of a common issue expressed in both fields, and both fields have employed similar-yet-distinct approaches to make 'black-box' models more interpretable. In particular, sensitivity analysis in mechanistic modeling is analogous to feature importance in machine learning. Both fields would benefit from evaluating the techniques utilized within the opposite field. While our lab has utilized surrogate models as a tool to perform antibiotic dose optimization studies (56), I propose using surrogate models as a method for analyzing the relationship between model parameters and model outcomes. For example, for any *GranSim* simulation, we can consider model parameters as the 'features' of our dataset and the binary outcome of granuloma sterilization (1 for sterilization, 0 for uncontrolled bacterial growth) as our prediction. Then, if we fit a random forest to this *GranSim* dataset, we could utilize a feature importance algorithm, like SHAP values (57), to identify the features (i.e. *GranSim* parameters) that were weighted most heavily in predicting whether that granuloma would sterilize or not. This type of analysis could be paired with traditional sensitivity analysis approaches (such as PRCC (58)) to strengthen conclusions about important drivers in granuloma outcomes. In this example, I have suggested pairing machine learning techniques with *GranSim*, as *GranSim* (particularly in 3D) can be computationally expensive, but this type of analysis could be incorporated within *HostSim* or any other modeling framework.

8.2.5 Future directions for TB vaccination – how can we develop a clinically effective vaccine?

The final year of my dissertation was completed remotely due to the COVID-19 worldwide pandemic. In November of 2020, less than one year after sequencing the SARS-CoV-2 genome, phase III clinical trial results were announced for two vaccine candidates that utilized a novel mRNA platform: both had greater than 90% efficacy (59,60). This extraordinary achievement motivates an obvious comparison to TB, the other leading cause of death by infectious agent worldwide, that has no such clinically effective vaccine.

In the wake of an extraordinarily successful COVID-19 vaccine effort, we are still left with several outstanding questions about TB vaccinology. In the course of my dissertation (2016-2021), research in immunology has identified new memory T cell subsets (e.g., TRMs as a quick-responding adaptive immune cell), and research in vaccinology has discovered new platforms for dose administration (e.g., mRNA vaccines) and the TB research field will certainly incorporate these findings into the next-generation of vaccine candidates. However, we are still left with a lack of broader context: How does vaccine dose impact immunogenicity? Which vaccine platform will work in TB? What if the ultimately successful vaccine strategy requires a heterologous approach, wherein the first dose targets memory cell phenotype A using an mRNA platform, but the second dose targets memory cell phenotype B using a viral vector platform? Should vaccines induce all memory T cell subsets? Or is just 2 enough? Does a highly effective and durable vaccine strike some balance between memory T cell phenotypes?

These are the types of questions that are currently unanswerable in TB vaccine research, in part, due to the very long and expensive trials that are intrinsic to testing therapies for a chronic disease like TB. It is exactly these types of questions – 'what if' questions, timing questions, and comparisons of therapeutic strategies - that are ripe for mathematical and computational modeling in the form of virtual clinical trials. In this dissertation, I have outlined the utility of mathematical and computational modeling in characterizing the role of T cells across multiple scales during Mtb infection. I have predicted the importance of two cell types, CD8+ multifunctional T cells and resident memory T cells, that can be further evaluated for therapeutic or vaccination efforts. Further, I have developed a whole-host modeling framework that offers

the first step toward virtual clinical trials that might be able to address some of the above questions. Moving forward, the TB vaccine field needs to embrace modeling and virtual clinical trials as a crucial step toward identifying a highly effective clinical vaccine against TB.

8.3 References

1. WHO. WHO Global Tuberculosis Report 2019. World Health Organization Press. 2019.
2. Um PK, Bishai WR. Immunologic goalposts for TB vaccine development. Cell Host & Microbe [Internet]. 2021;29(2):158–9. Available from: https://www.sciencedirect.com/science/article/pii/S193131282100041X
3. Ginsberg AM, Ruhwald M, Mearns H, McShane H. TB vaccines in clinical development. Tuberculosis. 2016;99:S16–20.
4. Andersen P. Tuberculosis vaccines - An update. Nature Reviews Microbiology. 2007;5(7):484–7.
5. Gideon HP, Phuah JY, Myers AJ, Bryson BD, Rodgers MA, Coleman MT, et al. Variability in Tuberculosis Granuloma T Cell Responses Exists, but a Balance of Pro- and Anti-inflammatory Cytokines Is Associated with Sterilization. PLoS Pathogens. 2015;11(1):1–28.
6. Zuniga EI, Harker JA. T-cell exhaustion due to persistent antigen: Quantity not quality? European journal of immunology. 2012;42(9):2285–9.
7. Wherry EJ. T cell exhaustion. Nature Immunology [Internet]. 2011;12(6):492–9. Available from: https://doi.org/10.1038/ni.2035
8. Millar JA, Butler JR, Evans S, Mattila JT, Linderman JJ, Flynn JL, et al. Spatial Organization and Recruitment of Non-Specific T Cells May Limit T Cell-Macrophage Interactions Within *Mycobacterium tuberculosis* Granulomas. Frontiers in Immunology [Internet]. 2021;11:3496. Available from: https://www.frontiersin.org/article/10.3389/fimmu.2020.613638
9. Martin CJ, Cadena AM, Leung VW, Lin PL, Maiello P, Hicks N, et al. Digitally Barcoding *Mycobacterium tuberculosis* Reveals In Vivo Infection Dynamics in the Macaque Model of Tuberculosis . mBio. 2017;8(3).
10. Lin PL, Flynn JL. CD8 T cells and *Mycobacterium tuberculosis* infection. Seminars in Immunopathology [Internet]. 2015;37(3):239–49. Available from: http://link.springer.com/10.1007/s00281-015-0490-8
11. Andersen P, Doherty TM. Opinion: The success and failure of BCG — implications for a novel tuberculosis vaccine. Nature Reviews Microbiology [Internet]. 2005;3(8):656–62. Available from: http://www.nature.com/doifinder/10.1038/nrmicro1211
12. Tameris MD, Hatherill M, Landry BS, Scriba TJ, Snowden MA, Lockhart S, et al. Safety and efficacy of MVA85A, a new tuberculosis vaccine, in infants previously vaccinated with BCG: A randomised, placebo-controlled phase 2b trial. The Lancet. 2013;381(9871):1021–8.
13. Lin PL, Dietrich J, Tan E, Abalos RM, Burgos J, Bigbee C, et al. The multistage vaccine H56 boosts the effects of BCG to protect cynomolgus macaques against active tuberculosis and reactivation of latent *Mycobacterium tuberculosis* infection. Journal of Clinical Investigation. 2012;122(1):303–14.
14. Zwerling A, Behr MA, Verma A, Brewer TF, Menzies D, Pai M. The BCG World Atlas: A Database of Global BCG Vaccination Policies and Practices. PLoS Medicine. 2011;8(3):e1001012.
15. Walzl G, Ronacher K, Hanekom W, Scriba TJ, Zumla A. Immunological biomarkers of tuberculosis. Nature Reviews Immunology. 2011;11(5):343–54.
16. Whitworth HS, Aranday-Cortes E, Lalvani A. Biomarkers of tuberculosis: a research roadmap. Biomarkers in medicine. 2013;7(3):349–62.

17. Wallis RS, Kim P, Cole S, Hanna D, Andrade BB, Maeurer M, et al. Tuberculosis biomarkers discovery: developments, needs, and challenges. The Lancet infectious diseases. 2013;13(4):362–72.
18. MacLean E, Broger T, Yerlikaya S, Fernandez-Carballo BL, Pai M, Denkinger CM. A systematic review of biomarkers to detect active tuberculosis. Nature microbiology. 2019;4(5):748–58.
19. Belkaid Y, Tamoutounour S. The influence of skin microorganisms on cutaneous immunity. Vol. 16, Nature Reviews Immunology. 2016. p. 353–66.
20. Cadena AM, Hopkins FF, Maiello P, Carey AF, Wong EA, Martin CJ, et al. Concurrent infection with *Mycobacterium tuberculosis* confers robust protection against secondary infection in macaques. PLoS Pathogens. 2018;14(10).
21. Morris SE, Farber DL, Yates AJ. Tissue-Resident Memory T Cells in Mice and Humans: Towards a Quantitative Ecology. The Journal of Immunology [Internet]. 2019 Nov 15;203(10):2561. Available from: http://www.jimmunol.org/content/203/10/2561.abstract
22. Slütter B, Van NB-B, Abboud G, Varga SM, Salek-Ardakani S, Harty JT. Dynamics of influenza-induced lung-resident memory T cells underlie waning heterosubtypic immunity. Science immunology. 2017;2(7).
23. Ogongo P, Porterfield JZ, Leslie A. Lung Tissue Resident Memory T-Cells in the Immune Response to *Mycobacterium tuberculosis*. Frontiers in immunology [Internet]. 2019 May 3;10:992. Available from: https://pubmed.ncbi.nlm.nih.gov/31130965
24. Martin MD, Kim MT, Shan Q, Sompallae R, Xue HH, Harty JT, et al. Phenotypic and Functional Alterations in Circulating Memory CD8 T Cells with Time after Primary Infection. PLoS Pathogens. 2015;11(10).
25. Martin MD, Badovinac VP. Defining memory CD8 T cell. Vol. 9, Frontiers in Immunology. 2018.
26. Caccamo N, Dieli F. Are polyfunctional cells protective in M. tuberculosis infection. Understanding Tuberculosis—Analyzing the Origin of *Mycobacterium tuberculosis* Pathogenicity. 2012;10:35245.
27. Aagaard C, Hoang TTKT, Izzo A, Billeskov R, Troudt JL, Arnett K, et al. Protection and polyfunctional T cells induced by Ag85B-TB10.4/IC31® against *Mycobacterium tuberculosis* is highly dependent on the antigen dose. PLoS ONE. 2009;4(6).
28. Geldenhuys H, Mearns H, Miles DJC, Tameris M, Hokey D, Shi Z, et al. The tuberculosis vaccine H4: IC31 is safe and induces a persistent polyfunctional CD4 T cell response in South African adults: A randomized controlled trial. Vaccine. 2015;33(30):3592–9.
29. Ehlers S, Schaible U. The Granuloma in Tuberculosis: Dynamics of a Host–Pathogen Collusion. Frontiers in Immunology [Internet]. 2013;3:411. Available from: https://www.frontiersin.org/article/10.3389/fimmu.2012.00411
30. Scanga CA, Flynn JL. Modeling tuberculosis in nonhuman primates. Cold Spring Harbor Perspectives in Medicine. 2014;4(12).
31. Joslyn LR, Renardy M, Weissman C, Grant NL, Flynn JL, Butler JR, et al. Temporal and spatial analyses of TB granulomas to predict long-term outcomes. In: Complex Systems and Computational Biology Approaches to Acute Inflammation. Springer; 2021. p. 273–91.
32. Carow B, Hauling T, Qian X, Kramnik I, Nilsson M, Rottenberg ME. Spatial and temporal localization of immune transcripts defines hallmarks and diversity in the tuberculosis granuloma. Nature Communications [Internet]. 2019;10(1):1823. Available from: https://doi.org/10.1038/s41467-019-09816-4

33. Gideon HP, Phuah J, Junecko BA, Mattila JT. Neutrophils express pro- and anti-inflammatory cytokines in granulomas from *Mycobacterium tuberculosis*-infected cynomolgus macaques. Mucosal Immunology [Internet]. 2019;12(6):1370–81. Available from: https://doi.org/10.1038/s41385-019-0195-8
34. Paré PD, Nagano T, Coxson HO. Airway imaging in disease: gimmick or useful tool? Journal of applied physiology (Bethesda, Md : 1985) [Internet]. 2012/05/17. 2012 Aug 15;113(4):636–46. Available from: https://pubmed.ncbi.nlm.nih.gov/22604891
35. Luciw PA, Oslund KL, Yang X-W, Adamson L, Ravindran R, Canfield DR, et al. Stereological analysis of bacterial load and lung lesions in nonhuman primates (rhesus macaques) experimentally infected with *Mycobacterium tuberculosis*. American journal of physiology Lung cellular and molecular physiology [Internet]. 2011/08/26. 2011 Nov;301(5):L731–8. Available from: https://pubmed.ncbi.nlm.nih.gov/21873450
36. Ganchua SKC, White AG, Klein EC, Flynn JL. Lymph nodes—The neglected battlefield in tuberculosis. PLOS Pathogens [Internet]. 2020 Aug 13;16(8):e1008632-. Available from: https://doi.org/10.1371/journal.ppat.1008632
37. Ganchua SKC, Cadena AM, Maiello P, Gideon HP, Myers AJ, Junecko BF, et al. Lymph nodes are sites of prolonged bacterial persistence during *Mycobacterium tuberculosis* infection in macaques. PLOS Pathogens [Internet]. 2018 Nov 1;14(11):e1007337-. Available from: https://doi.org/10.1371/journal.ppat.1007337
38. Sudbury EL, Clifford V, Messina NL, Song R, Curtis N. *Mycobacterium tuberculosis*-specific cytokine biomarkers to differentiate active TB and LTBI: A systematic review. Journal of Infection [Internet]. 2020;81(6):873–81. Available from: https://www.sciencedirect.com/science/article/pii/S0163445320306319
39. Clifford V, Tebruegge M, Zufferey C, Germano S, Forbes B, Cosentino L, et al. Cytokine biomarkers for the diagnosis of tuberculosis infection and disease in adults in a low prevalence setting. Tuberculosis [Internet]. 2019;114:91–102. Available from: https://www.sciencedirect.com/science/article/pii/S1472979218301707
40. Kunnath-Velayudhan S, Gennaro ML. Immunodiagnosis of tuberculosis: a dynamic view of biomarker discovery. Clinical microbiology reviews [Internet]. 2011 Oct;24(4):792–805. Available from: https://pubmed.ncbi.nlm.nih.gov/21976609
41. Wang S, Li Y, Shen Y, Wu J, Gao Y, Zhang S, et al. Screening and identification of a six-cytokine biosignature for detecting TB infection and discriminating active from latent TB. Journal of translational medicine [Internet]. 2018 Jul 20;16(1):206. Available from: https://pubmed.ncbi.nlm.nih.gov/30029650
42. Wu J, Wang S, Lu C, Shao L, Gao Y, Zhou Z, et al. Multiple cytokine responses in discriminating between active tuberculosis and latent tuberculosis infection. Tuberculosis [Internet]. 2017;102:68–75. Available from: https://www.sciencedirect.com/science/article/pii/S1472979215302857
43. Goletti D, Lee M, Wang J, Walter N, Ottenhoff THM. Update on tuberculosis biomarkers: from correlates of risk, to correlates of active disease and of cure from disease. Respirology. 2018;23(5):455–66.
44. Weiner 3rd J, Parida SK, Maertzdorf J, Black GF, Repsilber D, Telaar A, et al. Biomarkers of inflammation, immunosuppression and stress with active disease are revealed by metabolomic profiling of tuberculosis patients. PloS one. 2012;7(7):e40221.

45. Sutherland JS, Hill PC, Adetifa IM, de Jong BC, Donkor S, Joosten SA, et al. Identification of probable early-onset biomarkers for tuberculosis disease progression. PloS one. 2011;6(9):e25230.
46. Sester U, Fousse M, Dirks J, Mack U, Prasse A, Singh M, et al. Whole-blood flow-cytometric analysis of antigen-specific CD4 T-cell cytokine profiles distinguishes active tuberculosis from non-active states. PloS one. 2011;6(3):e17813.
47. Rodo MJ, Rozot V, Nemes E, Dintwe O, Hatherill M, Little F, et al. A comparison of antigen-specific T cell responses induced by six novel tuberculosis vaccine candidates. PLOS Pathogens [Internet]. 2019 Mar 4;15(3):e1007643-. Available from: https://doi.org/10.1371/journal.ppat.1007643
48. Cicchese JM, Evans S, Hult C, Joslyn LR, Wessler T, Millar JA, et al. Dynamic balance of pro- and anti-inflammatory signals controls disease and limits pathology. Immunological Reviews. 2018;285(1):147–67.
49. Gideon HP, Hughes TK, Wadsworth MH, Tu AA, Gierahn TM, Hopkins FF, et al. Single-cell profiling of tuberculosis lung granulomas reveals functional lymphocyte signatures of bacterial control. bioRxiv [Internet]. 2020 Jan 1;2020.10.24.352492. Available from: http://biorxiv.org/content/early/2020/10/26/2020.10.24.352492.abstract
50. Rhodes SJ, Zelmer A, Knight GM, Prabowo SA, Stockdale L, Evans TG, et al. The TB vaccine H56+ IC31 dose-response curve is peaked not saturating: data generation for new mathematical modelling methods to inform vaccine dose decisions. Vaccine. 2016;34(50):6285–91.
51. Rhodes SJ, Guedj J, Fletcher HA, Lindenstrøm T, Scriba TJ, Evans TG, et al. Using vaccine Immunostimulation/Immunodynamic modelling methods to inform vaccine dose decision-making. npj Vaccines [Internet]. 2018;3(1):36. Available from: https://doi.org/10.1038/s41541-018-0075-3
52. Rhodes SJ, Knight GM, Kirschner DE, White RG, Evans TG. Dose finding for new vaccines: The role for immunostimulation/immunodynamic modelling. Journal of theoretical biology [Internet]. 2019/01/10. 2019 Mar 21;465:51–5. Available from: https://pubmed.ncbi.nlm.nih.gov/30639297
53. Gaw N, Hawkins-Daarud A, Hu LS, Yoon H, Wang L, Xu Y, et al. Integration of machine learning and mechanistic models accurately predicts variation in cell density of glioblastoma using multiparametric MRI. Scientific Reports [Internet]. 2019;9(1):10063. Available from: https://doi.org/10.1038/s41598-019-46296-4
54. Kirschner DE, Hunt CA, Marino S, Fallahi-Sichani M, Linderman JJ. Tuneable resolution as a systems biology approach for multi-scale, multi-compartment computational models. Vol. 6, Wiley Interdisciplinary Reviews: Systems Biology and Medicine. 2014. p. 225–45.
55. Lu Y, Lee MY, Zhu S, Sinno T, Diamond SL. Multiscale simulation of thrombus growth and vessel occlusion triggered by collagen/tissue factor using a data-driven model of combinatorial platelet signalling. Mathematical medicine and biology : a journal of the IMA [Internet]. 2017 Dec 11;34(4):523–46. Available from: https://pubmed.ncbi.nlm.nih.gov/27672182
56. Cicchese JM, Pienaar E, Kirschner DE, Linderman JJ. Applying Optimization Algorithms to Tuberculosis Antibiotic Treatment Regimens. Cellular and Molecular Bioengineering. 2017;10(6):523–35.

57. Lundberg S, Lee S-I. A unified approach to interpreting model predictions. arXiv preprint arXiv:170507874. 2017;
58. Marino S, Hogue IB, Ray CJ, Kirschner DE. A methodology for performing global uncertainty and sensitivity analysis in systems biology. Vol. 254, Journal of Theoretical Biology. 2008. p. 178–96.
59. Baden LR, el Sahly HM, Essink B, Kotloff K, Frey S, Novak R, et al. Efficacy and Safety of the mRNA-1273 SARS-CoV-2 Vaccine. New England Journal of Medicine [Internet]. 2020 Dec 30;384(5):403–16. Available from: https://doi.org/10.1056/NEJMoa2035389
60. Polack FP, Thomas SJ, Kitchin N, Absalon J, Gurtman A, Lockhart S, et al. Safety and Efficacy of the BNT162b2 mRNA Covid-19 Vaccine. New England Journal of Medicine [Internet]. 2020 Dec 10;383(27):2603–15. Available from: https://doi.org/10.1056/NEJMoa2034577

9 Appendices

Appendix A Supporting Information for Chapter 2

Table A.1 Parameter Table for *in silico* granuloma repositories.
All ranges, with the exception of the *exhaustionThreshold*, were performed within the ranges outlined by previous versions of *GranSim*. Our methods section details how we assigned the ranges for the *exhaustionThreshold*.

Parameter Name	Description	Range	Units	Ref
growthExtMtbBound	Upper bound of number of external Mtb used in growth function	[180,240]	Number of bacteria	(1-6)
growthRateIntMtb	Fractional growth rate of intracellular bacteria	[0.001,0.005]	Unitless	(1-6)
growthRateExtMtb	Fractional growth rate of extracellular bacteria	[0.001,0.003]	Unitless	(1-6)
deathRateExtMtbCaseated	Upper bound on the number of external Mtb used in growth function	[1,2]	Number of bacteria	(1-6)
Core				
estBoundFactorTNF	Adjustment for coarse grained internalized fraction estimate	[0.4,0.5]	Unitless	(1-6)
estBoundFactorIL10	Adjustment for coarse grained internalized fraction estimate	[0.4,0.6]	Unitless	(1-6)

estConsRateTNF	Scaling Factor for coarse grained TNF dynamics	[5e-4,9e-4]	Unitless	(1-6)
estConsRateIL10	Scaling Factor for coarse grained IL10 dynamics	[2e-4,6e-4]	Unitless	(1-6)
estIntPartitionTNF	Scaling Factor for coarse grained internalization of bound TNFR1	[9,13]	Unitless	(1-6)
nrKillingCaseation	Number of killings for a compartment to become caseated	[7,13]	Number	(1-6)
caseationHealingTime	Time it takes for a caseated compartment to heal	[1700,2600]	Timesteps	(1-6)
sourceDensity	Density of vascular sources on the gridspace	[0.002,0.05]	Unitless	(1-6)
diffusivityTNF	TNF diffusivity	[4e-08, 6e-08]	Cm^2/second	(1-6)
diffusivityChemokines	Chemokine diffusivity	[4e-08,6e-08]	Cm^2/second	(1-6)
diffusivityIL10	IL10 diffusivity	[4e-08,6e-08]	Cm^2/second	(1-6)
ChemokinekDeg	Chemokine degradation rate constant	[0.0005,0.005]	1/second	(1-6)
kDeg	TNF degradation rate constant	[0.0005,0.005]	1/second	(1-6)
Ikdeg	Degradation rate constant for IL10	[0.0003,0.003]	1/second	(1-6)
IC50ChemokineIL10	IC50 of IL10 inhibition of chemokine secretion	[1,10]	Molecules/mL	(1-6)
thresholdApoptosisTNF	TNF threshold for TNF-induced apoptosis	[1000, 5000]	Unitless	(1-6)
kApoptosis	Rate of apoptosis happening	[1e-07, 2e-6]	1/second	(1-6)
saturationApoptosisTNF	Signal saturation of number of internal bound TNFR1 Molecules	[5000, 9000]	Molecules	(1-6)

minChemotaxis	Minimum of Chemotaxis sensitivity range	[1, 50]	Molecules	(1-6)
maxChemotaxis	Maximum of Chemotaxis sensitivity range	[100,1000]	Molecules	(1-6)
maxIL10Inhibition	Coarse grained TNF/IL10 dose dependence parameter beta	[0.05, 0.3]	Log10(ng/mL)	(1-6)
Mac				
initDensity	Initial density of macrophages on the gridspace	[0.005,0.03]	Unitless	(1-6)
movementRest	Time required for a resting macrophage to move one microcompartment	[1,10]	Timesteps	(1-6)
movementAct	Time required for an activated macrophage to move one microcompartment	[10,50]	Timesteps	(1-6)
movementInf	Time required for an infected macrophage to move one microcompartment	[100,200]	Timesteps	(1-6)
dTNF	Secretion rate of TNF by a macrophage	[1.3,1.7]	Molecules/second	(1-6)
dCCL2	Secretion rate of CCL2 by a macrophage	[4,8]	Molecules/second	(1-6)
dCCL5	Secretion rate of CCL5 by a macrophage	[4,8]	Molecules/second	(1-6)
dIL10Act	Secretion rate of IL10 by an activated macrophage	[0.2, 0.4]	Molecules/second	(1-6)
halfSatIL10	Half saturation for TNF induction of IL10 in an	[170,210]	Number/cell	(1-6)

	activated macrophage			
thresholdNFkBTNF	TNF threshold for NFkB activation	[75,115]	Molecules	(1-6)
kNFkB	Rate of NFkB activation	[0.7e-5, 1e-5]	Fraction	(1-6)
probKillExtMtbRest	Probability of a resting macrophage to kill extracellular bacteria	[0.05, 0.3]	Unitless	(1-6)
fKillExtMtbRest	Fractional increase of a resting macrophage to kill extracellular bacteria when STAT1 or NFkB pathways are on	[0.3,0.5]	Unitless	(1-6)
nrExtMtbNFkB	Number of extracellular bacteria for NFkB activation in an infected macrophage	[150, 250]	Bacteria	(1-6)
nrIntMtbCInf	Number of intracellular bacteria necessary for an infected macrophage to become chronically infected	[8,12]	Bacteria	(1-6)
nrIntMtbBurstCInf	Number of intracellular bacteria necessary for a chronically infected mac to burst	[13,20]	Bacteria	(1-6)
nrExtMtbUptakeAct	Number of extracellular bacteria an activated macrophage can uptake and kill	[3,7]	Bacteria	(1-6)

Stat1ActivationTime	Time a macrophage is Stat1 activated	[400,460]	Timesteps	(1-6)
nfkbActivationTime	Time a macrophage is NFkB activated	[13,17]	Timesteps	(1-6)
Stat3ActivationTime	Time a macrophage is Stat3 activated	[75,125]	Timesteps	(1-6)
thresholdSTAT3IL10	Threshold of IL10 to IL10R1 for STAT3 signaling	[5,15]	Unitless	(1-6)
kSTAT3IL10	Rate constant of bound IL10 to IL10R1 for STAT3 signaling	[5e-4, 1.5e-3]	Unitless	(1-6)
probHealCaseation	Rate constant for wound healing	[0.005, 0.05]	Unitless	(1-6)
T cell				
maxAge	Maximum age of a T cell	[400,460]	Timesteps	(1-6)
exhaustionThreshold	Threshold of Exposure Events for an individual T cell before it becomes exhausted	[200, 10000] (5236 during generation of 2nd biorepository)	Count	Estimated
probMoveToMac	Probability of a T cell moving into a compartment already containing a macrophage	[0.01, 0.2]	Unitless	(1-6)
probMoveToTcell	Probability of a T cell moving into a compartment already containing another T cell	[0.01, 0.2]	Unitless	(1-6)

maxDivisions	Maximum number of times a T cell can create a daughter cell	[3,5]	Timesteps	(1-6)
γ-producing T cells				
dTNF	Secretion rate of TNF by γproducing T cell	[0.1, 0.2]	Molecules/second	(1-6)
maxTimeReg	Time span during which a γ producing T cell remains downregulated	[30,40]	Timesteps	(1-6)
probApoptosisFasFasL	Probability of Fas/FasL induced apoptosis by a γproducing T cell	[0.01,0.03]	Unitless	(1-6)
probTNFProducer	Probability that a γproducing T cell can produce TNF	[0.04, 0.1]	Unitless	(1-6)
probIFNProducer	Probability that a γproducing T cell can produce IFNγ	[0.3, 0.4]	Unitless	(1-6)
probIFNMooreExtend	Probability a macrophage will be IFNγ/STAT1 activated in the extended Moore Neighborhood.	[0.2, 0.3]	Unitless	(1-6)
Cytotoxic T cells				
dTNF	Secretion rate of TNF by a cytotoxic T cell	[0.01, 0.02]	Molecules/second	(1-6)
maxTimeReg	Time span during which a cytotoxic T cell remains downregulated	[30,40]	Timesteps	(1-6)

probKillMac	Probability of a cytotoxic T cell killing a chronically infected mac	[0.005, 0.015]	Unitless	(1-6)
probKillMacCleanly	Probability of a cytotoxic T cell killing a chronically infected mac cleanly	[0.6, 0.9]	Unitless	(1-6)
probTNFProducer	Probability that a cytotoxic T cell is producing TNF	[0.05, 0.09]	Unitless	(1-6)
Regulatory T cells				
dIL10	Secretion of IL10 by a regulatory T cell	[0.7, 0.8]	Molecules/second	(1-6)
probTregDeactivate	Probability of successful downregulation by a regulatory T cell	[0.01, 0.02]	Unitless	(1-6)
factorDeactIL10	Factor when a regulatory T cell is making IL10 to scale probTregDeactivate	[1,3]	Unitless	(1-6)

Appendix B Supporting Information for Chapter 3

$$\frac{dB_E}{dt} = \alpha_{20}B_E + k_{17}NM_I\left(\frac{B_I^2}{B_I^2 + N^2M_I^2}\right) + k_{14a}N_{fracc}\frac{B_I}{M_I}M_I\left(\frac{\left(\frac{T_C + w_3T_1}{M_I}\right)}{\left(\frac{T_C + w_3T_1}{M_I}\right) + c_4}\right) + k_{14b}N_{fraca}\frac{B_I}{M_I}M_I\left(\frac{F_\alpha}{F_\alpha + f_9I_{10} + s_{4b}}\right) - k_2\frac{N}{2}M_R\left(\frac{B_E}{B_E + c_9}\right) - k_{15}M_AB_E - k_{18}M_RB_E - \mu_{B_E}B_E + \mu_{M_I}N_{fracd}\frac{B_I}{M_I}M_I$$

$$\frac{dB_I}{dt} = \alpha_{19}B_I(NM_I - B_I) + k_2\frac{N}{2}M_R\left(\frac{B_E}{B_E + c_9}\right) - k_{17}NM_I\left(\frac{B_I^2}{B_I^2 + N^2M_I^2}\right) - k_{14a}\frac{B_I}{M_I}M_I\left(\frac{\left(\frac{T_C + w_3T_1}{M_I}\right)}{\left(\frac{T_C + w_3T_1}{M_I}\right) + c_4}\right) - k_{14b}\frac{B_I}{M_I}M_I\left(\frac{F_\alpha}{F_\alpha + f_9I_{10} + s_{4b}}\right) - k_{52}\frac{B_I}{M_I}M_I\left(\frac{\left(\frac{T_C\left(\frac{T_1}{T_1 + c_{T_1}}\right) + w_1T_1}{M_I}\right)}{\left(\frac{T_C\left(\frac{T_1}{T_1 + c_{T_1}}\right) + w_1T_1}{M_I}\right) + c_{52}}\right) - \mu_{B_I}B_I + \mu_{M_I}\frac{B_I}{M_I}M_I$$

$$\frac{dM_R}{dt} = Sr_M + \alpha_{4a}(M_A + w_2M_I) + Sr_{4b}\left(\frac{F_\alpha}{F_\alpha + f_8I_{10} + s_{4b}}\right) - k_2M_R\left(\frac{B_E}{B_E + c_9}\right) - k_3M_R\left(\frac{B_E + wB_I + \beta F_\alpha}{B_E + wB_I + \beta F_\alpha + c_8}\right)\left(\frac{I_\gamma}{I_\gamma + f_1I_4 + f_7I_{10} + s_1}\right) - \mu_{M_R}M_R$$

$$\frac{dM_I}{dt} = k_2M_R\left(\frac{B_E}{B_E + c_9}\right) - k_{17}M_I\left(\frac{B_I^2}{B_I^2 + N^2M_I^2}\right) - k_{14a}M_I\left(\frac{\left(\frac{T_C + w_3T_1}{M_I}\right)}{\left(\frac{T_C + w_3T_1}{M_I}\right) + c_4}\right) - k_{14b}M_I\left(\frac{F_\alpha}{F_\alpha + f_9I_{10} + s_{4b}}\right) - k_{52}M_I\left(\frac{\left(\frac{T_C\left(\frac{T_1}{T_1 + c_{T_1}}\right) + w_1T_1}{M_I}\right)}{\left(\frac{T_C\left(\frac{T_1}{T_1 + c_{T_1}}\right) + w_1T_1}{M_I}\right) + c_{52}}\right) - \mu_{M_I}M_I$$

$$\frac{dM_A}{dt} = k_3M_R\left(\frac{B_E + wB_I + \beta F_\alpha}{B_E + wB_I + \beta F_\alpha + c_8}\right)\left(\frac{I_\gamma}{I_\gamma + f_1I_4 + f_7I_{10} + s_1}\right) - k_4M_A\left(\frac{I_{10}}{I_{10} + s_8}\right) - \mu_{M_A}M_A$$

$$\frac{dT_0}{dt} = \alpha_{1a}(M_A + w_2M_I) + Sr_{1b}\left(\frac{F_\alpha}{F_\alpha + f_8I_{10} + s_{4b2}}\right) + \alpha_2T_0\left(\frac{M_A}{M_A + c_{15}}\right) - k_6I_{12}T_0\left(\frac{I_\gamma}{I_\gamma + f_1I_4 + f_7I_{10} + s_1}\right) - k_7T_0\left(\frac{I_4}{I_4 + f_2I_\gamma + s_2}\right) - \mu_{T_0}T_0$$

$\frac{dT_1}{dt} = \alpha_{3a}(M_A + w_2 M_I) + Sr_{3b}\left(\frac{F_\alpha}{F_\alpha + f_8 I_{10} + s_{4b1}}\right) + k_6 I_{12} T_0 \left(\frac{I_\gamma}{I_\gamma + f_1 I_4 + f_7 I_{10} + s_1}\right) + k_{31} T_{4EM} M_I - \mu_{T_\gamma}\left(\frac{I_\gamma}{I_\gamma + c}\right) T_1 M_A - \mu_{T_1} T_1$
$\frac{dT_2}{dt} = \alpha_{3a2}(M_A + w_2 M_I) + Sr_{3b2}\left(\frac{F_\alpha}{F_\alpha + f_8 I_{10} + s_{4b1}}\right) + k_7 T_0 \left(\frac{I_4}{I_4 + f_2 I_\gamma + s_2}\right) + k_{32} T_{4EM} M_A - \mu_{T_2} T_2$
$\frac{dT_{80}}{dt} = \alpha_{1a}(M_A + w_2 M_I) + Sr_{1b}\left(\frac{F_\alpha}{F_\alpha + f_8 I_{10} + s_{4b2}}\right) + \alpha_2 T_{80}\left(\frac{M_A}{M_A + c_{15}}\right) - k_6 I_{12} T_{80}\left(\frac{I_\gamma}{I_\gamma + f_1 I_4 + f_7 I_{10} + s_1}\right) - \mu_{T_{80}} T_{80}$
$\frac{dT_8}{dt} = m\alpha_{3ac}(M_A + w_2 M_I) + mSr_{3bc}\left(\frac{F_\alpha}{F_\alpha + f_8 I_{10} + s_{4b1}}\right) + mk_6 I_{12} T_{80}\left(\frac{I_\gamma}{I_\gamma + f_1 I_4 + f_7 I_{10} + s_1}\right) + k_{34} T_{8EM} M_I - \mu_{T_{c\gamma}}\left(\frac{I_\gamma}{I_\gamma + c_c}\right) T_8 M_A - \mu_{T_C} T_8$
$\frac{dT_C}{dt} = m\alpha_{3ac}(M_A + w_2 M_I) + mSr_{3bc}\left(\frac{F_\alpha}{F_\alpha + f_8 I_{10} + s_{4b1}}\right) + mk_6 I_{12} T_{80}\left(\frac{I_\gamma}{I_\gamma + f_1 I_4 + f_7 I_{10} + s_1}\right) + k_{33} T_{8EM} M_I - \mu_{T_{c\gamma}}\left(\frac{I_\gamma}{I_\gamma + c_c}\right) T_C M_A - \mu_{T_C} T_C$
$\frac{dT_{4EM}}{dt} = Sr_{4EM}\left(\frac{F_\alpha}{F_\alpha + hs_{4EM}}\right) - k_{31} T_{4EM} M_I - k_{32} T_{4EM} M_A - \mu_{T_{4EM}} T_{4EM}$
$\frac{dT_{8EM}}{dt} = Sr_{8EM}\left(\frac{F_\alpha}{F_\alpha + hs_{8EM}}\right) - k_{33} T_{8EM} M_I - k_{34} T_{8EM} M_I - \mu_{T_{8EM}} T_{8EM}$
$\frac{dT_{4N\,on}}{dt} = Sr_{4N\,on}\left(\frac{F_\alpha}{F_\alpha + hs_{4N\,on}}\right) - \mu_{T_{4N\,on}} T_{4N\,on}$
$\frac{dT_{8N\,on}}{dt} = Sr_{8N\,on}\left(\frac{F_\alpha}{F_\alpha + hs_{8N\,on}}\right) - \mu_{T_{8N\,on}} T_{8N\,on}$
$\frac{dF_\alpha}{dt} = \alpha_{30} M_I + \alpha_{31} M_A \left(\frac{I_\gamma + \beta_2(B_E + wB_I)}{I_\gamma + \beta_2(B_E + wB_I) + f_1 I_4 + f_7 I_{10} + s_{10}}\right) + \alpha_{32} T_1 + \alpha_{33}\left(\frac{T_C + T_8}{2m}\right) - \mu_{F_\alpha} F_\alpha$
$\frac{dI_\gamma}{dt} = s_g\left(\frac{B_E + wB_I}{B_E + wB_I + c_{10}}\right)\left(\frac{I_{12}}{I_{12} + s_7}\right) + \alpha_{5a} T_1\left(\frac{M_A}{M_A + c_{5a}}\right) + \alpha_{5b} T_8\left(\frac{M_A}{M_A + c_{5b}}\right) + \alpha_{5c} M_I + \alpha_7 T_0\left(\frac{I_{12}}{I_{12} + f_4 I_{10} + s_4}\right) + \alpha_7 T_{80}\left(\frac{I_{12}}{I_{12} + f_4 I_{10} + s_4}\right) - \mu_{I_\gamma} I_\gamma$
$\frac{dI_{12}}{dt} = s_{12}\left(\frac{B_E + wB_I}{B_E + wB_I + c_{230}}\right) + \alpha_{23} M_R\left(\frac{B_E + wB_I}{B_E + wB_I + c_{23}}\right) + \alpha_8 M_A\left(\frac{s}{s + I_{10}}\right) - \mu_{I_{12}} I_{12}$
$\frac{dI_{10}}{dt} = \delta_7(M_I + M_A)\left(\frac{s_6}{I_{10} + f_6 I_\gamma + s_6}\right) + \alpha_{16} T_1 + \alpha_{17} T_2 + \alpha_{18}\left(\frac{T_C + T_8}{2m}\right) - \mu_{I_{10}} I_{10}$
$\frac{dI_4}{dt} = \alpha_{11} T_0 + \alpha_{12} T_2 - \mu_{I_4} I_4$

Table B.1 Granuloma Ordinary Differential Equations

***Note: in these equations m is the same as CD8MultiFunc in the text. m is defined as $\boldsymbol{m = (frac + 1)/2}$, where frac is the fraction of all new CD8+ T cells that are multifunctional.**

Parameter name	Min	Max	Units	Ref	Description
Srm	0	0	1/day	fit	MR recruitment rate
alpha4a	0.57	0.83	1/day	[1], [2], fit	Macrophage recruitment of MR
w	0.29	0.33	--	[3], [2], fit	Contribution of BI to MR activation
w3	0.23	0.37	--	[1], [2], fit	Max contribution of Th1 to MI apoptosis
w2	1	1	--	[3], [2], fit	Contribution of MI to MR recruitment
Sr4b	650	750	1/day	[1], [2], fit	Falpha-dependent recruitment of MR
f8	0.002	0.002	--	fit	Ratio adjustment IL-10/Falpha on MR recruitment
f9	0.6	0.6	--	fit	Ratio adjustment Falpha/IL-10
s4b	3210	4860	pg/ml	[4], [2], fit	Half saturation of Falpha on MR recruitment
s4b1	6780	9410	pg/ml	[1], [2], fit	Half saturation of Falpha dependent Th1 recruitment
s4b2	5340	9420	pg/ml	[4], [2], fit	Half saturation of Falpha-dependent T0 recruitment
k4	0.074	0.17	1/day	[3], [2], fit	MA deactivation by IL-10
s8	200	940	pg/ml	[3], [2], fit	Half saturation of IL-10 on MA deactivation
k2	0.43	2.2	1/day	[3], [2], fit	MR infection rate
c9	1190	7450	count	[3], [2], fit	Half saturation of BE on MR infection
k3	0.04	0.04	1/day	[3], [2], fit	MR activation rate
f1	150	150	--	[3], [2], fit	Adjustment IL-4/IFNg
s1	54	450	pg/ml	[3], [2], fit	Half saturation of IFNg-dependent MR activation
Beta	1.00E+07	1.00E+07	1/pg	[1], [2], fit	Scaling factor of Falpha for MR activation
c8	175370	363170	count	fit	Half saturation of BE and BI on MR activation
nuMR	0.005	0.005	1/day	[3], [2], fit	MR death rate
k17	0.1	0.3	1/day	[3], [2], fit	Max rate of MI bursting
N	20	25	count	[3], [2], [5], fit	Carrying capacity of MI
k14a	0.06	0.34	1/day	[1], [2], fit	T cell induced apoptosis of MI
c4	400	880	--	[3], [2], fit	Half saturation of Th1/MI ratio on MI apoptosis
k14b	0.63	0.86	1/day	[1], [2], fit	Falpha induced apoptosis of MI
k52	0.6	0.7	1/day	[1], [2]	Cytotoxic killing of MI
w1	0.2	0.7	--	[1], [2], fit	Max contribution of Th1 to cytotoxic killing
c52	103290	246770	--	fit	Half saturation of TC on MI killing
cT1	35	35	--	fit	Half saturation of Th1 on cytotoxic killing
nuMI	0.0033	0.0033	1/day	[3], [2], [5]	MI death rate
nuMA	0.17	0.17	1/day	[3], [2], fit	MA death rate
alpha1a	0.03	0.55	1/day	[6], [2], fit	Macrophage recruitment of T0
Sr1b	2E+04	5E+4	1/day	[6], [2], fit	Falpha dependent T0 recruitment
alpha2	0.12	0.36	1/day	[3], [2], fit	Max growth rate of T0
c15	2.75E+06	4.09E+06	--	[3], [2], fit	Half saturation of MA on IFNg production by Th1
k6	0.1	0.2	ml/(pg day)	[3], [2], fit	Max T0 to Th1 rate

f7	7	30	--	[1], [2], fit	Effect of IL-10 on IFNg induced differentiation of T0 to Th1
k7	0.25	0.64	ml/(pg day)	[3], [2], fit	Max T0 to Th2 rate
f2	0.2	0.4	--	fit	Adjustment IFNg/IL-4
s2	400	900	pg/day	fit	Half saturation IL-4
nuT0	0.22	0.22	1/day	[3], [2], fit	T0 death rate
CD8MultiFunc	0.7	0.9	--	[1], [2], fit	overlap between TC and T8 function
alpha3a	0.4	0.8	1/day	fit	Macrophage recruitment of Th1
Sr3b	15	80	1/day	Fit	Falpha dependent recruitment of Th2
alpha3a2	0.22	0.75	1/day	fit	Macrophage recruitment of Th2
Sr3b2	50	90	1/day	fit	Falpha dependent recruitment of Th2
nuTg	0.24	0.75	1/day	fit	IFNg induced apoptosis of Th1
c	270	690	pg/ml	fit	Half saturation IFNg on Th1 apoptosis
nuT1	0.33	0.33	1/day	[3], [2]	Th1 death rate
nuT2	0.33	0.33	1/day	[3], [2]	Th2 death rate
alpha3ac	0.25	0.77	1/day	fit	Macrophage recruitment of TC and T8
Sr3bc	14	26	1/day	fit	Falpha dependent recruitment of TC and T8
nuTCg	0.45	0.83	1/day	fit	IFNg induced apoptosis of TC and T8
cc	350	590	pg/ml	[7], [2], fit	Half saturation of IL on TC and T8 apoptosis
nuTC	0.3	0.3	1/day	[1]	TC death rate
sg	2375	7340	pg/(ml day)	fit	IFNg production by cells
c10	5.50E+05	6.35E+06	count	[3], [2], fit	Half saturation of Mtb on IFNg production by cells
s7	590	820	pg/ml	fit	Half saturation of IL-12 on IFNg production by cells
alpha5a	0.6	0.8	pg/day	[1], [2], fit	IFNg production by Th1
c5a	315	630	1/ml	fit	Half saturation of MA on IFNg production by Th1
alpha5b	0.15	0.58	pg/day	[1], [2], fit	IFNg production by T8
alpha5c	0.08	0.35	pg/ml	[1], [2], fit	IFNg production by MI
c5b	160	795	count	fit	Half saturation of MA on IFNg production by T8
alpha7	0.012	0.16	pg/ml	[3], [2], fit	IFNg production by T0
f4	1.5	1.5	--	[3], [2], fit	Adjustment of IL-10/IL-12 on IFNg
s4	270	890	pg/ml	[3], [2], fit	Half saturation of IL-12 on IFNg
nuIG	6	9	1/day	[3], [2], fit	IFNg decay rate
alpha23	0.004	0.004	pg/ml	[1], [2], fit	IL-12 production by MR
c23	140	525	1/ml	[1], [2], fit	Half saturation of Mtb on IL-12 production by MR
alpha8	0.38	0.80	pg/day	[3], [2], fit	IL-12 Production by MA
s12	2330	3650	pg/(ml day)	[1], [2], fit	Cell production of IL-12
c230	390	710	count	Fit	Half saturation of Mtb on IL-12 production by DC's
nuIL-12	1.1	1.1	1/day	[3]	IL-12 death rate
s	170	650	pg/ml	fit	IL-10 effect on IL-12 production by MA
s6	680	770	pg/ml	Fit	Half saturation of IL-10 self-inhibition in MA
f6	0.35	0.35	--	[3]	Adjustment IFNg on IL-10
delta7	0.40	0.8	pg/ml	fit	IL-10 production by MA

alpha16	0.33	0.8	pg/day	Fit, [5]	IL-10 production by Th1
alpha17	0.3	0.5	pg/day	Fit, [5]	IL-10 production by Th2
alpha18	0.5	0.7	pg/day	Fit, [5]	IL-10 production by TC and T8
nuIL-10	1.81	4.1	1/day	[3], fit	IL-10 decay rate
alpha11	0.0033	0.073	pg/day	[3], fit	IL-4 production by T0
alpha12	0.02	0.06	pg/day	[3], fit	IL-4 production by Th2
nuIL-4	2.7	2.7	1/day	[3]	IL-4 decay rate
alpha30	0.05	0.09	pg/(ml day)	[1], fit	Falpha production by MI
alpha31	0.15	0.78	pg/(ml day)	[1], fit	Falpha production by MA
beta2	12000	12000	1/pg	[1], fit	Scaling factor of Mtb for Falpha production by MA
s10	100	300	pg/ml	[1], fit	Half saturation of IFNg on Falpha production by MA
alpha32	0.2	0.3	pg/(ml day)	fit	Falpha production by Th1
alpha33	0.2	0.3	pg/(ml day)	Fit	Falpha production by T8
nuTNF	1.1	1.1	1/day	[8]	Falpha decay rate
alpha19	0.87	1.27	1/day	[3], fit	BI replication rate
alpha20	0.3	0.4	1/day	[3], fit	BE replication rate
Nfracc	0.06	0.06	--	[3]	Fraction BI released by T cell apoptosis of MI
Nfraca	0.06	0.06	--	[3]	Fraction BI released by TNF apoptosis of MI
k15	0.0002	0.001	1/day	[3], fit	BE killing by MA
k18	0.0001	0.0007	1/day	[3], fit	BE killing by MR
nI	6.3E-05	8.3E-05	1/day	[1], fit	BI death rate
nE	4.4E-09	6.65E-09	1/day	[1], fit	BE death rate
Nfracd	0.001	0.001	--	fit	Fraction of BI released by natural death of MI

Table B.2 ODE model parameters that govern individual granuloma formation and growth across time.

*For each disseminating granuloma, we allow for the option to sample each parameter from a subrange smaller than its parent's ranges. We do this by using a fraction between 0 and 1 (inclusive) to determine the limits of the range. The fraction represents the percent of values between the parent's value and either extrema (minimum and maximum) to include in the range. 0 means the range includes only the parent's value; 1 means that the original range is used. References follow below.

REFERENCES

1. Sud D, Bigbee C, Flynn JL, Kirschner DE. Contribution of CD8+ T Cells to Control of *Mycobacterium tuberculosis* Infection. J Immunol. 2014;176: 4296–4314. doi:10.4049/jimmunol.176.7.4296
2. Guzzetta G, Kirschner D. The Roles of Immune Memory and Aging in Protective Immunity and Endogenous Reactivation of Tuberculosis. PLoS One. 2013;8. doi:10.1371/journal.pone.0060425
3. Wigginton JE, Kirschner D. A Model to Predict Cell-Mediated Immune Regulatory Mechanisms During Human Infection with *Mycobacterium tuberculosis*. J Immunol. 2001;166: 1951–1967. doi:10.4049/jimmunol.166.3.1951
4. Gilbertson B, Zhong J, Cheers C. Anergy, IFN-gamma production, and apoptosis in terminal infection of mice with Mycobacterium avium. J Immunol. 1999;163: 2073–2080.
5. Cilfone NA, Ford CB, Marino S, Mattila JT, Gideon HP, Flynn JL, et al. Computational Modeling Predicts IL-10 Control of Lesion Sterilization by Balancing Early Host Immunity–Mediated Antimicrobial Responses with Caseation during *Mycobacterium tuberculosis* Infection . J Immunol. 2015;194: 664–677. doi:10.4049/jimmunol.1400734
6. Tsukaguchi K, De Lange B, Boom WH. Differential regulation of IFN-γ, TNF-α, and IL-10 production by CD4+ αβTCR+ T cells and Vδ2+ γδ T cells in response to monocytes infected with *Mycobacterium tuberculosis*-H37Ra. Cell Immunol. 1999;194: 12–20. doi:10.1006/cimm.1999.1497

7. Oddo M, Renno T, Attinger A, Bakker T, MacDonald HR, Meylan PR. Fas ligand-induced apoptosis of infected human macrophages reduces the viability of intracellular *Mycobacterium tuberculosis*. J Immunol. 1998;160: 5448–54. Available: http://www.ncbi.nlm.nih.gov/pubmed/9605147
8. D'Amico G, Frascaroli G, Bianchi G, Transidico P, Doni A, Vecchi A, et al. Uncoupling of inflammatory chemokine receptors by IL-10: Generation of functional decoys. Nat Immunol. 2000;1: 387–391. doi:10.1038/80819

Parameter name	Value	Units	Ref	Description
diamMacs	20	microns	(40)	Diameter of Macrophage
diamTCells	5	microns	(40)	Diameter of T cell
dt	1	day	~	Agent time step

Table B.3 Other parameters for size of granulomas and runtime execution.
References follow Chapter 3 references

Parameter name	Min	Max	Units	Reference	Description
DissemDistMean	10^0	10^1	um	Fit, Based on data (1)	Mean distance of local dissemination
Lambda_Local	10^{-3}	10^{-1}	CFU/sec	Fit, Based on data [1]	Max probability of local dissemination
CFU_Half_Local	10^3	10^4	CFU	Fit, Based on data [1]	Value for half of max rate of local dissemination
Lambda_NonLocal	$10^{-3.5}$	$10^{-1.5}$	CFU/sec	Fit, Based on data [1]	Max probability of non-local dissemination
CFU_Half_NonLocal	$10^{3.5}$	$10^{4.5}$	CFU	Fit, Based on data [1]	Value for half of max rate of non-local dissemination
TcellFracDonateMu	1/100	1/10	--	estimated	Mean fraction of all of the parent granuloma's T cells that move to the daughter granuloma during a local dissemination event
TcellFracDonateSig	10^{-3}	10^{-2}	--	estimated	Standard deviation from the mean fraction of all of the parent granuloma's Tcells that move to the daughter granuloma during a local dissemination event

Table B.4 Dissemination Parameters.
These seven parameters dictate dissemination dynamics in *MultiGran*. Parameters were fit to barcode data or varied using Uncertainty Analysis to find an estimation. References follow below

REFERENCES
1. Martin CJ, Cadena AM, Leung VW, Lin PL, Maiello P, Hicks N, et al. Digitally Barcoding *Mycobacterium tuberculosis* Reveals *In vivo* Infection Dynamics in the Macaque Model of Tuberculosis . MBio. 2017;8. doi:10.1128/mbio.00312-17

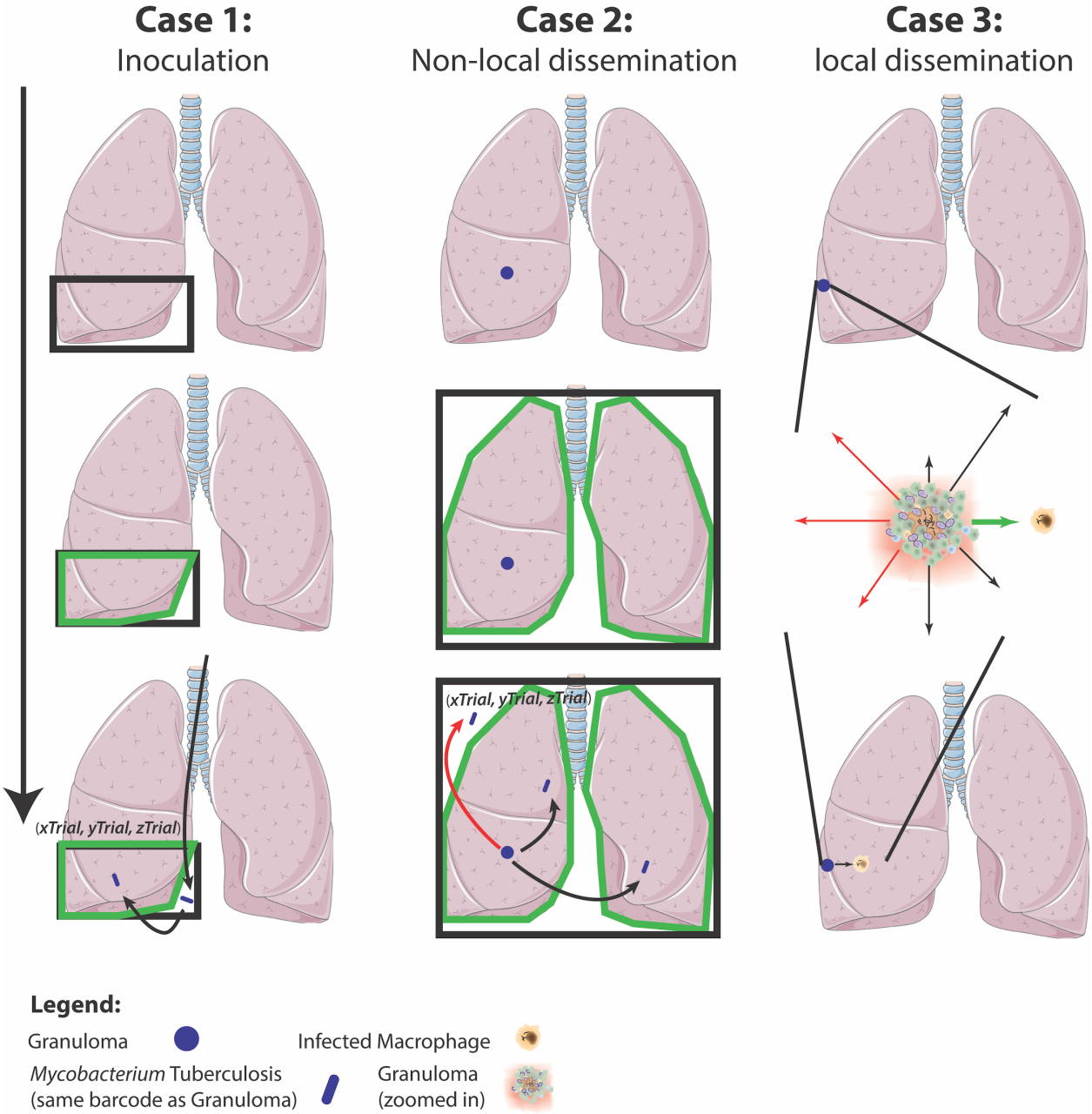

Figure B.1 The rules of granuloma establishment and dissemination within *MultiGran*.
Case 1 – Inoculation. Inoculation deposits bacteria in a specific lung region at position (xTrial, yTrail, zTrial). The black box designates inoculation region (row 1), wherein the specific within-lung region destined for inoculation is highlighted in green (row 2). The third row demonstrates successful inoculation of a single bacterium–the black box was sampled randomly until the sampled coordinates lie within the green region. Cases 2 and 3 define granuloma placement following dissemination. Case2 –non-local dissemination. When non-local dissemination occurs, a bacterium escapes a single granuloma (row 1) and can be placed in any region (shown in black in row 2) that encompasses the entire lung. The green highlighted region is the area in which the bacterial placement will be accepted. Row 3 shows three trial placements: two realizations of accepted bacterial placement (black arrows) and one unaccepted placement (red arrow) at (xTrial, yTrial, zTrial). Case 3– local dissemination. Local dissemination is the only form of granuloma placement which does not utilize random placement within a region of lung space. Rather, an infected macrophage from the parent granuloma is placed in a random direction away from the parent granuloma. Row 2 shows several options for granuloma infected macrophage placement. Note that the arrows are of

different length to represent our assumption that local dissemination likely follows a normal distribution with respect to parent granuloma location. Here, the green and black arrows show valid directions for the new placement for the infected macrophage, while red arrows show invalid directions. A new granuloma will begin to develop in the chosen (green) valid location (Row 3). Note that in both **(A)** and **(B)** bacteria, granulomas, and infected macrophages are not to scale. Lung image from Servier Medical Art.

Appendix C Supporting Information for Chapter 4

Important terms:

Immunogenicity Dataspace: The space defined by experimental results that contains the T-cell response to each antigen.

Parameter Range: The range of values for a parameter that are biologically feasible and are assigned to represent values of the mechanism for which that parameter represents. Values (and ranges) are assigned according to biological observations, experimental results, or mathematical estimation.

Parameter Space: The set of all combinations of parameter values for a particular model, as defined by the parameter ranges for each parameter.

Uncertainty and Sensitivity Analysis: A series of techniques used to evaluate the influence a parameter has on model outcomes. Influence of individual mechanism can be assessed (see Methods for more details).

Calibration: The process of varying parameters until the model behavior reaches a preferred end state or predetermined goal (usually the dataspace).

Initial Conditions: The predefined initial values of each variable in a mathematical model prior to simulating the model. In this work, initial conditions were also varied during model calibration as initial condition could represent pre-existing immune memory cells.

Radar Charts: A graphical visualization of multivariate data across multiple axis. We use radar charts to display the parameter space of our simulations.

Description of lymph node and blood mathematical model

This Appendix text describes the system of ordinary differential equations (ODEs) for CD4+ antigen-specific T cells dynamics.

Measure units are cell count in the lymph compartment and cell/mm^3 in the blood compartment. However, upon comparison to experimental data, we converted antigen-specific T cell units into percentages of total (specific and nonspecific) CD4+ T cells in the blood. The term α, represents

the volume of blood in μL and is used for scaling cells when they traffic between the blood compartment and the lymph compartment. All parameters are defined with units, values, and references provided in Table C.1.

Lymph Node

Antigen presentation and priming in lymph node compartment is driven by the following equation

$$\frac{dAPC}{dt} = -\mu_5 APC \tag{0.1}$$

which tracks antigen presenting cells (APCs) in the lymph node at any time during or after vaccination. If the number of APCs doesn't increase (a vaccination event would be an example of increasing the APC population), the APC number decreases following an exponential decay, at the rate μ_5.

Naïve T cells (Eqn. (0.2)) represented by (N_4^{LN}) are recruited to the lymph node at a rate (k_1) dependent on cytokine production in the lymph node. Since we do not track cytokines in the lymph node model, we use APC also as a proxy for cytokine production (modeled as a Michaelis-Menten term in Eqn. (0.2)). Other terms included influx (ξ_1) and efflux (ξ_2), as well as mass action priming to precursor cells (k_2).

$$\frac{dN_4^{LN}}{dt} = \alpha\left(V_{primeN} + V_{Ninflux}\right) - V_{Nefflux} - V_{NdiffP} \tag{0.2}$$

$$V_{primeN} = k_1 N_4^B \left(\frac{APC}{APC + hs_1}\right)$$

$$V_{NdiffP} = k_2 N_4^{LN} APC$$

$$V_{Nefflux} = \xi_2 N_4^{LN}$$

$$V_{Ninflux} = \xi_1 N_4^B$$

Precursor CD4+ T cells (P_4^{LN}) (Eqn. (0.3)) are generated through priming of antigen-specific naïve T cells (k_2) as well as through re-activation of antigen-specific central memory T cells (k_3); both processes are expressed as mass action terms. Proliferation is modeled as logistic growth.

$$\frac{dP_4^{LN}}{dt} = \left(V_{NdiffP} + V_{CMdiffP}\right) + V_{prolif} - V_{PdiffE} - V_{PdiffCM} - \mu_6 P_4^{LN} \tag{0.3}$$

$$V_{CMdiffP} = k_3 CM_4^{LN} APC$$

$$V_{prolif} = k_4 P_4^{LN}\left(1 - \left(\frac{P_4^{LN}}{\rho_1}\right)\right)\left(\frac{APC}{APC + hs_4}\right)$$

$$V_{PdiffE} = k_5 P_4^{LN}\left(\frac{APC}{APC + hs_5}\right)$$

$$V_{PdiffCM} = k_6 P_4^{LN}\left(1 - \left(\frac{APC}{APC + hs_5}\right)\right)$$

A Michaelis-Menten term based on antigen stimulation (APC levels) was used to adjust proliferation (k_4) and differentiation rates (k_5 and k_6). The likelihood of precursor cells differentiating into effector cells is directly proportional to the amount of antigen stimulation (k_5). The opposite assumption was applied to the likelihood of precursor cells differentiating into central memory (k_6). A death term (μ_6) ensured that the precursor population did not persist in the absence of infection. No precursor populations exit the lymph node.

Effector CD4+ T cells are modeled in Eqn. (0.4), as E_4^{LN}:

$$\frac{dE_4^{LN}}{dt} = V_{PdiffE} - V_{Eefflux} - V_{EdiffEM} \quad (0.4)$$

$$V_{Eefflux} = \xi_3 E_4^{LN}$$

$$V_{EdiffEM} = k_7 E_4^{LN}$$

Terms in the equation include efflux to the blood (ξ_3), and a linear differentiation to the effector memory T cell population (k_7). We assumed that no effector T cells die in the lymph node (they can die in the blood).

Similar to naïve cells, central memory T cells (Eqn. (0.5)) are recruited to the lymph node (k_8) in addition to an influx rate (ξ_4). Other terms include differentiation from precursor cells (k_6), reactivation to precursor cells (k_3) and efflux into the blood (ξ_5). Given their relatively long lifespan compared to the length of the *in-silico* simulation (i.e., 200 days at most) we do not have a death term in Eqn. (0.5), as CM_4^{LN}:

$$\frac{dCM_4^{LN}}{dt} = \alpha\left(V_{primeCM} + \xi_4 CM_4^B\right) + V_{PdiffCM} - V_{CMdiffP} - V_{CMefflux} \quad (0.5)$$

$$V_{primeCM} = k_8 CM_4^B \left(\frac{APC}{APC + hs_8}\right)$$

$$V_{CMinflux} = \xi_4 CM_4^B$$

$$V_{CMefflux} = \xi_5 CM_4^{LN}$$

Effector memory cell formation is described in Eqn. (0.6), as EM_4^{LN}. A linear term captures the differentiation of CD4+ effector T cells into CD4+ effector memory (k_7). The last term represented efflux to the blood (ξ_6). Due to the longevity of these cells, we did not introduce a death term in the lymph node. Like effector T cells, effector memory T cells do not enter the lymph node directly from the blood.

$$\frac{dEM_4^{LN}}{dt} = V_{EdiffEM} - V_{EMefflux} \quad (0.6)$$

$$V_{EMefflux} = \xi_6 EM_4^{LN}$$

Blood

For the blood compartment, we track 4 different T cell antigen-specific phenotypes. The antigen-specific naïve CD4+ T cell blood population is modeled by Eqn. (0.7) (N_4^B). We have terms for a constant source supplied from the thymus (multiplied by the antigen-specific frequency i.e. λs_{N_4}) to track specific and non-specific cells, migration from the lymph node (ξ_2), extra recruitment to the lymph node (k_1), migration to the lymph node (ξ_1), and death (μ_8).

$$\frac{dN_4^B}{dt} = \lambda s_{N_4} + \alpha^{-1} V_{Nefflux} - V_{primeN} - V_{Ninflux} - \mu_8 N_4^B \quad (0.7)$$

The values for s_{N_4} and μ_8 are chosen to maintain equilibrium in the total Naïve T cell populations (based on the initial conditions taken from the NHP blood data in previous work [1]).

Eqn. (0.8) describes effector CD4+ T cells dynamics (E_4^B) in the blood with two terms: migration from the lymph node (ξ_3) and death (μ_1).

$$\frac{dE_4^B}{dt} = \alpha^{-1} V_{Eefflux} - \mu_1 E_4^B \quad (0.8)$$

Central memory cells in the blood (Eqn. (0.9)) (CM_4^B) migrate from (ξ_5) and to the lymph node (ξ_4). Central memory cells are not recruited to the site of infection.

$$\frac{dCM_4^B}{dt} = \alpha^{-1}V_{CMefflux} - V_{CMinflux} - V_{primeCM} \quad (0.9)$$

Effector memory cells in the blood (Eqn.(0.10)) (EM_4^B) are modeled by two terms: migration from the lymph node (ξ_6) and death (μ_2). Similar to effector cells these were recruited to the site of infection.

$$\frac{dEM_4^B}{dt} = \alpha^{-1}V_{EMefflux} - \mu_2 EM_4^B \quad (0.10)$$

Non-antigen-specific CD4+ lymphocytes

Our computational model similarly keeps track of non-specific T cells. However, non-antigen-specific T cells do not respond to antigen, therefore, no priming occurs in any cell population and no precursor cells are generated. Also, since we assume neither effector nor effector memory T cells enter the lymph compartment from the blood, we do not model effector or effector memory cell populations within the lymph node compartment (as shown in Figure 2). The production of the non-specific effector cells was modeled as a source term in the blood compartment and was included to meet the assumption that the previous pre-infection data describes homeostasis. The equations for non-antigen-specific CD4+ T cells are shown below. Moreover, including non-antigen-specific cells in the model makes model predictions more realistic due to the total cell numbers more accurately reflecting the actual numbers in blood.

Naïve CD4+ non-antigen-specific (N_{nc4}^{LN})

$$\frac{dN_{nc4}^{LN}}{dt} = \alpha\left(k_1 N_{nc4}^B\left(\frac{APC}{APC+hs_1}\right)+\xi_1 N_{nc4}^B\right)-\xi_2 N_{nc4}^{LN} \quad (1.11)$$

Central Memory CD4+ non-antigen-specific - LN (CM_{nc4}^{LN})

$$\frac{dCM_{nc4}^{LN}}{dt} = \alpha\left(k_8 CM_{nc4}^B\left(\frac{APC}{APC+hs_8}\right)+\xi_4 CM_{nc4}^B\right)-\xi_5 CM_{nc4}^{LN} \quad (1.12)$$

Naïve CD4+ non-antigen-specific – Blood (N_{nc4}^B)

$$\frac{dN_{nc4}^B}{dt} = (1-\lambda)s_{N_4}+\alpha^{-1}\xi_2 N_{nc4}^{LN}-k_1 N_{nc4}^B\left(\frac{APC}{APC+hs_1}\right)-\xi_1 N_{nc4}^B-\mu_8 N_{nc4}^B \quad (1.13)$$

Effector CD4+ non-antigen-specific - Blood (E_{nc4}^B)

$$\frac{dE_{nc4}^{B}}{dt} = s_{E_{nc4}} - \mu_1 E_{nc4}^{B} \tag{1.14}$$

As non Mtb-specific effector cells in the blood must be produced somewhere in the body, they are modeled as source and a death rate equal to that of their antigen-specific counterparts

Central Memory CD4+ non Mtb-specific – Blood (CM_{nc4}^{B})

$$\frac{dCM_{nc4}^{B}}{dt} = \alpha^{-1}\xi_5 CM_{nc4}^{LN} - \xi_4 CM_{nc4}^{B} - k_8 CM_{nc4}^{B}\left(\frac{APC}{APC + hs_8}\right) \tag{1.15}$$

Effector Memory CD4+ non-antigen-specific - Blood (EM_{nc4}^{B})

$$\frac{dEM_{nc4}^{B}}{dt} = s_{EM_{nc4}} - \mu_2 EM_{nc4}^{B} \tag{1.16}$$

			ESAT6				Ag85B				
			NHP		Human		NHP		Human		
Parameter Name	Description	Units	min	max	min	max	min	max	min	max	Reference
alpha	Conversion from Blood to LN	uL	2803389	4203247	3238553	3957346	2805260	4201462	3239508	3957875	Estimated and [31-32]
host_Ln	Involved Lymph Nodes in host	count	3	4	18	31	3	4	18	31	Estimated and [31-32]
lambda	frequency of specific Naïve T cells in system	count	0.0007	0.0010	0.0006	0.0010	0.0007	0.0010	0.0006	0.0010	Estimated and [31-32]
hs1	Naïve CD4+ T cell recruitment half saturation	count	14	21	26	31	14	21	26	31	Estimated from Uncertainty Analysis
hs4	Precursor CD4+ T cell proliferation half saturation	count	5	8	5	19	5	8	5	19	Estimated from Uncertainty Analysis
hs5	Precursor CD4+ T cell differentiation half saturation	count	374	561	56	93	10	50	56	93	Estimated from Uncertainty Analysis
hs8	Central Memory CD4+ T cell recruitment half saturation	count	6	9	46	56	6	9	46	56	Estimated from Uncertainty Analysis

k1	Naïve CD4+ T cell recruitment rate	day^{-1}	0.85	1.28	0.35	0.59	0.85	1.28	0.35	0.59	Estimated from Uncertainty Analysis
k2	Naïve CD4+ T cell priming rate	day^{-1}	0.048	0.071	0.050	0.100	0.005	0.020	0.050	0.100	Estimated from Uncertainty Analysis
k3	Central Memory CD4+ T cell reactivation rate	day^{-1}	0.0091	0.0899	0.0116	0.0142	0.0009	0.0090	0.0101	0.0119	Estimated from Uncertainty Analysis
k4	Precursor CD4+ T cell proliferation rate	day^{-1}	0.70	1.30	1.50	2.00	0.50	1.00	1.50	2.00	Estimated from Uncertainty Analysis
k5	Precursor CD4+ T cell differentiation to effector T cell	day^{-1}	0.009	0.160	0.050	0.075	0.007	0.090	0.015	0.030	Estimated from Uncertainty Analysis
k6	Precursor CD4+ T cell differentiation to central memory T cell	day^{-1}	0.0010	0.0100	0.0005	0.0010	0.0009	0.0250	0.0010	0.0020	Estimated from Uncertainty Analysis
k7	Effector CD4+ T cell differentiation to effector Memory	day^{-1}	0.7	1.5	2.8	4.2	0.6	0.9	0.9	1.7	Estimated from Uncertainty Analysis
k8	Central Memory CD4+ T cell recruitment rate	day^{-1}	0.19	0.19	0.10	0.34	0.19	0.19	0.05	0.14	Estimated from Uncertainty Analysis

mu1	Effector CD4+ T cell death rate	day^{-1}	0.07	0.10	0.10	0.67	0.07	0.10	0.07	0.67	Estimated from Uncertainty Analysis
mu2	Effector memory CD4+ T cell death rate	day^{-1}	0.05	0.07	0.005	0.010	0.01	0.07	0.006	0.009	Estimated from Uncertainty Analysis
mu5	APC death rate	day^{-1}	0.28	0.41	0.65	1.08	0.28	0.41	0.65	1.08	Estimated from Uncertainty Analysis
mu6	Precursor CD4+ T cell death rate	day^{-1}	0.19	0.29	0.11	0.19	0.19	0.29	0.11	0.19	Estimated from Uncertainty Analysis
mu8	Naïve CD4+ T cell death rate	day^{-1}	0.000393	0.000393	0.000393	0.000393	0.000393	0.000393	0.000393	0.000393	[32]
rho1	Precursor Carrying Capacity	count	300000000	3000000000	300000000	300000000	300000000	300000000	300000000	300000000	[32]
xi2	Naïve CD4+ Lymph Efflux	day^{-1}	1.0	1.5	0.8	0.9	1.0	1.5	0.8	0.9	Estimated and [31-32]
xi3	Effector CD4+ Lymph Efflux	day^{-1}	3	4	1	1	3	4	1	1	Estimated and [31-32]
xi5	Central Memory CD4+ Lymph Efflux	day^{-1}	1.7	2.6	0.3	0.3	1.7	2.6	0.3	0.3	Estimated and [31-32]
xi6	Effector memory CD4+ Lymph Efflux	day^{-1}	2.0	3.1	4.0	5.0	2.1	3.1	2.0	5.0	Estimated and [31-32]
xi1****	Naïve CD4+	day^{-1}	0.25	0.54	0.03	0.05	0.25	0.54	0.03	0.05	

	Lymph Influx										
xi4****	Central Memory Lymph Influx	day^{-1}	0.446	0.956	0.009	0.017	0.452	0.959	0.009	0.017	
Sn4****	Thymic Output of Naive CD4+ T cells	Cell/uL * day	0.063	0.095	0.039	0.236	0.095	0.142	0.023	0.107	
Senc4****	frequency of nonspecific effector CD4+ T cells	Cell/uL * day	14.3	78.9	62.8	702.6	31.8	64.5	33.4	539.0	
Semnc4****	frequency of nonspecific effector memory CD4+ T cells	Cell/uL * day	0.063	10.278	0.007	0.215	0.034	20.499	0.003	3.169	
BlN4	frequency of Naïve CD4+ T cells in blood/LN	$cell/mm^3$	161	241	100	600	241	361	60	273	Estimated from Uncertainty Analysis
BlCM4	Initial frequency of Central Memory CD4+ T cells in blood/LN	$cell/mm^3$	1	3	0.01	10.00	1	100	10	100	Estimated from Uncertainty Analysis
BlCM4CogFraction	Fraction of Central Memory CD4+ T	unitless	0.001	0.002	0.001	0.003	0.001	0.002	0.002	0.003	Estimated from Uncertainty Analysis

	cells that are antigen-specific										
BlE4	Initial frequency of Nonspecific Effector CD4+ T cells	cell/mm^3	201	799	538	1095	446	668	359	875	Estimated from Uncertainty Analysis
BlEM4	Initial frequency of Effector Memory CD4+ T cells	cell/mm^3	1	150	1	22	1	300	0.34	371	Estimated from Uncertainty Analysis
BlEM4CogFraction	Fraction of Effector Memory CD4+ T cells that are antigen-specific	count	0.002	0.003	0.003	0.007	0.002	0.003	0.003	0.007	Estimated from Uncertainty Analysis
			20% around median	10% range around median	20% around median	10% range around median					

Table C.1 Parameter ranges for NHP and human ESAT6 and Ag85B fits.

**** signifies that parameter ranges were based on other parameter values. As specified in Marino et al. 2016 Computation paper (see reference in main document [32]) red text marks parameters that have a parameter range which is narrower than 20% range around the median value (for NHPs) or less than 10% range around the median value (for humans)

Visual comparison of parameter ranges for simulation curves

This appendix text presents the parameter ranges for human and NHP ESAT6 and Ag85b immunogenicity dataspaces. Figure C.1's shows the radarcharts that visually display the parameter ranges. Radarchart construction is outlined in the Methods section of the main paper. Briefly, this chart is to be read from left to right. That is, the charts are constructed such that in the ESAT6 (or Ag85b) row, we can compare the parameter ranges that fit the NHP response (blue) to those that fit the Human response (red). A small table is shown beneath the figure, to provide the reader with a legend for parameter names.

While sensitivity and uncertainty analysis (discussed in Chapter 4) reveals the parameters that generally control responses to each antigen, it is important to broadly consider the differential parameter spaces whereupon these responses reside. Uncertainty and sensitivity analysis suggested that parameters for Precursor cell proliferation (k4), differentiation (k5 and k6), recruitment rates of Naïve (k1) and Central Memory (k8), and half-saturation values (hs1-hs8) all played important roles in at least one of the three main blood T cell subtype outcomes. However, examination of Figure C.1's charts allows for direct comparison of each species' parameter ranges for each of these parameters. These charts reveal that each species resides in a separate parameter space for the majority of these parameters. Thus, despite the similar (revealed by uncertainty and sensitivity analysis) processes of each species, the parameters that dictate these processes actually differ in value.

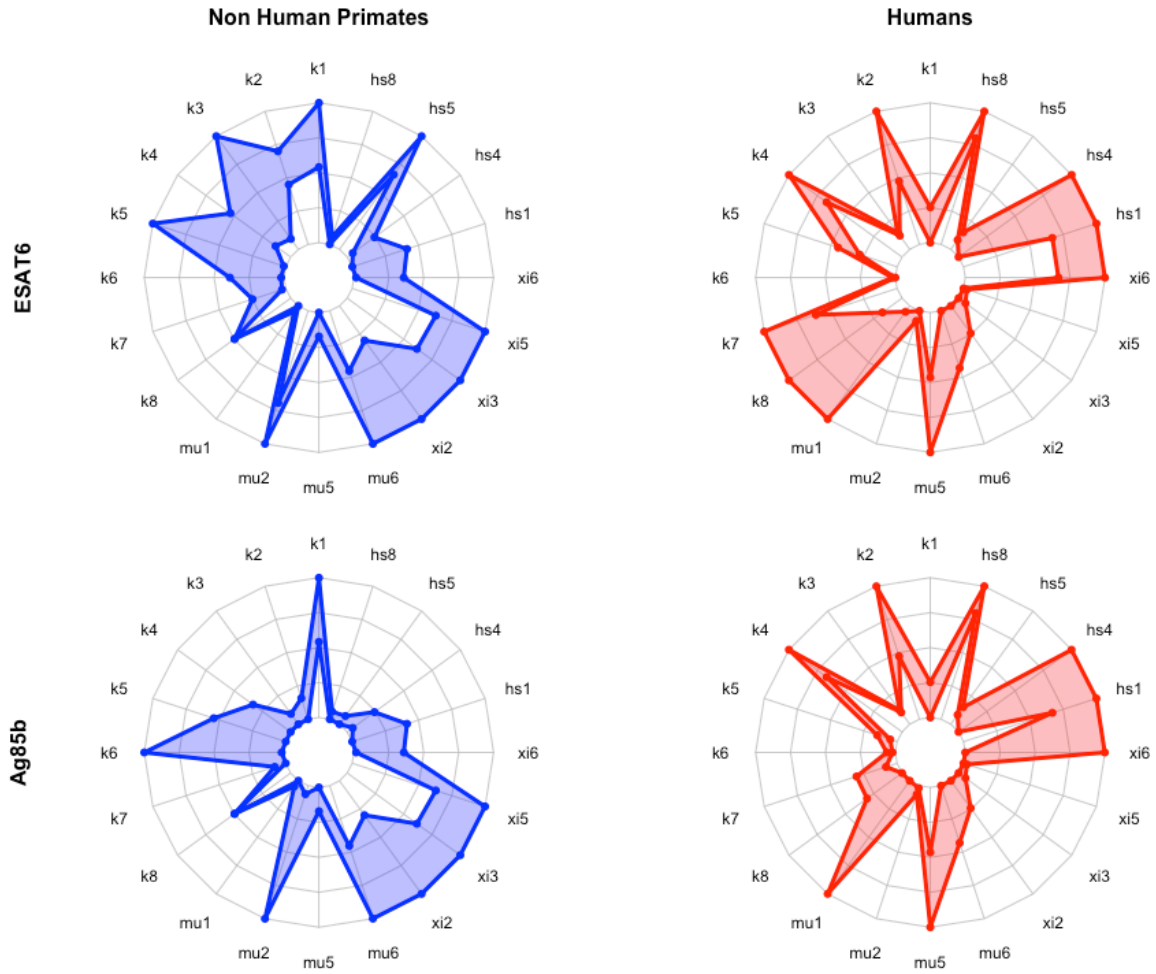

Figure C.1 Radar charts reveal parameter space differences between species.
Each parameter space is represented by a blue (NHP) or red (human) band, which represents the min and max parameter value for each model fit. Each chart displays parameter names around its outside boundary, at each axis. Parameter names are ordered alphabetically starting with 'hs1' and 'ending with xi6'. Points near the center of each axis represent a lower value whereas points near the outer edges of each axis represent larger values. To compare parameter ranges across species, we calculated the minimum and maximum for each axis on the charts as the minimum and maximum value for each parameter across all species and antigen specific fits. It should be noted that in this type of visualization, the placement of each parameter along the polar coordinate system can influence the visualization and therefore, the conclusions. In this work, I've ensured that each parameter does not change placement across individual radarcharts and each parameter is placed alphabetically. However, one could choose to cluster all parameters with wide ranges near one another on the charts. Care should be exercised when visualizing parameter space using these charts.

Parameter Name	Description
hs1	Naïve CD4+ T cell recruitment half saturation
hs4	Precursor CD4+ T cell proliferation half saturation
hs5	Precursor CD4+ T cell differentiation half saturation
hs8	Central Memory CD4+ T cell recruitment half saturation
k1	Naïve CD4+ T cell recruitment rate
k2	Naïve CD4+ T cell priming rate
k3	Central Memory CD4+ T cell reactivation rate
k4	Precursor CD4+ T cell proliferation rate
k5	Precursor CD4+ T cell differentiation to effector T cell
k6	Precursor CD4+ T cell differentiation to central memory T cell
k7	Effector CD4+ T cell differentiation to effector Memory
k8	Central Memory CD4+ T cell recruitment rate
mu1	Effector CD4+ T cell death rate
mu2	Effector memory CD4+ T cell death rate
mu5	APC death rate
mu6	Precursor CD4+ T cell death rate
xi2	Naïve CD4+ Lymph Efflux
xi3	Effector CD4+ Lymph Efflux
xi5	Central Memory CD4+ Lymph Efflux
xi6	Effector memory CD4+ Lymph Efflux

Table C.2 Parameter names in radar charts.
The leftmost column shows the name of each parameter. The rightmost column displays a short description of each parameter.

Appendix D Supporting Information for Chapter 5

MultiGran Equations with the addition of Effector Memory T cells

This model, composed of a system of 20 ODEs, captures bacterial, T cell, macrophage and cytokine dynamics within a single granuloma lesion. Below, we have listed equations, variable names and a brief explanation of the dynamics of each equation. Parameter symbols generally adhere to the following guidelines: α parameters are growth rates. k parameters are rate constants involving other variables. μ parameters are death or decay rates. c parameters are half-saturation values. Sr parameters are recruitment rate values to represent recruitment of cells from other areas of the body, for example. β and f parameters are scaling constants.

Extracellular Bacteria concentrations within the granuloma are represented as BE across time. Extracellular bacteria can grow ($alpha20$), or can be released when infected macrophages (MI) undergo apoptosis from cytotoxic T cells (TC) or TNF ($F\alpha$). Activated macrophages (MA) or resting Macrophages (MR) can kill extracellular bacteria.

$$\frac{dB_E}{dt} = \alpha_{20}B_E + k_{17}NM_I\left(\frac{B_I^2}{B_I^2 + N^2M_I^2}\right) + k_{14a}N_{fracc}\frac{B_I}{M_I}M_I\left(\frac{\left(\frac{T_C + w_3T_1}{M_I}\right)}{\left(\frac{T_C + w_3T_1}{M_I}\right) + c_4}\right) + k_{14b}N_{fraca}\frac{B_I}{M_I}M_I\left(\frac{F_\alpha}{F_\alpha + f_9I_{10} + s_{4b}}\right)$$
$$- k_2\frac{N}{2}M_R\left(\frac{B_E}{B_E + c_9}\right) - k_{15}M_AB_E - k_{18}M_RB_E - \mu_{B_E}B_E + \mu_{M_I}N_{fracd}\frac{B_I}{M_I}M_I$$

Intracellular Bacteria concentrations are represented as B_I across time. B_I happens in the model as resting macrophages (M_R) engulf extracellular bacteria at a rate of k_2. Intracellular bacteria can die and can also become extracellular bacteria when infected macrophages undergo apoptosis. The intracellular bacterial growth term (beginning with α_{19}) has been slightly modified from MultiGran (35) so it now follows logistic growth function with a carrying capacity (N) per infected macrophage (M_I).

$$\frac{dB_I}{dt} = \alpha_{19}\frac{B_I}{M_I}M_I\left(1 - \frac{\frac{B_I}{M_I}}{N}\right) + k_2\frac{N}{2}M_R\left(\frac{B_E}{B_E + c_9}\right) - k_{17}NM_I\left(\frac{B_I^2}{B_I^2 + N^2M_I^2}\right) - k_{14a}\frac{B_I}{M_I}M_I\left(\frac{\left(\frac{T_C + w_3T_1}{M_I}\right)}{\left(\frac{T_C + w_3T_1}{M_I}\right) + c_4}\right)$$
$$- k_{14b}\frac{B_I}{M_I}M_I\left(\frac{F_\alpha}{F_\alpha + f_9I_{10} + s_{4b}}\right) - k_{52}\frac{B_I}{M_I}M_I\left(\frac{\left(\frac{\frac{T_C}{B_i + 1}\left(\frac{T_1}{T_1 + c_{T_1}}\right) + w_1T_1}{M_I}\right)}{\left(\frac{\frac{T_C}{B_i + 1}\left(\frac{T_1}{T_1 + c_{T_1}}\right) + w_1T_1}{M_I}\right) + c_{52}}\right) - \mu_{B_I}B_I + \mu_{M_I}\frac{B_I}{M_I}M_I$$

Resting Macrophages (MR) are recruited to the granuloma according to the number of activated Macrophages (MA), the number of infected macrophages (MI) and the concentration of TNF ($F\alpha$) in the granuloma. MR can become activated or infected macrophages, or die.

$$\frac{dM_R}{dt} = Sr_M + \alpha_{4a}(M_A + w_2 M_I) + Sr_{4b}\left(\frac{F_\alpha}{F_\alpha + f_8 I_{10} + s_{4b}}\right) - k_2 M_R\left(\frac{B_E}{B_E + c_9}\right) - k_3 M_R\left(\frac{B_E + wB_I + \beta F_\alpha}{B_E + wB_I + \beta F_\alpha + c_8}\right)\left(\frac{I_\gamma}{I_\gamma + f_1 I_4 + f_7 I_{10} + s_1}\right) - \mu_{M_R} M_R$$

Infected Macrophages (MI) become infected when a resting macrophage engulfs extracellular bacteria (BE). MI can burst when BI growth exceeds carrying capacity (N) and can die through TNF- or cytotoxic T cell- mediated apoptosis.

$$\frac{dM_I}{dt} = k_2 M_R\left(\frac{B_E}{B_E + c_9}\right) - k_{17} M_I\left(\frac{B_I^2}{B_I^2 + N^2 M_I^2}\right) - k_{14a} M_I\left(\frac{\left(\frac{T_C + w_3 T_1}{M_I}\right)}{\left(\frac{T_C + w_3 T_1}{M_I}\right) + c_4}\right) - k_{14b} M_I\left(\frac{F_\alpha}{F_\alpha + f_9 I_{10} + s_{4b}}\right) - k_{52} M_I\left(\frac{\left(\frac{T_C\left(\frac{T_1}{T_1 + c_{T_1}}\right) + w_1 T_1}{M_I}\right)}{\left(\frac{T_C\left(\frac{T_1}{T_1 + c_{T_1}}\right) + w_1 T_1}{M_I}\right) + c_{52}}\right) - \mu_{M_I} M_I$$

Activated Macrophages (MA) become activated through resting Macrophages (MR) interactions with extracellular bacteria (BE) and IFN-γ ($I\gamma$) in the granuloma. MA can be de-activated by IL-10 ($I10$) cytokines or die.

$$\frac{dM_A}{dt} = k_3 M_R\left(\frac{B_E + wB_I + \beta F_\alpha}{B_E + wB_I + \beta F_\alpha + c_8}\right)\left(\frac{I_\gamma}{I_\gamma + f_1 I_4 + f_7 I_{10} + s_1}\right) - k_4 M_A\left(\frac{I_{10}}{I_{10} + s_8}\right) - \mu_{M_A} M_A$$

Primed CD4+ T cells (T_0) can proliferate at the site of the granuloma based on numbers of activated macrophages. Additionally, they are recruited to the site according to M_I, M_A, F_α concentrations in the granuloma. Differentiation of primed cells to effector states is based on cytokine concentrations across the granuloma. Primed cells can die.

$$\frac{dT_0}{dt} = \alpha_{1a}(M_A + w_2 M_I) + Sr_{1b}\left(\frac{F_\alpha}{F_\alpha + f_8 I_{10} + s_{4b2}}\right) + \alpha_2 T_0\left(\frac{M_A}{M_A + c_{15}}\right) - k_6 I_{12} T_0\left(\frac{I_\gamma}{I_\gamma + f_1 I_4 + f_7 I_{10} + s_1}\right) - k_7 T_0\left(\frac{I_4}{I_4 + f_2 I_\gamma + s_2}\right) - \mu_{T_0} T_0$$

Effector Th1 T cells ($T1$) are recruited to the granuloma according to MI, MA, and $F\alpha$. They are a differentiated T cell state originating from primed CD4+ T cells or effector memory CD8+ T cells. They can die from too much IFN-γ ($I\gamma$).

$$\frac{dT_1}{dt} = \alpha_{3a}(M_A + w_2 M_I) + Sr_{3b}\left(\frac{F_\alpha}{F_\alpha + f_8 I_{10} + s_{4b1}}\right) + k_6 I_{12} T_0 \left(\frac{I_\gamma}{I_\gamma + f_1 I_4 + f_7 I_{10} + s_1}\right) + k_{31} T_{4EM} M_I - \mu_{T_\gamma}\left(\frac{I_\gamma}{I_\gamma + c}\right) T_1 M_A - \mu_{T_1} T_1$$

Effector Th2 T cells (T_2) are recruited to the granuloma according to M_I, M_A, and F_α. They are a differentiated T cell state originating from primed CD4+ T cells or effector memory CD4+ T cells.

$$\frac{dT_2}{dt} = \alpha_{3a2}(M_A + w_2 M_I) + Sr_{3b2}\left(\frac{F_\alpha}{F_\alpha + f_8 I_{10} + s_{4b1}}\right) + k_7 T_0 \left(\frac{I_4}{I_4 + f_2 I_\gamma + s_2}\right) + k_{32} T_{4EM} M_A - \mu_{T_2} T_2$$

Primed CD8+ T cells ($T80$) can proliferate at the site of the granuloma based on numbers of activated macrophages. Additionally, they are recruited to the site according to MI, MA, $F\alpha$ concentrations in the granuloma. Differentiation of primed cells to effector states is based on cytokine concentrations across the granuloma. Primed cells can die.

$$\frac{dT_{80}}{dt} = \alpha_{1a}(M_A + w_2 M_I) + Sr_{1b}\left(\frac{F_\alpha}{F_\alpha + f_8 I_{10} + s_{4b2}}\right) + \alpha_2 T_{80}\left(\frac{M_A}{M_A + c_{15}}\right) - k_6 I_{12} T_{80}\left(\frac{I_\gamma}{I_\gamma + f_1 I_4 + f_7 I_{10} + s_1}\right) - \mu_{T_{80}} T_{80}$$

Effector CD8+ T cells (T_8) are recruited to the granuloma according to M_I, M_A, and F_α. They are a differentiated T cell state originating from primed CD8+ T cells or effector memory CD8+ T cells and can die from IFN-γ (I_γ).

$$\frac{dT_8}{dt} = m\alpha_{3ac}(M_A + w_2 M_I) + mSr_{3bc}\left(\frac{F_\alpha}{F_\alpha + f_8 I_{10} + s_{4b1}}\right) + mk_6 I_{12} T_{80}\left(\frac{I_\gamma}{I_\gamma + f_1 I_4 + f_7 I_{10} + s_1}\right) + k_{34} T_{8EM} M_I - \mu_{T_{c\gamma}}\left(\frac{I_\gamma}{I_\gamma + c_c}\right) T_8 M_A - \mu_{T_C} T_8$$

Cytotoxic CD8+ T cells (T_C) are recruited to the granuloma according to M_I, M_A, and F_α. They are a differentiated T cell state originating from primed CD8+ T cells or effector memory CD8+ T cells and can die from IFN-γ (I_γ).

$$\frac{dT_C}{dt} = m\alpha_{3ac}(M_A + w_2 M_I) + mSr_{3bc}\left(\frac{F_\alpha}{F_\alpha + f_8 I_{10} + s_{4b1}}\right) + mk_6 I_{12} T_{80}\left(\frac{I_\gamma}{I_\gamma + f_1 I_4 + f_7 I_{10} + s_1}\right) + k_{33} T_{8EM} M_I - \mu_{T_{c\gamma}}\left(\frac{I_\gamma}{I_\gamma + c_c}\right) T_C M_A - \mu_{T_C} T_C$$

CD4+ effector memory T cells (T_{4EM}) can differentiate at the site of infection into effector cell states based on numbers of infected or activated macrophages. Additionally, they are recruited to the site according to F_α concentrations in the granuloma. These cells can die at the site of infection.

$$\frac{dT_{4EM}}{dt} = Sr_{4EM}\left(\frac{F_\alpha}{F_\alpha + hs_{4EM}}\right) - k_{31} T_{4EM} M_I - k_{32} T_{4EM} M_A - \mu_{T_{4EM}} T_{4EM}$$

CD8+ effector memory T cells (T_{8EM}) can differentiate at the site of infection into effector cell states based on numbers of infected macrophages. Additionally, they are recruited to the site according to F_α concentrations in the granuloma. These cells can die at the site of infection.

$$\frac{dT_{8EM}}{dt} = Sr_{8EM}\left(\frac{F_\alpha}{F_\alpha + hs_{8EM}}\right) - k_{33}T_{8EM}M_I - k_{34}T_{8EM}M_I - \mu_{T_{8EM}}T_{8EM}$$

CD4+ non-specific T cells (T_{4Non}) represent a generic class of T cells that do not respond to Mtb antigens but are recruited to the site according to F_α concentrations in the granuloma. These cells do not perform effector functions within the granuloma and die at the site of infection.

$$\frac{dT_{4N\,on}}{dt} = Sr_{4N\,on}\left(\frac{F_\alpha}{F_\alpha + hs_{4N\,on}}\right) - \mu_{T_{4N\,on}}T_{4N\,on}$$

CD8+ non-specific T cells (T_{8Non}) represent a generic class of T cells that do not respond to Mtb antigens but are recruited to the site according to F_α concentrations in the granuloma. These cells do not perform effector functions within the granuloma and die at the site of infection.

$$\frac{dT_{8N\,on}}{dt} = Sr_{8N\,on}\left(\frac{F_\alpha}{F_\alpha + hs_{8N\,on}}\right) - \mu_{T_{8N\,on}}T_{8N\,on}$$

TNF (F_α) is an inflammatory cytokine in the granuloma and is secreted by M_I, M_A, T_1, T_C and T_8 cells. It also decays in the granuloma.

$$\frac{dF_\alpha}{dt} = \alpha_{30}M_I + \alpha_{31}M_A\left(\frac{I_\gamma + \beta_2(B_E + wB_I)}{I_\gamma + \beta_2(B_E + wB_I) + f_1I_4 + f_7I_{10} + s_{10}}\right) + \alpha_{32}T_1 + \alpha_{33}\left(\frac{T_C + T_8}{2m}\right) - \mu_{F_\alpha}F_\alpha$$

IFN-γ (I_γ) is an inflammatory cytokine in the granuloma and is secreted by M_I, M_A, T_0, T_1, T_80, T_C and T_8 cells. It also decays in the granuloma.

$$\frac{dI_\gamma}{dt} = s_g\left(\frac{B_E + wB_I}{B_E + wB_I + c_{10}}\right)\left(\frac{I_{12}}{I_{12} + s_7}\right) + \alpha_{5a}T_1\left(\frac{M_A}{M_A + c_{5a}}\right) + \alpha_{5b}T_8\left(\frac{M_A}{M_A + c_{5b}}\right) + \alpha_{5c}M_I + \alpha_7T_0\left(\frac{I_{12}}{I_{12} + f_4I_{10} + s_4}\right) + \alpha_7T_{80}\left(\frac{I_{12}}{I_{12} + f_4I_{10} + s_4}\right) - \mu_{I_\gamma}I_\gamma$$

IL-12 (I_{12}) is secreted by M_R and M_A cells before decaying in the granuloma.

$$\frac{dI_{12}}{dt} = s_{12}\left(\frac{B_E + wB_I}{B_E + wB_I + c_{230}}\right) + \alpha_{23}M_R\left(\frac{B_E + wB_I}{B_E + wB_I + c_{23}}\right) + \alpha_8M_A\left(\frac{s}{s + I_{10}}\right) - \mu_{I_{12}}I_{12}$$

IL-10 (I_{10}) is secreted by M_I, M_A, T_1, T_2, T_C and T_8 before decaying in the granuloma.

$$\frac{dI_{10}}{dt} = \delta_7(M_I + M_A)\left(\frac{s_6}{I_{10} + f_6I_\gamma + s_6}\right) + \alpha_{16}T_1 + \alpha_{17}T_2 + \alpha_{18}\left(\frac{T_C + T_8}{2m}\right) - \mu_{I_{10}}I_{10}$$

IL-4 (I_4) is secreted by T_0 and T_2 before decaying in the granuloma.

$$\frac{dI_4}{dt} = \alpha_{11}T_0 + \alpha_{12}T_2 - \mu_{I_4}I_4$$

Blood and Lymph node equations

This two-compartment model represents the dynamics of specific and non-specific T cells in the lymph node and blood following antigen presentation by antigen-presenting cells (APCs) in the lymph node. Measure units are cell counts in the lymph compartment and cell/mm^3 in the blood compartment. The term α represents the volume of blood in μL and is used for scaling cells when they traffic between the blood compartment and the lymph compartment.

Lymph Node CD4+ T cells
Antigen presentation and priming in lymph node compartment is driven by the following equation:

$$\frac{dAPC}{dt} = -\mu_5 APC \tag{0.11}$$

which tracks antigen presenting cells (APCs) in the lymph node at any time during or after infection. If the number of APCs doesn't increase (a reinfection event would be an example of increasing the APC population), the APC number decreases following an exponential decay, at the rate μ_5.
Naïve T cells (Eqn. (0.2)) represented by (N_4^{LN}) are recruited to the lymph node at a rate (k_1) dependent on cytokine production in the lymph node. Since we do not track cytokines in the lymph node model, we use APC also as a proxy for cytokine production (modeled as a Michaelis-Menten term in Eqn. (0.2)). Other terms included influx (ξ_1) and efflux (ξ_2), as well as mass action priming to precursor cells (k_2).

$$\frac{dN_4^{LN}}{dt} = \alpha\left(V_{primeN} + V_{Ninflux}\right) - V_{Nefflux} - V_{NdiffP} \tag{0.12}$$
$$V_{primeN} = k_1 N_4^B \left(\frac{APC}{APC + hs_1}\right)$$
$$V_{NdiffP} = k_2 N_4^{LN} APC$$
$$V_{Nefflux} = \xi_2 N_4^{LN}$$
$$V_{Ninflux} = \xi_1 N_4^B$$

Precursor CD4+ T cells (P_4^{LN}) (Eqn. (0.3)) are generated through priming of antigen-specific naïve T cells (k_2) as well as through re-activation of antigen-specific central memory T cells (k_3); both processes are expressed as mass action terms. Proliferation is modeled as logistic growth.

$$\frac{dP_4^{LN}}{dt} = \left(V_{NdiffP} + V_{CMdiffP}\right) + V_{prolif} - V_{PdiffE} - V_{PdiffCM} - \mu_6 P_4^{LN} \tag{0.13}$$

$$V_{CMdiffP} = k_3 CM_4^{LN} APC$$

$$V_{prolif} = k_4 P_4^{LN}\left(1 - \left(\frac{P_4^{LN}}{\rho_1}\right)\right)\left(\frac{APC}{APC + hs_4}\right)$$
$$V_{PdiffE} = k_5 P_4^{LN}\left(\frac{APC}{APC + hs_5}\right)$$
$$V_{PdiffCM} = k_6 P_4^{LN}\left(1 - \left(\frac{APC}{APC + hs_5}\right)\right)$$

A Michaelis-Menten term based on antigen stimulation (APC levels) was used to adjust proliferation (k_4) and differentiation rates (k_5 and k_6). The likelihood of precursor cells differentiating into effector cells is directly proportional to the amount of antigen stimulation (k_5). The opposite assumption was applied to the likelihood of precursor cells differentiating into central memory (k_6). A death term (μ_6) ensured that the precursor population did not persist in the absence of infection. No precursor populations exit the lymph node.
Effector CD4+ T cells are modeled in Eqn. (0.4), as E_4^{LN}:

$$\frac{dE_4^{LN}}{dt} = V_{PdiffE} - V_{Eefflux} - V_{EdiffEM} \quad (0.14)$$
$$V_{Eefflux} = \xi_3 E_4^{LN}$$
$$V_{EdiffEM} = k_7 E_4^{LN}$$

Terms in the equation include efflux to the blood (ξ_3), and a linear differentiation to the effector memory T cell population (k_7). We assumed that no effector T cells die in the lymph node (they can die in the blood).
Similar to naïve cells, central memory T cells (Eqn. (0.5)) are recruited to the lymph node (k_8) in addition to an influx rate (ξ_4). Other terms include differentiation from precursor cells (k_6), reactivation to precursor cells (k_3) and efflux into the blood (ξ_5). Given their relatively long lifespan compared to the length of the *in-silico* simulation (i.e., 200 days at most) we do not have a death term in Eqn. (0.5), as CM_4^{LN}:

$$\frac{dCM_4^{LN}}{dt} = \alpha\left(V_{primeCM} + \xi_4 CM_4^B\right) + V_{PdiffCM} - V_{CMdiffP} - V_{CMefflux} \quad (0.15)$$
$$V_{primeCM} = k_8 CM_4^B\left(\frac{APC}{APC + hs_8}\right)$$
$$V_{CMinflux} = \xi_4 CM_4^B$$
$$V_{CMefflux} = \xi_5 CM_4^{LN}$$

Effector memory cell formation is described in Eqn. (0.6), as EM_4^{LN}. A linear term captures the differentiation of CD4+ effector T cells into CD4+ effector memory (k_7). The last term represented efflux to the blood (ξ_6). Due to the longevity of these cells, we did not introduce a death term in the lymph node. Like effector T cells, effector memory T cells do not enter the lymph node directly from the blood.

$$\frac{dEM_4^{LN}}{dt} = V_{EdiffEM} - V_{EMefflux} \quad (0.16)$$
$$V_{EMefflux} = \xi_6 EM_4^{LN}$$

Blood CD4+ T cells

For the blood compartment, we track 4 different T cell antigen-specific phenotypes. The antigen-specific naïve CD4+ T cell blood population is modeled by Eqn. (0.7) (N_4^B). We have terms for a constant source supplied from the thymus (multiplied by the antigen-specific frequency i.e. λs_{N_4}) to track specific and non-specific cells, migration from the lymph node (ξ_2), extra recruitment to the lymph node (k_1), migration to the lymph node (ξ_1), and death (μ_8).

$$\frac{dN_4^B}{dt} = \lambda s_{N_4} + \alpha^{-1} V_{Nefflux} - V_{primeN} - V_{Ninflux} - \mu_8 N_4^B \quad (0.17)$$

The values for s_{N_4} and μ_8 are chosen to maintain equilibrium in the total Naïve T cell populations (based on the initial conditions taken from the NHP blood data in previous work (47)).
Eqn. (0.8) describes effector CD4+ T cells dynamics (E_4^B) in the blood with two terms: migration from the lymph node (ξ_3) and death (μ_1).

$$\frac{dE_4^B}{dt} = \alpha^{-1} V_{Eefflux} - \mu_1 E_4^B \quad (0.18)$$

Central memory cells in the blood (Eqn. (0.9)) (CM_4^B) migrate from (ξ_5) and to the lymph node (ξ_4). Central memory cells are not recruited to the site of infection.

$$\frac{dCM_4^B}{dt} = \alpha^{-1} V_{CMefflux} - V_{CMinflux} - V_{primeCM} \quad (0.19)$$

Effector memory cells in the blood (Eqn.(0.10)) (EM_4^B) are modeled by two terms: migration from the lymph node (ξ_6) and death (μ_2). Similar to effector cells these were recruited to the site of infection.

$$\frac{dEM_4^B}{dt} = \alpha^{-1} V_{EMefflux} - \mu_2 EM_4^B \quad (0.20)$$

Non-Mtb-specific CD4+ lymphocytes
Our computational model similarly keeps track of non-specific T cells. However, non-Mtb-specific T cells do not respond to antigen, therefore, no priming occurs in any cell population and no precursor cells are generated. Also, since we assume neither effector nor effector memory T cells enter the lymph compartment from the blood, we do not model effector or effector memory cell populations within the lymph node compartment (as shown in Figure 2). The production of the non-specific effector cells was modeled as a source term in the blood compartment and was included to meet the assumption that the previous pre-infection data describes homeostasis. The equations for non-Mtb-specific CD4+ T cells are shown below. Moreover, including non-Mtb-specific cells in the model makes model predictions more realistic due to the total cell numbers more accurately reflecting the actual numbers in blood.

Naïve CD4+ non-Mtb-specific (N_{nc4}^{LN})

$$\frac{dN_{nc4}^{LN}}{dt} = \alpha\left(k_1 N_{nc4}^{B}\left(\frac{APC}{APC+hs_1}\right)+\xi_1 N_{nc4}^{B}\right)-\xi_2 N_{nc4}^{LN} \tag{1.11}$$

Central Memory CD4+ non-Mtb-specific - LN (CM_{nc4}^{LN})

$$\frac{dCM_{nc4}^{LN}}{dt} = \alpha\left(k_8 CM_{nc4}^{B}\left(\frac{APC}{APC+hs_8}\right)+\xi_4 CM_{nc4}^{B}\right)-\xi_5 CM_{nc4}^{LN} \tag{1.12}$$

Naïve CD4+ non-Mtb-specific – Blood (N_{nc4}^{B})

$$\frac{dN_{nc4}^{B}}{dt} = (1-\lambda)s_{N_4}+\alpha^{-1}\xi_2 N_{nc4}^{LN}-k_1 N_{nc4}^{B}\left(\frac{APC}{APC+hs_1}\right)-\xi_1 N_{nc4}^{B}-\mu_8 N_{nc4}^{B} \tag{1.13}$$

Effector CD4+ non-Mtb-specific - Blood (E_{nc4}^{B})

$$\frac{dE_{nc4}^{B}}{dt} = s_{E_{nc4}}-\mu_1 E_{nc4}^{B} \tag{1.14}$$

As non Mtb-specific effector cells in the blood must be produced somewhere in the body, they are modeled as source and a death rate equal to that of their antigen-specific counterparts.

Central Memory CD4+ non Mtb-specific – Blood (CM_{nc4}^{B})

$$\frac{dCM_{nc4}^{B}}{dt} = \alpha^{-1}\xi_5 CM_{nc4}^{LN}-\xi_4 CM_{nc4}^{B}-k_8 CM_{nc4}^{B}\left(\frac{APC}{APC+hs_8}\right) \tag{1.15}$$

Effector Memory CD4+ non-Mtb-specific - Blood (EM_{nc4}^{B})

$$\frac{dEM_{nc4}^{B}}{dt} = s_{EM_{nc4}}-\mu_2 EM_{nc4}^{B} \tag{1.16}$$

Lymph Node and Blood Mtb-specific T cells

There are only slight differences in our modeling of CD8+ and CD4+ T cells. Importantly, the priming of Mtb-specific naïve CD8+ T cells is impacted by cytokines released by activated CD4+ T cells in the lymph node. Again, as we do not directly model cytokine expression in the lymph nodes, this is modeled indirectly by a Michaelis-Menten term that includes activated CD4+ T effector cells and a weighted term for precursor CD4+ T cells. We display these equations below:

$$\frac{dN_8^{LN}}{dt} = \alpha\left(k_{10} N_8^{B}\left(\frac{DC}{DC+hs_{10}}\right)+\xi_7 N_8^{B}\right)-\xi_8 N_8^{LN}- \\ -k_{11} N_8^{LN} DC\left(\frac{[E_4^{LN}+W_{P_4}P_4^{LN}]}{[E_4^{LN}+W_{P_4}P_4^{LN}]+hs_{11}}\right) \tag{1.17}$$

$$\frac{dP_8^{LN}}{dt} = k_{11}N_8^{LN}DC\left(\frac{[E_4^{LN} + W_{P_4}P_4^{LN}]}{[E_4^{LN} + W_{P_4}P_4^{LN}] + hs_{11}}\right) + k_{12}CM_8^{LN}DC$$
$$+k_{13}P_8^{LN}\left(1 - \frac{P_4^{LN} + P_8^{LN}}{\rho_1}\right)\left(\frac{DC}{DC + hs_{13}}\right) - k_{14}P_8^{LN}\left(\frac{DC}{DC + hs_{14}}\right) -$$
$$-k_{15}P_8^{LN}\left(1 - \left(\frac{DC}{DC + hs_{14}}\right)\right) - \mu_7 P_8^{LN} \tag{1.18}$$

Effector CD8+ T cells in lymph node

$$\frac{dE_8^{LN}}{dt} = k_{14}P_8^{LN}\left(\frac{DC}{DC+hs_{14}}\right) - \xi_9 E_8^{LN} - k_{16}E_8^{LN} \tag{1.19}$$

Central Memory CD8+ T cells in lymph node

$$\frac{dCM_8^{LN}}{dt} = \alpha\left(k_{17}CM_8^B\left(\frac{DC}{DC + hs_{17}}\right) + \xi_{10}CM_8^B\right) +$$
$$k_{15}P_8^{LN}\left(1 - \left(\frac{DC}{DC + hs_{14}}\right)\right) - k_{12}CM_8^{LN}DC - \xi_{11}CM_8^{LN} \tag{1.20}$$

Effector Memory CD8+ T cells in lymph node

$$\frac{dEM_8^{LN}}{dt} = k_{16}E^{LN}{}_8 - \xi_{12}EM_8^{LN} \tag{1.21}$$

Naive CD8+ T cells in blood

$$\frac{dN_8^B}{dt} = \lambda s_{N_8} + \alpha^{-1}\xi_8 N_8^{LN} - k_{10}N_8^B\left(\frac{DC}{DC + hs_{10}}\right) - \xi_7 N_8^B - \mu_9 N_8^B \tag{1.22}$$

Effector CD8+ T cells in blood

$$\frac{dE_8^B}{dt} = \alpha^{-1}\xi_9 E_8^{LN} - \mu_3 E_8^B \tag{1.23}$$

Central Memory CD8+ T cells in blood

$$\frac{dCM_8^B}{dt} = \alpha^{-1}\xi_{11}CM_8^{LN} - \xi_{10}CM_8^B - k_{17}CM_8^B\left(\frac{DC}{DC+hs_{17}}\right) \tag{1.24}$$

Effector Memory CD8+ T cells in blood

$$\frac{dEM_8^B}{dt} = \alpha^{-1}\xi_{12}EM_8^{LN} - \mu_4 EM_8^B \tag{1.25}$$

Lymph Node and Blood non-Mtb-specific CD8+ T cells

Modeled in an identical approach as the CD4+ T cell pools that were non-Mtb-specific.

Non-Mtb-specific Naive CD8+ T cells in lymph node

$$\frac{dN_{nc8}^{LN}}{dt} = \alpha\left(k_{10}N_{nc8}^B\left(\frac{DC}{DC+hs_{10}}\right) + \xi_7 N_{nc8}^B\right) - \xi_8 N_{nc8}^{LN} \tag{1.26}$$

Non-Mtb-specific Central Memory CD8+ T cells in lymph node

$$\frac{dCM_{nc8}^{LN}}{dt} = \alpha\left(k_{17}CM_{nc8}^B\left(\frac{DC}{DC+hs_{17}}\right) + \xi_{10}CM_{nc8}^B\right) - \xi_{11}CM_{nc8}^{LN} \tag{1.27}$$

Non-Mtb-specific Naive CD8+ T cells in blood

$$\frac{dN_{nc8}^B}{dt} = (1-\lambda)s_{N_4} + \alpha^{-1}\xi_8 N_{nc8}^{LN} - k_{10}N_{nc8}^B\left(\frac{DC}{DC+hs_{10}}\right) - \xi_7 N_{nc8}^B - \mu_9 N_{nc8}^B \tag{1.28}$$

Non-Mtb-specific Effector CD8+ T cells in blood

$$\frac{dE_{nc8}^B}{dt} = s_{E_{nc8}} - \mu_3 E_{nc8}^B \tag{1.29}$$

Non-Mtb-specific Central Memory CD8+ T cells in blood

$$\frac{dCM_{nc8}^B}{dt} = \alpha^{-1}\xi_{11}CM_{nc8}^{LN} - \xi_{10}CM_{nc8}^B - k_{17}CM_{nc8}^B\left(\frac{DC}{DC+hs_{17}}\right) \tag{1.30}$$

Non-Mtb-specific Effector Memory CD8+ T cells in blood

$$\frac{dEM_{nc8}^B}{dt} = s_{EM_{nc8}} - \mu_4 EM_{nc8}^B \tag{1.31}$$

Table D.1 Parameter table for granuloma model and lymph node & blood model

Parameter Name Granuloma ODE	Units	Parameter Description	Minimum Value	Maximum Value
Srm	1/day	MR recruitment rate	0	0
alpha4a	1/day	Macrophage recruitment of MR	0.7	1.0
beta	1/pg	Scaling factor of Falpha for MR activation	8.65E+06	1.14E+07
w	N/A	Contribution of BI to MR activation	0.26	0.36
w3	N/A	Max contribution of Th1 to MI apoptosis	0.2	0.8
w2	N/A	Contribution of MI to MR recruitment	0.9	1.2
Sr4b	1/day	Falpha dependent recruitment of MR	592	864
f8	N/A	Ratio adjustment I10/Falpha on MR recruitment	1.74E-03	2.25E-03
f9	N/A	Ratio adjustment Falpha/I10	0.523	0.673
s4b	pg/ml	Half saturation of Falpha on MR recruitment	2920	5250
k4	1/day	MA deactivation by I10	0.08	0.17
s8	pg/ml	Half saturation of I10 on MA deactivation	244	1003
k2	1/day	MR infection rate	0.84	2.31
c9	count	Half saturation of BE on MR infection	1622	7868
k3	1/day	MR activation rate	0.034	0.045
f1	N/A	Adjustment I4/IGamma	126	165
s1	pg/ml	Half saturation of IGamma dependent MR activation	83	479
c8	count	Half saturation of BE and BI on MR activation	1.64E+05	4.09E+05
nuMR	1/day	MR death rate	0.004	0.006
k17	1/day	Max rate of MI bursting	0.088	0.238
N	count	Carrying capacity of MI	5	25
k14a	1/day	T cell induced apoptosis of MI	0.07	1.7
c4	count	Half saturation of Th1/MI ratio on MI apoptosis	397	951
k14b	1/day	Falpha induced apoptosis of MI	0.59	0.92
k52	1/day	Cytotoxic killing of MI	0.54	0.78
w1	N/A	Max contribution of Th1 to cytotoxic killing	0.22	0.74
c52	count	Half saturation of TC on MI killing	1.08E+05	2.51E+05
cT1	count	Half saturation of Th1 on cytotoxic killing	30	40
nuMI	1/day	MI death rate	0.003	0.004
nuMA	1/day	MA death rate	0.15	0.20
alpha1a	1/day	Macrophage recruitment of T0	0.08	0.57
Sr1b	1/day	F/alpha dependent T0 recruitment	25007	54088
s4b2	pg/ml	Half saturation of Falpha dependent T0 recruitment	4834	10175
alpha2	1/day	Max growth rate of T0	0.1	1
c15	count	Half saturation of MA proliferation of T0	5	25

k6	1/day	Max T0 to Th1 rate	0.10	0.23
f7	N/A	Effect of I10 on IGamma induced differentiation of T0 to Th1	8.2	32.3
k7	1/day	Max T0 to Th2 rate	0.24	0.61
f2	N/A	Adjustment IGamma/I4	0.2	0.4
s2	pg/ml	Half saturation I4	429	955
nuT0	1/day	T0 death rate	0.19	0.25
m	N/A	Percentage overlap between TC and T8	0.68	0.90
alpha3a	1/day	Macrophage recruitment of Th1	0.39	0.82
Sr3b	1/day	Falpha dependent recruitment of Th2	19	83
s4b1	pg/ml	Half saturation of Falpha dependent Th1 recruitment	6131	10162
alpha3a2	1/day	Macrophage recruitment of Th2	0.25	0.79
Sr3b2	1/day	Falpha dependent recruitment of Th2	47.5	99.0
nuTg	1/day	Igamma induced apoptosis of Th1	0.290	0.762
c	pg/ml	Half saturation Igamma on Th1 apoptosis	284	727
nuT1	1/day	Th1 death rate	0.28	0.37
nuT2	1/day	Th2 death rate	0.29	0.37
alpha3ac	1/day	Macrophage recruitment of TC and T8	0.25	0.80
Sr3bc	1/day	Falpha dependent recruitment of TC and T8	13	28
nuTCg	1/day	Igamma induced apoptosis of Tc and T8	0.46	0.90
cc	pg/ml	Half saturation IFN-g on TC and T8 apoptosis	337	673
nuTC	1/day	TC death rate	0.26	0.33
alpha30	pg/(ml* day)	Falpha production by MI	0.05	0.10
alpha31	pg/(ml* day)	Falpha production by MA	0.19	0.82
beta2	1/pg	Scaling factor of Mtb for Falpha production by MA	10466	13466
s10	pg/ml	Half saturation of Igamma on Falpha production by MA	103	313
alpha32	pg/(ml* day)	Falpha production by Th1	0.20	0.34
alpha33	pg/(ml* day)	Falpha production by T8	0.18	0.33
nuTNF	1/day	Falpha decay rate	0.93	1.21
sg	pg/(ml* day)	Igamma production by dendritic cells (DCs)	2667	7944
c10	count	Half saturation of Mtb on Igamma production by DCs	980813	6876625
s7	pg/ml	Half saturation of I12 on Igamma production by DCs	538	883
alpha5a	pg/day	Igamma production by Th1	0.54	0.87
c5a	count	Half saturation of MA on Igamma production by Th1	304	687
alpha5b	pg/day	Igamma production by T8	0.18	0.60

alpha5c	pg/day	Igamma production by MI	0.12	0.36
c5b	count	Half saturation of MA on Igamma production by T8	235.8	846.6
alpha7	pg/day	Igamma production by T0	0.04	0.17
f4	N/A	Adjustment of I10/I12 on Igamma	1.30	1.67
s4	pg/ml	Half saturation of I12 on Igamma	285	810
nuIG	1/day	Igamma decay rate	5.448	9.693
alpha23	pg/day	I12 production by MR	0.003	0.005
c23	pg/ml	Half saturation of Mtb on I12 production by MR	157	525
alpha8	pg/day	I12 production by MA	0.38	0.86
s12	pg/day	Dendritic cell production of I12	2361	4061
c230	count	Half saturation of Mtb on I12 production by DCs	366	762
nuI12	1/day	I12 decay rate	0.93	1.24
s	pg/ml	I10 effect on I12 production by MA	192	694
delta7	pg/day	I10 production by MA	0.38	0.85
s6	pg/ml	Half saturation of I10 self	587	859
f6	N/A	Adjustment Igamma on I10	0.30	0.39
alpha16	pg/day	I10 production by Th1	0.33	0.79
alpha17	pg/day	I10 production by Th2	0.28	0.53
alpha18	pg/day	I10 production by TC and T8	0.46	0.78
nuI10	1/day	I10 decay rate	1.80	4.53
alpha11	pg/day	I4 production by T0	0.01	0.06
alpha12	pg/day	I4 production by Th2	0.02	0.06
nuI4	1/day	I4 decay rate	2.37	3.09
alpha19	1/day	BI growth rate	0.82	1.36
alpha20	1/day	BE growth rate	0.25	0.43
Nfracc	N/A	Fraction BI released by T cell apoptosis of MI	0.05	0.07
Nfraca	N/A	Fraction BI released by TNF apoptosis of MI	0.05	0.07
k15	1/day	BE killing by MA	0.0003	0.0011
k18	1/day	BE killing by MR	0.0003	0.0008
Nfracd	N/A	fraction of BI released during MI natural death to become BE	0.0009	0.0011
power	N/A	scaling factor	2	2
nI	1/day	BI death rate	5.95E-05	9.04E-05
nE	1/day	BE death rate	4.11E-09	7.41E-09
Sr4Non	1/day	TNFalpha dependent recruitment of CD4 non-specific T cells	156	504
hs4Non	pg/ml	half sat of TNFalpha dependent recruitment of CD4 non-specific T cells	5	50
mui4Non	1/day	death rate of CD4 non-specific T cells	0.3	0.4
Sr8Non	1/day	TNFalpha dependent recruitment of CD8 non	153	509

hs8Non	pg/day	half sat of TNFalpha dependent recruitment of CD8 non	5	50
mui8Non	1/day	death rate of CD8 non-specific T cells	0.3	0.4
Sr4EM	1/day	TNFalpha dependent recruitment of CD4 EM T cells	48	102
hs4EM	pg/ml	half sat of TNFalpha dependent recruitment of CD4 EM T cells	0.001	0.001
mui4EM	1/day	death rate of CD4 EM T cells	0.16	0.32
k31	1/day	differentiaton rate of CD4 EM T cells to Th1 cells	0.04	0.11
k32	1/day	differentiaton rate of CD4 EM T cells to Th2 cells	0.07	0.11
Sr8EM	1/day	TNFalpha dependent recruitment of CD8 EM T cells	53	107
hs8EM	pg/ml	half sat of TNFalpha dependent recruitment of CD8 EM T cells	0.001	0.001
mui8EM	1/day	death rate of CD8 EM T cells	0.17	0.31
k33	1/day	differentiaton rate of CD8 EM T cells to cytotoxic CD8 T cells	0.05	0.11
k34	1/day	differentiaton rate of CD8 EM T cells to Effector CD8 T cells	0.05	0.11
k99	1/day	killing rate constant of BI by TRM	0.3	0.8
APCtimeStart	day	when APCs leave and enter the lymph node	5	28
APCtimeEnd	day	APCs stop leaving granuloma	50	105
APCleave	N/A	Percentage of infected macs considered APCs in granuloma	5	25
localDissemCFUHalf	count	half sat CFU for local dissemination events	6.98E+03	9.71E+03
localDissemLambda	N/A	max probability of local dissemination	0.0005	0.025
nonLocalDissemCFUHalf	count	half sat CFU for non local dissemination	5.22E+03	1.06E+04
nonLocalDissemLambda	N/A	max probability of non local dissemination	0.0001	0.005
MR	count	Resting macrophages	0	0
MI	count	Infected macrophages	1	1
MA	count	Activated macrophages	0	0
T0	count	Primed CD4+ T cells	0	0
T1	count	Th1 cells	0	0
T2	count	Th2 cells	0	0
T80	count	Primed CD8+ T cells	0	0
TC	count	Cytotoxic T cells	0	0
T8	count	Effector CD8+ T cells	0	0
TNF	pg/ml	Tumour Necrosis Factor	0	0
IFNG	pg/ml	interferon	0	0
IL12	pg/ml	Interleukin	0	0
IL10	pg/ml	Interleukin	0	0
IL4	pg/ml	Interleukin	0	0

BI	count	Intracellular Bacteria	1	1
BE	count	Extracellular Bacteria	0	0
CD4Non	count	Nonspecific CD4 T cells	0	0
CD8Non	count	Nonspecific CD8 T cells	0	0
EMCD4	count	Effector Memory CD4 T cells	0	0
EMCD8	count	Effector Memory CD8 T cells	0	0
Parameter Name (LN & Blood)	**Units**	**Parameter Description**	**Minimum Value**	**Maximum Value**
alfa	uL	Conversion from Blood to LN	360000	360000
host_Ln	count	Involved Lymph Nodes in Host	5	5
lambda	count	frequency of specific Naive T cells in system	0.0001	0.0001
hs1	count	half sat of Naive CD4+ T cell recruitment	14	71
hs10	count	half sat of Naive CD8+ T cell recruitment	46	88
hs11	count	half sat of Naive CD8+ T cell priming	13	48
hs13	count	half sat of precursor CD8+ T cell proliferation	2684	4056
hs14	count	half sat of precursor CD8+ T cell differentiation	1904	4144
hs17	count	half sat of Central Memory CD8+ T cell recruitment	66	403
hs4	count	half sat of Precursor CD4+ T cell proliferation	1319	4318
hs5	count	half sat of Precursor CD4+ T cell differentiation	1257	3719
hs8	count	half sat of Central Memory CD4+ T cell recruitment	40	57
k1	1/day	Naive CD4+ T cell recruitment rate	0.12	0.47
k10	1/day	Naive CD8+ T cell recruitment rate	0.77	0.97
k11	1/day	Naive CD8+ T cell priming rate	0.00010	0.00023
k12	1/day	Central Memory CD8+ T cell reactivation rate	0.00012	0.00075
k13	1/day	Precursor CD8+ T cell proliferation rate	0.20	0.80
k14	1/day	Precursor CD8+ T cell differentiation to Effector rate	0.25	0.74
k15	1/day	Precursor CD8+ T cell differentiation to CM rate	0.53	0.86
k16	1/day	Precursor CD8+ T cell differentiation to EM rate	0.16	0.82
k17	1/day	Central Memory CD8+ T cell recruitment rate	0.35	0.90
k2	1/day	Naive CD4+ T cell priming rate	0.33	0.87
k3	1/day	Central Memory CD4+ T cell reactivation rate	0.022	0.080
k4	1/day	Precursor CD4+ T cell proliferation rate	0.30	1.36
k5	1/day	Precursor CD4+ T cell differentation to effector T cell	0.27	0.90
k6	1/day	Precursor CD4+ T cell differentiation to central memory T cell	0.3	0.9
k7	1/day	Effector CD4+ T cell differentiation to EM	0.1	0.6
k8	1/day	Central Memory CD4+ T cell recruitment rate	0.026	0.070
mu1	1/day	Effector CD4+ T cell death rate	0.2	0.2

mu2	1/day	Effector Memory CD4+ T cell death rate	0.04	0.04
mu3	1/day	Effector CD8+ T cell death rate	0.2	0.2
mu4	1/day	EM CD8+ T cell death rate	0.018	0.018
mu5	1/day	APC death rate	0.05	0.05
mu6	1/day	Precursor CD4+ T cell death rate	0.0005	0.0005
mu7	1/day	Precurosr CD8+ T cell death rate	0.015	0.015
mu8	1/day	Naive CD4+ T cell death rate	0.3	0.3
mu9	1/day	Naive CD8+ T cell death rate	0.05	0.05
rho1	count	Precursor Carrying Capacity	300000000	300000000
Wp4	N/A	Weight factor for Precursor CD4+ T cell in CD8+ T cell priming	0.7355	0.7355
xi11	1/day	Central Memory CD8+ Lymph efflux rate	0.275	1.223
xi12	1/day	EM CD8 Lymph efflux rate	0.219	1.521
xi2	1/day	Naive CD4+ Lymph Efflux rate	2	5
xi3	1/day	Effector CD4+ Lymph Efflux rate	1	4
xi5	1/day	Central Memory CD4+ Lymph Efflux rate	1	4
xi6	1/day	Effector Memory CD4+ Lymph Efflux rate	3	4
xi8	1/day	naive CD8 lymph efflux rate	1	2
xi9	1/day	effector CD8 lymph efflux rate	2	4

Table D.2 Effect size measure comparisons for Figure 5.6C.
Vargha and Delaney's A measure calculated pairwise between the three separate groups for differences between fold change of cell entry into lung. When A < 0.56, differences are considered small, if A> 0.71, the differences are considered to be large. Measure values are rounded to the nearest hundredth.

	LTBI vs Active TB groups	TB eliminator vs Active TB groups	TB eliminator vs LTBI groups
CD4+ Effector T cell	0.9	0.91	0.54
CD4+ Effector Memory T cell	0.53	0.64	0.6
CD8+ Effector T cell	0.64	0.84	0.7
CD8+ Effector Memory T cell	0.52	0.67	0.65

Table D.3 PRCC values for host-scale sensitivity analysis.

Parameter Names	Description	PRCC values
LN_k13	Precursor CD8+ T cell proliferation	0.22

LN_k14	CD8+ Precursor differentiation rate to CD8+ Effector T cell	-0.18
LN_k4	Precursor CD4+ T cell proliferation	0.32
LN_k5	CD4+ Precursor differentiation rate to CD4+ Effector T cell	-0.15

Table D.4 PRCC values from granuloma-scale sensitivity analysis for active TB case.

Parameter Names	Description	PRCC values
w3	Max percentage contribution of Th1 cells to Fas-FasL apoptosis of MI	-0.12
s4b		0.13
k2	MR infection rate	0.11
c9	Half-sat of BE on MR infection	-0.14
k17	MI death rate due to BI	0.36
N	Carrying capacity of MI	0.26
k14a	Fas-FasL induced apoptosis of MI	-0.17
k14b	TNF induced apoptosis of MI	-0.15
Sr1b	TNF dependent recruitment of primed CD4+ T cells	-0.21
s4b2	Half-sat of TNF dependent recruitment of primed CD4+ T cells	0.19
k6	Max rate of primed CD4+ T cells differentiating to Th1	-0.22
k7	Max rate of primed CD4+ T cells differentiating to Th2	0.11
s2	Half-sat of IL-4 production	-0.1
c	Half-sat of IFN-γ on Th1 death	-0.12
alpha32	TNF produced by Th1 cells	-0.24
nuTNF	Decay rate of TNF	0.12
alpha7	IFN-γ production by primed CD4+ T cells	-0.19
s12	IL-12 production	-0.19
c230	Half-sat of BI on IL-12 production	0.19
nuIL12	Decay rate of IL-12	0.13
nuIL10	Decay rate of IL-10	-0.13

alpha11	IL-4 produced by primed CD4+ T cells	0.26
alpha20	BE growth rate	0.17
k18	BE killing by MR	-0.22

Table D.5 PRCC values from granuloma-scale sensitivity analysis for TB eliminator case

Parameter Names	Description	PRCC values
k2	MR infection rate	0.11
c9	Half-sat of BE on MR infection	-0.14
k17	MI death rate due to BI	0.22
N	Carrying capacity of MI	0.11
k14a	Fas-FasL induced apoptosis of MI	-0.62
c4	Half-sat of cytotoxic and Th1 cells per MI on MI apoptosis	0.17
alpha11	IL-4 produced by primed CD4+ T cells	0.11
k18	BE killing by MR	-0.12

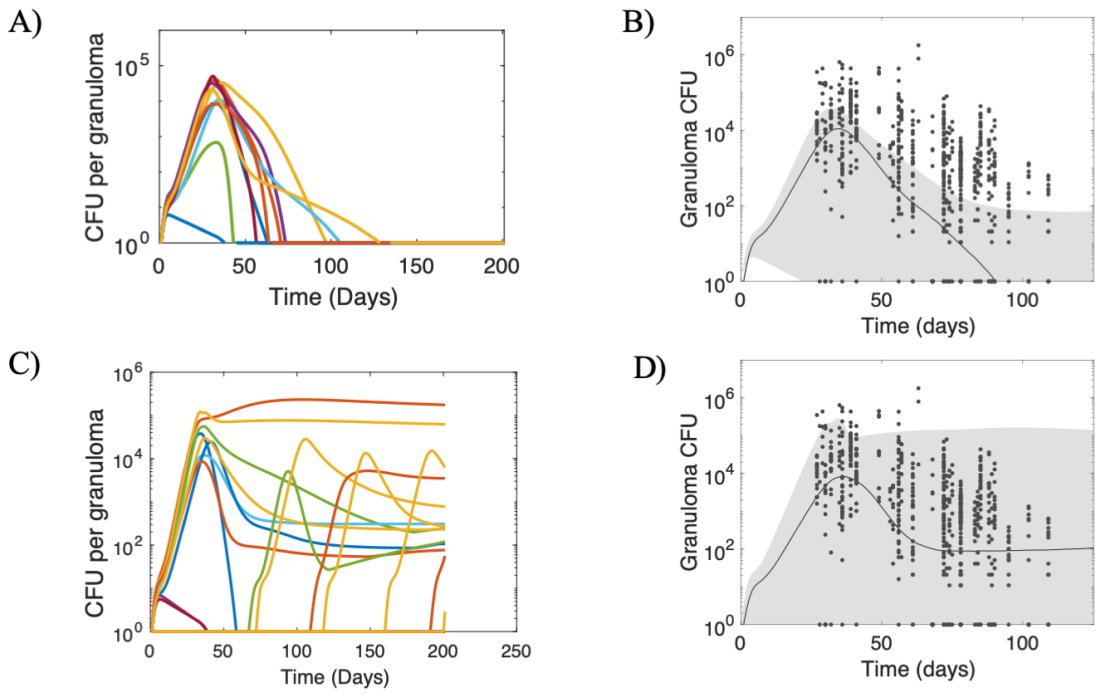

Figure D.1 Representative simulations for intra-compartment sensitivity analysis.
A) CFU trajectories within a single TB eliminator host. B) Minimum, median and maximum CFU trajectories for the TB eliminator host, re-simulated 500 times, varying only granuloma-scale parameters. C) CFU trajectories within a single active TB host. D) Minimum, median and maximum CFU trajectories for the active TB host, re-simulated 500 times, varying only granuloma-scale parameters.

Appendix E Supporting Information for Chapter 6

HostSim Equations with the addition of Resident Memory T cells

The *HostSim* granuloma model equations are shown in full detail in Chapter 5. Briefly, the system of 20 ODEs captures intracellular and extracellular bacterial numbers, various macrophages, various T cells and pro- and anti-inflammatory cytokines across time. In this Chapter, we add a resident memory T cell population (TRM) to reinfection granulomas:

$$T_{RM} = T_{RM}(0)e^{d_{TRM}t}$$

where d_{TRM} is the death rate of TRM and is assigned as 0.03, 0.0012, or 0.0001 cells/day, depending on the study. $T_{RM}(0)$ = [1-10] and is sampled according to a Latin Hypercube sampling scheme, like other parameters in *HostSim*. All other equations remain unchanged, except intracellular bacteria (B_I), which now includes a term from interactions between macrophages and TRM cells that leads to intracellular bacterial death:

$$\frac{dB_I}{dt} = full\ equation\ from\ Chapter\ 5 - k_{BIdeathTRM} * M_I * TRM * \frac{B_I}{M_I}$$

Where $k_{BIdeathTRM}$ = [0.3, 0.8] bacteria/day consistent with rate constants of intracellular bacteria death from interactions with other T cells in *HostSim*, and identified via manual tuning to match the reinfection CFU dynamics of the NHP study by Cadena et al.

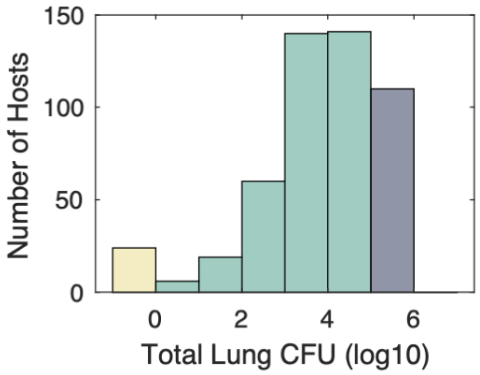

Figure E.1 Histogram of Total Lung CFU in *HostSim* virtual population 500 hosts. Total lung CFU calculated by summing CFU across all granulomas in a host at day 200 following primary infection. Yellow represents hosts that are classified as TB eliminators (total Lung CFU < 1), dark blue represents hosts classified as active TB cases (total Lung CFU > 10^5) and green represents latently infected individuals (LTBI) - those that control infection. Across a

population of 500 hosts, 110 are classified as active TB cases, 366 are classified as LTBI, and 24 are classified as TB eliminators. This breakdown of responses across a virtual population of 500 individuals represents our expected outcomes when calculating reduced risks of developing active TB following reinfection.

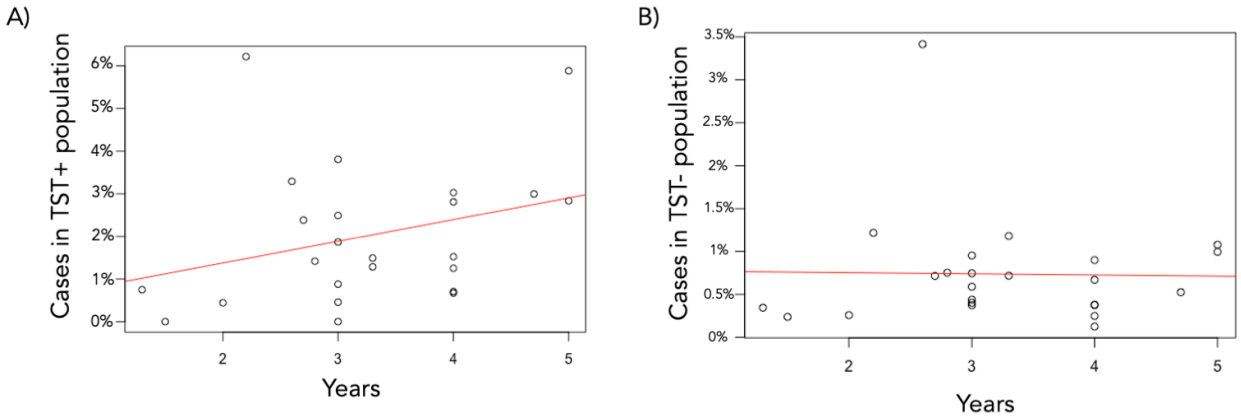

Figure E.2 Percentages of active TB cases per study for TST+/TST- individuals.
A) The percentage of TST+ individuals who develop active TB across time in the meta-analysis by Andrews et al. (ref 22 in Chapter 6). B) the percentage of TST- individuals who develop active TB across time. Each data point is a single study, where the x-axis represents the length of the study.

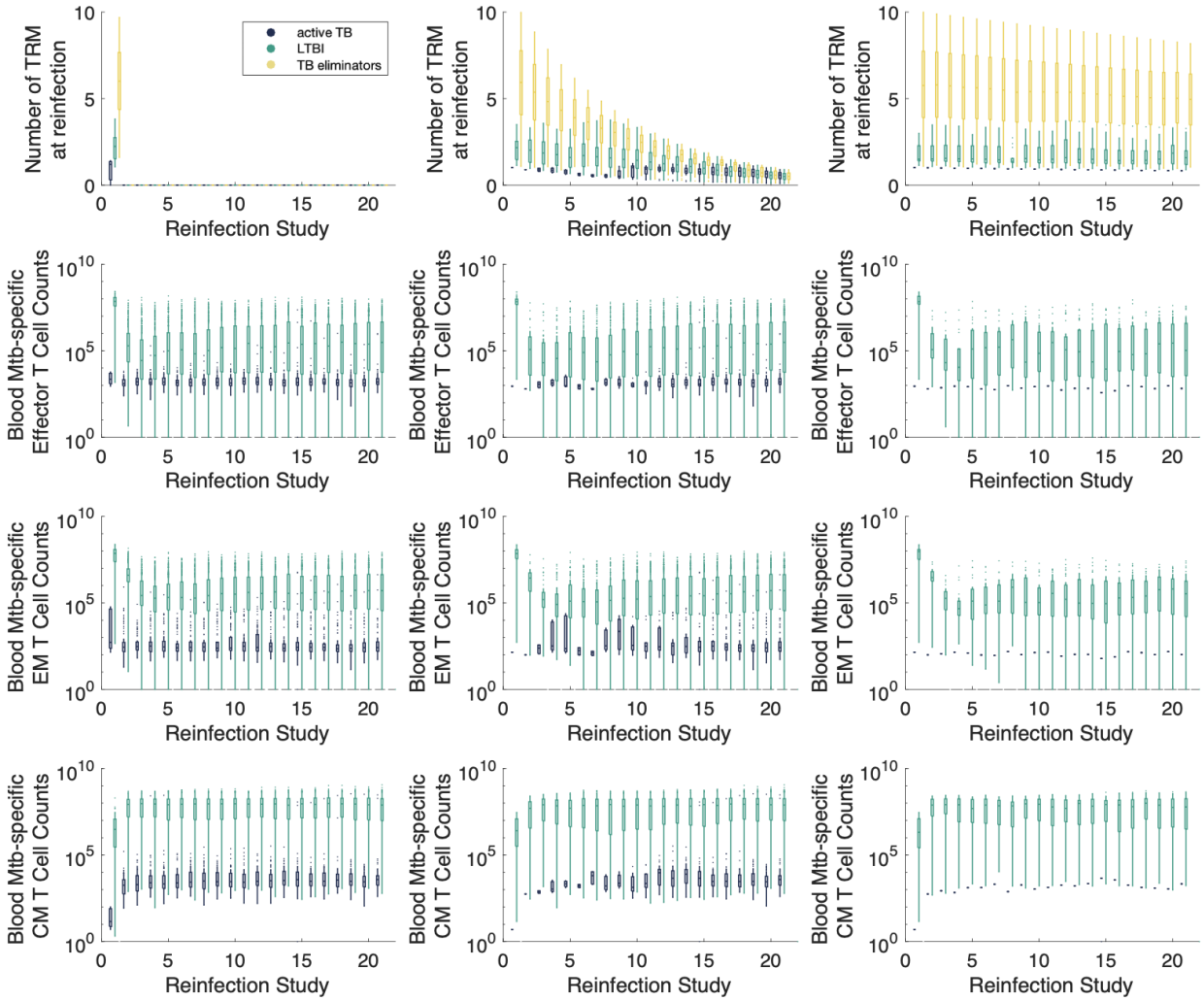

Figure E.3 Blood T-cell counts delineate active TB and LTBI cases for each set of reinfection studies.

Box-and-whisker plots show the distribution of TRM, Mtb-specific effector, effector memory and central memory T cells in the blood for hosts that were active TB, LTBI or TB eliminators following reinfection. Dark blue=active TB, Green = LTBI, yellow=TB eliminator. Each column represents each set of the three reinfection studies; where the death rate of TRM cells from left to right is d_{TRM}=0.03, d_{TRM}=0.0012, and d_{TRM}=0.0001 cells/day.

Appendix F Supplementary Material for Chapter 7

Box 1:
initial parameter ranges -- The widest range for each parameter that are biologically feasible, which includes all previous estimates that have been derived via experimental studies or other models.

pass set definition – Modeler-defined rules that identify the set of model simulations that provide satisfying fits to the experimental datasets. In our examples, the pass set definition outlines a model simulation must pass within the bounds of the range of data points for each time point, across each dataset.

pass run set – The set of model simulations that satisfy the pass set definition. The *fail run set* is the set of model simulations that failed to satisfy the pass set definition.

pass parameter range set – The set of parameter values corresponding to the model simulations that satisfy the pass set definition. The *fail parameter range set* is the set of parameter values for model simulations that failed to satisfy the pass set definition.

termination criterion – The modeler sets this singular value between 0 and 100% that determines when calibration is complete. *CaliPro* iterations continue until the percentage of total model runs that belong to the pass run set is greater than this value. We typically use 75% to 90%, as we prefer not to overfit to any given dataset.

Example 1 Equations: predator-prey model
All equations and parameters are included in the main body of the text for this two-equation model. Additionally, we provide a directory for download that includes all MATLAB scripts for running a fully automated version of *CaliPro* on this predator-prey model example. This includes model parameters, equations and execution. The webpage address where a reader can download the zipped directory is: http://malthus.micro.med.umich.edu/*CaliPro*

Example 2 Equations: ODE granuloma lesion model
As the second example, we apply *CaliPro* to a system of 16 ODEs that capture bacterial, T cell, macrophage and cytokine dynamics within a single granuloma lesion. These ODEs are the granuloma ODEs for the single granuloma model in *MultiGran*, the whole lung model that we presented in Chapter 3. The full set of ODEs is listed in Appendix B.

Example 3 Equations: transmission model of infectious disease

The model used for this example was initially shown in Menzies et al. (ref 35 in main text). More information can be found in their original paper, but briefly, the model includes 6 states including non-susceptible individuals (*N*), susceptible individuals (*S*), early disease cases (*E*), late disease cases (*L*), treatment cases (*T*), and dead individuals (*D*). The number of individuals by state and year (*t*) is given by N_t, S_t, E_t, L_t, T_t, respectively. Individuals enter the model as either non-susceptible or susceptible states, and transition between states to allow for infection (*S* to *E*) disease progression (*E* to *L*), treatment initiation (*E* and *L* to *T*), and death (all other states to *D*) via background and disease-specific mortality. μ parameters are death rates, λ_t is the force of infection based on contact rate, and α represents annual birth rate.

$$\frac{dN}{dt} = ab - \mu^B N$$

$$\frac{dS}{dt} = a(1-b) - \mu^B S - \lambda_t S$$

$$\frac{dE}{dt} = \lambda_t S - (\mu^B - \mu^E)E - r_t^E E - cE$$

$$\frac{dL}{dt} = cE - (\mu^B - \mu^L)L - r^L L$$

$$\frac{dT}{dt} = r_t^E E + r^L L - (\mu^B - \mu^T)T$$

$$\frac{dD}{dt} = \mu^B(N + S + E + L + T + \mu^E E + \mu^L L + \mu^T T)$$

Example 4 Model: agent-based model of granuloma formation

GranSim is an agent-based model of granuloma formation during *Mycobacterium tuberculosis* infection that has been curated for approximately 15 years within our lab. For this model example, we execute a 2D version of *GranSim* representing 4mm by 4mm section of lung tissue that tracks molecular, cellular, and tissue-scale events. We host a website (http://malthus.micro.med.umich.edu/*GranSim*) devoted to *GranSim*'s development and rules. Interested readers can download model parameter sets and a model executable as well.